

Photophysics of Upconversion: Towards Application in Upconversion Displays

zur Erlangung des akademischen Grades einer

DOKTOR-INGENIEURIN (Dr.-Ing.)

von der KIT-Fakultät für Elektrotechnik und Informationstechnik
des Karlsruher Instituts für Technologie (KIT)

genehmigte

DISSERTATION

von

M. Tech., Reetu Elza Joseph

geb. in: Kottayam, Kerala, Indien

Tag der mündlichen Prüfung: 17 Dezember 2020

Hauptreferent: Prof. Dr. Bryce Sydney Richards

Korreferent: Priv.-Doz. Dr. rer. nat. Karl W. Krämer



This document is licensed under a Creative Commons Attribution 4.0 International License (CC BY 4.0): <https://creativecommons.org/licenses/by/4.0/deed.en>

Kurzfassung

Der Regenbogen besteht aus sieben Farben. Von Violett nach Rot, nimmt die Photonenenergie des Lichts ab. Durch die Kombination der Energien von zwei roten Photonen kann ein blaues Photon erzeugt werden. Ein solcher Prozess wird als Upconversion (UC) bezeichnet. UC kann in organischen und anorganischen Systemen beobachtet werden. Zum Beispiel ist die Kombination von zwei roten Photonen zur Erzeugung von blauem Licht in einem organischen System möglich, das aus Platin(II)-Tetraphenyltetrabenzoporphyrin und Perylen besteht. In anorganischen Systemen ist die Umwandlung von Nah-Infrarot (Photonen mit einer Energie, die geringer ist als die der roten Photonen, mit Wellenlängen zwischen 780 und 2500 nm) in sichtbares Licht häufiger. Diese Energieumwandlung wird durch Energieübertragung zwischen den leiterartigen, angeregten Energiezuständen ermöglicht, die in bestimmten Lanthanid-Ionen existieren. Insbesondere das dreiwertige Erbium-Ion (Er^{3+}) ist wegen der Positionen seiner höheren angeregten Energiezustände, die bei Vielfachen tiefer liegender angeregter Zustände liegen, hervorzuheben. Bei der Sensibilisierung mit einem dreiwertigen Ytterbium-Ion (Yb^{3+}), das effektiv nahinfrarotes Licht um 980 nm absorbiert und die Energie auf ein Er^{3+} -Ion übertragen kann, werden vom Er^{3+} -Ion verschiedene Emissionslinien im Sichtbaren beobachtet, wobei die stärksten im grünen und roten Bereich liegen. Damit solche Energieübertragungen stattfinden können, sollten diese Ionen in einem Kristallgitter eingebettet sein. Mehrere Faktoren beeinflussen die Effizienz der anorganischen UC. Dazu gehören die Konzentration der dotierten Ionen, Kristallinität und Phononenenergie des Gitters, und die Ortschaftsymmetrie der Ionen. Noch wichtiger ist, dass die Effizienz der UC aufgrund ihrer nichtlinearen Natur stark von der Anregungsleistungsdichte (EPD von engl. excitation-power-density) abhängt. Ein Ziel dieser Arbeit ist die Untersuchung der Photophysik der UC, insbesondere der Vergleich verschiedener Materialien, die UC zeigen, basierend darauf, wie sie abhängig von der EPD funktionieren. Außerdem ist diejenige EPD zu identifizieren, bei welcher die UC-Emission eines Materials am effizientesten ist. Die Kenntnis dieser Untergrenze würde bei der Kategorisierung der UC-Materialien für verschiedene Anwendungen helfen, die bei verschiedenen EPDs funktionieren.

Um die EPD-Abhängigkeit der UC-Emission eines Materials genau zu untersuchen, müssen zunächst die durch laserinduzierte Erwärmung verursachten Effekte korrigiert werden. Es wurde festgestellt, dass mikrokristallines $\beta\text{-NaYF}_4$, das mit 18% Yb^{3+} und 2% Er^{3+} dotiert ist, einen Temperaturanstieg von 60 K aufweist, wenn es mit 980 nm Laserstrahlung bei einer

EPD von 240 W cm^{-2} angeregt wird. Dieser Effekt führt zu einer Unterschätzung der gemessenen UC-Intensität, die ohne laserinduzierte Erwärmung 24% niedriger als die tatsächliche UC-Intensität ist. Der Effekt ist bei Materialien mit schlechter Wärmeübertragung stärker ausgeprägt. Im Rahmen dieser Arbeit wird eine Methode zur Korrektur der EPD-Abhängigkeit der UC entwickelt, so dass ein effektiver Vergleich der EPD-Abhängigkeiten ermöglicht wird.

Für den Vergleich der EPD-Abhängigkeiten verschiedener UC-Materialien wird ein analytisches Modell entwickelt, das als „Critical Power Density“ (CPD)-Modell bezeichnet wird. Durch Anpassung dieses Modells an die EPD-Abhängigkeiten einer UC-Emission kann eine wichtige Kenngröße, die sogenannte CPD, extrahiert werden. Ein Material mit einem niedrigeren CPD-Wert ist bei einem niedrigeren EPD-Wert ein besserer Upconverter. Dem Modell zufolge ist der CPD-Wert bei einem Material mit langer Lebensdauer im Zwischenstadium niedriger. Darüber hinaus bietet das CPD-Modell zwei verschiedene Möglichkeiten zur Bestimmung der Sättigungs-PLQY der UC, ohne dass die UC durch Anregung bei sehr hohen EPDs in die Sättigung getrieben werden muss, was eine Probedegradation durch Erwärmung verhindert. Erstens beträgt die Sättigungs-PLQY das 5,8-fache des Wertes, der am CPD gemessenen PLQY und zweitens beträgt die Sättigungs-PLQY die Hälfte der PLQY, die durch direkte Anregung des Energiezustandes, dessen PLQY gemessen werden soll, gemessen wird. Es wird festgestellt, dass die experimentell gemessene Sättigungs-PLQY mit den Werten der Sättigungs-PLQY übereinstimmt, die mit dem CPD-Modell ausgewertet wurden.

Schließlich werden die Anforderungen an eine UC-Anzeige diskutiert, nachdem Erkenntnisse über die Funktion der verschiedenen UC-Mechanismen auf der Grundlage des CPD-Modells bei Zwei-Wellenlängen-Anregung (980 nm und 1550 nm) gewonnen wurden. Unter Berücksichtigung der Anforderungen an ein solches Persistence-of-Vision (POV)-Display wird ein Proof-of-Principle eines monochromen UC-Displays demonstriert. Durch Verwendung des Materials $\beta\text{-NaYF}_4$: 18% Yb^{3+} , 2% Er^{3+} , bei einer moderaten EPD von 100 W cm^{-2} , für jede der 980 nm und 1550 nm Anregungen, konnte eine Leuchtdichte von $8 \times 10^6 \text{ cd m}^{-2}$ erreicht werden. Diese Emission wäre bei Umgebungslicht immer noch sichtbar, wenn eine Reduzierung um fünf Größenordnungen durch das Scannen auf POV und die reduzierte Absorption in einem dünnen Film berücksichtigt würde. Im Material SrF_2 : 18% Yb^{3+} , 2% Er^{3+} , konnte durch Wechsel zwischen den beiden verschiedenen Anregungswellenlängen und durch gleichzeitige Anregung die Emissionsfarbe von Rot über Gelb bis Grün variiert werden. Diese Emission wäre aufgrund ihrer geringeren Leuchtdichte, dann für Anwendungen geeignet, die eine Nicht-POV-Anzeige im Dunkeln erfordern.

Abstract

The rainbow has seven colours. As we move from violet to red, the energy of a photon of light decreases. By combining the energies of two red photons, a blue photon can be made. Such a process is called upconversion (UC). UC can be implemented in organic and inorganic systems. For example, combining two red photons to generate blue light is possible in the organic system consisting of platinum(II) tetraphenyltetrabenzoporphyrin and perylene. In inorganic systems, near-infrared (photons with energy less than that of red photons, with wavelengths lying between 780 and 2500 nm) to visible light conversion is more common. This energy conversion is made possible by energy transfer between the ladder-like excited energy states present in certain lanthanide ions. In particular, the trivalent erbium ion (Er^{3+}) is noteworthy owing to the positions of its excited energy states, which are at multiples of energy corresponding to the lower-lying excited states. When sensitized with the trivalent ytterbium ion (Yb^{3+}), which can effectively absorb near infrared light around 980 nm and transfer the energy to the Er^{3+} ion, multiple visible light emissions are observed from the Er^{3+} ion, the strongest being in the green and the red. These ions are usually embedded in a crystal lattice so that these energy transfers can take place. Multiple factors affect the efficiency of inorganic UC like the concentration of the doped ions, crystallinity and phonon energy of the lattice and site symmetry of the ions. Due to its non-linear nature, the efficiency of UC is highly dependent on the excitation-power-density (EPD). An objective of this thesis is to study the photophysics of UC, particularly to compare different materials exhibiting UC based on how they perform as a function of the EPD and to identify the EPD at which the UC emission from a material becomes efficient. Knowing this lower limit, would help in categorizing the UC materials for different applications, which work at different EPDs.

To study the EPD dependence of the UC emission of a material accurately, first the effects caused by laser-induced heating need to be corrected. Microcrystalline $\beta\text{-NaYF}_4$ doped with 18% Yb^{3+} and 2% Er^{3+} is found to have a temperature rise of 60 K when excited with 980 nm laser radiation at an EPD of 240 W cm^{-2} . This effect leads to an underestimation of the measured UC intensity, which was found to be 24% lower than the actual UC intensity if laser-induced heating was absent. This problem is more pronounced in materials with poor thermal transport. A method to correct for the EPD dependence of UC is developed in the course of this work, so that effective comparison of the EPD dependences is made possible.

For comparing the EPD dependences of different UC materials, an analytical model is developed, called the “Critical Power Density” (CPD) model. By fitting this model to the EPD dependence of a two-photon UC emission, an important figure-of-merit, called the CPD can be extracted. A material with a lower value of CPD is a better upconverter at a lower EPD. According to the model, the CPD is lower for a material with long intermediate-state lifetimes. In addition, the CPD model offers two different ways of determining the saturation PLQY of UC without having to drive the UC to saturation by exciting at very high EPDs, which prevents misestimation due to heating. Firstly, the saturation PLQY is 5.8 times the value of the PLQY measured at the CPD and, secondly, the saturation PLQY is half of the PLQY measured by directly exciting the energy-state whose PLQY is to be measured. The accuracy of these novel methods of estimating the saturation PLQY is evaluated and found to be good.

Finally, requirements for a UC display are discussed after gaining knowledge on how the different UC mechanisms work based on the CPD model, upon dual-wavelength-excitation (980 nm and 1550 nm). By considering the requirements of such a persistence-of-vision (POV) display, a proof-of-principle of a monochrome UC display is demonstrated. By using the material β -NaYF₄: 18% Yb³⁺, 2% Er³⁺, at a moderate EPD of 100 W cm⁻², for each of 980 nm and 1550 nm excitations, a luminance of 8×10^6 cd m⁻² could be achieved. This emission would still be visible under ambient light, considering five orders of magnitude reduction due to scanning for POV and reduced absorption in a thin film. In the material SrF₂: 18% Yb³⁺, 2% Er³⁺, by alternating between the two different excitation wavelengths and by simultaneous excitation, the emission colour could be varied from red to yellow to green. This emission would then be suitable for applications, which require a non-POV display in the dark due to its lower luminance.

Table of Contents

Kurzfassung	iii
Abstract.....	v
List of Acronyms	xi
Acknowledgement.....	xiii
List of Journal Publications.....	xv
List of Conference Contributions.....	xvii
1. Introduction	1
1.1. Organic UC	1
1.2. Inorganic UC	2
1.3. Applications of UC	5
1.4. Factors affecting Efficiency of UC	3
1.5. Outline	4
2. Background	5
2.1. Theory of Inorganic Upconversion	5
2.1.1. Coupling of Electronic Angular Momenta.....	5
2.1.2. Determination of Energy states.....	8
2.1.3. Judd-Ofelt Theory.....	10
2.1.4. Energy Transfer between Ions.....	11
2.1.5. UC Mechanisms	13
2.1.6. Mechanisms limiting UC	17
2.2. State-of-the-art of UC Materials and applications to UC Displays.....	22
2.2.1 Luminance Requirements for Displays	25
2.2.2. UC Colour Tuning Methods for Display Applications.....	26
2.3. Summary	29
3. Methods	31
3.1. UC Material Synthesis.....	31

3.1.1. β -NaYF ₄ : 18% Yb ³⁺ , 2% Er ³⁺ Preparation	31
3.1.2. YF ₃ : 18% Yb ³⁺ , 2% Er ³⁺ Preparation	32
3.1.3. La ₂ O ₃ : 18% Yb ³⁺ , 2% Er ³⁺ Preparation.....	33
3.1.4. YCl ₃ : 18% Yb ³⁺ , 2% Er ³⁺ Preparation.....	34
3.1.5. SrF ₂ : 18% Yb ³⁺ , 2% Er ³⁺ Preparation.....	35
3.1.6. β -NaYF ₄ : 18% Yb ³⁺ , 2% Er ³⁺ nanocrystal preparation.....	36
3.2. Steady-State Photoluminescence Spectroscopy	37
3.2.1. Emission Spectroscopy	39
3.2.2. Intensity Dependence	40
3.2.3. PLQY Measurement	40
3.3. Two-Colour Excitation	43
3.4. Time-Resolved Measurements	44
3.4.1. Photoluminescence Decay with Photomultiplier Tube / Multichannel Scaling	44
3.4.2. Evolution of UC Intensity with Time	46
3.5. Analysis of Spectroscopic Data.....	47
3.5.1. Temperature Estimation from Ratio of UC Peaks	48
3.5.2. Multivariate Curve resolution –Alternative Least Squares (MCR-ALS).....	49
3.6. CIE Colour Coordinates and Luminance Determination	52
3.6.1. CIE Chromaticity diagram.....	53
3.6.2. Luminance calculation	54
4. Correcting the Effects of Laser-Induced Heating in Upconversion Measurements ..	57
4.1. Introduction	57
4.2. UC Intensity-EPD Dependence.....	58
4.3. Temperature Determination	59
4.4. Intensity Correction	62
4.5. Excitation-laser-induced heating in liquid samples	65
4.6. Outlook	66
4.7. Summary	67
5. Critical Power Density as a Figure-of-Merit for Upconversion.....	69
5.1. The Critical Power Density Model	70

5.1.1. Balancing Power Density Model	74
5.1.2. Saturation Intensity Model	75
5.2. Identifying Two-photon and Three-photon UC processes.....	75
5.2.1. β -NaYF ₄ : 18% Yb ³⁺ , 2% Er ³⁺	78
5.2.2. YF ₃ : 18% Yb ³⁺ , 2% Er ³⁺	81
5.2.3. La ₂ O ₃ : 18% Yb ³⁺ , 2% Er ³⁺	82
5.2.4. YCl ₃ : 18% Yb ³⁺ , 2% Er ³⁺	84
5.3. Fitting the UC-EPD dependence with the CPD model.....	87
5.4. Comparison with Balancing Power Density model	89
5.5. CPD and UC mechanisms	90
5.6. CPD as an indicator of intermediate-state lifetimes	92
5.7. CPD and saturation Quantum Yield	94
5.8. Calculating the saturation PLQY with CPD model.....	95
5.8.1. Experimental Determination of PLQY and Correction for Thermal Effects	97
5.8.2. Calculation from PLQY at CPD.....	98
5.8.3. Calculation of UC saturation PLQY from Direct Excitation	99
5.8.4. Comparison of PLQY _{sat} estimated with the three methods.....	101
5.9. Summary and Implications for UC displays	102
6. Colour Modification through Dual-Wavelength Pumping.....	105
6.1. UC Colour for Mono-excitation	106
6.2. UC Colour for Dual-excitation.....	109
6.3. Limitations of Dynamic UC displays in a Transparent Medium	112
6.4. Colour Tuning in the Dark	113
6.5. Monochrome UC Display	114
6.6. Summary	117
7. Conclusion.....	119
7.1. Effects of Laser-induced Heating in UC Measurements	119
7.2. Figures-of-Merit for UC Materials	120
7.3. UC Displays	120
7.4. Future work.....	121

References	123
Appendix	133
A.1. Method to find the ground term.....	133
A.2. Microstate approach for finding all the energy levels of a configuration	134
A.3. Calculation of Scaling Factor	144
A.3.1. Using SrF ₂ spectra	144
A.3.2. Using NaYF ₄ spectra.....	145
A.4. Comparison of Calculated and Measured Luminance.....	145
A.4.1. 980 nm @ 10 W cm ⁻² and 1550 nm @ 10 W cm ⁻² in SrF ₂	146
A.4.2. 980 nm @ 100 W cm ⁻² and 1550 nm @ 10 W cm ⁻² in NaYF ₄	147
A.4.3. 980 nm @ 50 W cm ⁻² and 1550 nm @ 10 W cm ⁻² in SrF ₂	148
A.4.4. 980 nm @ 100 W cm ⁻² and 1550 nm @ 10 W cm ⁻² in SrF ₂	149
A.5. Estimation of errors	150

List of Acronyms

UC- Upconversion

DC-Downconversion

DS-Downshifting

LSC-Luminescent solar concentrator

TTA- Triplet triplet annihilation

CPD- Critical power density

PLQY- Photoluminescent quantum yield

PLQY_{sat}- Saturation UC photoluminescent quantum yield

POV-Persistence of vision

BPD- Balancing power density

SI- Saturation intensity

MPR- Multi phonon relaxation

EPD- Excitation power density

MCR-Multivariate curve resolution

CCD- Charge coupled device

LUMO- Lowest unoccupied molecular orbital

HOMO- Highest occupied molecular orbital

TTET- Triplet to triplet energy transfer

ISC- Inter system crossing

DET- Dexter energy transfer

FRET- Förster resonant energy transfer

Acknowledgement

“For in his hand are both we, and our words, and all wisdom, and the works of science, and instruction”
Wisdom 7:16, The Bible

The ways of the Lord are so mysterious that I can nothing but stop in awe looking at where I am now and where I was 5 years ago. All that I am is due to him and my life is forever indebted to him.

Around my 25th birthday, I received an unexpected email from Prof. Bryce Richards offering me an opportunity for a Ph.D. project. The silly me had no idea of how a Ph.D. application is made in Germany and had only applied through the application portal instead of contacting Bryce directly and waited a few months for a response. When I asked the HR people about the status of the application, they redirected it to Bryce and he kindly took note of my application and agreed to be my supervisor. My Ph.D. journey was filled with many hurdles including scholarship-extension rejections, the Corona virus pandemic and three pregnancies. He has always been supportive and helped me throughout the course of my work, giving constructive criticism and encouragement when I needed it and bringing me back on track when I lost focus. Thank you, Bryce, for being a real “Doktorvater”.

“The light shines in the darkness, and the darkness has not overcome it. There was a man sent from God, whose name was John.”
John 1:6, The Bible

Only lately, did I realize that “Ian” is the Scottish version of the name John. Dr. Ian Howard has been a godsend. Every single time I learned something new from him. He has supported me in my ups and downs, always guided me to the right thoughts that would end up in the right solutions and challenged me to bring out the best in me. Always considerate, he helped me by going out of his way, when the kids got sick and or something unexpected came up. Thank you, Ian, for all the new learnings and re-directions.

Dr. Dmitry Busko had the answers for almost all problems in the Optics labs. He was my go-to-guy when something broke or when results did not make sense. Thank you, Dmitry, for your LabVIEW programs, and the experimental skills you transferred to me.

Dr. Damien Hudry and Dr. Guojun Gao synthesized the samples used in this Thesis. Moreover, along with Dr. Andrey Turshatov, when more detailed information was needed from the material science point of view, expert counsel was always at hand. They made sure that the photophysical considerations made sense in a chemist’s point of view. Thank you, Damien, Guojun and Andrey for the samples and helpful discussions.

Dr. Karl Krämer and Daniel Biner from the University of Bern were always ready to share their know-how about material synthesis and helped me expand my knowledge of UC. Being co-authors of the three publications described in this thesis, they were always available for my last minute questions and requests, even on holidays. Thank you, dear Karl and Daniel, for sharing your knowledge and good will.

Dr. Ritesh Haldar gave me the opportunity to work with him and help widen my knowledge. Spectroscopic measurements and analysis I did along with him on crystalline coordinated networks resulted in two peer-reviewed publications. Thank you, Ritesh, for giving me this interdisciplinary opportunity.

My colleagues have been an integral part of my PhD. From helping me to get accustomed with new instruments, problem solving, constructive criticism, and providing well-needed distraction at times, they have enriched my PhD life. Thank you Ngei, Michael Adams, Nicolo, Michael Oldenburg, Stephan, Marius, Sheying, Natalia, Vinay, Milian, Deski, Aiman, Lwitiko and Pariya. A special thanks to Ngei for proof-reading my thesis. Thanks to my office mates over the years, I got a lot of international experience and insight into the German culture. Thank you, Sebastian, Pascal, Tom, Katsumasa, Andrey, Niels, Paul and Adrian.

Being part of the Karlsruhe School of Optics and Photonics (KSOP) was a delight. The different interdisciplinary courses, conferences and seminars conducted by KSOP and the support provided by the KSOP team were priceless. Thank you, dear Denica Angelova-Jackstadt, Miriam Sonnenbichler, Stephanie Peer, Dr. Huijuan Zhou and Dr. Franco Weth.

The German academic exchange service (DAAD) funded my research with their Ph.D. scholarship which made all this possible. Thank you, Anuroopa Dixit, Bettina Mömesheim and Antje Langerbein for advising me and supporting me all throughout my scholarship period.

Meinen Freunden in Deutschland, insbesondere Lina, Gertrud, Alois, Oma Rosa, Tessy, Aby, Jane, Kiran, Riya und allen anderen in der Gebetsgruppe, die in meinem Leben außerhalb des KIT eine sehr wichtige Rolle gespielt haben, möchte ich ebenfalls meinen größten Dank übermitteln. Ihre Liebe und Fürsorge haben mir nie das Heimweh getrieben und uns in all unseren Höhen und Tiefen unterstützt.

My family has been always supportive of my career decisions. My dear husband Joe took the risk of taking a break in his career for my Ph.D. dream. His constant encouragement and support helped me navigate the hard days of Ph.D. life. My eldest daughter Rosanne is as old as my Ph.D. I flew to Germany from India when she was just 56 days old. Mariette and Jeremy were born during my research period. The three bundles of joy made sure that I feel top of the world every time I came home. From earnest comments like “I like it most Mama, when you wear jeans and go to work” and saying “I love you mama” a thousand times, they encouraged me and surprised me with their wisdom. My parents Joseph and Raji, and Joe’s parents Mathai and Annamma have always wanted the best for us and supported us by helping in the times after the deliveries and took care of the kids during summer holidays, travelling all the way from India. My brothers Jos and Jim have contributed to everyday joy, even taking up remote childcare. Thank you, dear family. No words are enough to thank you all.

List of Journal Publications

Articles in peer-reviewed journals as first author:

1. **R. E. Joseph**, C. Jimenez, D. Hudry, G. Gao, D. Busko, D. Biner, A. Turshatov, K. Krämer, B. S. Richards, and I. A. Howard, "Critical Power Density: A Metric To Compare the Excitation Power Density Dependence of Photon Upconversion in Different Inorganic Host Materials," *Journal of Physical Chemistry A* 123(31), 6799–6811 (2019).
2. **R. E. Joseph**, D. Busko, D. Hudry, G. Gao, D. Biner, K. Krämer, A. Turshatov, B. S. Richards, and I. A. Howard, "A Method for Correcting the Excitation Power Density Dependence of Upconversion Emission due to Laser-Induced Heating," *Optical Materials* 82, 65–70 (8).
3. **R. E. Joseph**, D. Busko, D. Hudry, G. Gao, D. Biner, K. Krämer, A. Turshatov, B. S. Richards, and I. A. Howard, "Bright constant color upconversion based on dual 980 and 1550 nm excitation of SrF₂:Yb³⁺, Er³⁺ and β-NaYF₄:Yb³⁺, Er³⁺ micropowders; considerations for persistence of vision displays," *Optical Materials* (2020), DOI:10.1016/j.optmat.2020.110598

Co-authored articles based on theoretical and experimental knowledge of photophysics of upconversion and other spectral conversions:

1. R. Haldar, Z. Fu, **R. Joseph**, D. Herrero, L. Martín-Gomis, B. S. Richards, I. A. Howard, A. Sastre-Santos, and C. Wöll, "Guest-responsive polaritons in a porous framework: chromophoric sponges in optical QED cavities," *Chemical Science*. 11(30), 7972–7978 (2020).
2. R. Haldar, A. Mazel, **R. Joseph**, M. Adams, I. A. Howard, B. S. Richards, M. Tsotsalas, E. Redel, S. Diring, F. Odobel, and C. Wöll, "Excitonically Coupled States in Crystalline Coordination Networks," *Chemistry – A European Journal* 23(57), 14316–14322 (2017).
3. G. Gao, A. Turshatov, I. A. Howard, D. Busko, **R. Joseph**, D. Hudry, and B. S. Richards, "Up-Conversion Fluorescent Labels for Plastic Recycling: A Review," *Advanced Sustainable Systems* 1(5), 1600033 (2017).

4. G. Gao, D. Busko, **R. Joseph**, A. Turshatov, I. A. Howard, and B. S. Richards, "High Quantum Yield Single-Band Green Upconversion in $\text{La}_2\text{O}_3:\text{Yb}^{3+}, \text{Ho}^{3+}$ Microcrystals for Anticounterfeiting and Plastic Recycling," *Particle & Particle Systems Characterization* 36(3), 1800462 (2019).
5. G. Gao, D. Busko, **R. Joseph**, I. A. Howard, A. Turshatov, and B. S. Richards, "Highly efficient $\text{La}_2\text{O}_3:\text{Yb}^{3+}, \text{Tm}^{3+}$ single-band NIR-to-NIR upconverting microcrystals for anti-counterfeiting applications," *ACS Applied Materials & Interfaces* 10, 39851–39859 (2018).
6. G. Gao, N. Katumo, E. Madirov, **R. Joseph**, D. Busko, I. A. Howard, A. Turshatov, and B. S. Richards "Ratiometric luminescent thermometry with excellent sensitivity over a broad temperature range utilizing the absolute increase and decrease with temperature of thermally-assisted and multiphoton upconversion in triply doped $\text{La}_2\text{O}_3:\text{Yb}^{3+}/\text{Er}^{3+}/\text{Nd}^{3+}$ " *Advanced Optical Materials* (2020) Accepted.

List of Conference Contributions

1. **R. E. Joseph**, C. Jimenez, D. Hudry, G. Gao, D. Busko, A. Turshatov, B. S. Richards, and I. A. Howard, "An analytical model for the excitation power density dependence of two-photon upconversion in lanthanide-doped micropowders", EMRS Spring Meeting, Nice, France, May 27-31, 2019, oral presentation
2. **R. E. Joseph**, C. Jimenez, D. Hudry, G. Gao, D. Busko, D. Biner, A. Turshatov, K. Krämer, B. S. Richards, and I. A. Howard, "Correction of Intensity Dependence of Upconversion due to Laser Induced Heating", 7th Meeting of Women in Photonics, Karlsruhe, Germany, March 14, 2018, poster
3. **R. E. Joseph**, C. Jimenez, D. Hudry, G. Gao, D. Busko, D. Biner, A. Turshatov, K. Krämer, B. S. Richards, and I. A. Howard "Characteristic Threshold for Inorganic Upconversion", KSOP Summer School; Bad Herrenalb, Germany, November 7-9, 2018, poster
4. **R. E. Joseph**, D. Hudry, G. Gao, D. Busko, D. Biner, A. Turshatov, K. Krämer, B. S. Richards, and I. A. Howard "Investigation of Photophysics of UC", Karlsruhe Days of Optics and Photonics; Karlsruhe, Germany, September 9-10, 2019, poster
5. **R. E. Joseph**, D. Hudry, G. Gao, D. Busko, D. Biner, A. Turshatov, K. Krämer, B. S. Richards, and I. A. Howard "Investigation of Photophysics of Upconversion", KSOP Qmat Summer School; Online conference, September 3-4, 2020, poster

1. Introduction

Upconversion (UC) is a process by which low energy radiation is converted to higher energy. Essentially the energies of two or more photons are combined to generate a higher energy photon. It is distinct from two-photon-excited fluorescence in the sense that an actual intermediate state is always present in the case of UC. Two-photon-excited fluorescence on the other hand depends upon the process of two-photon absorption [1], wherein simultaneous excitation of two photons via a virtual intermediate state populates the excited state from which radiative emission takes place. Two-photon-excited fluorescence is generally an intramolecular process [2] with much lower efficiency [3], whereas UC can take place within a single ion or when two ions interact with each other. Just as two-photon-excited fluorescence, UC is observed in both organic and inorganic systems. The following sections briefly discuss the working principle of UC and its applications.

1.1. Organic UC

In organic systems, the chief mechanism of UC is triplet-triplet annihilation (TTA). The Jablonski diagram provided in Figure 1.1 gives an overview of the TTA UC process. Two sensitizer molecules in their singlet ground states (S_0) absorb a photon each and move into their first excited singlet states (S_1). In other words, excitons (electron-hole pairs) are created in the sensitizer molecules as the electron accepts the energy from the photon and moves into the lowest unoccupied molecular orbital (LUMO), leaving a hole in the highest occupied molecular orbital (HOMO). This electron retains the same direction of spin it had in the HOMO, which is complementary to the spin of the other electron in the same orbital according to Pauli's exclusion principle [4]. Due to the presence of a heavy metal ion such as Pd(II) or Pt(II), the electron undergoes intersystem crossing (ISC), thereby its direction of spin reverses, and the molecule moves to a triplet state, T_1 [5,6]. The triplet sensitizer molecules transfer their energies to the emitter molecules which get promoted directly from their singlet ground states to their first triplet states, and as a result, the sensitizers return to the ground state. This energy transfer is called triplet to triplet energy transfer (TTET). Two emitter triplets interact with each other resulting in one emitter molecule being promoted to its first excited singlet state and the other one moving back to the ground state. This singlet exciton of the emitter decays eventually, resulting in a delayed fluorescence with lifetimes of the order of microseconds. The lifetimes of this fluorescence are longer as compared to that of conventional fluorescence

which has lifetimes of the order of nanoseconds. The emitted energy is higher than the excitation-energy and the process is thus called TTA upconversion.

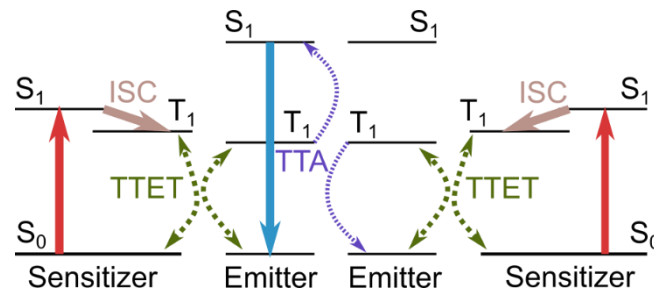


Figure 1.1 Jablonski diagram showing the most common scheme of TTA UC

Classic sensitizers are heavy metal containing porphyrins [7,8], however colloidal nanocrystals can be also used as sensitizers for upconversion from the near infrared (NIR) to visible range [9,10]. Different pathways can also be implemented for TTA upconversion like temperature activated delayed fluorescence (TADF) sensitizers with relatively high gains due to lower energy loss in the ISC step and sensitizers with direct singlet to triplet (S-T) absorption to completely bypass the inter system crossing (ISC) loss [11,12].

1.2. Inorganic UC

Inorganic UC is observed in host materials doped with ions of certain f-block and d-block elements. It was first proposed by Bloembergen in 1959 for a solid-state infrared (IR) quantum counter [13] (device for detecting and counting IR photons). It was first experimentally observed by Auzel in 1966 [14]. He converted NIR light into visible green emission (using Yb^{3+} - Er^{3+} ion pair). In the same year, UC was observed by Ovsyankin and Feofilov by converting IR light into visible blue emission (Yb^{3+} - Tm^{3+} ion pair) [15]. The basic working principle of inorganic UC is that the f-block elements have well-defined ladder like excited energy states which facilitate combination and radiative relaxation of energy. Through an initial photon-absorption, some ions reach an intermediate excited state. The neighbouring ions transfer their energies between each other through different processes and finally one ion reaches an excited meta-stable state. Radiative relaxation from this state results in UC emission which has two, three, or four times the energy of the absorbed photons based on the order of the UC process. Though not common, UC emissions resulting from seven photons are also observed [16]. The Dieke diagram (Figure 1.2) gives an overview of the excited energy states possible for trivalent lanthanides [17,18]. Commonly observed radiatively emitting energy states are marked with a filled semicircle under the representation for the state.

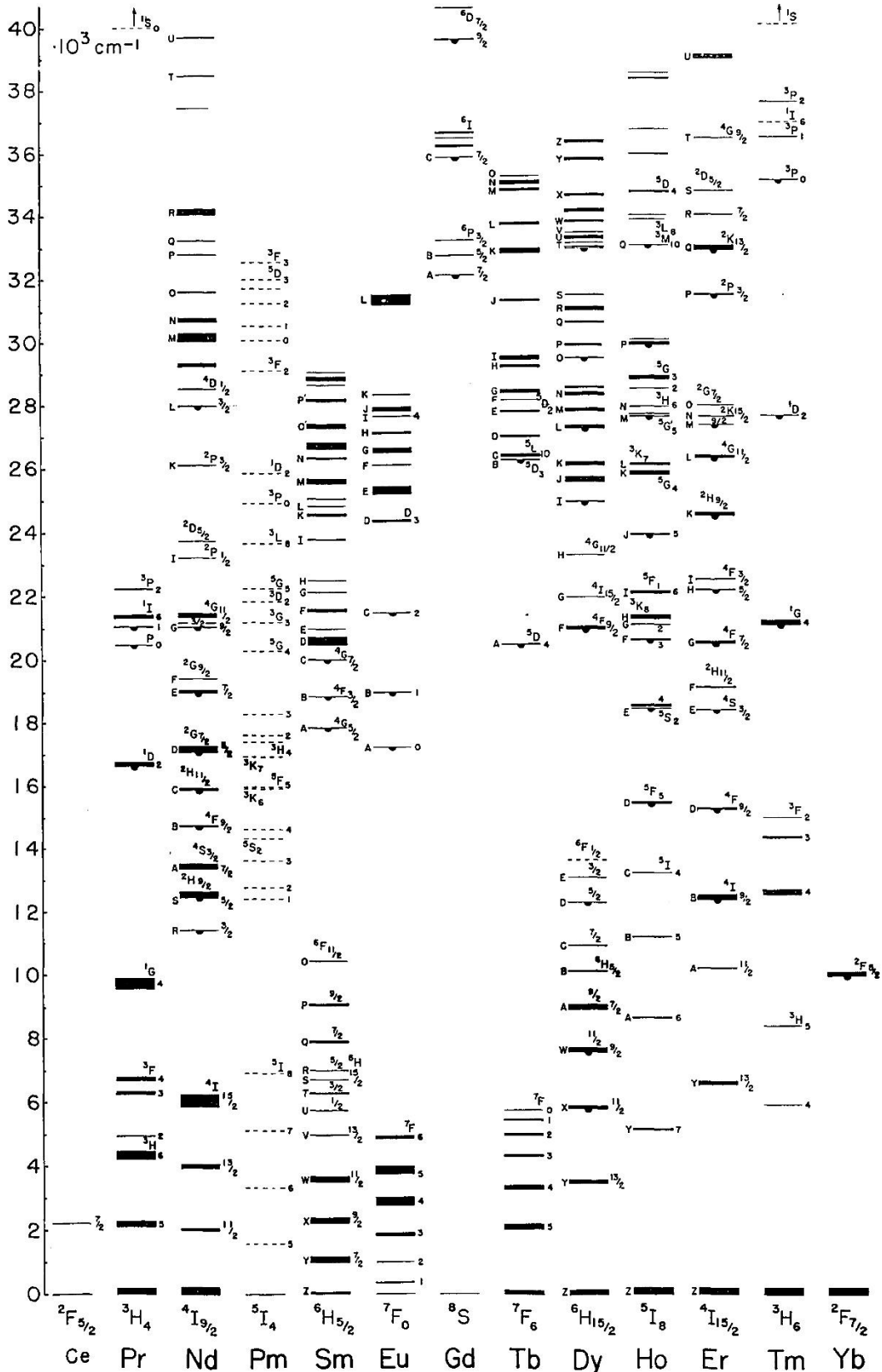


Figure 1.2. Classic Dieke diagram showing the excited energy states of trivalent lanthanides [17]

As UC is a multi-order process, the UC intensity has a non-linear behaviour with respect to the excitation-power-density (EPD) of the incident radiation. Therefore, the intensity of UC emission does not have a linear dependence to the excitation power density (EPD) throughout. Non-linearity can be easily observed on the double logarithmic plot of the UC intensity vs EPD. For a linear process, the slope of the dependence plot would remain 1 and the plot will be a straight line. On the other hand, for a non-linear process, the slopes vary as the EPD changes resulting in a curve instead of a straight line. Figure 1.3 presents an example of such a UC-EPD dependence curve. The slopes of the double-logarithmic plot decrease from 2.5 to 1 as the EPD increases. The straight line drawn in blue is a guide to the eyes to show the deviation from linearity. Section 2.1 in Chapter 2 is dedicated for explaining the working principle of inorganic UC which includes more details about the non-linear behaviour.

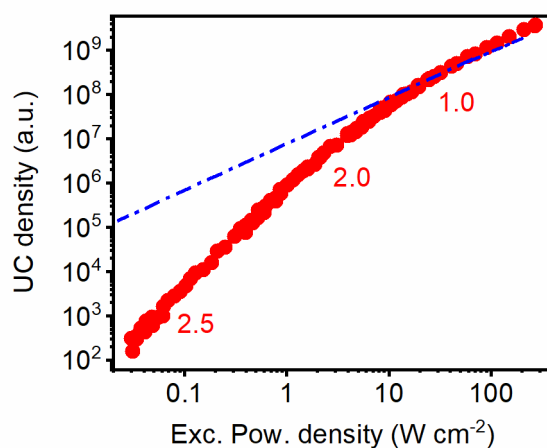


Figure 1.3. Double-logarithmic plot of UC density vs EPD for the red emission from an erbium doped material showing the non-linearity of the UC process. The blue line is a guide for the eyes with a slope of 1. The numbers in red indicate the slopes at in the corresponding regions.

The main differences in the properties of lanthanide based inorganic UC and TTA based organic UC are summarized in Table 1.1. TTA UC suffers from a lower value of anti-stokes shift because, it essentially can combine only the energies of two photons, whereas lanthanide based UC emissions can combine the energies of more than two photons based on the lanthanide system used. Though the absorption cross-sections of TTA sensitizers in the visible regime are very high, the triplet states are highly sensitive to oxygen and water content. Molecular oxygen in its natural form is in the triplet state and presence of oxygen in a potential TTA UC mixture will highly quench the triplet states formed leading to poor UC emission. Lanthanide based UC on the other hand is not sensitive to oxygen. Organic dyes which can effectively absorb an excitation-wavelength below 845 nm and sensitize TTA UC are yet to be discovered, which limits the range of excitation-wavelengths for TTA-UC to the beginning or the NIR regime, whereas lanthanide UC can benefit from much longer excitation-wavelengths based on the excited energy states of the lanthanide involved [19,20]. Trivalent erbium based

UC has an absorption peak around 1530 nm which opens possibilities for making use of otherwise unused part of the solar spectrum for photovoltaic applications. Generally the overall photoluminescent quantum yield (PLQY) is higher for TTA-UC as compared to lanthanide based UC [19]. Researchers are now trying to develop hybrid upconversion systems which would have increased efficiencies than TTA and lanthanide UC [21,22].

Table 1.1. Comparison of properties of TTA-UC and lanthanide based inorganic UC

Property	TTA-UC	Lanthanide UC
Anti-Stokes Shift	Low (only two-photon UC)	High (up to 7 photon UC possible) [16]
Stability in oxygen and aqueous environments	Low	High
Absorption bandwidth	High	Low
Visible light absorption	High	Low
Efficiency at low EPD	High	Low
NIR light absorption	Only up to 845 nm [20]	High

1.3. Applications of UC

Exceptional properties of UC like anti-Stokes emission, delayed fluorescence, and narrow bandwidth make these materials ideal candidates for different applications such as lasers [23], spectral conversion for photovoltaics [24], analytical sensors [25], security inks [26], plastic recycling [27] and 3D volumetric displays [28]. For biological applications, UC is advantageous because of the absence of auto-fluorescence, low cytotoxicity, ability to penetrate deeply in tissues, and non-invasive property. Therefore UC is employed in phototherapy [29], biological imaging and sensing [30,31], and luminescence thermometry [32].

Normal lasers emit at a wavelength which is longer than that of the pump wavelength. In case of most UC lasers, the emitted wavelength is normally shorter than that of the pump light. So such lasers can be used in place of frequency doubling devices [33]. Erbium based lasers when excited around 980 nm emit green laser light [34], thulium based lasers emit blue light upon excitation between 1120-1140 nm [35], and praseodymium/ytterbium-based lasers can emit blue, green, orange or red colour when excited around 860 nm [36]. Most of these lasers are constructed using fluorozirconate glass fibres ($ZrF_4 - BaF_2 - LaF_3 - AlF_3 - NaF$ (ZBLAN)).

Another class of UC based lasers, act similarly to normal lasers and emit light of lower frequency than that of pump light. These make use of the radiative transitions from the excited state to the intermediate states, and emit in the IR regime [23,37,38].

In spectral conversion applications, a UC layer is ideally attached to the rear-side of a bi-facial solar cell [39]. Two or more photons are absorbed by the upconverting material to emit a photon of higher energy that can be absorbed by the solar cell. For trivalent erbium based UC layers, light is absorbed around 1500 nm and chiefly emitted in the near infrared (NIR) region of the spectra, though a minute percentage of the emissions are in the blue, green, and red regions. Under concentrated sunlight (94 suns), an additional photocurrent of 9.4 mA/cm² is obtained for a solar cell fitted with a UC layer containing microcrystalline β -NaYF₄ doped with 25 % Er³⁺ [24]. Though it provides an alternative way of overcoming the Shockley–Queisser limit for single-bandgap solar cells, the efficiencies resulting from UC under normal sunlight is strikingly low, underlining the need for further research [40].

Security marking and plastic recycling rely on the capability of different UC materials to emit visible light of different wavelengths based on the composition of the materials [27]. The security marking/QR codes or colour markers embedded in the polymer become visible only under NIR illumination (~980 nm) and hence cannot be easily replicated as the composition of the UC materials needs to be known [26].

There are three biological windows in which biological tissues are transparent to radiation. The first biological window spans from 700 to 950 nm, the second biological window from 1000 to 1350 nm, and the third biological window from 1550 to 1870 nm [41]. By making use of the biological windows, UC materials can be used for bio-imaging and phototherapy. The non-linear nature of UC emissions ensures background-free and high-contrast images at lower EPDs, enabling non-invasive deep tissue imaging which does not harm the living cells [42]. Most of the UC materials are also non-toxic, and can be safely used for therapeutic applications which include drug-delivery [43,44], photodynamic therapy [30,45], and photothermal therapy [46].

The idea of 3D display based on UC was proposed by Lewis *et al.* in 1971 [47] and such a display based on excited state absorption (ESA) was developed by Downing *et al.* in 1996 [48]. These displays made use of two lasers with different excitation-wavelengths which were made to intersect at an angle, where the UC material will emit to trace the required pattern/figure. The advantage of such a volumetric display is that the medium can remain static, while the image can be drawn by raster-scanning of the two excitation lasers [49]. Using 979 nm excitation on trivalent erbium doped ZBLAN glass, Honda *et al.* demonstrated a 3D display using only one excitation wavelength for the first time in 1998 [50]. Such a display makes use

of the energy-transfer UC (ETU) process and is of higher efficiency than the ESA based displays. A detailed explanation of the ESA and ETU processes is provided in section 2.1.5. Different kinds of media are suggested for such volumetric displays which include index matched polymers, colloids, single crystals, gases and optical gels [49,51,52]. In this work, a proof-of-principle of a UC display based on erbium/ytterbium doped hexagonal NaYF₄ microcrystals is demonstrated in chapter 6. The efficiency of UC in this case is much enhanced due to the co-doping of the trivalent erbium ion with the trivalent ytterbium ion as compared to the display proposed by Honda et al. Additionally hexagonal NaYF₄ is a well-known host in which the UC has very high PLQY [53,54].

1.4. Factors affecting Efficiency of UC

Different factors contribute to the efficiency of UC in inorganic hosts which include host composition, optimization of the concentration of the dopants, co-doping with multiple ions, different host architectures, and excitation with multiple wavelengths [55]. Understanding the photophysics of UC is key to finding new materials of higher efficiency and new applications for this technology. It is not yet clear to the scientific community if new hosts should be discovered which would increase the efficiency of UC, or if more focus is to be provided in improving the properties of the fluoride hosts, which seem to be the champions in case of UC. Considering the maximum phonon energy alone, chlorides are supposed to be better hosts for UC as compared to fluorides as they have generally lesser phonon energies, but experimental results do not support this theory completely [39]. The site symmetry of the dopant ions is also found to play a role in the PLQY of the UC, as the relative intensity-ratios between different transitions are affected which in turn affects the PLQY and total energy yield [56]. The coupling between electrons and phonons, the crystallinity of the host material, also its morphology and size also affect the efficiency of UC [57,58]. Generally single-crystals and microcrystals have higher PLQYs as compared to nanocrystals, but the crystal sizes limit the applicability for specific purposes [59]. The inter-ionic distance (indirectly doping concentration) also plays a major role in the transfer of energy between the different lanthanide molecules, but then the UC is also limited by concentration quenching effects [60,61]. Laser-induced heating is also found to adversely affect the PLQY, but in some cases it actually facilitates biological applications like treatment of tumours [62–64].

Thus, a vast amount of research work has been performed on UC in the past few decades, but still many questions remain unanswered. Proper characterization of UC materials is the first step to effective comparison and analysis. In this work, therefore, a figure-of-merit is developed to compare how UC materials perform as a function of excitation power density, specifically looking at which excitation power density does the UC for a given material system becomes efficient. Understanding this lower limit is important for applications that would benefit from UC

at lower excitation power densities, including UC displays and the aforementioned solar spectral conversion.

1.5. Outline

The thesis is structured into seven chapters. The second chapter provides the Background for the results presented in this Thesis. In this chapter, the theory of inorganic UC is described in detail and the state-of-the-art UC materials are presented with respect to their application in UC displays. The reason for the presence of the ladder like energy states of the trivalent lanthanides is explained from fundamental principles and the different mechanisms of UC are elucidated. The third chapter presents the methods used in collection and analysis of the data presented in this work. The experimental results are then systematically presented in chapters 4 to 6. In chapter 4, the effect of laser-induced heating on measurement of excitation-power-density dependence of UC is discussed. The temperature of the material is estimated using luminescence thermometry and a method to correct the dependence is developed. In chapter 5, an important figure-of-merit for comparison between UC materials called the critical power density is estimated from the UC vs excitation-power-density curve for different UC materials. The materials are then ranked based on the critical power density and the saturation photoluminescent quantum yields of these materials are estimated with the help of the critical power density model. In chapter 6, UC upon two-colour excitation is discussed and the proof-of-concept of a monochrome display based on excitation with two different wavelengths is demonstrated. Chapter 7 summarizes the work and discusses the future outlook of the work.

2. Background

This chapter provides the framework for understanding the experimental results in chapters 4 through 6. The first part deals specifically with the theory of inorganic UC and the second part discusses the state-of-the-art materials used for UC displays. Section 2.1.1 deals with the quantum mechanics of lanthanide ions and their energy states. Section 2.1.2 explains how the energy states of an ion or atom can be determined. Section 2.1.3 explains the mechanism of energy transfer between two ions. Section 2.1.4 presents the Judd-Ofelt theory, which is used to calculate the intensities and probabilities of energy transfers between these energy states. Sections 2.1.5 and 2.1.6 present the mechanisms driving UC and the mechanisms limiting UC, respectively. Section 2.2 discusses the state-of-the-art of UC materials and explains the choice of the materials used in this work. The requirements for a UC display to be visible under ambient light are elucidated in Section 2.2.1 and the different colour tuning methods used UC displays are explained in Section 2.2.2. Finally, Section 2.3 provides a brief summary.

2.1. Theory of Inorganic Upconversion

2.1.1. Coupling of Electronic Angular Momenta

To understand the basic principle of UC, we first need to understand how the electrons in an atom/ion interact with each other forming quantized energy states. A set of four quantum numbers describe the state of an electron in an atom, as predicted by the Schrödinger wave equation [65]:

$$\mathcal{H}\Psi_n = E_n\Psi_n \quad . \quad (2.1)$$

Here, \mathcal{H} is the Hamiltonian operator which is the sum of the kinetic and potential energies of a system. Ψ_n is the set of all the wavefunctions, the square of which called the probability density (Ψ_n^2), gives the probability of finding the particle it describes at a position marked by the coordinates. The energies E_n gives the eigenvalues of Ψ_n . The set of all the probabilities for a particular Ψ_n is termed an orbital.

The four quantum numbers which define a wavefunction Ψ are the principal quantum number (n), azimuthal quantum number (ℓ), magnetic quantum number (m_ℓ) and spin quantum number (m_s). The principal quantum number describes the electron shell or the energy level, the

azimuthal quantum number or the orbital momentum quantum number gives the subshell or shape of the orbital, the magnetic quantum number gives the projection of the orbital angular momentum along a particular axis, and the spin quantum number gives the direction of the spin. Table 2.1 gives a list of the possible quantum numbers that an electron in an atom can take with the permissible range of values.

Table 2.1. Four quantum numbers describing the state of an electron in an atom

Name	Symbol	Range of values	Meaning
Principal quantum number	n	$1 \leq n$	shell
Azimuthal quantum number	ℓ	$0 \leq \ell < n$	sub-shell
Magnetic quantum number	m_ℓ	$-\ell \leq m \leq \ell$	orientation of sub-shell
Spin quantum number	m_s	$-1/2$ or $1/2$	direction of spin

For a multi-electron system in its ground state like that of an atom, the electrons occupy the orbitals in the order of increasing energy ($n+\ell$) according to the well-known Aufbau principle. For sub-shells with the same value of ($n+\ell$), the ones with lower n are filled first. Among the many orbitals in the same sub-shell, the electron behaviour is according to the Hund's rule and Pauli's exclusion principle. When an atom receives energy from a photon, which is more than its work function, it becomes free of the attraction of the nucleus of the atom, as described by the photoelectric effect. Then the atom becomes a positive ion. If this energy is not sufficient for it to be released out of the atom, the electron moves into an excited state, but still remains under the influence of the nucleus. These excited states are of well-defined energies and are regulated by the interaction of the spin and orbital angular momenta. The spin and orbit of a single particle can interact with each other, causing fine splitting of the energy levels of an atom. When more than one electron is involved, the orbital angular momenta also interact with each other due to Coulomb forces. Another possibility is the interaction of spins of two particles. Therefore, for a multi-particle system, the possible excited energy states that can be assumed by the electrons are a result of the combined effect of orbit-orbit, orbit-spin and spin-spin interactions.

For light atoms (atomic number, $Z < 30$), the spin-orbit coupling is negligible, so the spin angular momentum generated by all intrinsic spins can be added together and considered with the total orbital angular momentum to find out the net angular momentum of the system such that [66]:

$$S = \sum_i s_i \quad , \quad (2.2)$$

$$\text{and } L = \sum_i \ell_i \quad . \quad (2.3)$$

Spectroscopic notation ascribes the letters S,P,D,F,G,H,I,K,L,...,Z for the total orbital angular momentum for values of $L=0,1,2,3,4,5,6,7,8,\dots,20$ [67]. For values of $L>20$, letters are not used. This representation of L is different from the conventional name for the orbital in which the electron is existing and it is merely used to indicate the sum of the magnetic quantum numbers of the occupied sub-orbitals. Then the total angular momentum J can be expressed as:

$$J = L + S \quad . \quad (2.4)$$

The magnitude of J varies between $L+S$ and $|L-S|$ as L and S are vectors that do not always point in the same direction as shown in Figure 2.1. When the total number of valence electrons are such that the orbitals are less than half-filled, the ground state term will have a J value of $|L-S|$ and when the orbitals are more than half-filled, the ground state term will have a J value of $L+S$. This coupling scheme is called Russel-Saunders coupling or LS coupling [68].

According to this scheme, *spin – spin coupling* > *orbit – orbit coupling* > *spin – orbit coupling* .

The total angular momentum J remains a constant according to the law of conservation of angular momentum. For heavier elements ($Z>40$), this coupling scheme cannot be reliably used, and another coupling scheme called JJ coupling is used [66]. In this case, the value of the total angular momentum of each electron has to be individually determined and then added together to yield the net angular momentum of the system. Then computational techniques are used to find the excited energy states [69]. Still, it is common practice to determine the excited energy levels of the lanthanides using LS coupling, though it could lead to some very minute errors [70].

To summarize, due to the orbit-orbit coupling, an orbital is split into different spectroscopic terms which are further split into different spectroscopic levels/energy states due to the spin-orbit coupling. Radiative transitions can take place between different spectroscopic levels, whereas multi-phonon relaxation can occur between different microstates or spectroscopic levels. Each spectroscopic level has $2J+1$ degenerate micro-states and can be described using the term symbol notation as $^{2S+1}L_J$ in the LS coupling scheme.

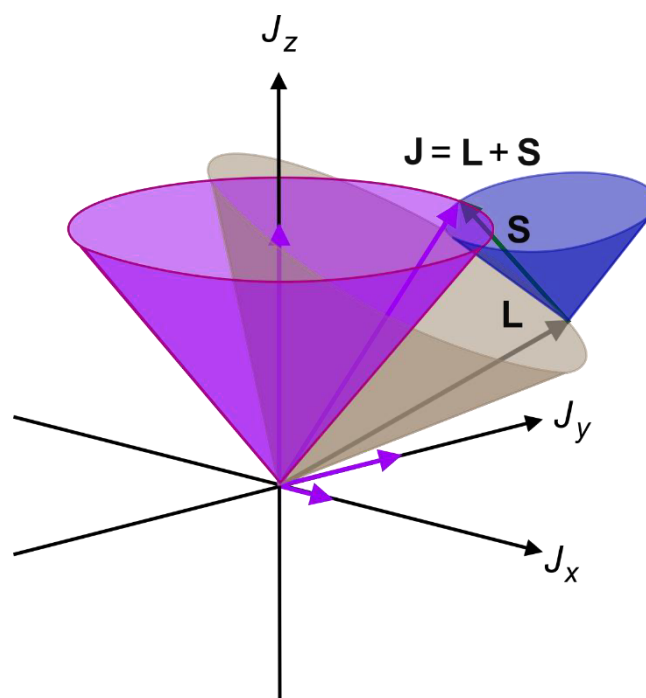


Figure 2.1. LS Coupling showing vector addition of orbital angular momentum L and spin angular momentum S resulting in total angular momentum J . Adapted from Maschen [71]. CC-BY license

The total number of microstates in an orbital is given by the equation:

$$\text{no. of microstates} = \frac{t!}{(t-n)!n!} \quad (2.5)$$

where t is the maximum number of electrons the orbital can hold i.e., $2(2\ell + 1)$ and n is the number of valence electrons in the orbital.

2.1.2. Determination of Energy states

The trivalent ytterbium (Yb^{3+}) ion is used herein to demonstrate how the energy states in the lanthanides (Ln^{3+}) are determined. For Yb^{3+} ion, with the electronic configuration $[\text{Xe}] 4f^{13}$, the total number of microstates in the f orbital is 14 as calculated using Equation 2.5 as $t = 14$ and $n = 13$. The total spin is then calculated using Equation 2.2 as, $S = 7 \times \frac{1}{2} + 6 \times -\frac{1}{2} = \frac{1}{2}$. The maximum possible angular momentum is obtained by adding the orbital angular momentum (the magnetic quantum number for the orbital) for each electron as per Equation 2.3. $L = \sum \ell_i = 3 + 2 + 1 + 0 + -1 + -2 + -3 + 3 + 2 + 1 + 0 + -1 + -2 = 3$ (corresponding to F , according to the spectroscopic notation). As the orbital is more than half-filled ($13 > 7$), the value of J for the ground state (level) is given by $J = L + S = 3 + \frac{1}{2} = \frac{7}{2}$. Therefore, the ground state of the Yb^{3+} ion is denoted with the term symbol $^{2S+1}L_J = {}^2F_{7/2}$ with $(2J+1) = 8$ degenerate microstates. The first excited state of the Yb^{3+} ion is then denoted with the term symbol ${}^2F_{5/2}$ with $(2J+1) = 6$ degenerate microstates. More examples of determination of term symbols of spectroscopic

levels with detailed step-by-step procedures are provided in the sections A.1-A.2 of the Appendix.

The more orbitals in a subshell, the more excited energy states are possible due to orbit-orbit and spin-orbit coupling effects. Therefore, elements/ions having electrons in the f-subshell have more excited energy states. This work focuses exclusively on the combination of the two trivalent lanthanides Er^{3+} and Yb^{3+} . The combination of their orbit-orbit, and spin-orbit coupling yields ladder-like excited energy states as shown in the Dieke diagram (Figure 1.2). The original Dieke diagram was drawn by Gerhard Dieke in 1963, who systematically studied the trivalent lanthanide ions in different crystal lattices (mostly using LaCl_3) and experimentally observed their energy states. The excited energy states were identified according to the term symbol notation and the radiative energy states were also marked in the Dieke diagram [17]. Later, a Dieke diagram was made for the trivalent lanthanides doped in the host LaF_3 by Carnall *et al.* in 1977 [72,73], and an extended version in the same host was made by Peijzel *et al.* in 2005 [74]. Figure 2.2 gives an energy level diagram showing the ladder-like excited energy states of Er^{3+} and Yb^{3+} . The two lines at the bottom of the figure show the ground states of Er^{3+} and Yb^{3+} . The first excited state of Yb^{3+} , namely $^2F_{5/2}$, and $^4I_{11/2}$ second excited state of Er^{3+} have similar energies, which enable sensitizing Er^{3+} with Yb^{3+} . These energy states lose their degeneracy and undergo further splitting and displacement due to crystal field splitting, if the species is embedded in a crystal lattice [70].

As an ion receives energy, it gets promoted to an excited energy state and the electron density shifts accordingly. Depending on the lifetime of this metastable excited state, the extra energy is released either radiatively or non-radiatively and the ion returns to its more stable ground state. Radiative emission results if an ion is promoted to any of the radiatively decaying energy levels shown in Fig 2.2, through any UC mechanism described in the following section or if the ions are directly pumped using photons with the same energy the energy state.

Usually, an energy state is termed as a singlet, doublet, triplet, quartet, or quintet based on its spin multiplicity [75]. The spin multiplicity is calculated with the expression:

$$\text{spin multiplicity} = 2S + 1 \quad , \quad (2.6)$$

where S is calculated by adding the individual spins of the unpaired electrons according to Equation 2.2.

When $S=1$ for a spectroscopic term, spin multiplicity = $(2S+1) = 3$, \rightarrow triplet. Similarly, when $S=1/2$ for a spectroscopic term, spin multiplicity = $(2S+1) = 2$, \rightarrow doublet. Also, when $S=0$ for a spectroscopic term, spin multiplicity = $(2S+1) = 1$, \rightarrow singlet. For example, the ground state

$4I_{15/2}$ of Er^{3+} has quartet spin multiplicity, which means that there are three more energy states ($4I_{13/2}$, $4I_{11/2}$ and $4I_{9/2}$) which belong to the same spectroscopic term (value of $L = I$) as observed in Figure 2.2.

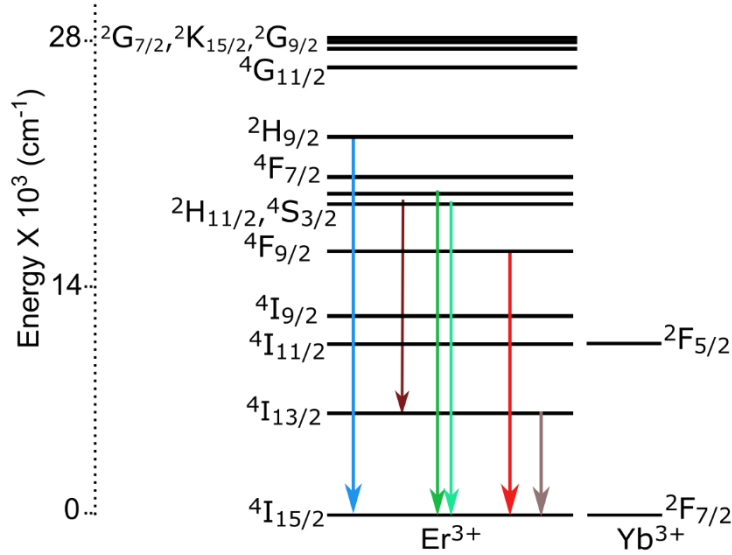


Figure 2.2. Energy level diagram of Er^{3+} and Yb^{3+} along showing energy states from which radiative emissions are commonly observed

2.1.3. Judd-Ofelt Theory

The Judd-Ofelt theory provides a mathematical model for describing the intensities of the 4f transitions by making use of the crystal field theory [76]. It considers the spin-orbit coupling to be in the frame of the intermediate coupling regime (total Hamiltonian operator is the sum of only the electrostatic and spin-orbital hamiltonians). The dipole strength between two states Ψ and Ψ' in the units of 10^{36} debye² is given by:

$$D_{ED} = e^2 \sum_{\lambda=2,4,6} \Omega_{\lambda} |\langle \Psi | U^{\lambda} | \Psi' \rangle|^2, \quad (2.7)$$

where e is the charge of the electron, U^{λ} are the irreducible tensor forms of the electric-dipole (ED) operator, and Ω_{λ} are the Judd-Ofelt parameters, expressed in cm^2 . The Judd-Ofelt parameters are calculated from the measured absorption spectrum $\varepsilon(\bar{\nu})$.

The experimental dipole strength in a solution or crystal is defined by the expression [77]:

$$D(exp) = \frac{4\varepsilon_0 m_e c^2 \times 10 \ln(10)}{e^2 N_A} \int \varepsilon(\bar{\nu}) d\bar{\nu} = 4.319 \times 10^{-9} \int \varepsilon(\bar{\nu}) d\bar{\nu}, \quad (2.8)$$

where $\varepsilon(\bar{\nu})$ is the molar extinction coefficient in units of $\text{mol}^{-1} \text{cm}^{-1}$, and $\bar{\nu}$ is the energy given in units of cm^{-1} . The integral is determined by plotting the absorption spectrum $\varepsilon(\bar{\nu})$ over the respective band as a function of $\bar{\nu}$. The permittivity of vacuum is given by ε_0 , mass of an electron by m_e , the speed of light by c , and the Avogadro constant by N_A .

Now, the Judd-Ofelt parameters are extracted using numerical techniques by minimizing the relative root-mean-square differences between the experimentally determined and calculated electric-dipole strengths from Equations 2.7 and 2.8:

$$RMS_{rel} = \sqrt{\frac{1}{n-p} \sum_{i=1}^n \left(\frac{D_i^{exp} - D_i^{cal}}{D_i^{exp}} \right)^2} . \quad (2.9)$$

Once the Judd-Ofelt parameters Ω_λ are known, several other parameters can be determined. The rate of spontaneous decay for an electric-dipole transition A_{ED} is given by the equation [77]:

$$A_{ED} = \frac{8\pi h \nu^3}{c^3} B_{ED} , \quad (2.10)$$

where B_{ED} is the Einstein coefficient calculated from the dipole strength D_{ED} using the following relation with the help of the Judd-Ofelt parameters Ω_λ from the equation 2.7:

$$B_{ED} = \frac{e^2}{4hm_e\varepsilon_0\nu} D_{ED} . \quad (2.11)$$

An electron in an excited state can radiatively decay to all the lower lying energy states. The branching ratio β gives the relative contribution of a particular transition to the total decay from that energy state. It is calculated by finding the ratio of the radiative decay-rate of a particular transition to the sum of all the radiative decay-rates.

In addition to radiative decays, a particular energy state can have other depopulation channels, like UC to higher excited states, cross relaxation, multiphonon relaxations, or energy transfer to neighbouring ions which decrease the effective lifetime of an ion in that energy state. These processes are discussed in the following sections.

2.1.4. Energy Transfer between Ions

Energy transfer between two ions can be broadly classified into the resonant type or the non-resonant type. In resonant transfer, there are no energy losses incurred. In other words, the acceptor ion gains the energy given by the sensitizer ion in its entirety. In non-resonant energy transfer, some energy is lost to phonons or gained due to phonons of the host lattice in which the ions are embedded. Resonant transfer can be again classified into radiative and non-radiative type. In radiative type of energy transfer, the sensitizer emits a photon, and the acceptor absorbs this photon. The efficiency of the energy transfer depends on the shape and configuration of the sample. The efficiency of such radiative energy transfer also depends upon how much the absorption spectrum of the acceptor overlaps with the emission spectrum of the sensitizer. The emission spectra observed from the sensitizer will then depend on the concentration of the acceptor ion. Probability of such a radiative transfer between two ions at a distance R can be expressed with the equation [78]:

$$\rho_{SA}(R) = \frac{\sigma_A}{4\pi R^2 \tau_s} \int g_s(\nu) g_A(\nu) d\nu \quad . \quad (2.12)$$

The sensitizer lifetime is denoted by τ_s , the absorption cross-section is denoted by σ_A , and the integral denotes the overlap of the emission spectrum of the sensitizer ion and the absorption spectrum of the acceptor ion.

In the case of non-radiative energy transfer, the interaction between two ions are essentially coulomb interactions of the van der Waals type. Lanthanide ions are capable of three different types of electronic interactions. They are 4f-4f transitions, 4f-5d transitions and charge-transfer transitions. The 4f-4f transitions result in sharp emission lines [65]. Laporte's parity selection rule says that for a centrosymmetric system, transitions are forbidden if the parity is conserved; this excludes the possibility of transitions within the same orbital [79]. But when the lanthanide ion is embedded in a crystal lattice, the crystal field disturbs the symmetry of the system, and induced (forced) electric dipole transitions take place. These electric dipole-dipole transitions are of the Dexter type (DET) [80] as they include transitions involving the same parity. Then the energy transfer rate between the sensitizer and acceptor can then be written as:

$$k_{dexter} = K J e^{-\frac{2R}{L}} \quad , \quad (2.13)$$

where R is the distance between the sensitizer and acceptor ions, L is the sum of the van der Waal's radii of the two ions, K is a constant and J is the spectral overlap integral, such that:

$$J = \int g_s(\nu) g_A(\nu) d\nu \quad . \quad (2.14)$$

In case of DET, an actual exchange of electrons take place, so the wavefunctions of the orbitals of acceptor ion and sensitizer ion should overlap. Also, DET can only take place at close range, typically of the order of a few angstroms. Therefore, a sensitizer ion normally interacts with a few neighbouring acceptor ions. In his original paper, Dexter postulates that a sensitizer can sensitize up to 10^4 neighbouring lattice sites, though in some lattices, this could be much lower [80]. The rate of the Dexter transfer depends on the sensitizer concentration and the rate of diffusion in the crystal lattice. For very high concentrations of the sensitizer, the rate of energy transfer become no longer limited by the diffusion of the sensitizer ions, but instead becomes limited by the concentration of the activator ions. But for lower concentrations of the sensitizer, the rate of energy transfer is limited by diffusion.

2.1.5. UC Mechanisms

When a material absorbs light, it moves to a higher energy state. This energy is released either radiatively or non-radiatively in the form of phonons (thermal energy). The emitted radiation normally has an energy lower than that of the absorbed energy. This phenomenon is called Stokes shift [81]. However, some materials emit the radiation with an energy higher than that of the absorbed energy, displaying an Anti-Stokes shift with the help of phonons in the lattice which undergo thermal dissipation. This energy difference is generally of the order of $k_B T$ where k_B is the Boltzmann constant and T is the absolute temperature in kelvin. However, due to the presence of the excited energy states with relatively long lifetimes, some materials can absorb multiple photons sequentially and emit upconverted light at much higher energy than that of the absorbed photons ($10-100$ times $k_B T$), contrary to the normal range of Anti-Stokes emission [78]. The elements which are capable of UC are marked on the periodic table by Song *et al.* is given in Figure 2.3 [82]. This is possible due to the ladder-like energy state configurations of the lanthanides which are multiples of the energy of the excitation photons. Although a few transition elements are capable of UC, the UC emissions are generally observed at very low temperatures as opposed to the lanthanides which show UC at room temperature [83]. Recent findings based on UC from the divalent manganese ion sensitized with Yb^{3+} pave the way to room temperature UC from transition elements [84]. The intensity of the UC emission from the highest emitting state is found to be proportional to the n^{th} power of the EPD at lower EPDs and becomes proportional to the EPD as the UC saturates, where n is the number of excitation photons required for populating the emitting state [85]. The dominant mechanisms of UC are described in the following sub-section.

	IA	Elements capable of UC																VIII A	
1	H ¹																	He ²	
2	Li ³	Be ⁴																	Ne ¹⁰
3	Na ¹¹	Mg ¹²	III B	IV B	V B	VIB	VII B	VIII				IB	II B	Al ¹³	Si ¹⁴	P ¹⁵	S ¹⁶	Cl ¹⁷	Ar ¹⁸
4	K ¹⁹	Ca ²⁰	Sc ²¹	Ti ²²	V ²³	Cr ²⁴	Mn ²⁵	Fe ²⁶	Co ²⁷	Ni ²⁸	Cu ²⁹	Zn ³⁰	Ga ³¹	Ge ³²	As ³³	Se ³⁴	Br ³⁵	Kr ³⁶	
5	Rb ³⁷	Sr ³⁸	Y ³⁹	Zr ⁴⁰	Nb ⁴¹	Mo ⁴²	Tc ⁴³	Ru ⁴⁴	Rh ⁴⁵	Pd ⁴⁶	Ag ⁴⁷	Cd ⁴⁸	In ⁴⁹	Sn ⁵⁰	Sb ⁵¹	Te ⁵²	I ⁵³	Xe ⁵⁴	
6	Cs ⁵⁵	Ba ⁵⁶	La-Lu ⁵⁷⁻⁷¹	Hf ⁷²	Ta ⁷³	W ⁷⁴	Re ⁷⁵	Os ⁷⁶	Ir ⁷⁷	Pt ⁷⁸	Au ⁷⁹	Hg ⁸⁰	Tl ⁸¹	Pb ⁸²	Bi ⁸³	Po ⁸⁴	At ⁸⁵	Rn ⁸⁶	
7	Fr ⁸⁷	Ra ⁸⁸	Ac-Lr ⁸⁹⁻¹⁰³	Rf ¹⁰⁴	Db ¹⁰⁵	Sg ¹⁰⁶	Bh ¹⁰⁷	Hs ¹⁰⁸	Mt ¹⁰⁹	Ds ¹¹⁰	Rg ¹¹¹	Cn ¹¹²	Nh ¹¹³	Fl ¹¹⁴	Mc ¹¹⁵	Lv ¹¹⁶	Ts ¹¹⁷	Og ¹¹⁸	
Lanthanides		La ⁵⁷	Ce ⁵⁸	Pr ⁵⁹	Nd ⁶⁰	Pm ⁶¹	Sm ⁶²	Eu ⁶³	Gd ⁶⁴	Tb ⁶⁵	Dy ⁶⁶	Ho ⁶⁷	Er ⁶⁸	Tm ⁶⁹	Yb ⁷⁰	Lu ⁷¹			
Actinides		Ac ⁸⁹	Th ⁹⁰	Pa ⁹¹	U ⁹²	Np ⁹³	Pu ⁹⁴	Am ⁹⁵	Cm ⁹⁶	Bk ⁹⁷	Cf ⁹⁸	Es ⁹⁹	Fm ¹⁰⁰	Md ¹⁰¹	No ¹⁰²	Lr ¹⁰³			

Figure 2.3. Elements capable of UC are marked on the periodic table in green colour. Adapted with permission from Song et al. [82]

2.1.5.1. Ground-State-Absorption/Excited-State Absorption

This first step of this type of mechanism is called ground state absorption (GSA), wherein an ion in its ground state absorbs a photon and moves to an excited state. Before the ion in the excited state decays back into its ground state, it absorbs another photon and moves to an excited state of higher energy undergoing an excited state absorption (ESA). When the ion radiatively relaxes back to its ground state a UC emission is obtained (Figure 2.4 (a)). ESA has typical lower efficiencies of the order of 10^{-5} as the probability of the ion remaining long enough in the first excited state to get the energy from a subsequent photon is quite low [3]. So higher EPDs are required for UC via ESA.

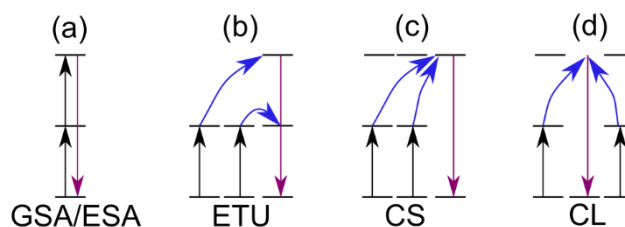


Figure 2.4. Dominant mechanisms of UC (a) ground state absorption/ excited state absorption, (b) energy transfer upconversion, (c) cooperative sensitization, and (d) cooperative luminescence

2.1.5.2. Energy Transfer UC

Energy transfer UC (ETU) is the most commonly used UC process due to its relatively high efficiency ($\sim 10^{-3}$ - 10^{-1}) [61,86]. The discovery of ETU is attributed to Auzel who gave it the French name “addition de photon par transferts d’énergie” (APTE) effect, though it is more commonly called ETU [87]. Two sensitizer ions absorb a photon each and get promoted to their excited states. One of the sensitizer ions transfers its energy to an emitter ion which then gets promoted to its first excited state. The other sensitizer ion then transfers its energy to the emitter ion, which gets promoted to its second excited state, from where it radiatively decays producing photoluminescence. What distinguishes ETU from normal resonance energy transfers is that the emitter ion in the excited state accepts energy from the sensitizer ion, which makes multiple energy transfer steps possible [78]. In the Yb^{3+} - Er^{3+} system, two-photon and three-photon UC processes are therefore simultaneously observed. If the sensitizer ion has a greater absorption cross-section as compared to the emitter ion, then the ETU process becomes advantageous as compared to ESA. For the Yb^{3+} - Er^{3+} system, Yb^{3+} has a much higher absorption cross-section around 980 nm as shown in Figure 2.5 which greatly aids ETU yielding high efficiencies [88].

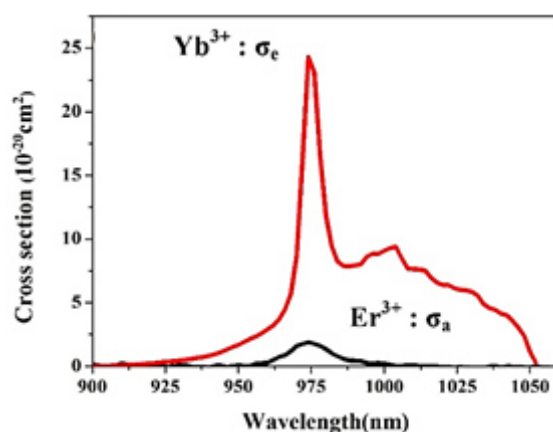


Figure 2.5. Absorption and emission cross sections of Yb^{3+} and Er^{3+} around 980 nm. Reproduced from Huang et al. [88], CC-BY license

Pollnau and colleagues provide an analysis of the slope dependence of UC via ETU and ESA based on rate equation modelling [85]. The slope of the log-log plot of the UC intensity vs the EPD gives the number of photons involved in the UC process, in the limit of low EPDs (Figure 2.6). The slope of the UC emission from intermediate states can be used to distinguish between ESA and ETU in the limit of high EPDs as shown in Table 2.2.

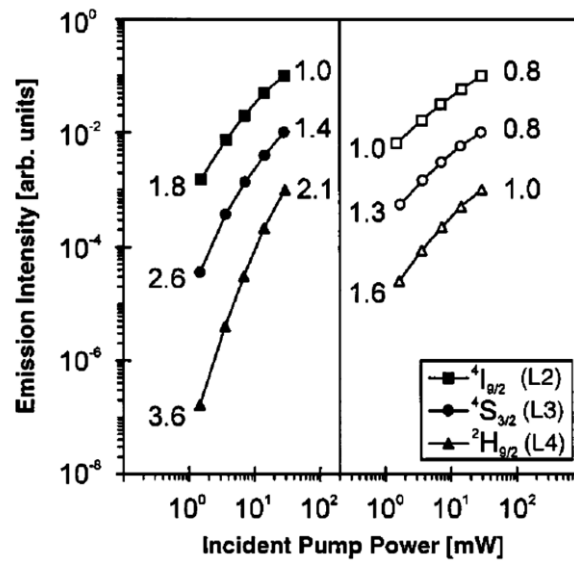


Figure 2.6. Double logarithmic plot of the UC intensity vs excitation power at 1540 nm from different excited states of Er^{3+} observed in $\text{Cs}_3\text{Lu}_2\text{Cl}_9:1\% \text{Er}^{3+}$ (closed symbols) and $\text{Cs}_3\text{Er}_2\text{Cl}_9$ (open symbols). The numbers denote the slopes at the extremities. L2, L3 and L4 correspond to 2, 3 and 4-photon UC emissions. The slopes in the limit of low pump power indicate the order of the UC process. Reproduced with permission from Pollnau et al. [85]

Table 2.2. Dependence of UC intensity on excitation power density (EPD) for excited state-absorption (ESA) and energy transfer upconversion (ETU) processes. Adapted with permission from Pollnau et al [85]

Influence of UC	UC mechanism	Predominant decay route	Fraction of absorbed pump power	Power dependence	From level
Small	ETU or ESA	next lower state or ground state	small or large	EPD^i	$i=1, \dots, n$
Large	ETU	next lower state	small or large	$\text{EPD}^{i/n}$	$i=1, \dots, n$
		Ground state	small or large	$\text{EPD}^{1/2}$	$i=1, \dots, n-1$
	ESA	next lower state	small	EPD^i	$i=1, \dots, n$
			large	$\text{EPD}^{i/n}$	$i=1, \dots, n$
		Ground state	small or large	EPD^0	$i=1, \dots, n-1$
			small or large	EPD	$i=n$

In the limit of high EPDs, the UC from the highest excited state to the ground state, shows a linear dependence on the EPD in case of both ESA and ETU. On the other hand, the UC intensity from the intermediate states to the ground state saturates and becomes independent of the EPD in case of ESA, whereas it becomes proportional to the square root of the EPD in case of ETU. Therefore, by observing the dependence of the UC emissions from intermediate states to the ground state, the mechanism of UC emission can be identified between ETU and

ESA. A simplified model of the ETU process developed in the course of this work to establish a figure-of-merit for comparing the UC of different materials is provided in Chapter 5 with rate equation modelling.

2.1.5.3. Cooperative Sensitization and Luminescence

In cooperative sensitization, two sensitizer ions cooperate and transfer their energy to an emitter ion in the ground state, so that it can get promoted to its excited state from which UC emission occurs. This is different from ETU in the sense that no metastable intermediate state of the emitter ion is involved. The emitter ion may or may not be the same as the sensitizer ion. In cooperative luminescence, two ions cooperate and combine the energy in their first excited states to release a higher energy photon and relax back to their ground states. An actually excited energy level is not required in this case [89]. The presence of a third ion is also not necessary as in the case of the cooperative sensitization process. The cooperative UC processes are 5-10 orders of magnitude lower than the ETU process [3,90], so they are seldom used in real-life applications. One such application is as a probe of the existence of Yb^{3+} ions clusters in glasses [91].

2.1.6. Mechanisms limiting UC

About 85-95% of the absorbed photons are upconverted through two- or three-photon processes based on the EPD [92]. As the EPD increases, more fraction of photons gets upconverted. Different factors contribute to limiting the efficiency of UC. Any process which decreases the concentration of ions in the excited states is detrimental to UC including various radiative and non-radiative decays. At the same time, when the concentration of ions increase, self-quenching also sets in, which decreases UC emissions. The major factors are briefly discussed below:

2.1.6.1. Multiphonon relaxation (MPR)

When the ions capable of UC are embedded in a crystal lattice, the energy states undergo splitting and some amount of energy shift due to crystal field effects. In addition, the crystal lattice has a specific phonon density of states, which means that it can vibrate with certain phonon energies. Figure 2.7. gives a compilation of the Raman Spectra measured for common UC host lattices from different literature sources [93–97]. The peaks on the Raman spectra indicate the phonon energies with which the lattice can vibrate. Note that the Fourier transform infrared (FTIR) spectra also reveals additional phonon energy peaks which are not visible in the Raman spectra. It is postulated that if the energy gap between two energy states is such that it can be bridged by 5-6 phonons or less, nonradiative decay will dominate [98]. This guideline is called the energy gap law [99,100]. Out of the five hosts studied in Figure 2.7, YCl_3

emerges as the winner, as it has a maximum phonon energy peak less than 300 cm^{-1} , thereby reducing the probability of non-radiative decay. The total decay rate of any metastable emitting state can be described as:

$$\frac{1}{\tau} = \frac{1}{\tau_{rad}} + W_{nr} \quad . \quad (2.15)$$

Here τ_{rad} is the total radiative lifetime and W_{nr} is the non-radiative decay rate. The energy gap law is defined for low temperatures as:

$$W_{nr} = \frac{1}{\tau_0} e^{-\frac{\alpha \Delta E}{h\nu_M}} \quad . \quad (2.16)$$

Here τ_0 is the radiative lifetime at 0 K and α is a pre-exponential constant which are determined empirically and ΔE is the energy gap between the excited state and the next lower lying state. For accuracy, this value is often taken as the difference between the lowest-lying crystal field state of the excited level and the highest crystal field state of the lower-lying energy level [101]. The Planck's constant is denoted by h and ν_M is the maximum phonon frequency of the host lattice. The MPR rates increase as a function of the temperature. For a temperature T , Equation 2.16 is modified to [99]:

$$W_{nr}(T) = \frac{1}{\tau_0} \left[\frac{e^{\frac{h\nu_M}{kT}}}{e^{\frac{h\nu_M}{kT}} - 1} \right]^{\frac{\Delta E}{h\nu_M}} \quad . \quad (2.17)$$

If the value of $\frac{\Delta E}{h\nu_M}$ is less than 6, then MPR becomes the dominant decay channel [39], especially at elevated temperature. Figure 2.8 gives a plot of the MPR rates vs the energy gap between adjacent energy states in different host lattices illustrated by Shalav *et al.* [39], based on measurements by Weber *et al.* [102]. The MPR rates decrease as the energy gap between adjacent energy states increases.

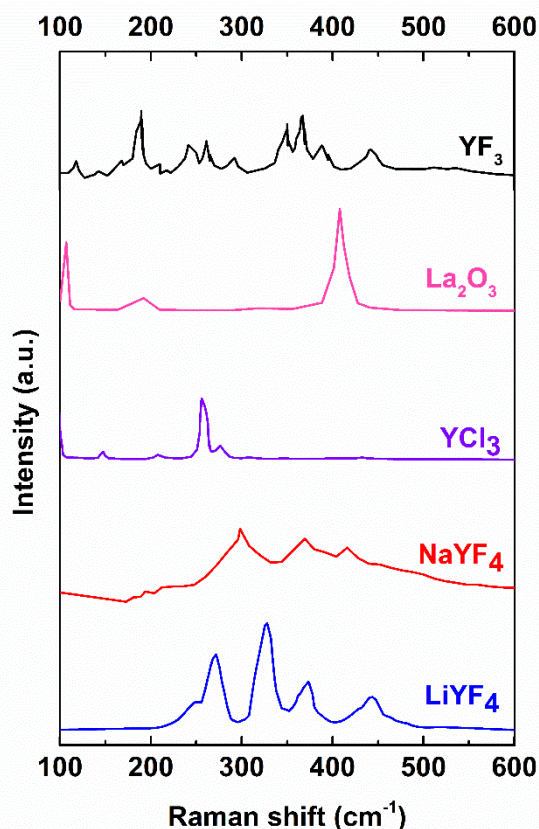


Figure 2.7. Raman spectra of selected crystal lattices. Adapted with permission from [93–97]

2.1.6.2. Radiative decay

A UC emission is normally from a higher energy excited state to the ground state. But if the emission happens to a lower-lying intermediate state, the efficiency of the original UC emission decreases. For example, in Figure 2.2 we see that there are two radiative emissions originating in the $^4S_{3/2}$ state, one is green in colour and the other is near-infrared (NIR) ~ 840 nm. Similarly, there can be radiative emissions to the other intermediate states which lie in between. All these radiative emissions will adversely affect the efficiency of the green UC emission. Certain applications of UC take advantage of these radiative transitions to the intermediate states, as in the case of NIR lasers based on Er^{3+} [23,38]. Figure 2.9 gives the possible lasing transitions based on Er^{3+} . Laser emission at 3500 nm and 4500 nm is obtained from Er^{3+} doped in YCl_3 when pumped at 660 nm and 800 nm respectively [23], while NIR laser around 2900 nm is obtained from the host LiYF_4 when pumped at 970 nm [103].

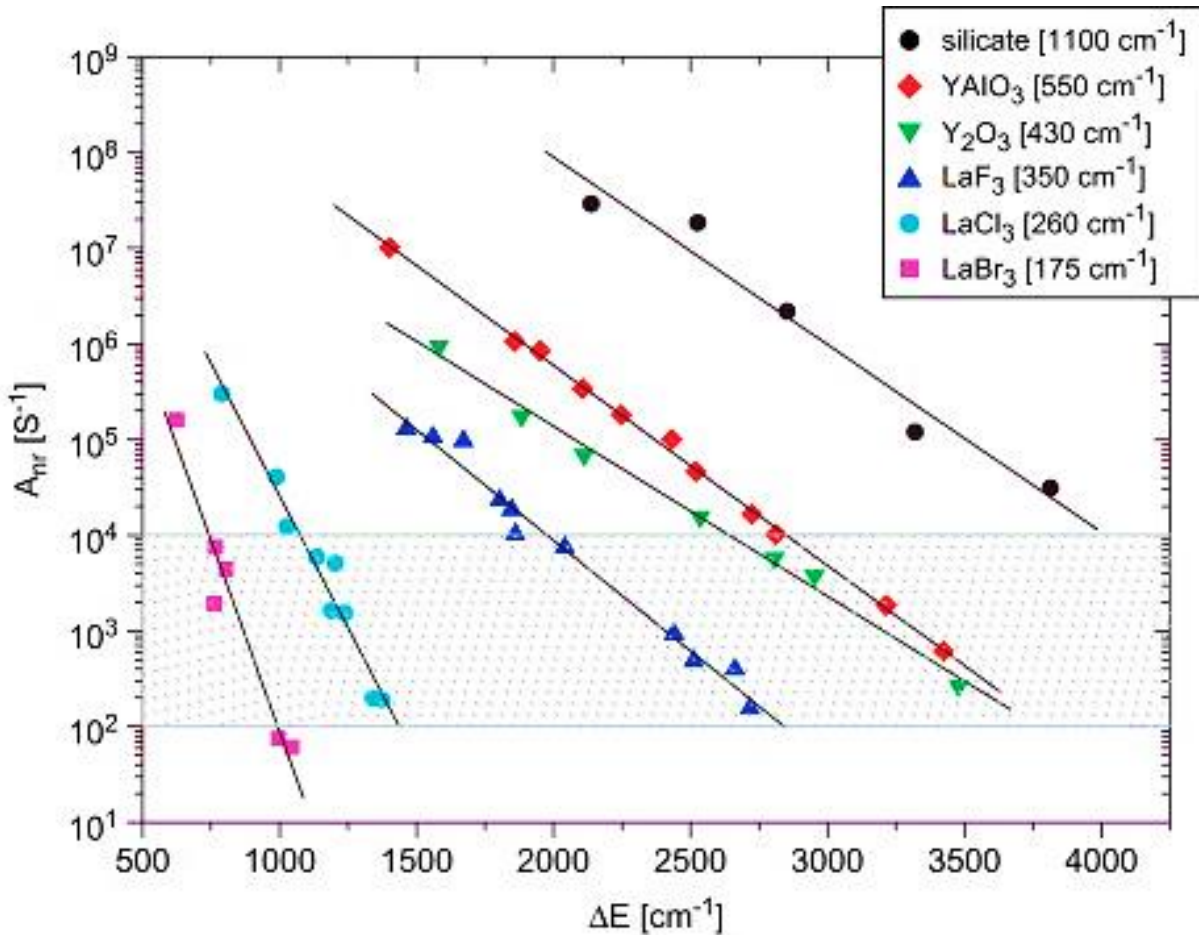


Figure 2.8. Multiphonon rates vs energy gap in different host lattices. The maximum phonon energies of the host lattices are given in the legend in square brackets in cm^{-1} . Reproduced with permission from Shalav et al [39].

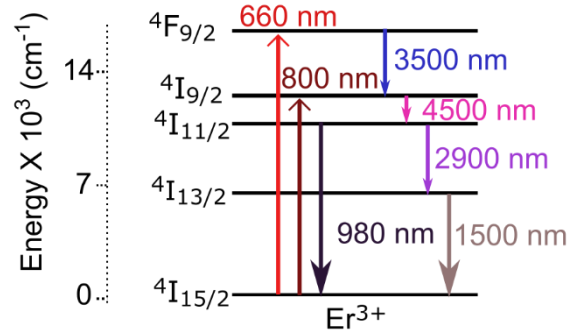


Figure 2.9. Possible lasing transitions at 3500 nm, 4500 nm and 2900 nm between intermediate states in Er^{3+}

The branching ratios of an excited energy state can be calculated with the help of Judd-Ofelt parameters as explained in Section 2.1.3. The branching ratio for a particular transition is the ratio of the radiative decay-rate of that transition to the sum of all the radiative decay-rates of all the transitions originating in that particular energy state. When the branching ratio (β) is greater than 0.5 for a particular transition, it can be potentially employed for displays and lasing applications [77].

2.1.6.3. Cross relaxation

Cross relaxation is fundamentally energy transfer between two ions in a way that the ion in the higher energy state moves down to a lower intermediate energy state and the ion in a lower energy state gain this energy and moves up to an intermediate energy state. Cross-relaxation often takes place between ions of the same type (quenching) or between a sensitizer and acceptor (also called Back Energy Transfer). Usually, the final states are the same or have the same energy. But the final states could also be different as illustrated in Figure 2.10. Here, an Er^{3+} ion in the green-emitting energy state $^4\text{S}_{3/2}$ undergoes a cross-relaxation with an Yb^{3+} ion in the ground state or another Er^{3+} ion in the ground state. Similarly, an Er^{3+} ion in the blue-emitting energy state $^2\text{H}_{9/2}$ undergoes a cross-relaxation with an Yb^{3+} ion in the ground state or another Er^{3+} ion in the ground state. Cross relaxation is sensitive to the concentration of the ions. It is proportional to the concentration of ions when the energy transfer is not limited by diffusion. Such a situation is observed in environments which exhibit weak quenching nature. On the contrary in environments which exhibit a strong quenching nature which limits the diffusion rates, the rate of cross relaxation is quadratically dependent on the concentration of the ions [78].

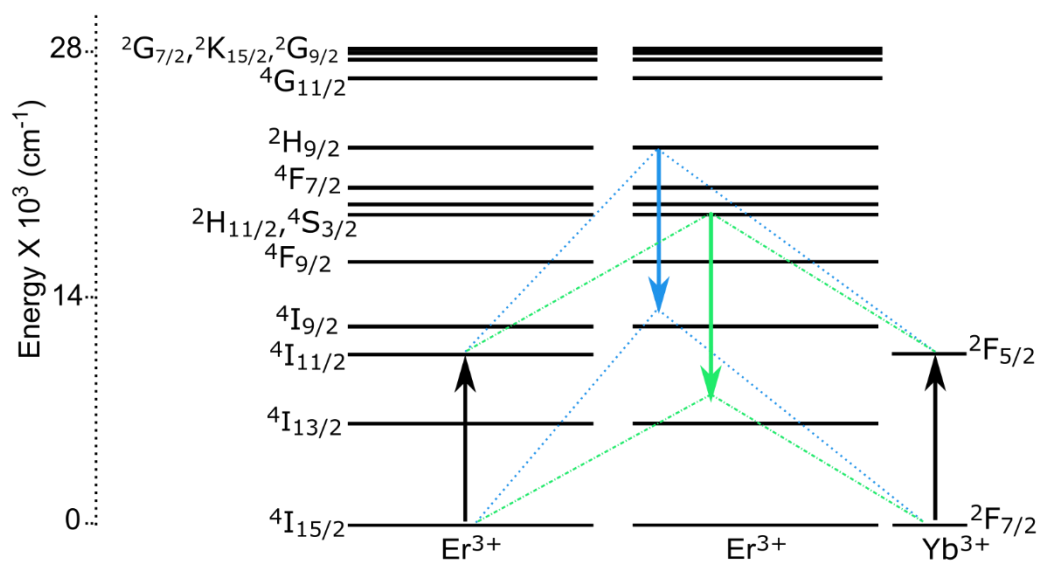


Figure 2.10. Possible cross-relaxation processes between Er^{3+} ions and Yb^{3+} ions, leading to depopulation of blue and green emitting states. Here, the final states of the interacting ions are not the same as opposed to normally observed cross-relaxation processes.

2.1.6.4. Energy transfer to Impurities/Quenching centres

Sometimes impurity ions could also be present in the host lattice. These impurities originate either from starting materials which were not originally ultra-pure (>99.999%) or from experimental errors during the synthesis. If energy transfer takes place between ions capable of emission and other impurities, the efficiency of UC is adversely affected. This quenching is

in the form of resonant energy transfer as in the case of DET or Förster resonant energy Transfer (FRET) [104]. The DET mechanism is briefly explained in Section 2.3. In FRET, the rate of energy transfer is proportional to $1/R^6$ where, R is the distance between the two ions, while in DET, the rate of energy transfer decreases exponentially according to Equation 2.13. In FRET, no actual electron exchange takes place, which means that the wavefunctions of the valence orbitals need not overlap with each other. However, the emission spectrum of the donor ion and the excitation spectrum of the acceptor ion must have a spectral overlap for FRET to take place. The impurity atom receives the energy from the lanthanide ion in its excited state and gets promoted to a metastable higher excited state. Then it relaxes back to the ground state through MPR or radiative relaxations. FRET typically takes place over a distance of 10 nm. Therefore, UC materials should have the least number of impurities possible. Therefore, the quality of the synthesis of the UC material is a definitive determinant of the efficiency of UC [105]. Generally bulk UC materials are annealed at a temperature greater than 500 °C to reduce the number of crystal defects [106]. On the other hand, certain impurities enhance the UC emission and are therefore purposefully introduced to the host lattice. For example, introduction of the Zn^{2+} ion in $BaTiO_3$ doped with Yb^{3+} - Er^{3+} increased the UC luminance upon 980 nm excitation because of a change in the local symmetry around the Er^{3+} ions [107].

In another perspective, ETU interaction with neighbouring ions, can also result in UC to higher excited states, which would actually decrease the emission from the current state. For example, the PLQY of two-photon UC from a particular excited energy state would decrease, if this particular state acts as an intermediate step for a three-photon UC process. Though this process is not really a mechanism limiting the UC, the PLQY of the two-photon UC emission and the total PLQY of UC from two and three-photon UC will be affected, as the total number of emitted photons decreases.

2.2. State-of-the-art of UC Materials and applications to UC Displays

As discussed in the two previous sub-sections, the efficiency of the UC emission depends on the competition between mechanisms which populate the emitting state and the mechanisms which tend to depopulate the emitting state. The material properties determine the prevalence of one mechanism over another. These factors were briefly discussed in Section 1.4. Till date, the best UC emitting material in terms of saturation PLQY upon 980 nm excitation is β - $NaYF_4: Yb^{3+}, Er^{3+}$, which was discovered in the early 1970s and still remains undisputedly one of the champions [61]. The β phase has a hexagonal lattice as opposed to the more common α phase which is cubic in nature. In this host, crystal field splitting enables efficient energy transfer between the second crystal field level of the $^2F_{5/2}$ energy state of Yb^{3+} and the $^4I_{11/2}$ state of Er^{3+} [53]. In addition, on close examination, the rare-earth ions were found to form small

clusters in the NaYF₄ crystal lattice which facilitated better interaction between the rare-earth ions in the cluster leading to more energy transfers [108,109]. The maximum phonon energy of the NaYF₄ lattice is also favourable (<500) as the probability of depopulation of radiative excited states is less [93]. The phonon peaks observed on the Raman spectra decrease in intensity upon annealing as the defects get healed, which is why the synthesis technique also is important for high UC efficiency [106]. Microcrystals of β-NaYF₄: Yb³⁺,Er³⁺ can be easily produced in bulk and is therefore available commercially.

For the experiments described in this work, β-NaYF₄: 18% Yb³⁺, 2% Er³⁺ is the most obvious choice as it is a well-established benchmark material with the highest known PLQY (reaching measured PLQYs of 11%, which when corrected for thermal effects is estimated to be 14% for two-photon UC). [78]. For effective comparison, the same rare-earth system is used, namely Yb³⁺-Er³⁺, in the same concentration 18% Yb³⁺ and 2% Er³⁺, and a couple of other microcrystal hosts are selected, namely orthorhombic YF₃, monoclinic YCl₃, and trigonal La₂O₃ which span a range of maximum phonon energies. The phase of NaYF₄ is specifically provided as β (hexagonal crystal system) in the course of this thesis to distinguish it from the α-phase (cubic crystal system) which is stable only above 600 °C [110]. The synthesis of pure hexagonal phase of NaYF₄ was optimized by controlling the doping concentrations, phase purity, ratio of sodium ions to rare-earth ions, preparation-temperature and annealing-time by Kramer *et al* [54]. Table 2.3. lists the different parameters of the crystal lattices of these four hosts. These four materials provide a wide range of variability in terms of these different properties and hence are chosen for analysis in Chapter 5. The actual number of activator ions are calculated using the molecular mass, density and doping concentration. Similarly, the effective activator distance (r_a) is calculated by considering the number of formula units in a unit cell (f), and the volume of a unit cell (V) with the doping percentage (c) as:

$$r_a = 2 \left(\frac{V}{fc} \frac{1}{\frac{4}{3}\pi} \right)^{\frac{1}{3}} . \quad (2.18)$$

The statistical distance to the nearest sensitizer is calculated by considering sensitizers and activators alike, so taking the total doping percentage of activators and sensitizers (c_t):

$$r_s = 2 \left(\frac{V}{fc_t} \frac{1}{\frac{4}{3}\pi} \right)^{\frac{1}{3}} . \quad (2.19)$$

For observing the effects of laser-induced heating in nanocrystals, as compared to microcrystals, nanocrystals of the same composition as the microcrystal β -NaYF₄: 18% Yb³⁺, 2% Er³⁺ are prepared in toluene. Such nanocrystals generally suffer from other issues like surface passivation and solvent effects. In addition, the scalability of production is also an issue. Nevertheless, β -NaYF₄: Yb³⁺,Er³⁺ core shell nanocrystals can demonstrate very high PLQYs around 10%, based on the synthesis technique [86].

Table 2.3. Material properties of the four different UC materials chosen for analysis showing the wide variability of the characteristics.

Host	Max phonon energy (cm ⁻¹)	Density (g cm ⁻³)	Molecular mass (g mol ⁻¹)	Unit cell volume (Å ³)	Formula units per cell	Actual no. of activator ions per cm ³	Effective activator distance (Å)	Statistical distance to nearest sensitizer ion (Å)
NaYF ₄	418	4.13	187.89	226.4	1.5	2.6×10 ²¹	18.57	8.62
La ₂ O ₃	450	6.56	325.81	82.41	1	2.4×10 ²¹	19.89	9.23
YF ₃	524	5.07	145.9	191.7	4	4.2×10 ²¹	16.60	7.71
YCl ₃	260	2.61	195.26	496.8	4	1.6×10 ²¹	22.80	10.58

For UC displays based on raster scanning, again β -NaYF₄: 18% Yb³⁺, 2% Er³⁺ is the obvious choice due to its very high PLQY. The UC material SrF₂: 18% Yb³⁺, 2% Er³⁺ is also investigated for display applications considering its wide-range colour tunability from green to red upon changing excitation wavelength from 980 nm to 1550 nm. On the other hand, the colour tunability of β -NaYF₄: 18% Yb³⁺, 2% Er³⁺ is only from green to yellow upon changing the excitation wavelength from 980 to 1550 nm. More details about the mechanisms causing this difference in the UC emissions between these two hosts are provided in Section 6.1. SrF₂ has also been tested for cytotoxicity and can be used in bio-imaging and bio-sensing applications [111]. SrF₂ forms a cubic lattice with a maximum phonon energy of 366 cm⁻¹ [112]. Trivalent ions form clusters when doped in SrF₂ matrix, because of the charge imbalance between the divalent Sr²⁺ and trivalent lanthanides like Yb³⁺ or Er³⁺ [113]. The formation of such clusters enhances the probability of energy transfer between the trivalent ions and tends to improve the ETU UC efficiency as in the case of β -NaYF₄. Commercially available NaYF₄:Yb³⁺, Er³⁺ microcrystals having a PLQY of 10% at an EPD of 10 W cm⁻² [59], and SrF₂:Yb³⁺,Er³⁺ microcrystals having a PLQY of 2.8% at an EPD of 10 W cm⁻² (prepared using the scalable synthesis method by calcination of the precipitate from aqueous solution) are therefore ideal candidates for a UC display [114]. The following section describes the basic

requirements on the UC luminance such that a UC display can be used in a well-lit environment.

2.2.1 Luminance Requirements for Displays

The standard Red-Green-Blue (sRGB) spec required for a PC monitor is 80 cd m⁻² as specified by the International Electrotechnical Commission [115]. Therefore, a luminescence of about 100 cd m⁻² would be sufficient for an indoor display, considering that the average luminance in a typical office room is about 36 cd m⁻² [116]. In comparison, a high-end HDR-television has a luminance of around 1000 cd m⁻². Commercially available head-up displays on the other hand have a luminance of around 1.2×10^4 cd m⁻² to be able to be visible under sunlight [117]. The sun has a luminance of 1.6×10^9 cd m⁻² at noon [118]. A clear sky at noon has 10^4 cd m⁻² luminance and a cloudy sky at noon about 10^3 cd m⁻² [119]. On the other hand, a cloudy sky at sunset has only 10 cd m⁻² luminance [120]. If a display is to be used in outdoor conditions during the day, then the luminance needs to be at least higher than 10^4 cd m⁻². The equation for the luminance (L) of UC at a given EPD is expressed as follows:

$$L = EPD \frac{\lambda_{ex}}{hc} \eta_{abs} \eta_{plqy} \eta_{ff} \frac{hc}{\lambda_{em}} 683.002 V(\lambda) \frac{1}{4\pi} . \quad (2.20)$$

Here, λ_{ex} and λ_{em} are the excitation- and emission-wavelengths, η_{abs} the fraction of photons absorbed, η_{ff} the fraction of time the excitation laser illuminates a given spot during a sweep, and $V(\lambda)$ the standard luminosity function. The number of excitation photons per unit energy is given by $\frac{\lambda_{ex}}{hc}$, and similarly the energy per emitted photon is given by $\frac{hc}{\lambda_{em}}$. Multiplying with $683 \times V(\lambda)$ converts the power in watts to lumens and multiplying by $\frac{1}{4\pi}$ converts lumens to candelas, assuming equal emission across all steradians. $V(\lambda) = 1$, at a wavelength of 545 nm, whereas due to the photopic vision of the human eye, it is only 0.1 at a wavelength of 650 nm [121,122]. Considering the weak absorption coefficients and the transparency needed by the display, η_{abs} is approximated to be 0.5.

Considering the requirements of persistence of vision and flicker fusion threshold of the eyes, each pixel needs to be illuminated again within 1/30th of a second, if a static image is to be seen after raster scan. A low cost galvanometric scanner is capable of covering 20 kilopoints per second, which translates to around 600 points in 1/30th of a second ($\eta_{ff} = \frac{1}{600} = 1.66 \times 10^{-3}$). Then each pixel would be excited for 50 μ s. In such a pulsed regime, which is shorter than the lifetime of the $^2F_{5/2}$ excited state of Yb³⁺ (ranging from microseconds to milliseconds based on the host material) [123], the PLQY is determined by the pulse energy density [124]. Berry *et al.* have noted that the PLQY of the green emission from their

microcrystalline β -NaYF₄:Yb³⁺, Er³⁺ sample, reaches its maximum at about 3% for a pulse energy density more than 25 mJ cm⁻². If low-cost laser diodes having an EPD of 100 W cm⁻² are used for excitation, to reach a pulse energy density of 25 mJ cm⁻², a dwell time of 250 μ s would be needed, which would drastically reduce the number of traceable pixels to 130. Using the same galvanometric scanner, only 5 mJ cm⁻² would be delivered in a pulse of width 50 μ s. Then the PLQY of their sample would drop to 1% [124]. But the microcrystalline β -NaYF₄: 18% Yb³⁺, 2% Er³⁺ sample used in this work has a green PLQY_{sat} of 7% instead of 3%, which would lead to a slightly increased luminance. Approximating the PLQY to 1% itself ($\eta_{plqy} = 0.01$) considering the short pulse-width, for 980 nm excitation at an EPD of 1×10^6 W m⁻² (or 100 W cm⁻², easily achievable by focusing a 10 mW laser to a spot of 100 μ m diameter), and emission at 545 nm, the luminance, L calculated is then 80 cd m⁻² according to Equation 2.20. Therefore, achieving required luminance in a room-lit environment for the UC emission from the microcrystalline sample of β -NaYF₄: 18% Yb³⁺, 2% Er³⁺ is definitely possible. If all the emitted photons were red, centred at 650 nm, then the luminance calculated would be only 1/10th of this value due to the lower value of the photopic luminosity function $V(\lambda)$ at this wavelength. But in the absence of background lighting, even a luminescence of 1 cd m⁻² is sufficient to be visible by the naked eye. On the other hand, a UC display cannot be used in an outdoor environment during the day, as the luminance requirements cannot be met.

2.2.2. UC Colour Tuning Methods for Display Applications

The colour of the UC emission can be changed using different techniques. Changing the EPD of the incident radiation is the easiest way. But due to the non-linear nature of UC, changing the EPD, would automatically change the intensity-ratios of different UC emissions. The green UC emission from ²H_{11/2} and ⁴S_{3/2} states of Er³⁺ doped in fluoride hosts, upon 980 nm excitation, results from a two-photon process as explained in the previous chapter. But the red UC emission results from a three-photon process. Therefore, as the EPD increases, the relative contribution of the red emission keeps on increasing and that of the green emission keeps on decreasing (Figure 2.11). As a result, when the EPD increases, the red-to-green (R/G) ratio of the total UC emission increases along with the intensity of the emission. The R/G ratios of the UC emissions calculated for NaYF₄: 18% Yb³⁺, 2% Er³⁺ and SrF₂: 18% Yb³⁺, 2% Er³⁺ upon EPD sweeps of the 980 nm excitation are given in Figures 2.12-2.13. This technique is very simple and easy to implement but the drawback is that the colour and the intensity cannot be independently controlled.

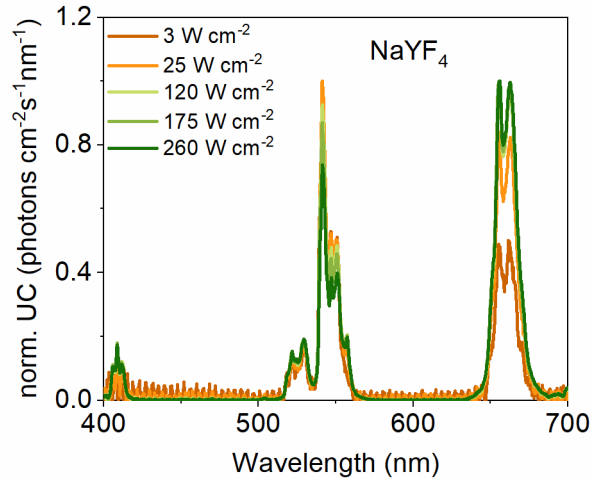


Figure 2.11. Relative growth of the red UC emission compared to the green UC emission in $\text{NaYF}_4: 18\% \text{Yb}^{3+}, 2\% \text{Er}^{3+}$ for EPDs of 980 nm radiation from 3 W cm^{-2} to 260 W cm^{-2} . Each spectrum is normalized to the highest peak. Adapted from Joseph et al. [125].

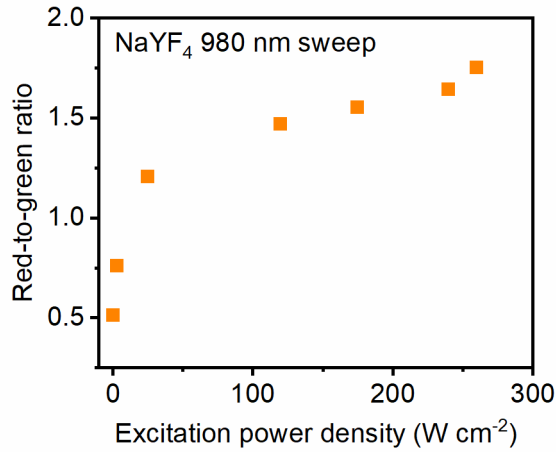


Figure 2.12. R/G ratio of UC emission increases as EPD of 980 nm radiation increases in $\text{NaYF}_4: 18\% \text{Yb}^{3+}, 2\% \text{Er}^{3+}$. Adapted from Joseph et al. [125].

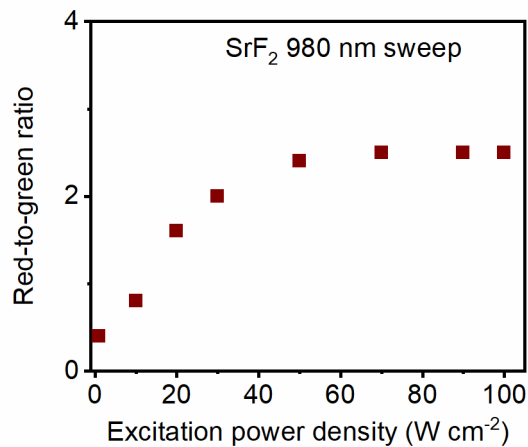


Figure 2.13. R/G ratio of UC emission increases as EPD of 980 nm radiation increases in $\text{SrF}_2: 18\% \text{Yb}^{3+}, 2\% \text{Er}^{3+}$. Adapted from Joseph et al. [125].

Another method for changing the emission colour is to synthesize different materials which emit different colours at the same EPD. There is a huge volume of work in the literature, which champion on changing the doping materials and their concentration in the well renowned host NaYF₄ [53,108,126]. Different concentrations of dopants at different excitation wavelengths were used by Chen *et al.* to obtain green (NaYF₄: 10% Yb³⁺, 1% Er³⁺ @ 976 nm), red (NaYF₄: 39% Yb³⁺, 1% Er³⁺ @ 976 nm) and yellow (NaYF₄: 10% Yb³⁺, 5% Er³⁺ @ 1532 nm) colour UC emission [127]. Yuan *et al.* added different concentrations of Mn²⁺ (ranging from x = 0 to 30 %) in NaYF₄: 18% Yb³⁺, 2% Er³⁺, x% Mn²⁺ for tuning the UC emission colour from green to red upon 980 nm excitation [128]. In another approach, different multi-shell nanocrystal structures can be incorporated, in which the energy migration can be controlled leading to different colours of UC emission [129,130]. Using this technique only a pixelated display can be realized, and the fabrication of such a display is complicated for each pixel is to be made with a different phosphor, and further requirements for scanning and focusing the laser increase the technical complexity.

A third technique involves manipulating the characteristics of the excitation like pulse-width, pulse-period and wavelength. The pulse-width and the excitation wavelength were varied for core-multi-shell nanocrystals by Liu and colleagues, to get blue, green and red UC emission [131]. These nanocrystals had an Yb³⁺ doped core with four concentric shells with different doping concentrations of Nd³⁺, Tm³⁺, Ho³⁺ and Ce³⁺. Similar core-multi-shell nanocrystals were used for obtaining different colours by changing the wavelength of steady-state excitation [132]. Similarly Luo *et al.* obtained intensity tuneable blue, green, and red UC emissions from a nanocrystals with a 4-shell architecture when excited with individually with 808 nm, 980 nm, and 1550 nm, respectively [133]. Their nanocrystals had a NaYbF₄ core doped with 25% Er³⁺. By taking advantage of the cross-relaxations observed in the Yb³⁺-Er³⁺ system at high concentrations of the dopant ions, they obtained red emission for 980 nm excitation and green emission from 1550 nm excitation [130,134,135]. Quite surprisingly, the results presented in Chapter 6 show the exact opposite behaviour. Using SrF₂: 18% Yb³⁺, 2% Er³⁺ microcrystals, red UC emission is obtained for 1550 nm excitation and green UC emission is obtained for 980 nm excitation as demonstrated later in Section 6.1. Though the core-multi-shell nanocrystals offer the amazing capability of changing the colour of the UC emission by only changing the excitation wavelength, scaling up their production is a challenge. Moreover, the PLQY of most nanocrystals are very low (<1%), for EPDs up to 100 W cm⁻², though this situation might change in the future as the technology advances [86]. Another difficulty is in the controlling of the interfaces between different shells and the core, such that the respective lanthanide ions are in the originally designed positions [130,136].

Using the same approach as in the ESA-UC displays, if dual wavelength excitation can be implemented in ETU systems, the intensity of the emission would be higher and hence suitable for well-lit environments and the possibility of the colour tuning would be an added benefit. Luo and co-workers have indeed demonstrated that such a UC display based on $\text{Y}_2\text{O}_2\text{S}:\text{Yb}^{3+}, \text{Er}^{3+}$ microcrystalline powder is possible albeit on a microscopic scale, by scanning the 980 nm and 1510 nm excitation lasers [137]. . Recent work by Gao *et al.* demonstrated a 2D UC display using $\beta\text{-NaYF}_4:\text{Yb}^{3+}, \text{Tm}^{3+}$ which could be seen under room lighting with a frame rate of 29 Hz, and a dwell-time of 20 μs [138]. The EPD in this case was three orders of magnitude higher than what is used in this work due to higher laser power and tighter focusing of the excitation beam, which makes the UC displays proposed in Chapter 6 more attractive.

2.3. Summary

“Lanthanons—These elements perplex us in our researches, baffle us in our speculations, and haunt us in our very dreams. They stretch like an unknown sea before us; mocking, mystifying and murmuring strange revelations and possibilities.” These were the words of Sir William Crookes in an address to the Royal Society in the year 1887. True to his words, the chemistry and physics of lanthanides are much intriguing. A humble attempt is made in this chapter to summarize the most important principles that one should keep in mind when trying to understand the photophysics of UC dealt with in this thesis. The basic requirements for an indoor UC display and discussion on UC-colour tuning methods lay the foundation for the results in Chapter 6, where a proof-of-principle of such a UC display is presented

3. Methods

This chapter deals with the synthesis methods, measurement systems and characterization techniques used in the course of this research work.

3.1. UC Material Synthesis

Five microcrystalline host systems doped with 18% Yb³⁺ and 2% Er³⁺ are used in the course of this thesis. These five hosts are β -NaYF₄, YF₃, La₂O₃, YCl₃, and SrF₂. Nanocrystals of β -NaYF₄ doped with the same concentration of Yb³⁺ and Er³⁺ are also used for comparison with the β -NaYF₄ microcrystals. The fluoride and chloride microcrystals doped with Yb³⁺ and Er³⁺ were synthesized by Damien Hudry and Daniel Biner at the University of Bern with the well-established method developed by Karl Krämer. The La₂O₃ microcrystals doped with Yb³⁺ and Er³⁺ were prepared by Guojun Gao at the KIT. The nanocrystals were synthesized by Damien Hudry at the KIT. The synthesis procedures of these UC materials are described in the following subsections.

3.1.1. β -NaYF₄: 18% Yb³⁺, 2% Er³⁺ Preparation

β -NaYF₄ is a highly efficient host material exhibiting highly efficient ETU with the Yb³⁺-Er³⁺ system, which serves as a benchmark material for UC. For the synthesis, the method described by Krämer *et al.* is used with materials of 99.999% (5N) or 99.9999% (6N) purity [54]. First 0.8 M Y₂O₃, 0.02 M Er₂O₃ and 0.18 M Yb₂O₃ are dissolved in a small quantity of 47% HBr acid in a beaker made of Teflon, evaporated till they are dry, again dissolved in water and precipitated as YF₃, ErF₃ and YbF₃ using 40% HF acid. This liquid is evaporated, and HF is again added to it. Na₂O₃ is taken in 2:1 ratio of Na:Y and dissolved in water in a beaker and slowly added to the mixture. In this stage, CO₂ evolves as a byproduct of this reaction, so special care is to be taken so that the mixture is not spilled. The products of this reaction are further dried, and HF is again added. This process of drying and HF treatment is repeated at least five times. The remaining dried up product is ground up in a mortar and heated to 550 °C in a glassy carbon boat in HF/Ar gas stream for a period of 20 hours. After this heating step, NaYF₄ with excess NaF is formed. Further treatment with HF gas stream removes traces of O and Br. The powder is again ground up and heated up to a temperature of 590 °C in Ar gas stream for 20 hours to obtain the microcrystals with a very high UC efficiency. The powder is then washed in de-ionized-water (DI-water) to remove the excess NaF and then heated up to

100 °C to get the β -NaYF₄: 18% Yb³⁺, 2% Er³⁺ microcrystals. Throughout the synthesis, special HF resistant equipment is used considering the highly corrosive nature of HF.

X-ray powder diffraction (XPD) pattern of the β -NaYF₄: 18% Yb³⁺, 2% Er³⁺ microcrystals obtained with an X-ray powder diffractometer (Bruker, D2 Phaser) using Cu K α radiation (1.5405 Å) is provided in Figure 3.1. This XPD pattern is consistent with Joint Committee on Powder Diffraction Standards (JCPDS) file No. 16-334 confirming the β phase of NaYF₄.

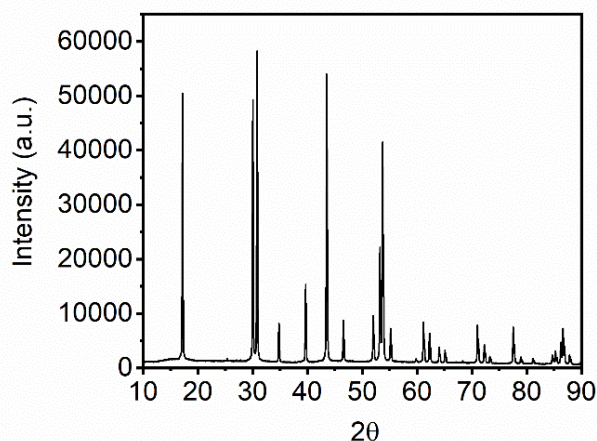


Figure 3.1. XPD image of the synthesized microcrystals of β -NaYF₄: 18% Yb³⁺, 2% Er³⁺ (JCPDS No. 16-0334) [139]

The scanning electron microscopy images of the same microcrystals obtained using a scanning electron microscope (Zeiss, Supra 60 VP) are provided in Figure 3.2. The particles are highly agglomerated as is evident from the images, but at 4000X, the hexagonal shape of the crystals can be seen.

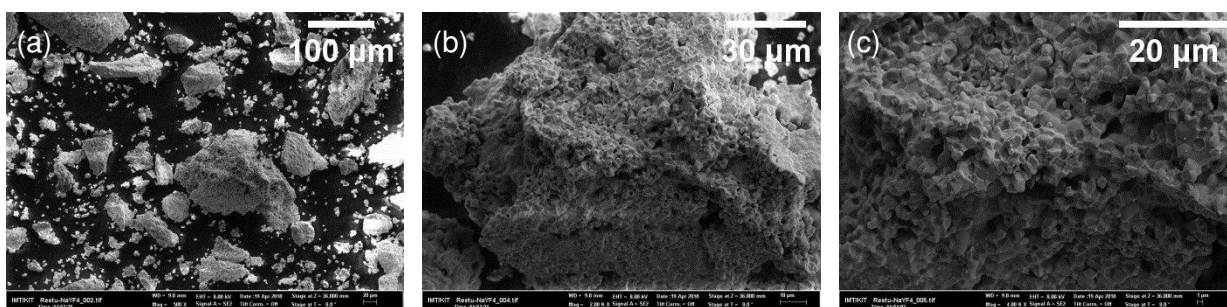


Figure 3.2. SEM images at 500X (a), 2000X (b) and 4000X (c) showing highly agglomerated faceted particles with either hexagonal or irregular shapes (1-5 μ m). Reproduced from Joseph et al. [139]

3.1.2. YF₃: 18% Yb³⁺, 2% Er³⁺ Preparation

The same procedure used for synthesizing β -NaYF₄: 18% Yb³⁺, 2% Er³⁺ is used for YF₃: 18% Yb³⁺, 2% Er³⁺ preparation, except that the steps starting from the addition of Na₂CO₃ are not needed. The final powder mixture of YF₃, ErF₃ and YbF₃ is heated to a temperature of

450 °C under HF flow for about 24 hours. The resulting powder is allowed to cool and ground thoroughly in a mortar to get the microcrystals of $\text{YF}_3: 18\% \text{Yb}^{3+}, 2\% \text{Er}^{3+}$.

X-ray diffraction pattern of the $\text{YF}_3: 18\% \text{Yb}^{3+}, 2\% \text{Er}^{3+}$ microcrystals obtained with an X-ray powder diffractometer (Bruker, D2 Phaser) using $\text{Cu K}\alpha$ radiation (1.5405 Å) is provided in Figure 3.3. This XPD pattern is consistent with Inorganic Crystal Structure Database (ICSD) No: 26595 confirming the orthorhombic phase of YF_3 .

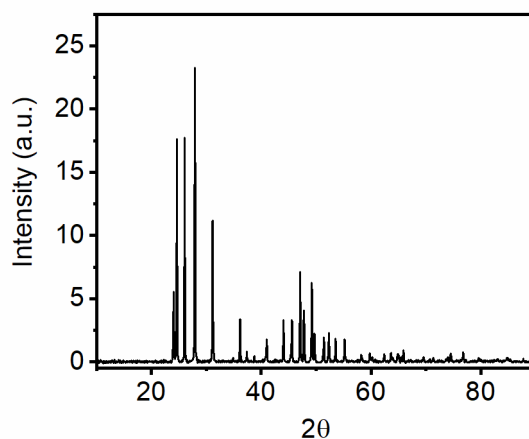


Figure 3.3. XPD image of the synthesized microcrystals of $\text{YF}_3: 18\% \text{Yb}^{3+}, 2\% \text{Er}^{3+}$ (ICSD No: 26595) confirming the orthorhombic phase of YF_3

The scanning electron microscopy images of the same microcrystals obtained using a scanning electron microscope (Zeiss, Supra 60 VP) are provided in Figure 3.4. The particles are loosely bound together and form faceted microcrystals with well separated grain boundaries as observed at higher magnifications of 5000X and 60000X.

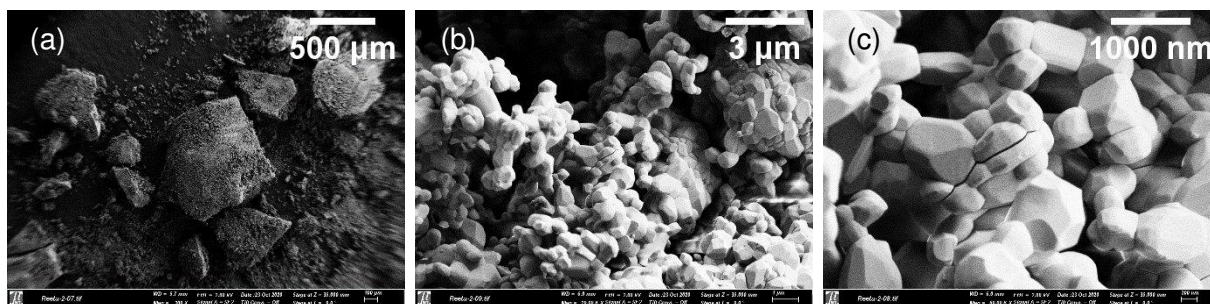


Figure 3.4. SEM images of microcrystals of $\text{YF}_3: 18\% \text{Yb}^{3+}, 2\% \text{Er}^{3+}$ at 100X (a), 5000X (b) and 60000X (c) showing faceted microcrystals ($< 1 \mu\text{m}$) with well separated grain boundaries

3.1.3. $\text{La}_2\text{O}_3: 18\% \text{Yb}^{3+}, 2\% \text{Er}^{3+}$ Preparation

The microcrystals of $\text{La}_2\text{O}_3: 18\% \text{Yb}^{3+}, 2\% \text{Er}^{3+}$ are prepared using a solid-state reaction as described by Gao *et al* [97]. The starting materials La_2O_3 (99.9% pure), Yb_2O_3 (99.9% pure), and Er_2O_3 (99.9% pure) were bought from ChemPur Feinchemikalien und Forschungsbedarf

GmbH. They are measured in stoichiometric quantities, mixed, well ground and pre-sintered at a temperature of 1300 °C for 4 hours in a drop-down furnace (Carbolite, BLF 1700). The powders are again ground and sintered at 1300-1650 °C for 3-12 hours in air with two steps of intermediate grinding to get the desired microcrystals of La_2O_3 doped with Yb^{3+} and Er^{3+} .

X-ray diffraction pattern of the La_2O_3 : 18% Yb^{3+} , 2% Er^{3+} microcrystals obtained with an X-ray powder diffractometer (Bruker, D2 Phaser) using $\text{Cu K}\alpha$ radiation (1.5405 Å), is provided in Figure 3.5. This XPD pattern is consistent with ICSD no. 100204 confirming the trigonal phase of La_2O_3 .

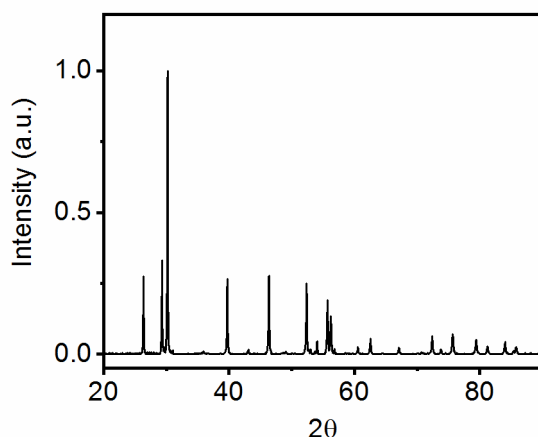


Figure 3.5. XPD image of the synthesized microcrystals of La_2O_3 (ICSD no. 100204) confirming the trigonal phase of La_2O_3

The scanning electron microscopy images of the same microcrystals obtained using a scanning electron microscope (Zeiss, Supra 60 VP) are provided in Figure 3.6. The particles are highly agglomerated with irregular shapes and largely fused together to form huge clumps.

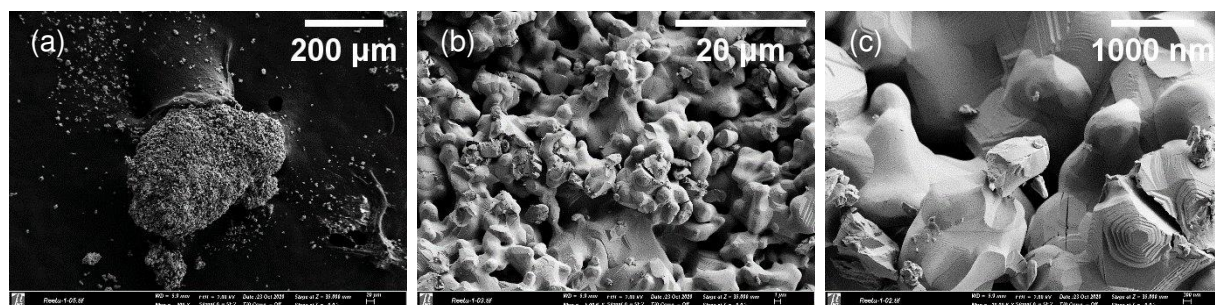


Figure 3.6. SEM images of microcrystals of La_2O_3 : 18% Yb^{3+} , 2% Er^{3+} at 309X (a), 5000X (b) and 20000X (c) showing highly agglomerated particles with irregular shapes which are largely fused together to form huge clumps (< 500 μm).

3.1.4. YCl_3 : 18% Yb^{3+} , 2% Er^{3+} Preparation

High purity oxides (5N) of Y_2O_3 , Yb_2O_3 , and Er_2O_3 are treated with NH_4Cl and HCl to get the anhydrous ternary chlorides $(\text{NH}_4)_3\text{YCl}_6$, $(\text{NH}_4)_3\text{YbCl}_6$ and $(\text{NH}_4)_3\text{ErCl}_6$, respectively according

to the procedure described by Meyer [140]. These salts are dried and decomposed in vacuum to get YCl_3 , YbCl_3 and ErCl_3 . These chlorides are sublimed in vacuum at about $800\text{ }^\circ\text{C}$ to make them highly pure, absolutely dry and oxygen-free as starting materials for the next step. Then 0.8 M YCl_3 , 0.02 M ErCl_3 , and 0.18 M YbCl_3 are mixed in a sealed silica ampoule. It is then heated to a temperature of $880\text{ }^\circ\text{C}$ to melt the salts. The melt is mixed well and allowed to cool down overnight. Finally, the cooled-down product is ground thoroughly into microcrystals in a mortar to get $\text{YCl}_3: 18\% \text{ Yb}^{3+}, 2\% \text{ Er}^{3+}$. XPD pattern of the $\text{YCl}_3: 18\% \text{ Yb}^{3+}, 2\% \text{ Er}^{3+}$ microcrystals obtained with an X-ray powder diffractometer (STOE) using $\text{Cu K}\alpha$ radiation (1.5405 \AA), is provided in Figure 3.7. This XPD pattern is consistent with ICSD no. 15684 confirming the monoclinic phase of YCl_3 .

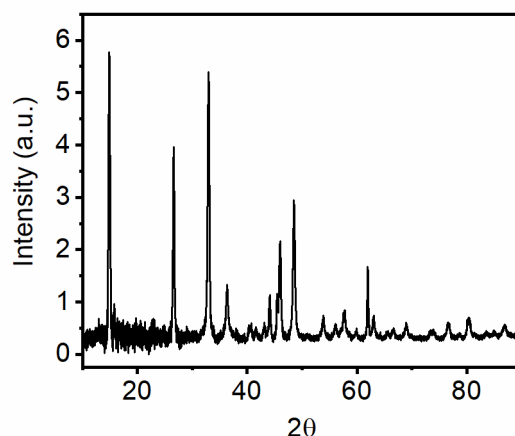


Figure 3.7. XPD image of the synthesized microcrystals of $\text{YCl}_3: 18\% \text{ Yb}^{3+}, 2\% \text{ Er}^{3+}$ (ICSD no. 15684) confirming the monoclinic phase of YCl_3

3.1.5. $\text{SrF}_2: 18\% \text{ Yb}^{3+}, 2\% \text{ Er}^{3+}$ Preparation

For the synthesis of $\text{SrF}_2: 18\% \text{ Yb}^{3+}, 2\% \text{ Er}^{3+}$, first two separate stock solutions are made. The first stock solution is made by a reaction of strontium carbonate (SrCO_3) with nitric acid (HNO_3) water to obtain strontium nitrate $\text{Sr}(\text{NO}_3)_2$ which is then dissolved in de-ionized (DI) water. For the second stock solution, Yb_2O_3 and Er_2O_3 are mixed in 65% nitric acid (HNO_3). Then both the stock solutions are mixed and precipitated with the help of 40% HF acid. The precipitate is then dried, and the obtained solid is heated to a temperature of $700\text{ }^\circ\text{C}$ (for 24 hours) under Ar/HF atmosphere to obtain the $\text{SrF}_2: 18\% \text{ Yb}^{3+}, 2\% \text{ Er}^{3+}$ microcrystals. XPD pattern of the $\text{SrF}_2: 18\% \text{ Yb}^{3+}, 2\% \text{ Er}^{3+}$ microcrystals obtained with an X-ray powder diffractometer (Bruker, D2 Phaser) using $\text{Cu K}\alpha$ radiation (1.5405 \AA), is provided in Figure 3.8. This XPD pattern is consistent with ICSD no. 260881 confirming the cubic phase of SrF_2 .

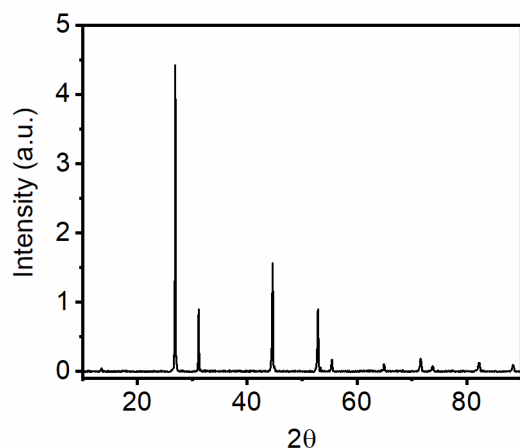


Figure 3.8. XPD image of the synthesized microcrystals of $\text{SrF}_2: 18\% \text{Yb}^{3+}, 2\% \text{Er}^{3+}$ (ICSD no. 260881) confirming the cubic phase of SrF_2

The scanning electron microscopy images of the same microcrystals obtained using a scanning electron microscope (Zeiss, Supra 60 VP) are provided in Figure 3.9. The particles are partially fused together though some grain boundaries can also be observed at higher magnifications.

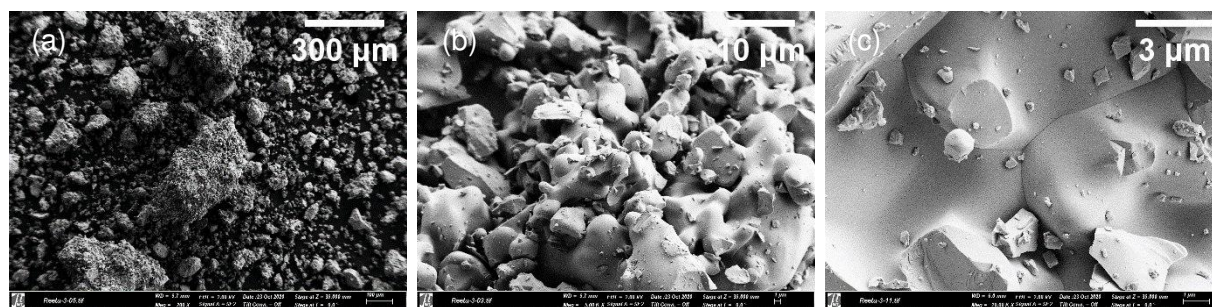


Figure 3.9. SEM images of microcrystals of $\text{SrF}_2: 18\% \text{Yb}^{3+}, 2\% \text{Er}^{3+}$ at 200X (a), 5000X (b) and 20000X (c) showing faceted particles which are partially fused together.

3.1.6. $\beta\text{-NaYF}_4: 18\% \text{Yb}^{3+}, 2\% \text{Er}^{3+}$ nanocrystal preparation

The $\beta\text{-NaYF}_4: 18\% \text{Yb}^{3+}, 2\% \text{Er}^{3+}$ nanoparticles are synthesized using the same method described by Hudry *et al.* for synthesizing NaGdF_4 core-nanocrystals [136]. Instead of gadolinium acetate hydrate ($\text{Gd}(\text{OAc})_3 \cdot x\text{H}_2\text{O}$, 99.9%), yttrium acetate hydrate ($\text{Y}(\text{OAc})_3 \cdot x\text{H}_2\text{O}$, 99.9 %) is used to obtain $\beta\text{-NaYF}_4: 18\% \text{Yb}^{3+}, 2\% \text{Er}^{3+}$ core-nanocrystals. XPD pattern of the synthesized nanocrystals obtained with an X-ray powder diffractometer (Bruker, D2 Phaser) using $\text{Cu K}\alpha$ radiation (1.5405 Å) is provided in Figure 3.10. This XPD pattern is consistent with JCPDS file No. 16-334 confirming the β phase of NaYF_4 . Anisotropic nano particles of size 20x30 nm dispersed in toluene solution are obtained through this technique as revealed from transmission electron microscopy measurements (Figure 3.11).

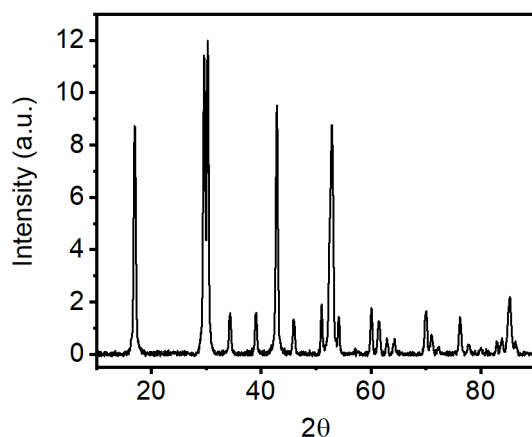


Figure 3.10. Measured XPD pattern of core-nanocrystals in conformance with JCPDS 16-0334 indicating β - NaYF_4

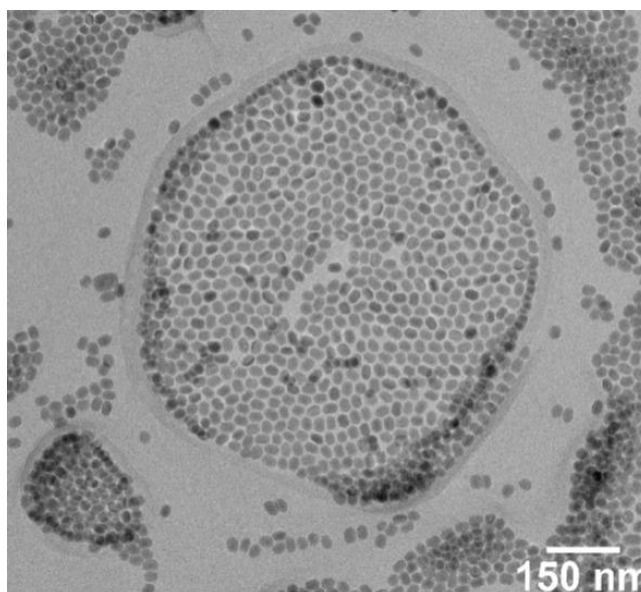


Figure 3.11. Transmission electron micrograph of the β - NaYF_4 core-nanocrystals

3.2. Steady-State Photoluminescence Spectroscopy

Spectroscopy is the study of the effect of electromagnetic radiation on matter as a function of the wavelength or energy. Steady-state photoluminescence (PL) spectroscopy deals with observing the emission and excitation spectra as continuous wave radiation excites the samples. The trivalent lanthanide ions doped in appropriate host materials, absorb electromagnetic radiation of particular frequencies. They then emit photons with energies corresponding to the transitions between their ladder-like energy levels. By observing the spectra of these transitions, we gain information about the photophysics of the energy conversion process. For observing such UC emission, a spectrophotometer cannot be reliably used as the in-built excitation is not always purely monochromatic and stray light often creates errors in measurement. UC is non-linear in nature, which means that it is highly dependent on the EPD [141], and the all-purpose illumination sources used in spectrophotometers do not

necessarily meet the EPD requirements. Thus, laser diodes are used as excitation sources, as they give monochromatic light at the required wavelength and power, typically 200 mW. The EPD is then adjusted using a variable neutral density (ND) rotary filter and various optics are used to focus the beam.

Figure 3.12 gives the scheme of the experimental set up used for steady-state PL measurements. The laser source is usually 980 nm laser diode (Thorlabs, L980P200) which is mounted on a temperature-controlled mount (Thorlabs, TCLDM9) stabilized by a laser driver controller (Thorlabs, ITC4001). For direct excitation of the green emitting states, another laser diode (Roithner, LD-515-10MG) of 525 nm is used. An automated shutter with the help of a shutter controller (Thorlabs, SC10) is used to turn the excitation on and off. An automated filter wheel (Thorlabs, NDC-100C-2) of continuously variable ND (optical density 0 to 2) is used to vary the power of incident beam with the help of a stepper motor. Then a plano-convex lens (Thorlabs, LA1978) with a focal length of 750 mm is used to focus the beam to increase the EPD. This lens can be replaced with another one of a lower focal length to further increase the EPD, as the spot size decreases due to a tighter focus. The lens can be also removed for obtaining much lower EPDs. A glass slide is inserted at an angle in the beam line to measure the power inline. The glass slide reflects ~8% of the incident beam at an angle equal to the angle of incidence to the incident beam and this reflected beam is measured by a power meter (Thorlabs, PM320E) with the help of a photodiode power sensor (Thorlabs, S121C), whose reading is calibrated to the actual power at the sample position. The sample is kept inside an integrating sphere of diameter 4 inches (Labsphere, 3P-LPM-060-SL). The integrating sphere is not necessary for simple PL measurements, but is nevertheless used as the same system is also calibrated for absolute PLQY measurements. The light coming out of the exit port of the integrating sphere is passed through a 950 nm short pass filter (Semrock, FF01-950/SP-25) to remove the component of the excitation laser and is coupled using an optical fibre (Thorlabs, FP1000URT), with a charge-coupled devices (CCD) spectrometer having an integrated cooling element (Avantes, AvaSpec-ULS2048x64TEC). The EPD is calculated by dividing the actual power with the area of the excitation spot. The area of the spot is calculated by using the formula for an ellipse from the 2σ measurements of the semi-major and semi-minor axes using by a beam profiler (Thorlabs, BP209-IR/M). The area of the ellipse is calculated as $4.6 \times 10^{-3} \text{ cm}^2$. The whole system is intensity calibrated together with the integrating sphere using a calibration lamp (Ocean Optics, HL-3plus). The whole measurement system is automated with the help of a LabVIEW [142] virtual instrument, developed by Dmitry Busko.

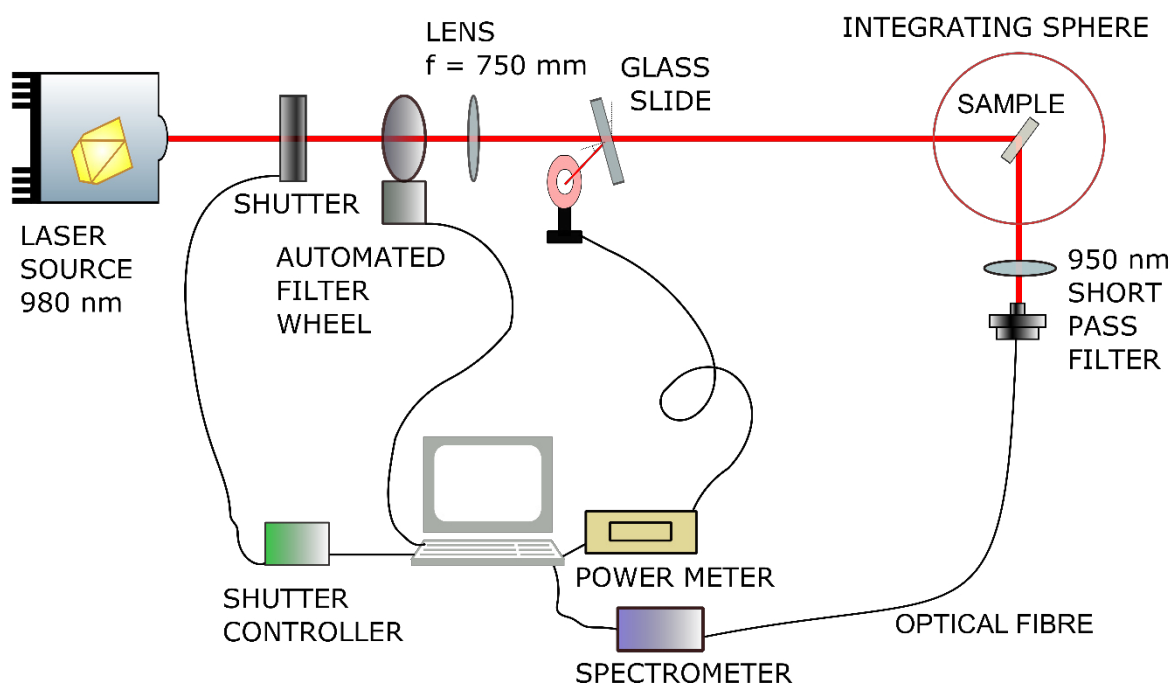


Figure 3.12. Scheme of the experimental set-up used for steady-state photoluminescence measurement

3.2.1. Emission Spectroscopy

For emission spectroscopy, the sample is kept at the centre of the integrating sphere in the beam path. A scheme of the close up view of a micropowder sample is shown in Figure 3.13. Such samples are housed in square capillaries of borosilicate glass with 1 mm × 1 mm cross-section, and hermetically sealed to prevent any sample degradation. The sample is excited with 980 nm at a fixed EPD and the resulting emission from the sample is measured with the CCD fibre coupled spectrometer (Avantes, AvaSpec-ULS2048x64TEC) through a short pass filter to filter out the excitation wavelength [143]. The excitation-spot on the sample is in the shape of an ellipse. The UC emission from the sample is then analysed. The individual peaks corresponding to the transitions from higher energy states of the trivalent lanthanides to lower energy states are identified and analysed. The integrated area under the spectrum gives the total number of photons emitted per second per unit area.

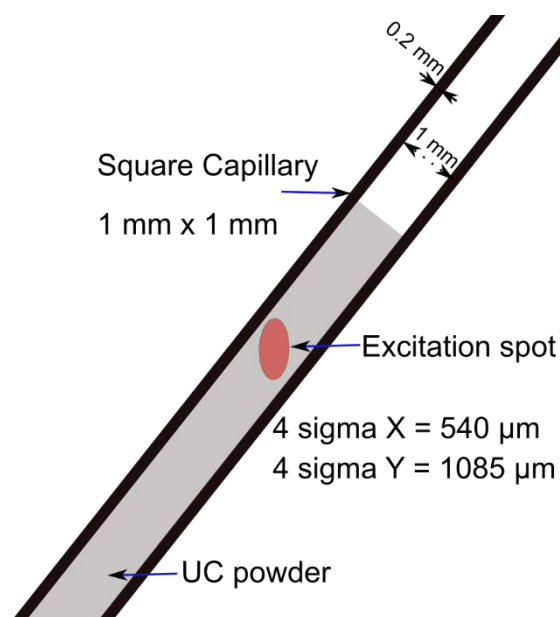


Figure 3.13. Zoomed-in view of the sample showing the excitation spot (the excitation-laser beam is incident in the direction perpendicular to the plane) and the dimensions of the square capillary in which the sample is housed. Adapted with permission from Joseph *et al.* [144] Copyright 2019 American Chemical Society.

3.2.2. Intensity Dependence

For intensity dependence measurements, a series of UC emission spectra are captured while changing the EPD gradually, by rotating the continuous variable ND filters from the highest optical density to the lowest, using a stepper motor driven by an Arduino microcontroller. The integration time required for the lowest optical density setting needs to be manually set by observing the maximum intensity on the UC spectra. Thereafter, the integration time is automatically reduced as the UC emission intensity increases as EPD increases, as the LabVIEW programme is executed. However, there is a caveat in intensity dependence measurements due to the effect caused by the laser-induced heating of the sample. For samples with very small particle sizes (few micrometres), just switching off the excitation laser for a few microseconds in between measurements is sufficient, but for samples with larger particle sizes, this effect is more pronounced, and the intensity dependence measurements need to be corrected. A method to correct the intensity dependence measurements is described in Chapter 4.

3.2.3. PLQY Measurement

Absolute PLQY measurements are performed according to the 3M method in an integrating sphere as described by de Mello *et al.* [145,146]. The absolute method for determining PLQYs is superior to the relative method because it can be used in situations where relative methods cannot be reliably used. Namely for: 1) samples that absorb/emit in regions where no reliable standards are generally available, for e.g. IR emitters with $\lambda > 950$ nm (Styryl-13 dye is an exception), 2) materials that have a non-linear emission with respect to the EPD, like UC

materials, 3) solid samples or highly scattering samples like microcrystals [147]. The use of an integrating sphere distinguishes the absolute method from the relative one. A scheme of the integrating sphere and the sample position inside it is provided in Figure 3.14. An integrating sphere collects all the light emitted/scattered by a sample across all solid angles as opposed to a normal spectrometer that collects only from a specific solid angle. An integrating sphere spatially integrates the radiant flux. The diameter of the integrating sphere, the size of the input and exit ports and the reflectance of the sphere coating affect the total radiance from an integrating sphere [148]. Integrating spheres from Labsphere are used, which are coated with Spectralon® which has a reflectance of > 99% from 250 nm to 2500 nm. The radiance from an integrating sphere is given by the formula:

$$L = \frac{\Phi_i}{\pi A_s} \times \frac{\rho_0}{1 - \rho_w(1 - \sum_{i=0}^n f_i) - \sum_{i=0}^n \rho_i f_i} , \quad (3.1)$$

where Φ_i is the input flux, A_s the area of the sphere, ρ_0 the initial reflectance for incident flux, ρ_w the reflectance of the sphere wall, ρ_i the reflectance of the port opening and f_i the fractional area of the port opening. A baffle is used in the integrating sphere to block any direct reflections from the excitation from reaching the exit port. Direct reflections would cause a false response, as the integrating effect is attained after multiple reflections, driving the system to steady-state.

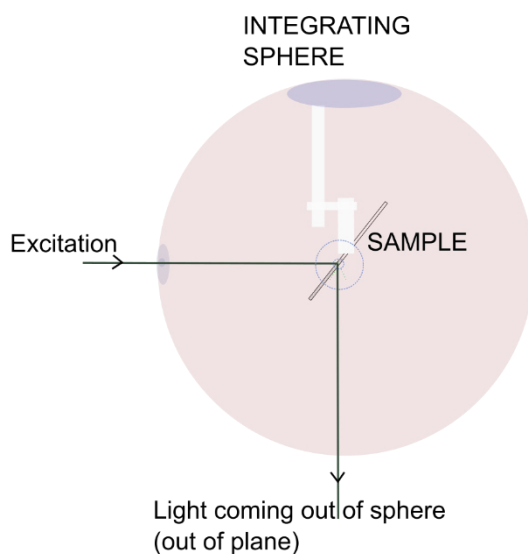


Figure 3.14. Image of the Integrating sphere showing sample placement

In the 3M method of measuring PLQY, first the spectrum is measured without the sample inside the sphere. The integrated area of the laser in this case is named empty sphere (ES), corresponding to a sphere with no sample. Then, the sample is placed inside the sphere in the direct path of the excitation beam and the spectrum is measured. This spectrum has two regions, one corresponding to the excitation laser, which has a lower peak as compared to the empty sphere case, the integral of which is named laser direct (LD), and a second region corresponding to the photoluminescence emission, the integral of which is named

photoluminescence direct (PD). Now the sample is rotated and kept away from the direct path of the excitation laser, so that only laser excitation reflected from the surface of the sphere shines on the sample. The spectrum has two regions again, one corresponding to the photoluminescence having a peak value less than that of PD and a second one corresponding to the excitation laser having a peak value more than that of LD. The photoluminescence region in this case is named photoluminescence indirect (PI) and the excitation laser region is named Laser Indirect (LI). With these three measurements we obtain the PLQY of the sample, hence the method is named 3M method. Therefore, $ES > LI > LD$ and $PD > PI$ as shown in Figure 3.15 and Figure 3.16. The peaks of the laser spectra are magnified in the inset figure of Figure 3.15 showing that ES is higher than LI. The difference between ES and LD is the total number of photons absorbed by the sample, while the difference between LI and LD is the number of photons absorbed in the first incidence of the laser excitation beam with the sample. The difference between ES and LI is the number of photons absorbed due to the reflections impinging on the sample from the walls of the integrating sphere.

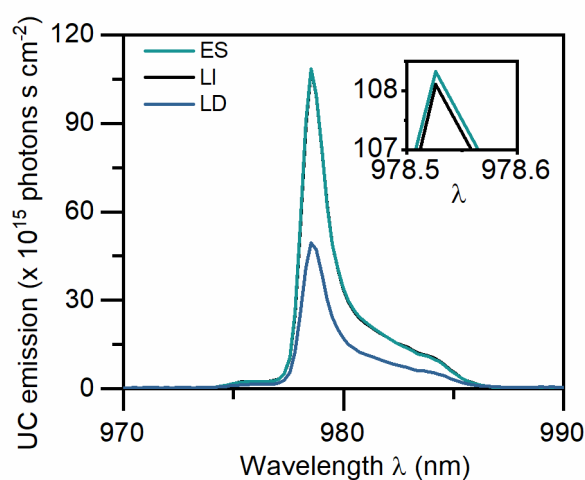


Figure 3.15. Spectra of the laser when a sample of $\beta\text{-NaYF}_4: 18\% \text{Yb}^{3+}, 2\% \text{Er}^{3+}$ micropowder is placed in the three different positions as required by 3M method. The inset shows that the ES spectrum is slightly higher in intensity than the LI spectrum.

In actual practice, the spectrometers have varying sensitivities in different wavelength regions and the minimum integration times possible for the spectrometers limit the maximum intensity that can be measured in a way that the individual photodiodes (pixels) of the CCDs are not saturated. For PLQY measurement of UC, where the excitation and emission are entirely in two different regions, two different spectrometers have to be used. For the laser readings, namely ES, LD and LI, a small CCD spectrometer from Thorlabs is used (Thorlabs, CCS200/M). This spectrometer from Thorlabs has a minimum integration time of 10 μs while the Avantes Spectrometer has a minimum integration time ~ 30 ms. The Avantes spectrometer is used in combination with a 950 nm short pass filter (Semrock, FF01-950/SP-25) to block the laser light for the photoluminescence measurements. This configuration requires actually five

different measurements instead of three, though the sample is only held in three different positions as required by the 3M method. This configuration helps in obtaining better data, as the integration-times can be adjusted separately for the PL and excitation laser measurements.

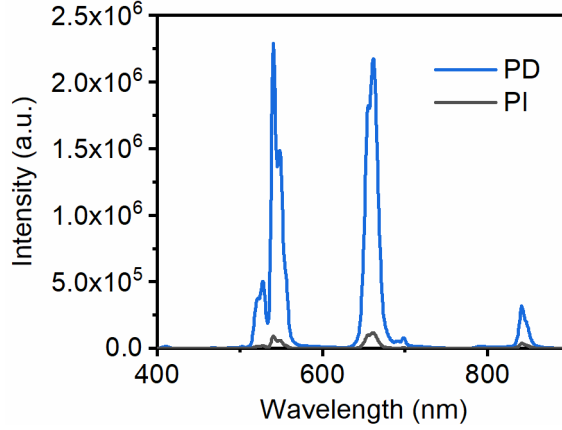


Figure 3.16. Spectra of the photoluminescence when a sample of β - NaYF_4 : 18% Yb^{3+} , 2% Er^{3+} micropowder is placed in the three different positions as required by 3M method.

Internal PLQY is defined as the ratio of number of photons emitted to the number of photons absorbed, while external PLQY is the ratio of the number of photons emitted to the number of photons incident on the sample. Assume A is the fraction of photons absorbed in the first incidence of the excitation beam, such that:

$$A = 1 - \frac{LD}{LI} \quad (3.2)$$

With the 3M method, when the sample is excited such that the excitation spot is smaller than the sample size (all the photons impinge on the sample at least once, regardless of whether they are absorbed or not), the photoluminescence measured when the sample is directly excited is given by:

$$PD = ES \times A \times PLQY + (1 - A)(ES - LI) \times PLQY \quad (3.3)$$

The photoluminescence when the sample is indirectly hit is given by:

$$PI = PLQY(ES - LI) \quad (3.4)$$

Then PLQY is calculated with the equation:

$$PLQY = \frac{PD - (1 - A)PI}{A \times ES} \quad (3.5)$$

3.3. Two-Colour Excitation

To facilitate simultaneous excitation of a UC sample with two different wavelengths, a separate experimental setup is required. The scheme of this set up is given in Figure 3.17. Source 1 is a wavelength tuneable CW laser (M Squared, SolsTiS) set at 980 nm and Source 2 is a diode

laser (Thorlabs, FPL1055T) with a wavelength of 1550 nm. EPD of the excitation beams are controlled using ND filters. The reflective ND filter kit from Thorlabs (Thorlabs, NDK01) is used for this purpose. The two excitation beams are merged into one path by using a long-pass dichroic mirror (Thorlabs, DMLP900) and a short-pass dichroic mirror (Thorlabs, DMSP1180). By using a lens (Thorlabs, LA1027), the merged excitation beam is focussed onto the sample. The UC emission is collected using the same lens and using the long-pass dichroic mirror and another lens (Thorlabs, LA1131), the emission is fibre coupled (Thorlabs, FP1000URT) to a spectrometer (Avantes, AvaSpec-Uls3648).

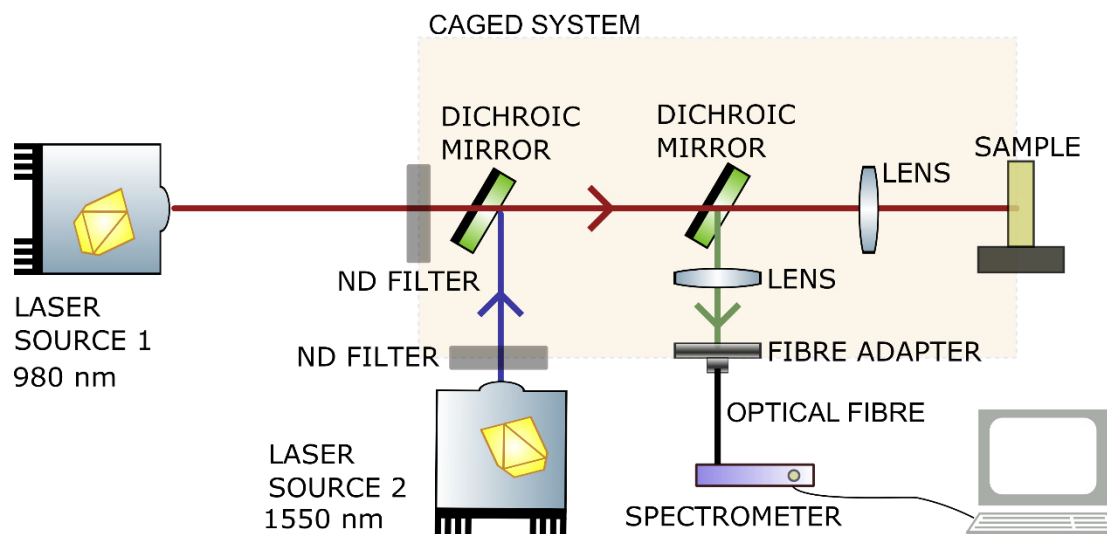


Figure 3.17. Scheme of experimental set-up for UC experiments with simultaneous excitation with two different wavelengths

3.4. Time-Resolved Measurements

Time-resolved measurements give information about the changes occurring in the sample as time proceeds. Lifetime measurements are important as they give an idea of the possible UC mechanisms in a material and of its PLQY. When comparing between two different materials, the PLQY of the UC emission from a higher energy state is dependent on the lifetime of the first intermediate state, as explained later in Chapter 5. For a particular material, the PLQY decreases as the non-radiative decay channels increase, leading to faster decays and therefore shorter lifetimes.

3.4.1. Photoluminescence Decay with Photomultiplier Tube / Multichannel Scaling

Lifetime of an emitting species is the average time it remains in the excited state. The emission can happen at random times, resulting in a range of lifetimes [149]. By time domain measurements, it is possible to obtain a decay curve of the total emission. The decay curve gives a statistical distribution of the emissions, from which the lifetime can be estimated when the type of decay is known (for example, mono-exponential or bi-exponential). The lifetimes of UC emissions are of the order of milliseconds or hundreds of microseconds [123]. The green

emitting state of $\beta\text{-NaYF}_4: 18\% \text{Yb}^{3+}, \text{Er}^{3+}$ has a lifetime of $200 \mu\text{s}$ [144]. Therefore, multi-channel scaling (MCS) electronics is used instead of time correlated single photon counting (TCSPC) to have realistic acquisition times. For TCSPC, the detection rate should be as low as one photon per 100 excitation pulses. However, for the case of MCS, an emission rate of one photon per excitation pulse is enough, resulting in realistic acquisition times for UC lifetimes. Figure 3.18 gives a schematic diagram of the PL decay measurement system.

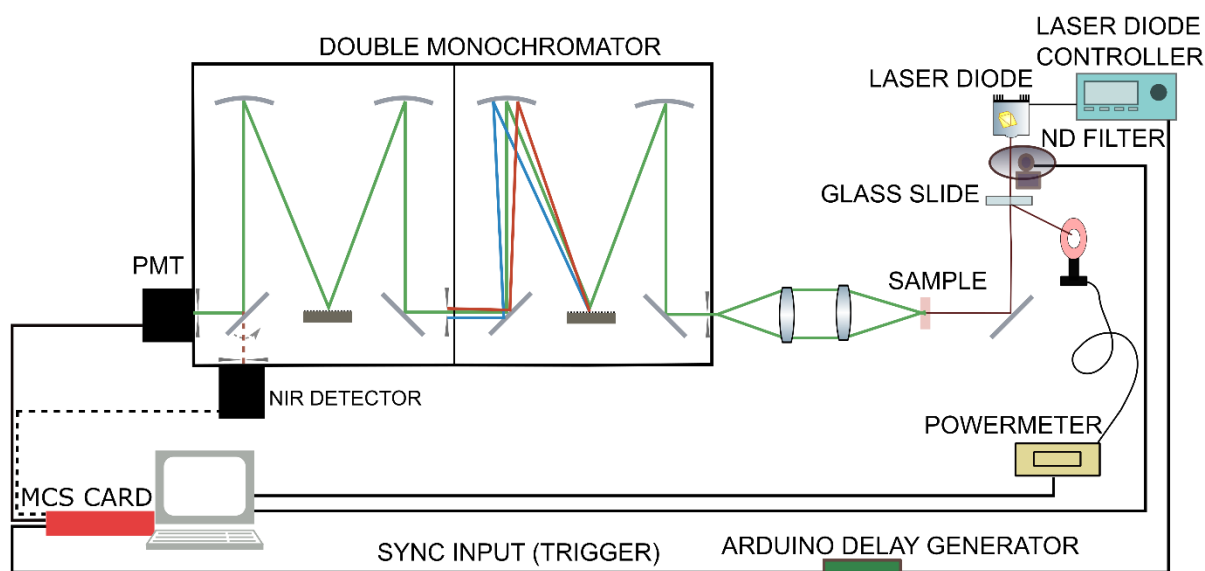


Figure 3.18. Scheme of experimental setup for lifetime determination using MCS

The sample is excited using a diode laser of the required excitation wavelength and power. The power is controlled using a variable ND filter wheel (Thorlabs, NDC-100C-2). The diode laser is driven in quasi-CW mode using a laser diode controller (Thorlabs, ITC4020). The trigger output from the laser diode controller is provided to the multichannel scaling (MCS) card (PicoQuant, TimeHarp 260 NANO) to synchronise it with the quasi-CW excitation. An appropriate delay ($\sim 10 \mu\text{s}$) is inserted into the sync line by using a microcontroller (Arduino, UNO) based delay generator to account for electronic delays in the signal. The emission from the sample is collected using a lens system consisting of two lenses and focussed into the input slit of a double monochromator (Bentham, DTMS300). The monochromator isolates the selected wavelength and passes it to one of the sensitive detectors. The double monochromator is used to decrease stray light (re-entrant spectra) entering the detector. A circular cage photomultiplier tube (PMT) (Hamamatsu, R928P) is used with a preamplifier (PicoQuant, PAM-102P) as the detector in the visible range (185 to 900 nm) whereas another single photon detector (ID Quantique, ID220) is used in the infrared range (900-1700 nm). The signal from the detector is passed on to the MCS card connected to the PC. The Timeharp 260 NANO card has a dead time $< 2 \text{ ns}$. After every detection event, a new detection can only be registered after the dead time. Accordingly, the intensity of emission from the sample has to be decreased such that all photons are counted. Using the Timeharp software [150], a

histogram of the detection of the emitted photons is obtained from which lifetimes can be estimated by fitting the decay curve with the suitable exponential decay function.

3.4.2. Evolution of UC Intensity with Time

Different factors contribute to a sudden change of the UC intensity upon sample excitation. Materials that have a higher maximum phonon energy, for example will have more non-radiative decay channels causing a sudden dip in the UC intensity as a result of laser-induced heating. A detailed discussion of this phenomenon is provided in Chapter 4. A scheme of the experimental setup used to investigate this phenomenon is given in Figure 3.19. A 980 nm laser diode (Thorlabs, L980P200) mounted on a temperature-controlled mount (Thorlabs, TCLDM9) and stabilized with a laser driver controller (Thorlabs, ITC4001) is used as the excitation source. An automated shutter is used to turn the excitation on and off using a shutter controller (Thorlabs, SC10). An automated filter wheel (Thorlabs, NDC-100C-2) of variable neutral density can change the excitation power shining on the sample. A plano-convex lens (Thorlabs, LA1978) of 750 mm focal length is used to focus the excitation beam on the sample. A glass slide is inserted at an angle in the beam path for inline measurement of power. The glass slide reflects a portion of the excitation beam, which corresponds to 8% of the power of the beam at the sample position. The power of this beam is measured using a power meter (Thorlabs, PM320E) in combination with a sensor (Thorlabs, S121C). The area of the beam is calculated using a beam profiler (Thorlabs, BP209-IR/M). The emission from the sample is isolated using a 950 nm short pass filter (Semrock, FF01-950/SP-25) and focussed to the optical fibre (Thorlabs, FP1000URT) using a lens of 35 mm focal length (Thorlabs, LA1027). The optical fibre is then connected to the spectrometer (Avantes, AvaSpec-ULS2048x64TEC).

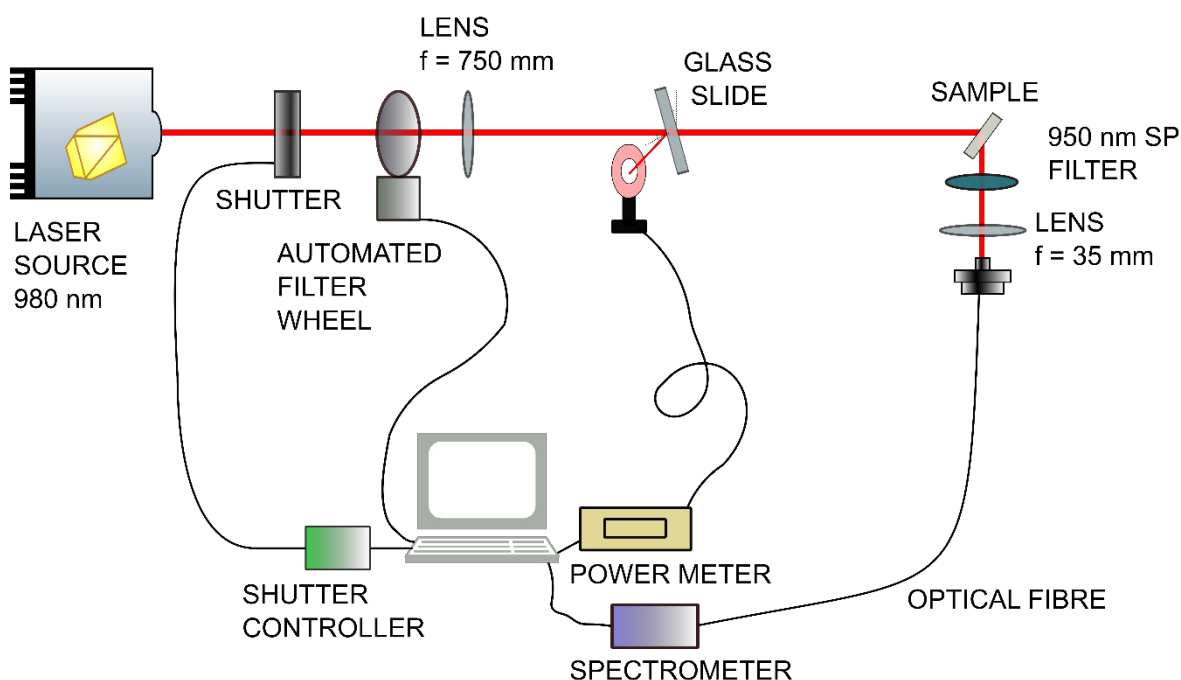


Figure 3.19. Scheme of experimental setup for observing instantaneous change in UC intensity after excitation

The spectrometer is set to the least integration time possible (~ 30 ms) for this measurement. The laser diode is turned on early enough so that it is in steady-state. Before every measurement, the filter wheel is adjusted so that the required power density would be shining on the sample. Then acquisition of the spectrum is started on the spectrometer VI realised through a LabVIEW® [142] virtual instrument. Finally, the shutter is turned on and the spectra are continuously acquired until a set time is reached (60-120 s). By integrating over the range of wavelengths corresponding to a certain peak, we are able to get the initial rise in the UC signal and the change in the signal after the signal reaches its peak. The progress of individual peaks can be analysed in the program, and this gives an idea of which states are more affected by laser-induced heating. Such a curve obtained by integrating the spectra over the green peak as a function of time is given in Figure 3.20.

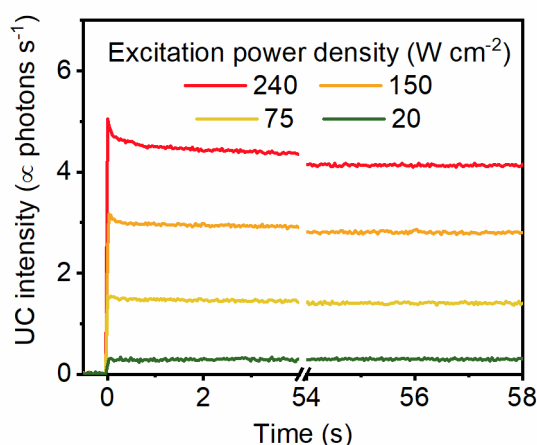


Figure 3.20. UC emission from $^2H_{11/2}$ and $^4S_{3/2}$ states of Er^{3+} doped in β - $NaYF_4$ micropowder vs time. Adapted from Joseph et al. [139].

3.5. Analysis of Spectroscopic Data

Spectroscopic data can give valuable information about the composition, physical and chemical structure, temperature, size and speed of celestial objects etc. [151]. UC materials when doped in other materials can serve as photonic markers based on lifetimes or colours [27,152]. The spectroscopic analysis of these materials then gives information about the material. Some materials exhibiting UC have thermally coupled energy states. The ratio of the intensity of the peaks of two energy states (belonging to the same lanthanide or two different lanthanides) is indicative of the temperature of the material. If such a material is doped into biological tissue, using only the intensity-ratios of the peaks, the temperature of the tissue can be detected [63]. Additional advantages like good signal stability, low scattering and background noise make such detections accurate.

3.5.1. Temperature Estimation from Ratio of UC Peaks

In a single lanthanide, thermally coupled energy states are usually separated by a small energy gap. Then the population of the energy states can be described by the Boltzmann's Law:

$$n_i = N e^{\frac{-E_i}{k_B T}}, \quad (3.6)$$

where n_i is the population of the level i , E_i is the energy of the level relative to the ground level, N is the total number of electrons in the system, T is the absolute temperature in Kelvin, and k_B is the Boltzmann constant.

The integrated area under an emission peak gives the population of the level. The ratio of intensities of two thermally coupled peaks is given by [153,154]:

$$R(T) = \frac{\int I_2 d\lambda}{\int I_1 d\lambda} = C e^{\frac{-\Delta E}{k_B T}}, \quad (3.7)$$

where ΔE is the difference in energies between the energy levels and the constant C is dependent of the degeneracy of the level (g), spontaneous emission rate (ν), and optical absorption cross section (σ) [155], such that,

$$C = \frac{g_1 \nu_1 \sigma_1}{g_2 \nu_2 \sigma_2}. \quad (3.8)$$

Figure 3.21 gives the changes in a UC spectrum as the temperature increases. Certain peaks rise as temperature increases while other peaks decrease in magnitude. The two peaks marked I_2 and I_1 are well known thermally coupled levels of Er^{3+} .

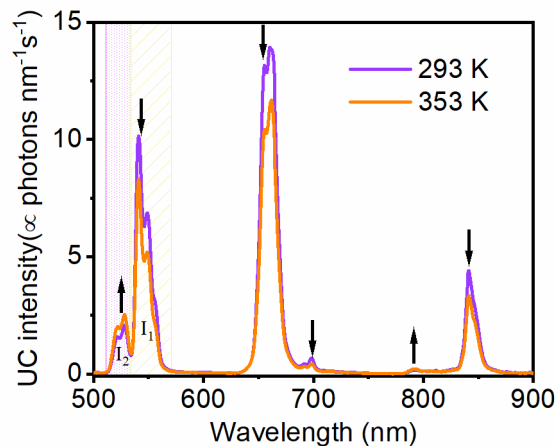


Figure 3.21. UC Emission from $\beta\text{-NaYF}_4:\text{Er}^{3+}, \text{Yb}^{3+}$ when excited with 980 nm at an EPD of 240 W cm^{-2} at two different temperatures

A calibration curve can be made of the logarithm of the intensity-ratios vs the inverse temperature. The temperature can be read out of a calibration curve defined for a material in a specific medium with constant properties like pressure, pH etc., if the intensity-ratio is

determined. In this way, the UC material functions as a secondary thermometer, which means that a calibration is required every time there is a change in the surrounding. The relative sensitivity of such a thermometer is given by the expression:

$$S_R = \frac{1}{R(T)} \frac{\partial R(T)}{\partial T} = \frac{\Delta E}{k_B T^2} \quad (3.9)$$

Secondary thermometers have the disadvantage that a recalibration needs to be done if the experimental conditions change, as the value of C changes. To circumvent this problem, an expression of the temperature, which does not use the constant C , needs to be used. The intensity-ratio $R(T)$ increases linearly as the EPD increases such that a straight line can be plotted with a y-axis intercept. The y-axis intercept gives the value of R_0 at which the pump power is zero and T_0 gives the room temperature at which the pump power is zero, and accordingly laser-induced heating is also zero (Figure 3.22). An equation for a primary thermometer can then be made for the material, knowing the value of R_0 and T_0 [156]:

$$\frac{1}{T} = \frac{1}{T_0} - \frac{k_B}{\Delta E} \log_e \frac{R(T)}{R_0} \quad (3.10)$$

The temperature of the sample can then be estimated from this equation by knowing the value of R_0 and the intensity-ratio of the peaks. Chapter 4 gives a detailed consideration of this method and presents data from multiple samples.

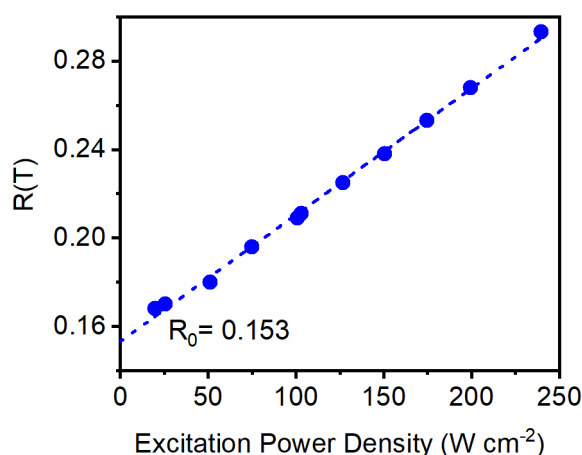


Figure 3.22. Plot of the intensity-ratios of the two thermally coupled peaks vs the EPD. The y-intercept gives the limit at which EPD is zero.

3.5.2. Multivariate Curve resolution –Alternative Least Squares (MCR-ALS)

MCR-ALS stands for Multivariate Curve Resolution (MCR) using the Alternating Least Squares (ALS) algorithm. MCR is a tool used for resolving pure response profiles when more than one species is involved [157,158]. For a system having a known number of constituents, which have distinct responses, when certain boundary conditions and initial conditions are known, the individual responses and the initial spectra of each of the constituents can be extracted

from the total response of the system using this technique. Two requirements need to be met: 1) the total response of the system can be expressed as a two-way data matrix or a multiset structure and that 2) a bilinear model can describe this data with a limited number of components. The total spectra matrix- D is written as a product of two matrices plus a matrix of residuals (E). The first one gives the pure spectra (S^T) of individual elements and the second one- C gives the concentration profiles, of these elements:

$$D = CS^T + E \quad . \quad (3.11)$$

The scheme of the algorithm is given in Figure 3.23. The developers of the method has implemented the tool in MATLAB as a graphical user interface (GUI) [159]. In the investigation of the photophysics of upconversion processes in Chapter 5, MCR-ALS is used to isolate two-photon processes and three-photon processes of UC as the EPD increases. The matrix D will be a matrix in which the spectra changes as the EPD increases. At each EPD, the UC intensity at each wavelength is divided by the total area of the spectrum, which corresponds to the total number of photons emitted. Therefore, the matrix D is a set of spectra normalized to the total number of emitted photons at each EPD. By loading the matrix D onto the MCR-ALS GUI, we expect to get the matrices C and S^T as result. First, an initial estimation of the number of components is required. Assuming only two- and three-photon processes are present, we can give the number of components as two. As the EPD increases, we know that the contribution of two-photon processes decreases, while that of three-photon processes increase. The concentration profiles of these two processes never become negative and they are unimodal, meaning that they change only in one direction. That is, as the EPD increases, the contribution from two-photon process will only decrease, but not decrease and later increase. This knowledge can be applied to give row and column constraints to the matrices. Then the ALS optimization is applied to the matrix along with the constraints yielding the matrices C and S^T . The concentration matrix C will be a function of the contributions of the two pure spectra as the EPD increases and the matrix S^T gives the two pure UC spectra if only two-photon processes were present or if only three-photon processes were present.

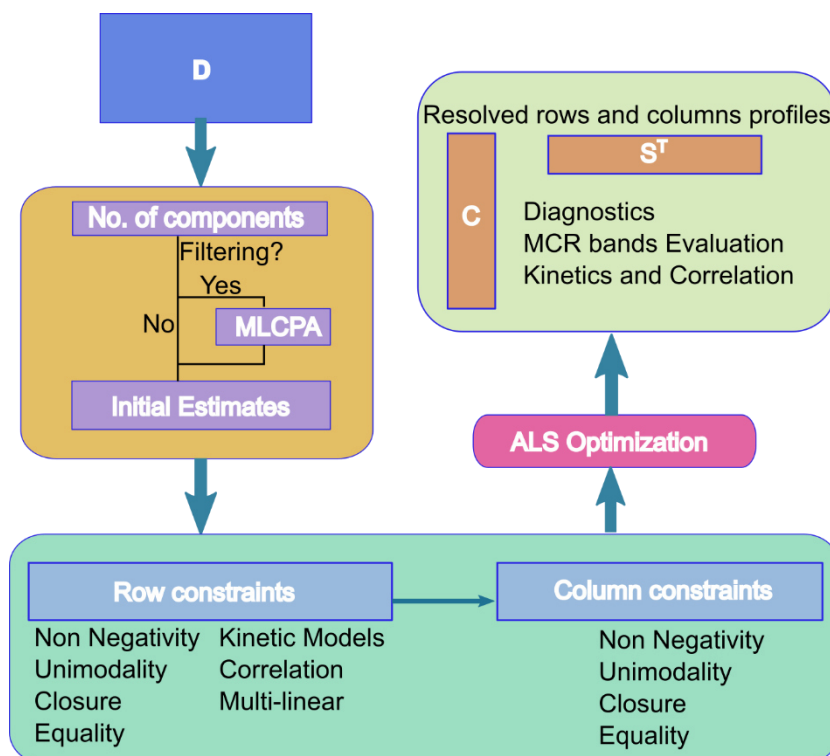


Figure 3.23. Scheme of the MCR-ALS algorithm. MLPCA stands for Maximum Likelihood Principal Component Analysis [160]. Adapted with permission from Tauler et. al. [159].

Figure 3.24 presents the results of MCR-ALS analysis on YCl_3 : 18% Yb^{3+} , 2% Er^{3+} to resolve the UC peaks from two- and three-photon processes upon 980 nm excitation as the EPD is increased. The number of components can be set as two. Following an initial estimate by MLPCA, the row constraints of non-negativity and unimodality is applied, knowing that the contributions either decrease or increase in one direction. Similarly, the column constraint of non-negativity can be applied as the UC peaks never become negative. Thereafter, the ALS optimization yields the spectra of the two- and three-photon peaks separately as the matrix S^T and the relative contributions of these spectra as the matrix C . Some of the peaks can be purely ascribed to two-photon processes, and some others to three-photon processes and some peaks show contribution from both three-photon and two-photon processes. More results of MCR-ALS analysis are presented in Chapter 5.

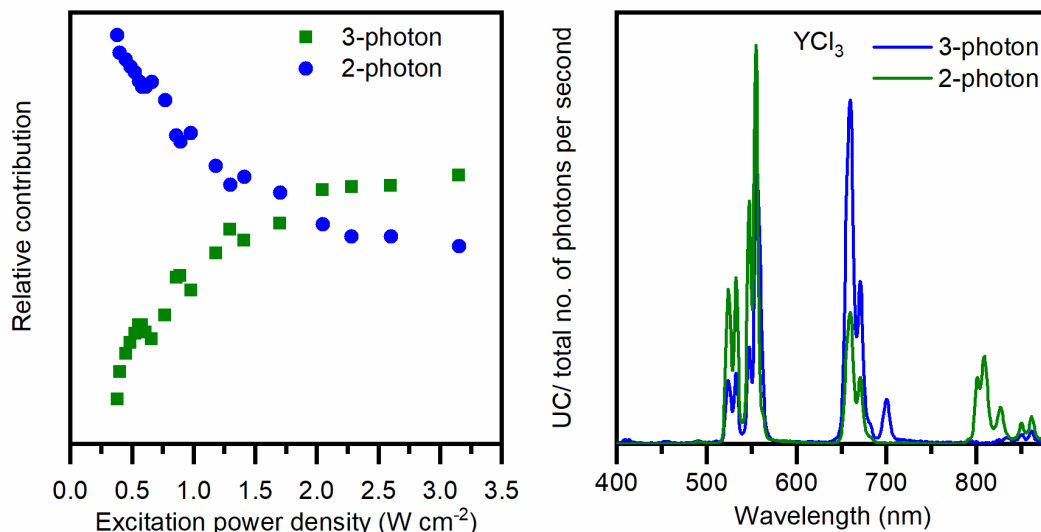


Figure 3.24. Resolved concentration and spectra profiles of 2-photon and 3-photon processes from Er^{3+} , Yb^{3+} UC emission from YCl_3 micropowder upon 980 nm excitation as the EPD is increased.

3.6. CIE Colour Coordinates and Luminance Determination

When a material emits radiation of different visible wavelengths at the same time, the human eyes perceive it as a single colour (due to additive colour mixing). In bright and moderately bright environments, this colour is based on the spectral sensitivities of the three kinds of cone cells in the retina of the eye. The normalised spectral sensitivities of the three types of cone cells are given in Figure 3.25. In low-light vision the rod cells of the eyes come into play as they are better photo-receptors in low-light.

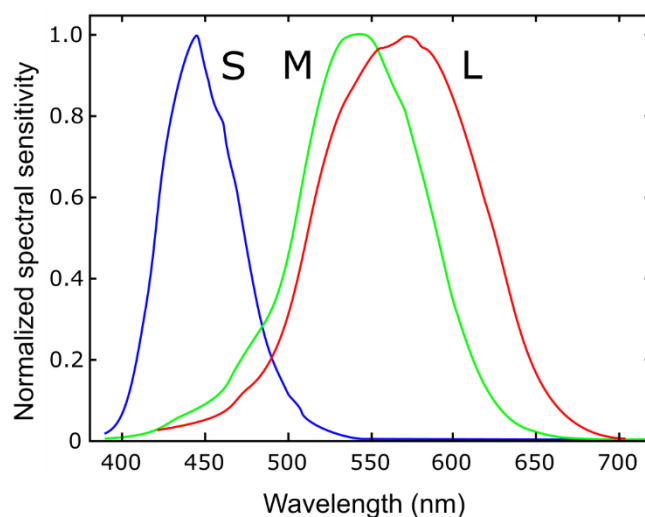


Figure 3.25. Normalized spectral sensitivities of the three types of cone-cells in the human eye. S (420 nm – 440 nm), M (530 nm – 540 nm), and L (560 nm – 580 nm) correspond to the three wavelength regions in which the cone cells are active.

3.6.1. CIE Chromaticity diagram

The "Commission Internationale de l'éclairage" (CIE), known in English as the International Commission on Illumination introduced the (red-green-blue) RGB and XYZ colour spaces to map these colours based on a coordinate system in 1931 based on experimental data from human observers. The CIE tristimulus values - X, Y and Z can be easily calculated by integrating the product of the spectra with corresponding colour matching functions over the wavelength range 380 nm to 780 nm. The RGB tristimulus values can also be calculated in the same way. These colour matching functions are published by the CIE in the form of look up tables but can also be approximated as a sum of gaussian functions [161]. Colour consists of two aspects: brightness and chromaticity. For example, white and grey have the same chromaticity but different brightness. The CIE Y value is designed to be an indicator of the luminance of the colour. Three parameters (x,y,z) can be derived from the CIE tristimulus values, out of which x and y give the chromaticity:

$$x = \frac{X}{X + Y + Z} \quad , \quad (3.12)$$

$$y = \frac{Y}{X + Y + Z} \quad , \quad (3.13)$$

$$z = \frac{Z}{X + Y + Z} = 1 - x - y \quad . \quad (3.14)$$

The CIE 1931 xy chromaticity diagram is a horse-shoe shaped region which shows the colours that can be observable with the human eye. It is formed using the chromaticity values - x and y and a spectral locus as shown in Figure 3.26. The spectral locus consists of the colours observed with monochromatic light between 380 and 780 nm, as is indicated in the CIE 1931 diagram. The base of the horse-shoe region consists of a "line of purples" which do not correspond to any monochromatic colour of the spectrum.

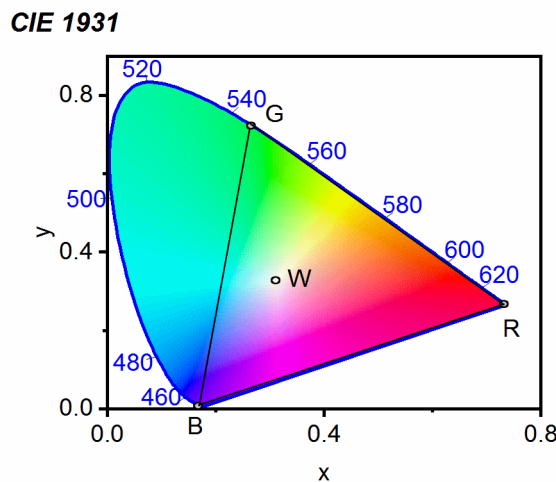


Figure 3.26. CIE 1931 xy chromaticity diagram, showing the positions of the three primary colours and the colour white, along with the triangle representing the gamut of the RGB colour space.

In the CIE xy chromaticity diagram, white colour is at the CIE coordinates (0.33, 0.33). Pure green, red and blue are monochromatic and hence ascribed to the wavelengths 546.1 nm, 700 nm and 435.8 nm, respectively, which lie on the spectral locus of the CIE 1931 diagram. Therefore, the RGB colour space can be drawn as a triangle inside the CIE 1931 xy chromaticity diagram.

As lanthanide doped UC materials can emit radiations of multiple wavelengths, the colour perceived by the eye needs to be known for display applications. For this purpose, the total emission spectra in each case is integrated over wavelength with the CIE-XYZ colour matching functions obtained as a table from the colour and vision research laboratory (CVRL) database, which is part of the University College London. Thereafter, the chromaticity coordinates are calculated and plotted on the CIE 1931 chromaticity diagram. These calculations are performed using MATLAB.

3.6.2. Luminance calculation

Luminance is different from intensity in the sense that it gives the brightness perceived by the eye. The human eye is not equally sensitive to all wavelengths in the visible spectrum. Vision is divided into three categories based on the luminance levels. In normal daylight conditions (10^{-10} to 10^8 cd m⁻²), the cone cells on the retina are more sensitive and hence, we experience photopic vision. On the other hand, the rod cells are more sensitive in the dark ($< 10^{-3}$ cd m⁻²), where the vision moves into the scotopic regime [162]. In a moderately bright environment, (10^{-3} to 10 cd m⁻²), a combination of both kinds of vision called the mesopic vision is observed. Therefore, a separate unit called the “lumen” is defined for quantifying the brightness perceived by the eyes, i.e., luminance. Luminance is defined based on the scotopic and photopic luminous efficacy curves as shown in Figure 3.27.

The standard luminosity function is the normalized version of these luminous efficacy curves. For photopic vision, the luminance L can be calculated from the emission intensity I in W m⁻² sr⁻¹ nm⁻¹ with the expression:

$$L = 683.002 \frac{\text{lm}}{\text{W}} \int I(\lambda) \bar{y}(\lambda) d\lambda \quad , \quad (3.12)$$

where $\bar{y}(\lambda)$ is the standard luminosity function for photopic vision and λ is the wavelength. The unit for luminance is then lm sr⁻¹ m⁻² which can also be called in SI units as cd m⁻².

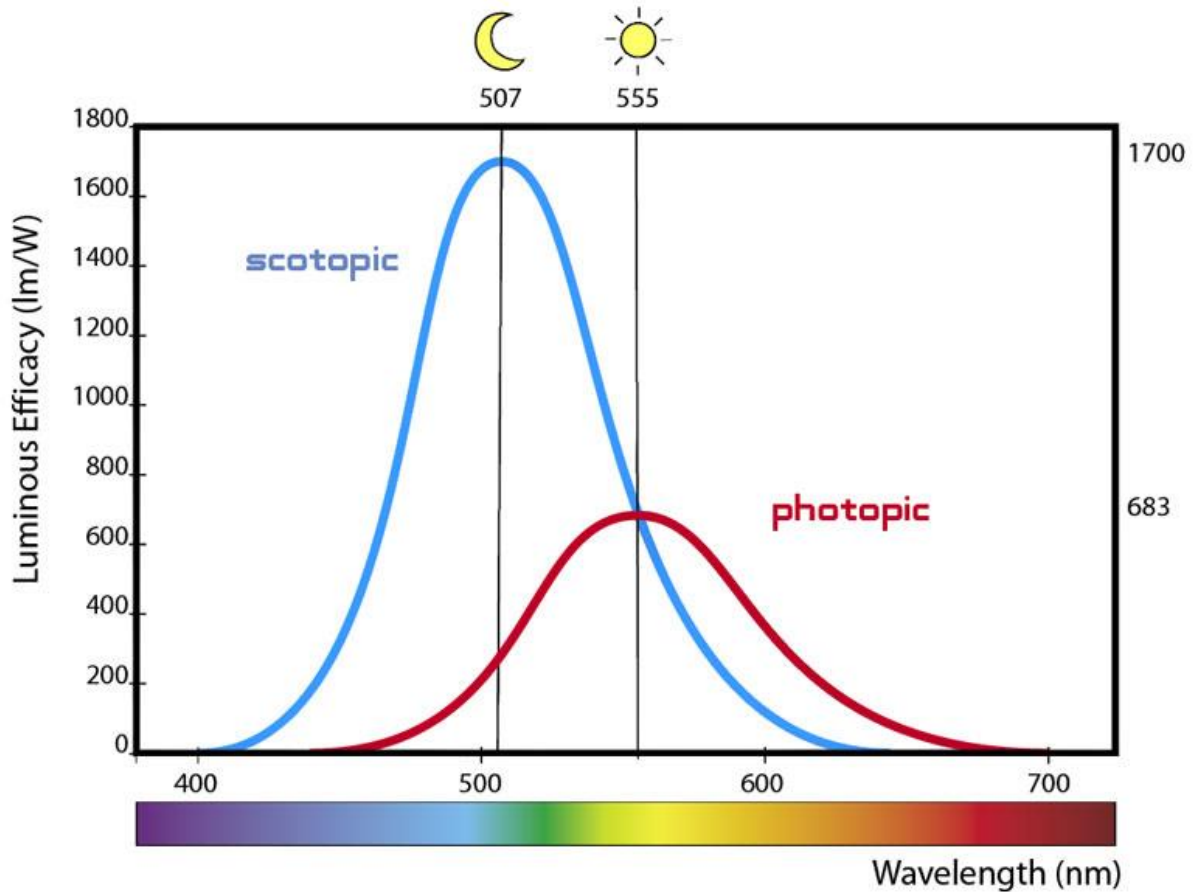


Figure 3.27. Luminous Efficacy for photopic and scotopic functions as a function of wavelength. The peaks of the scotopic and photopic functions are at 507 nm and 555 nm respectively, which correspond to luminous efficacies of 1700 and 683 lumen per watt. Reproduced from [163] Copyright 2007 Martin Dixon and Primalence UK

For the luminance calculations used in this work, the photopic standard luminosity function provided by the CIE consistent with the cone fundamentals defined by Sharpe et al. is used [116]. The measured spectra are converted to absolute units of photons $s^{-1} cm^{-2} nm^{-1}$ after calibration. For ease of calculations, all the emitted photons are assumed to be at the peak of the emission spectra (545 nm), for conversion into $W m^{-2}$ by multiplying with the standard luminosity function. For conversion into candelas, a solid angle of 4π sr is assumed. The calculations are performed using a MATLAB code.

4. Correcting the Effects of Laser-Induced Heating in Upconversion Measurements

This chapter deals with a common problem encountered in UC measurements, namely laser-induced heating. It is based on the first first-author-publication “A method for correcting the excitation power density dependence of upconversion emission due to laser-induced heating”, Optical Materials, Vol. 82, 2018 [139]. The idea for the publication was conceived by the author, Ian A. Howard and Dmitry Busko. Dmitry Busko helped in setting up the measurement system. The microcrystal sample was synthesized by Damien Hudry and Daniel Biner at the University of Bern under the guidance of Karl Krämer. The nanocrystals were synthesized by Damien Hudry in house. The steady state and time resolved measurements were performed by the author. Guojun Gao performed X-ray powder diffraction and scanning electron microscopy experiments of the samples. Andrey Turshatov, Ian A. Howard, Karl Krämer and Bryce S. Richards helped in interpreting the results and finalizing the draft.

4.1. Introduction

UC is a non-linear process. This means that the intensity of UC emission is not always proportional to the excitation power density (EPD). The measurement of the log-log plot of the UC intensity vs the EPD is an important characterization tool for UC. The slope of this curve gives valuable information about the order of the UC process and its underlying mechanism as tabulated in Table 2.2. For ETU processes, the slope of the log-log plot of the UC-EPD dependence at very low EPDs is equal to the number of photons involved in the UC process [85]. A two-photon process will have a slope of 2 at very low EPDs and a three-photon process will have a slope of 3 and so on. To properly understand the behaviour of a UC emission, the EPD must be swept for several orders of magnitude. Ideally in the limit of high EPDs, the slope of the log-log plot should be unity, as the UC saturates as explained in Section 2.1.5.2. But often the slopes become sub-unity indicating a reduction in the total UC intensity [164,165]. This drop in UC intensity is not theoretically explained, and not expected from the mechanism of UC. As the PLQY of UC emission is proportional to the UC intensity divided by the EPD, the slope of the PLQY vs EPD curve becomes 0 in the limit of high EPDs, i.e. in the regime that UC saturates. The PLQY at saturation is an important figure-of-merit for a UC material and is explained in detail in the subsequent Chapter. When the error introduced

by laser-induced heating is not corrected in the PLQY measurements, the PLQY decreases at higher EPDs instead of remaining constant as fundamentally expected. This under-estimation of the PLQY and the UC intensity, creates a roadblock to the development of applications for UC, which requires precise identification of the regimes of EPD in which a UC material operates. A method for correcting this unexplained change in UC intensity due to laser-induced heating is developed and presented in this Chapter. Section 4.1 briefly gives the synthesis techniques used for the samples analysed in this Chapter. Section 4.2 illustrates the intensity dependence of UC on a microcrystal sample and the problem of underestimation. Section 4.3 explains how the inherent properties of the UC material are used for determining the temperature of the sample and Section 4.4 explains the method proposed for correcting the UC dependence. In Section 4.5 a nanocrystal sample is examined for laser-induced heating. Finally, Section 4.6 summarizes the results presented in this chapter.

4.2. UC Intensity-EPD Dependence

Measurement of the EPD dependence of the UC intensity is an important characterization tool for identifying the mechanism of the UC and to understand the order of the UC process. Fig 4.1 illustrates an EPD dependence curve plotted on a double-logarithmic scale. Here, microcrystals of β -NaYF₄: 18% Yb³⁺, 2% Er³⁺, hermetically sealed in a quartz cuvette of 1 mm x 1 mm cross-section are excited with a 980 nm laser, spanning EPDs ranging from 1 - 250 W cm⁻². Then, the integrated UC intensity under the emission spectra ranging from 400 -880 nm is plotted against the corresponding EPDs on a log-log scale. The slopes of the curve at the two extremities are 1.5 and 0.9. A slope of 1.5 at low EPDs indicates a UC constituting mainly of two-photon UC processes, as the slope is greater than 1. If the material is excited at much lower EPDs, the slope would approach 2 as predicted by Pollnau *et al.* [85]. However, a slope of 0.9 is unwarranted for in the high EPD regime (grey rectangle), as a slope of 1 is expected at such high EPDs, and corresponding PLQY would show a downward trend, when it is expected to stabilize due to saturation [93,166]. Such behaviour indicates the presence of a quenching mechanism, which decreases the UC intensity. This quenching mechanism is due to laser-induced heating as elucidated in the sections which follow. A method to correct the EPD dependence curve of UC is developed based on estimation of the temperature of the material making use of the inherent thermally coupled states ²H_{11/2} and ⁴S_{3/2} of Er³⁺. The corrected curve is already provided with the measured curve in Figure 4.1, showing that the slope of the curve becomes 1 at high EPDs after the correction. Note that the difference between the two curves are already pronounced at EPDs around 50 W cm⁻². At an EPD of 240 W cm⁻², the corrected integrated UC intensity is already 24% higher than the measured value, which is really significant and shows the necessity of correcting for the effects of laser-

induced heating. The following section describes the method by which the temperature of the UC material is measured.

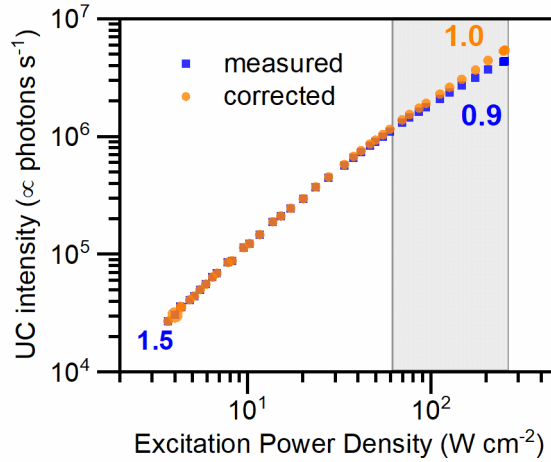


Figure 4.1. Double logarithmic plot of the Excitation Power Density (EPD) dependence of UC (400-880 nm) of microcrystals of β -NaYF₄: 18% Yb³⁺, 2% Er³⁺ excited at 980 nm. The blue squares show the measured data and the orange circles show the data corrected for laser-induced heating. The shaded region shows the regime in which the dependence is expected to be linear. The numbers at the extremities show the slopes of the plot in that region. Adapted from Joseph et al. [139].

4.3. Temperature Determination

The ²H_{11/2} and ⁴S_{3/2} states of Er³⁺ are thermally coupled and used extensively in luminescence thermometry [63,153]. The ratio of the UC emissions from these two states are related to the temperature. Figure 4.2. shows the UC spectra observed from the microcrystal sample of β -NaYF₄: 18% Yb³⁺, 2% Er³⁺, excited with 980 nm at an EPD of 240 W cm⁻², captured at 1 second after excitation and 60 seconds after excitation. For this measurement, the UC spectra are continuously measured every 30 ms to accurately follow the change in the ratio of the intensities of the two peaks. In comparison to the spectra at 1 second after excitation, only the emission peak around 520 nm is seen to rise in intensity, while all the other peaks decrease in intensity in the spectra at 60 s. This clearly indicates a rise in the temperature, as the ratio of the intensities of the two peaks - Δ , is related to the temperature as per the Boltzmann distribution [167]:

$$\Delta \equiv \frac{I_2}{I_1} = K \exp\left(\frac{-\Delta E}{k_B T}\right) . \quad (4.1)$$

where I_1 (510-533 nm, $^2H_{11/2} \rightarrow ^4I_{15/2}$) and I_2 (530-570 nm, $^4S_{3/2} \rightarrow ^4I_{15/2}$) are the integrated areas under the two peaks, k_B the Boltzmann constant, ΔE the energy difference between the two levels in joules, and T the absolute temperature in kelvin. The pre-exponential constant K depends on the degeneracies and radiative rates of the transitions from both energy states and is evaluated through external calibration.

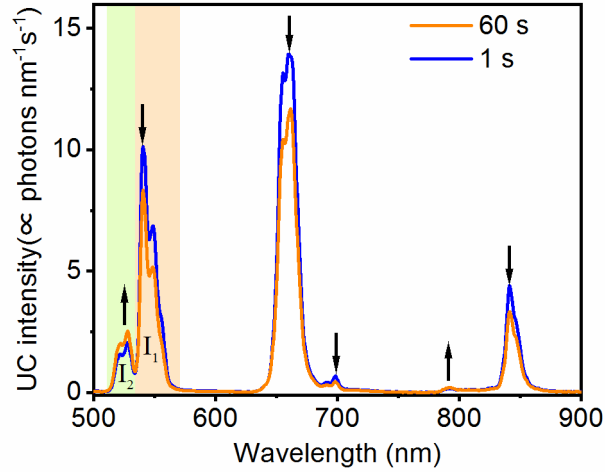


Figure 4.2. UC spectra of β -NaYF₄: 18% Yb³⁺, 2% Er³⁺, 1 s and 60 s after excitation with 980 nm radiation at an excitation power density of 240 W cm⁻². Adapted from Joseph *et al.* [139].

Figure 4.3 gives the ratios of the intensities of the two peaks as a function of time for different EPDs of 980 nm radiation in the same sample. A significant increase in the intensity-ratios is observed for an EPD as low as 50 W cm⁻². The ratio of the intensities of the two peaks first increases and reaches a steady-state value in each case. Knowing the intensity-ratios at each EPD, the temperature can be estimated using the method proposed by Balabhadra *et al.* using UC materials as primary thermometers without having to use another calibration using a thermocouple [156]:

$$\frac{1}{T} = \frac{1}{T_0} - \frac{k_B}{\Delta E} \ln \frac{\Delta}{\Delta_0} \quad (4.2)$$

where, T_0 is the room temperature when no excitation is provided (293 K) and Δ_0 is the ratio of I_2 to I_1 graphically estimated in the limit of zero pump power as shown in Figure 4.4 [168]. To estimate the value of Δ_0 , first the steady-state value of the ratios of the intensities are plotted with the corresponding EPDs. Then the y-intercept of the best linear fit gives the value of Δ_0 .

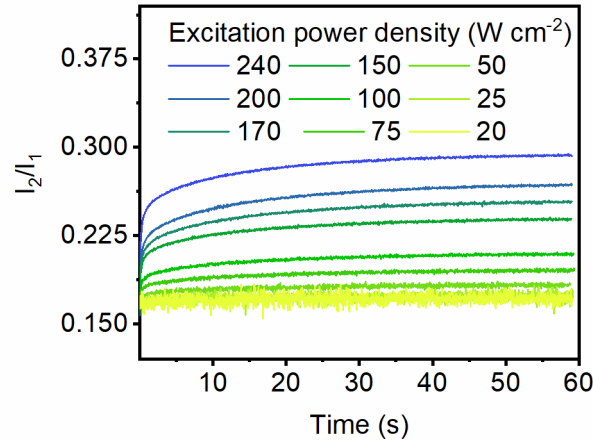


Figure 4.3. Intensity-ratios (I_2/I_1) of the two green emitting states ${}^2H_{11/2}$ and ${}^4S_{3/2}$ as a function of time at different excitation power densities of 980 nm radiation for $\beta\text{-NaYF}_4:\text{Yb}^{3+}/\text{Er}^{3+}$ (18/2%) micropowder. Adapted from Joseph et al. [139].

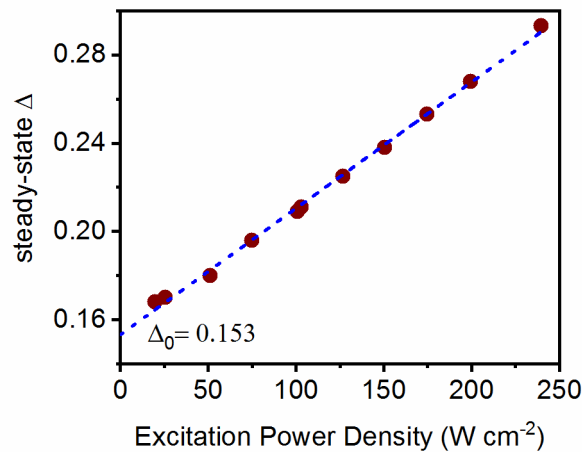


Figure 4.4. Calculation of Δ_0 from the plot of steady-state intensity-ratios vs excitation power density. Δ_0 is graphically determined by finding out the y-intercept of the best linear fit to the steady-state experimental values of I_2/I_1 ($r^2 > 0.997$). Adapted from Joseph et al. [139].

Once the value of Δ_0 is determined, using equation 4.2, the temperatures corresponding to each EPD can be calculated. The temperatures are plotted as a function of time in Figure 4.5. Just as in the case of the intensity-ratios, the temperatures rise sharply in the first couple of milliseconds, and then reaches a steady-state value, as a balance is established between the laser-induced heating and the thermal dissipation to the surroundings in the sample. The rise in temperature is more significant for higher EPDs. For an EPD of 240 W cm^{-2} , the temperature rose by 60 K. UC-EPD measurements are normally automated and as the laser is always shining on the sample, there is not enough time for the sample to cool down. The UC intensities are then always measured at these elevated temperatures causing erroneous measurements.

The effect of these elevated temperatures on the total UC intensity and the physics behind it, are discussed in the next section.

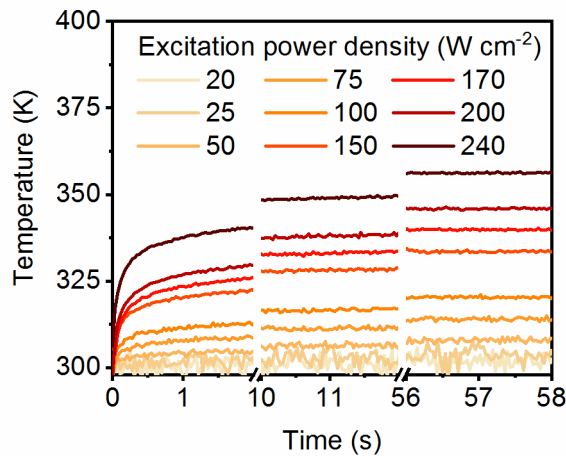


Figure 4.5. Temperature of the sample as a function of time after excitation with 980 nm at different excitation power densities. Adapted from Joseph et al. [139].

4.4. Intensity Correction

A plot of the total integrated UC intensity in the range 400-880 nm is given as a function of time following excitation with 980 nm radiation at different EPDs in Figure 4.6. The spectra are acquired every 30 ms, and then the total area under the spectra are calculated. For lower EPDs, the UC intensity shows no change in time, but for higher EPDs ($> 50 \text{ W cm}^{-2}$), the total integrated UC intensity starts to decrease non-trivially and approaches a steady-state value. For an EPD of 240 W cm^{-2} , the total integrated UC intensity decreased by 22%, which leads to a huge underestimation of the UC intensity and the PLQY.

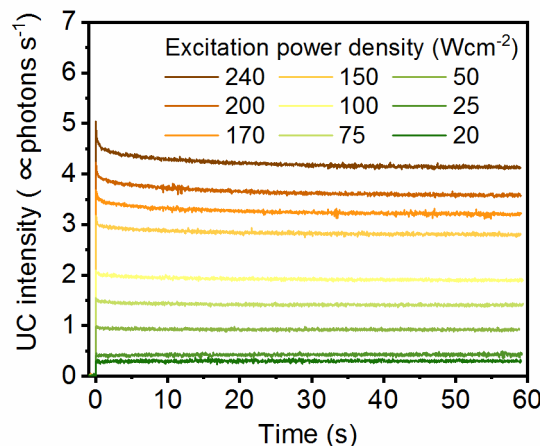


Figure 4.6. Variation in the total UC intensity in the first minute following 980 nm-excitation due to laser-induced heating. Adapted from Joseph et al. [139]

To correct the observed values of the total integrated UC intensity on the EPD dependence curve, first correction factors were calculated at selected EPDs. The correction factor is the ratio of the initial UC intensity (real value) to that of the steady-state UC intensity. When these correction factors are plotted as a function of the EPD, a linear behaviour is observed. This line correlates well with the plot of the calculated steady-state temperature vs EPD. Figure 4.7. illustrates this correlation between the correction factors and the steady-state temperatures.

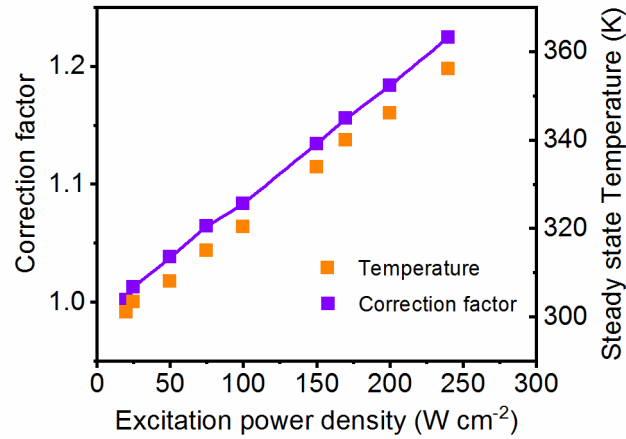


Figure 4.7. Calculated temperatures at each excitation power density showing a linear correlation with the correction factors required for correcting the total integrated UC emission. Adapted from Joseph et al. [139]

It is a known fact that the rate of multiphonon relaxation (MPR) increases as the temperature increases. When MPR increases, there is an increased probability of the excited energy states getting depopulated via non-radiative channels. The equation developed by Riseberg and Moos in the late 1960s, gives the expression for MPR rate, $W(T)$ as a function of the temperature T and the maximum phonon energy $h\nu_m$ of the lattice [100]:

$$W(T) = W(0) \left[\frac{\exp\left(\frac{h\nu_m}{kT}\right)}{\exp\left(\frac{h\nu_m}{kT}\right) - 1} \right]^{\frac{\Delta E}{h\nu_m}} \quad (4.3)$$

where $W(0)$ denotes the spontaneous transition rate at 0 K, ΔE the energy gap between an excited energy state and the one immediately below it and ν_m the maximum frequency of lattice vibrations that couple to the rare earth ion's electronic transition. This equation has an exponential dependence at temperatures below 300 K. But for higher temperatures, the equation shows a linear behaviour explaining why such a linear behaviour is observed in the plot of the dependence of correction factors on EPD [169]. Other factors like an increase in the

cross-relaxation rate or a reduction in the excitation cross-section at elevated temperatures could also contribute to the observed reduction in the UC intensity [93,166]. However, laser-induced heating is hypothesized to be the major factor affecting the UC intensity. To examine this claim further, the sample is excited at 940 nm, at which the sample shows decreased absorption. The diffuse reflectance spectrum of the sample is given in Figure 4.6. Clearly the absorption of the sample is much less at 940 nm as compared to 980 nm (about 43% lesser).

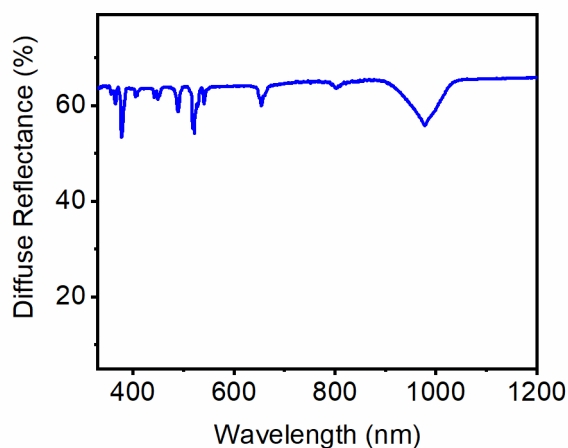


Figure 4.8. Diffuse reflectance spectrum of the β -NaYF₄: 18% Yb³⁺, 2% Er³⁺ (18/2%).

Reproduced from Joseph et al. [139]

If laser-induced heating is indeed the culprit, the temperature curve observed at an EPD of 250 W cm⁻² of 940 nm excitation, should lie below the temperature curve for 980 nm excitation at an EPD of 150 W cm⁻². True to this, when the calculated temperature for 250 W cm⁻² of 940 nm excitation is plotted along with the calculated temperature for 150 W cm⁻² of 980 nm excitation from Fig 4.5, the same behaviour is observed (Figure 4.9). Note that the y-axis scale in Figure 4.9. is shown only up to 350 K, as opposed to 400 K in Figure 4.5, which gives a false impression that the time taken to reach steady-state is longer, but is in fact, the same. Though the slight difference in the energy of excitation photons are neglected, the similar behaviour of the observed temperature curves shows that the rise in temperature is due to the MPR of absorbed photons, which were lesser in the case of 940 nm excitation.

To correct the EPD dependence of UC, the correction factors calculated at selected EPDs (as shown in Figure 4.7.) are linearly interpolated and applied to the measured data in Figure 4.1. The corrected data (orange circles) are plotted alongside the measured data. At an EPD of 240 W cm⁻², which was the highest EPD measured in this data-set, the corrected UC intensity was 24% higher than that of the observed UC intensity. The corrected data has a slope of unity in the limit of high EPDs, well in agreement with theoretical models developed for EPD dependence of UC. These results illustrate that increased caution and care is to be taken when

measuring the EPD dependence of the UC intensity or the EPD dependence of the PLQY of samples which cannot efficiently dissipate heat, namely samples like powders or single crystals.

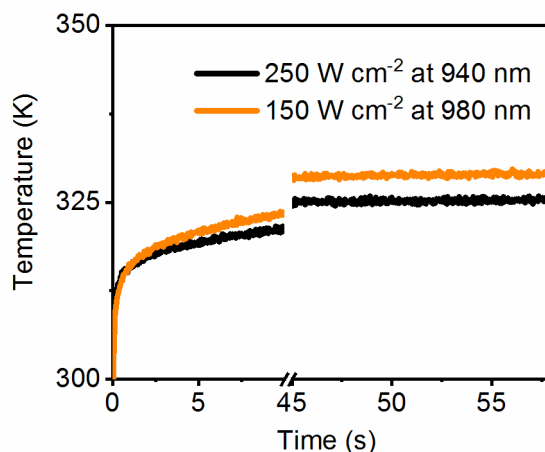


Figure 4.9. Calculated temperature as a function of time for 940nm and 980 nm excitation for 250 W cm⁻² and 150 W cm⁻² respectively. Adapted from Joseph et al. [139]

4.5. Excitation-laser-induced heating in liquid samples

To examine if such laser-induced heating effects are observed in samples in the liquid state, the EPD dependence of the UC of nanocrystals of the same material - β -NaYF₄: 18% Yb³⁺, 2% Er³⁺, dispersed in toluene are measured. The ratios of the intensities under the two thermally coupled peaks are provided in Figure 4.10. The intensity-ratios remain constant as time progresses unlike the previous scenario. The intensity-ratios have an average value of 0.18, which can then be used as Δ_0 to estimate the temperature of the sample using Equation 4.2. The estimated temperatures are plotted in Figure 4.11, as a function of the time following excitation with 980 nm.

The temperature of the nanocrystals remains constant for EPDs up to 250 W cm⁻². Therefore, effects of laser-induced heating are not observed in this regime, due to lesser absorption of the nanoparticles and increased heat transport to the solvent, in this case toluene. However, it is not uncommon for nanocrystals to be excited at EPDs greater than 1000 W cm⁻² [170]. In such cases, special care must be given so that laser-induced heating is accounted for, if at all present.

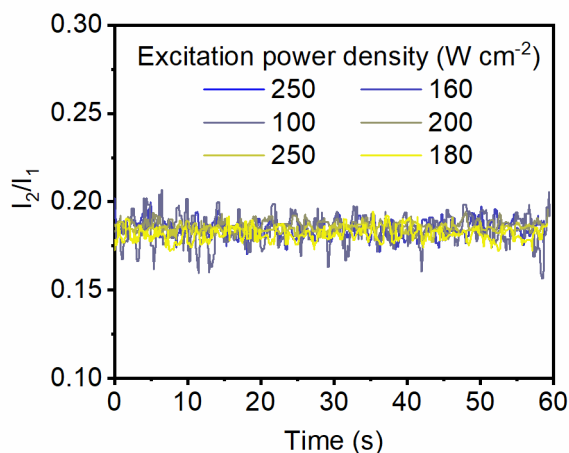


Figure 4.10. Ratio of the intensities of the two green emitting states ${}^2H_{11/2}$ and ${}^4S_{3/2}$, I_2/I_1 as a function of time for different excitation power densities for $\beta\text{-NaYF}_4\text{:Yb}^{3+}/\text{Er}^{3+}$ (18/2%) nanocrystals in toluene solution. Adapted from Joseph et al. [139].

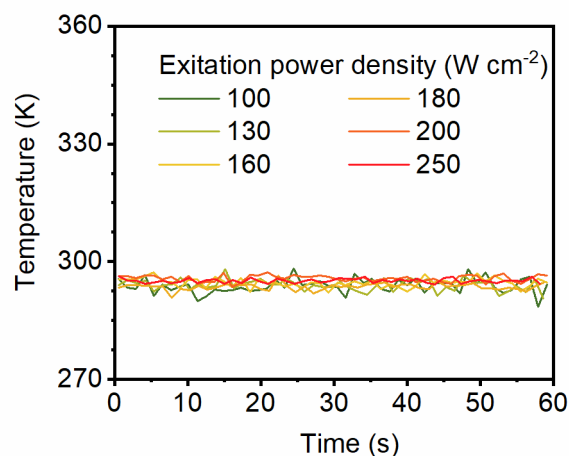


Figure 4.11. Temperatures calculated using ratiometric luminescence thermometry using the ${}^2H_{11/2}$ and ${}^4S_{3/2}$ states of Er^{3+} in for $\beta\text{-NaYF}_4$: 18% Yb^{3+} , 2% Er^{3+} nanocrystals dispersed in toluene. Adapted from Joseph et al. [139].

4.6. Outlook

The effect of laser-induced heating needs to be considered for applications of UC involving a solid host and high EPDs. Certain UC displays make use of very high EPDs of the order of MW cm^{-2} [138]. Generally, such 3D displays make use of a polymer matrix in which the UC materials are dispersed. The absorption of a UC material is much lower when embedded in a polymer matrix, and correspondingly the UC emission and PLQY would also be lower. Laser-induced heating would not be significant in such a scenario as the decreased absorption compensates for the effect caused by the increased EPD. Furthermore, if the display is

dynamic, scanning of the excitation laser to trace a POV picture decreases the exposure time drastically (typically in the order of microseconds), causing negligible heating.

For a single crystal used in a volumetric 3D display, the effect of laser-induced heating is negligible, as raster scanning results in very low exposure times of the order of microseconds. In addition, the EPDs used need not be very high ($< 200 \text{ W cm}^{-2}$) as demonstrated in Chapter 6. On the other hand, in a static UC display, where the excitation beam is not scanned, the effect of laser-induced heating is non-trivial and leads to a lowering of the UC intensity. In addition, if the UC material is doped in a thermally unstable polymer material, the heating may itself cause breakdown of the display device in the long run. Therefore, static UC displays need to be designed keeping in mind the effect of laser-induced heating also.

4.7. Summary

Laser-induced heating is found to cause unwanted underestimation of the UC intensity in EPD dependence measurements. Using the inherent thermally coupled energy states $^2\text{H}_{11/2}$ and $^4\text{S}_{3/2}$ of Er^{3+} present in microcrystals of $\beta\text{-NaYF}_4$: 18% Yb^{3+} , 2% Er^{3+} , the rise in temperature is estimated. For an EPD of 240 W cm^{-2} of 980 nm excitation, a rise in temperature of 60 K is observed under steady-state conditions. A method to correct for the reduction in UC intensity in the EPD dependence curve using interpolated values of the fractions of the real and observed UC intensities is proposed. Applying the correction on the EPD dependence curve, the corrected UC intensity is found to be 24% more than the measured value of UC intensity at an EPD of 240 W cm^{-2} . This EPD dependence is then found to obey the theoretical models describing UC behaviour and show a slope of unity in the range of high EPDs. At the same time, in liquid samples, such a heating effect is not observed for similar EPDs. This work highlights the need to be wary of the effects of laser-induced heating to correct the UC intensity and PLQY accordingly for accurate measurements. It also highlights the importance of considering the effect of laser-induced heating in the design of UC displays.

5. Critical Power Density as a Figure-of-Merit for Upconversion

This chapter is based on the second first-author- publication “Critical Power Density: A Metric to Compare the Excitation Power Density Dependence of Photon Upconversion in Different Inorganic Host Materials”, Journal of Physical Chemistry A, Vol. 123, 2019 [144]. The idea of developing figures-of-merits for UC was conceived by the author, Bryce S Richards, and Ian A Howard. The halide microcrystals doped with 18% Yb³⁺ and 2% Er³⁺ were prepared by Damien Hudry and Daniel Biner at the University of Bern under the guidance of Karl Krämer. Microcrystals of La₂O₃ doped with the same concentration of Yb³⁺ and Er³⁺ were prepared by Guojun Gao at the KIT. Dmitry Busko assisted in building up of the optical set-ups for measurement and wrote the LabVIEW program used for data acquisition. The intensity-dependent spectra and time-dependent spectra were acquired and analyzed by the author. Ian A Howard helped in separating the two-photon processes by using the MCR-ALS algorithm. Andrey Turshatov, Ian A. Howard, Karl Krämer and Bryce S. Richards were involved in interpreting the results and finalizing the draft.

The Critical power density (CPD) model is an analytical model which describes the UC intensity - EPD dependence of ETU with the help of a single parameter, namely the CPD and a scaling constant. The CPD is defined exclusively for two-photon UC and can be extracted from the UC intensity vs EPD curve for any particular material. In this chapter, the description of the CPD model and analysis of the data from four material systems in the light of the CPD model are presented. Section 5.1 explains the formulation and derivation of the CPD model and other analytical models developed in the last five years, which are comparable with the CPD model for describing the UC-EPD dependence. Then in Section 5.2, the synthesis procedures for the four UC materials used for validation of the CPD model are presented. Thereafter in Section 5.3, the two-photon UC processes are isolated using MCR-ALS algorithm to obtain their UC dependence and in Sections 5.4 and 5.5, the data is fitted with the CPD model as well as the BPD model. A comparison of both the models is made based on residual analysis. The extracted CPD values are then used to compare the materials. Sections 5.6 and 5.7 explain how two different UC emission peaks share the same value of CPD based on their common population mechanism and how larger intermediate-state lifetimes lead to lower CPDs. Section 5.8 explains how CPD can be used to determine the saturation PLQY (PLQY_{sat}). Then the

value of $PLQY_{sat}$ evaluated with the help of the CPD model is compared with the experimentally determined $PLQY_{sat}$ values. Section 5.9 summarizes the results of the chapter.

5.1. The Critical Power Density Model

Being a non-linear process, UC has different efficiencies at different EPDs. Different research groups report efficiencies in different ways, for example UC efficiency (output power/input power) and UC power efficiency (output power/absorbed power), etc. [171,172]. One commonly used way to describe the efficiency of UC is by using the saturation photoluminescent quantum yield (PLQY) [173]. The internal PLQY is defined as the ratio of the number of emitted photons to the number of absorbed photons. This PLQY is also called internal PLQY as it gives the true response of the material, once it absorbs energy. Saturation PLQY ($PLQY_{sat}$) is the PLQY in the limit of high EPDs, where the PLQY does not increase anymore but remains a constant with increasing EPD. External PLQY is on the other hand defined as the ratio of the number of photons emitted to the number of photons incident on the material. External PLQY is more relevant to devices, for which the efficiency needs to be defined in terms of the input power. Note that PLQY is different from energy efficiency, as the absorbed and emitted photons have different energies. For a material exhibiting both UC emissions resulting from three-photon processes and two-photon processes, the number of emitted photons from three-photon processes is less than the number of emitted photons from two-photon processes as in the case of Er^{3+} , the energy of a photon resulting from a three-photon UC process is normally higher than that of a photon resulting from a two-photon UC process, though there could be exceptions as in the case of the red emission from Er^{3+} doped in β - $NaYF_4$ [124].

The measurement of the $PLQY_{sat}$ is not trivial, as saturation is observed at very high EPDs which are associated with laser-induced heating as earlier explained in Chapter 4, besides other detrimental effects are also observed. Some nanocrystals exhibiting UC do not reach saturation at EPDs higher than 1000 W cm^{-2} [174]. For display applications of UC based on nanocrystals embedded in polymer films, EPDs of the order MW cm^{-2} are used [138]. Making use of the $PLQY_{sat}$ alone, to compare the efficiencies of different UC materials does not make sense as saturation is achieved at different EPDs. Due to this limitation, another figure-of-merit is required to describe a UC system fully in combination with the $PLQY_{sat}$, and to compare the EPD dependence of the UC intensities of different materials and to reveal the photophysics of the UC process. This figure-of-merit is termed as critical power density (CPD) and is defined exclusively for two-photon UC in the course of this research work. The ETU system can be defined using a set of analytical equations, in terms of the CPD. This model is termed as the CPD model.

According to the CPD model, an ETU process can be understood in terms of a three-level system as shown in Figure 5.1. The concentrations of the rare-earth ions capable of UC in the ground state, intermediate state and excited state are denoted by A_0 , A_1 , and A_2 , respectively. Each ETU process involves a sensitizer ion and an emitter ion. The excited state of the sensitizer ion is assumed to be in resonance with that of the intermediate state of the emitter ion such that the concentrations of sensitizer and emitter ions in the intermediate state can be described with one single parameter $-A_1$ and G is the rate at which emitter ions get promoted to their intermediate state, which includes the ground state absorption of the sensitizer ion to its excited state and subsequent energy transfer to the emitter ion from its ground state. The rate constant with which energy is transferred from a sensitizer ion in the excited state to an emitter ion in the intermediate state is denoted by k_{ET12} . After this ETU step, one ion in the intermediate state gets promoted to the second excited state and another ion moves down to its ground state. The rate constant with which ions in the second excited state and the intermediate state decay to the ground state are then denoted by k_2 and k_1 .

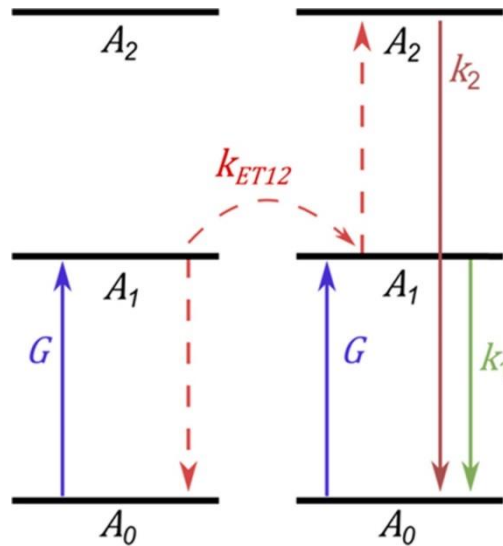


Figure 5.1. Three-level system describing two-photon UC. Reproduced with permission from Joseph et al. [144].

Copyright 2019 American Chemical Society

The concentrations of ions in the intermediate state and the second exciting state can be expressed in the form of rate equations as described below:

$$\frac{dA_1}{dt} = G - 2A_1^2 k_{ET12} - A_1 k_1 \quad , \text{ and} \quad (5.1)$$

$$\frac{dA_2}{dt} = -A_2 k_2 + A_1^2 k_{ET12} \quad . \quad (5.2)$$

Then $A_1^2 k_{ET12}$ gives the rate at which ions in the intermediate state undergo ETU, $A_1 k_1$ is the rate at which ions in intermediate state decays to the ground state and $A_2 k_2$ is the rate at

which the ions in their second excited state decays to the ground state. These decay rates include both the non-radiative and radiative decay rates.

If we consider that the system is in steady-state, the concentrations of ions in each state remain constant. Then Equations 5.1 and 5.2 can be rewritten as:

$$G = 2A_1^2 k_{ET12} + A_1 k_1 \quad , \text{ and} \quad (5.3)$$

$$A_2 = A_1^2 \frac{k_{ET12}}{k_2} \quad . \quad (5.4)$$

Equation 5.3 can be reformulated as:

$$2A_1^2 k_{ET12} + A_1 k_1 - G = 0 \quad . \quad (5.5)$$

Equation 5.5 is in the form of a quadratic equation, and the value of A_1 can be found out from the positive root of this equation:

$$A_1 = \frac{-k_1 \pm \sqrt{(k_1^2 + 8Gk_{ET12})}}{4k_{ET12}} \quad . \quad (5.6)$$

$$\Rightarrow A_1 = \frac{k_1}{4k_{ET12}} \left(\sqrt{1 + \frac{8Gk_{ET12}}{k_1^2}} - 1 \right) \quad . \quad (5.7)$$

Using Equations 5.4 and 5.7, we get an expression for the concentration of ions in the second excited state:

$$A_2 = \frac{k_1^2}{16k_2 k_{ET12}} \left(-1 + \sqrt{1 + \frac{G}{\frac{k_1^2}{8k_{ET12}}}} \right)^2 \quad . \quad (5.8)$$

If k_{2rad} is the radiative rate constant of the UC emission from the second excited state and $k_{2non-rad}$ is the non-radiative decay constant, such that $k_2 = k_{2rad} + k_{2non-rad}$, the intensity of UC emission can be expressed by:

$$UC = A_2 k_{2rad} = \frac{k_{2rad} k_1^2}{16 k_2 k_{ET12}} \left(-1 + \sqrt{1 + \frac{G}{\frac{k_1^2}{8 k_{ET12}}}} \right)^2 \quad (5.9)$$

Then $A_2 k_{2rad}$ is the rate of UC emission from the second excited state. The generation rate G depends upon the absorption coefficient α , the energy of the excitation photon $h\nu$ and the EPD, I using the relation:

$$G = \frac{I\alpha}{h\nu} \quad (5.10)$$

Using this expression of G in Equation 5.9, we get the following expression for UC:

$$UC = \frac{k_{2rad} k_1^2}{16 k_2 k_{ET12}} \left(-1 + \sqrt{1 + \frac{I}{CPD}} \right)^2 \quad (5.11)$$

$$\Rightarrow UC = C \left(-1 + \sqrt{1 + \frac{I}{CPD}} \right)^2 \quad (5.12)$$

where C is a constant that can be empirically fitted and CPD is the critical power density which has the unit $W\text{ cm}^{-2}$ and can be expressed as:

$$CPD = \frac{k_1^2 h\nu}{8 k_{ET12} \alpha} \quad (5.13)$$

The CPD is proportional to the square of the decay constant of the intermediate state, which means that the CPD will be lower for a material whose intermediate state has longer lifetimes. Also, the CPD will be lower for material with an increased energy transfer rate and increased absorption. The UC becomes more efficient at a lower EPD, if the CPD is lower. In a way, CPD gives the EPD at which the UC of a material turns on. When comparing materials exhibiting two-photon UC, therefore, the one with lower CPD emerges as the better upconverter. By fitting the UC vs EPD curve of material with Equation 5.12, we obtain the value of CPD for the material. Experimental results of CPD obtained for different UC materials are provided and discussed in the upcoming sections.

Two other models developed in the recent past also aim to describe UC-EPD dependence. A short description of these two models is provided in the following sections for comparison with

the CPD model. Though primarily developed for UC nanocrystals, these two models can also be used for microcrystals exhibiting UC.

5.1.1. Balancing Power Density Model

The Balancing power density (BPD) model developed by Liu *et al.* in 2013 attempts to describe the performance of UC materials using a parameter called the BPD in a way similar to the CPD model. In the BPD model, the EPD at which the rate of the decay of the intermediate state to the ground state becomes equal to the rate of ETU from the intermediate state to the second excited state is called the BPD [175]. In other words, it is the EPD at which the loss of concentration of ions in the intermediate state to both directions (the states above and below) become equal. As discussed in Section 2.3, the slope of the log-log plot of two-photon UC intensity vs EPD changes from 2 to 1 as the EPD increases. The BPD is defined as the EPD at which the slope of the plot becomes equal to 1.5. In Figure 5.2, the UC intensity vs EPD dependence for core (NaYF₄:Yb³⁺,Tm³⁺) and core-shell NaYF₄:Yb³⁺,Tm³⁺@NaYF₄ nanocrystals are given. The region where the slope is 1.5 is identified and the EPD at the centre of this region is defined as the BPD, in this case 1.3 W cm⁻² and 3.8 W cm⁻², respectively for core-shell and core nanocrystals. The BPD model has the following expression for the UC PLQY:

$$\eta = \frac{\eta_s \frac{I}{I_b}}{1 + \frac{I}{I_b}} \quad , \quad (5.14)$$

where η is the PLQY, η_s is the PLQY_{sat}, I is the EPD and I_b is the BPD. Then the expression for UC intensity becomes:

$$UC \propto \eta I = \frac{AI^2}{I_b + I} \quad . \quad (5.15)$$

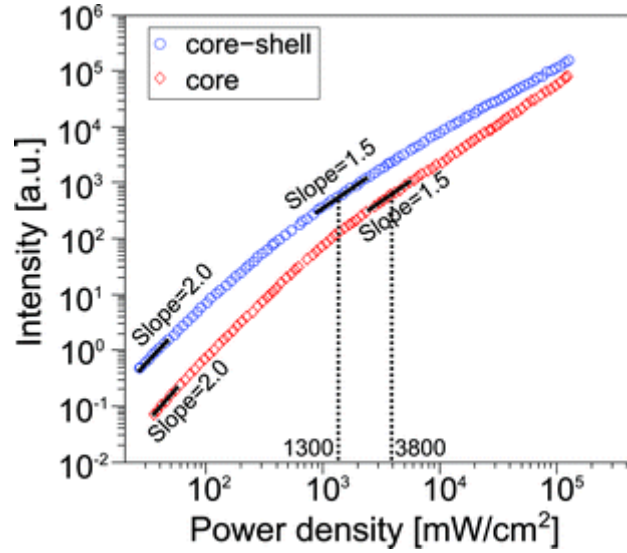


Figure 5.2. Determination of BPD from UC-EPD dependence. BPD is the EPD when slope of the double logarithmic plot of the EPD dependence of UC is equal to 1.5. Reproduced with permission from Liu *et al.* [175].

A comparison of the BPD model and the CPD model on experimental data of UC intensity-EPD dependence is provided in Section 5.4.

5.1.2. Saturation Intensity Model

The saturation intensity (SI) model developed by Christiansen *et al.* is analogous to the CPD model [176]. This model developed independently and at around the same time as the CPD model introduced by the author in the year 2019, was defined exclusively for the 1500 nm to 980 nm UC in Er^{3+} . They consider the similarity between ETU and organic TTA-UC and define the SI in a way analogous to the steady-state excitation threshold in TTA-UC. In TTA-UC the steady-state excitation threshold is defined as the EPD at which the annihilation rate of the triplets becomes dominant as compared to their monomolecular decay [177]. The SI model describes the UC intensity using the expression:

$$UC = NdA\Gamma_{eff} \left(1 - \sqrt{1 + \frac{I}{I_{sat}} + \frac{I}{2I_{sat}}} \right). \quad (5.16)$$

Here the UC material is assumed to be doped in a thin film of thickness d , with a concentration of Er^{3+} ions N . Γ_{eff} is a constant which depends on the absorption cross-section and decay rates from the second excited state. Equation 5.16 is analogous to Equation 5.12, when the square term in Equation 5.12 is expanded. So, the SI is the same thing as the CPD, though both models have been derived independently of each other.

5.2. Identifying Two-photon and Three-photon UC processes

The UC intensity vs EPD curve is obtained by integrating a particular region of the observed emission spectra as the EPD is increased in a step by step manner. For example, Figure 5.3 gives the UC intensity EPD dependence of the visible red emission from the four material systems as they are excited with 980 nm radiation. The slopes of the log-log plots of these curves in the limit of low UC intensities give the order of the ETU process. Except for the case of the host La_2O_3 (Figure 5.3(a)), all the other three hosts show a slope greater than 2, indicating a three-photon ETU mechanism [85]. In the host La_2O_3 , the slope of the red (630-690 nm) UC emission indicates that its mechanism is exclusively two-photon ETU, making the analysis of the red UC emission possible by the CPD model. For the other cases, the red emission cannot be used for the CPD model. The green emission is normally assumed to result from two-photon processes. However, multiple peaks are present in the green region of the UC spectra. This necessitates the need to identify exactly which peaks are produced by the radiative transitions possible from the energy states of Er^{3+} and to correctly identify them.

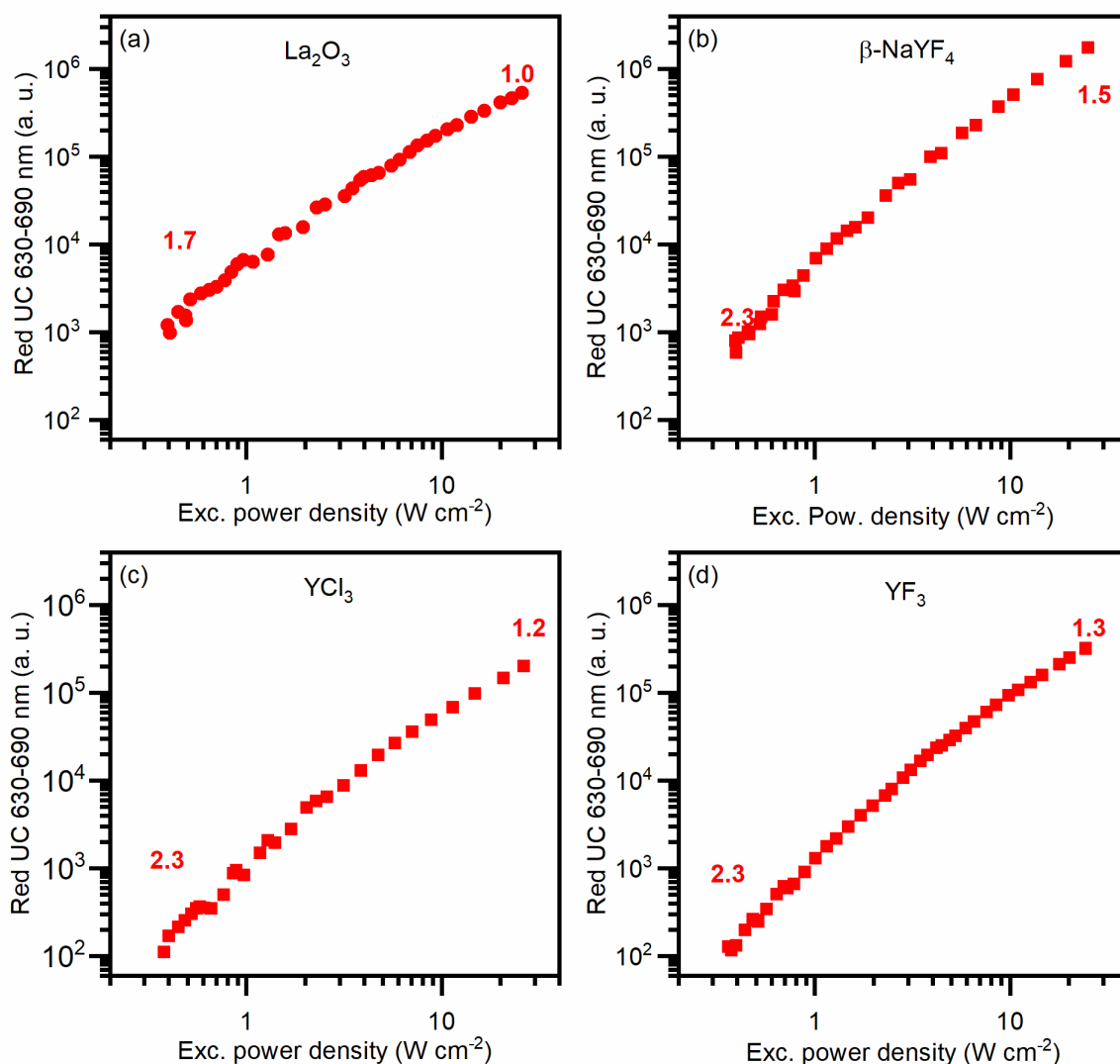


Figure 5.3. Log-log plot of the integrated UC spectra vs the excitation power density (of 980 nm radiation) of the visible red emission ($^4F_{9/2} \rightarrow ^4I_{15/2}$, 630-690 nm) of Er^{3+} (2%) sensitized with Yb^{3+} (18%) doped in four microcrystalline hosts: (a) La_2O_3 , (b) $\beta\text{-NaYF}_4$, (c) YCl_3 , and (d) YF_3 . The numbers indicate the slopes of the curves at their two extremities. Adapted with permission from Joseph et al. [144] Copyright 2019 American Chemical Society.

The MCR-ALS technique is used for analyzing the set of UC emission spectra obtained by increasing the EPD, and to identify the two-photon peaks and the three-photon peaks. The EPD is not high enough to cause four-photon processes in the materials used in this work, so any UC process in the observed spectra originates exclusively from either two-photon or three-photon processes. It is evident that, the contribution in UC spectra from three-photon processes increase as the EPD increases, whereas the contribution from two-photon processes decreases. To make a quantitative comparison of the UC spectra obtained at different EPDs, first the UC spectrum at each EPD needs to be normalized by dividing the UC spectra with the total number of emitted photons. The total number of emitted photons at each EPD is obtained by integrating the spectrum to obtain the total area under the spectrum. The UC spectrum at each EPD is normalized by dividing it with the total number of emitted photons,

and a matrix is made of these spectra that is then provided to the MCR-ALS graphical user interface implemented in MATLAB, along with a matrix of the increasing EPDs. The algorithm gives the two constituent spectra (two-photon UC processes and three-photon UC processes) and their relative contributions as a function of the EPD, as the output. Each of the four hosts is considered in a step by step manner as described in the following subsections.

5.2.1. β -NaYF₄: 18% Yb³⁺, 2% Er³⁺

Upon processing the 980 nm EPD dependent normalized UC spectra from β -NaYF₄: 18% Yb³⁺, 2% Er³⁺, the MCR-ALS algorithm gives the resultant spectra as shown in Figure 5.4. The resolved UC spectrum now has two components (Figure 5.4(a)), one shown in green colour (ascribed to two-photon UC processes) and another one shown in blue colour (ascribed to three-photon UC processes). The relative contribution of the blue spectra increases as the EPD increases. However, the relative contribution of the green spectra decreases as the EPD increases (Figure 5.4(b)).

A small UC peak originating from a three-photon process ($^2H_{9/2} \rightarrow ^4I_{13/2}$), is at the tail end of the green UC emission (510-570 nm), as can be seen in Figure 5.4(a). Care should be taken to exclude this peak from the UC intensity-EPD dependence to exclusively obtain the pure two-photon UC response of the system. Therefore, the regions 510–541 nm and 820–870 nm are selected for analysis with the CPD model in β -NaYF₄: 18% Yb³⁺, 2% Er³⁺. The energy level diagram of the Yb³⁺-Er³⁺ system is given in Figure 5.5, showing the transitions leading to the peaks marked in Figure 5.4(a). The regions of the UC spectra selected for analysis with the CPD model are marked with a light green box in Figure 5.5.

The UC processes in β -NaYF₄: 18% Yb³⁺, 2% Er³⁺ system can be described as follows: the Yb³⁺ ions gain energy from a 980 nm excitation photon by GSA. They transfer their energies to Er³⁺ ions by ETU (dotted arrows). Two-photon ETU populates the $^4F_{7/2}$ state of Er³⁺, from which the ions move down to the $^2H_{11/2}$ and $^4S_{3/2}$ states after MPR (curly lines in Figure 5.5). These two states are thermally coupled, which means that the ratio of radiative emissions from these two states depend upon the temperature of the system [153]. These two states also radiatively relax to the penultimate state $^4I_{13/2}$ in addition to the ground state $^4I_{15/2}$ leading to NIR emissions around 800 nm and 840 nm. Three-photon ETU populates the $^2G_{4K}$ group of energy states. After undergoing a series of MPR processes, the ions move to the $^2H_{9/2}$ state from which blue, green and red emissions are observed as the ions radiatively relax to the ground state $^4I_{15/2}$ and the two states $^4I_{13/2}$ and $^4I_{11/2}$ above the ground state. Surprisingly, a back-energy transfer (BET) step transfers a portion of the energy obtained by the Er³⁺ ion from three-photon ETU back to the Yb³⁺ ion. After this process, the Er³⁺ ion moves into the red-emitting state $^4F_{9/2}$. This means that red emission is a result of three-photon processes in β -

NaYF₄: 18% Yb³⁺, 2% Er³⁺ and green emission is predominantly a result of two-photon processes, even though the energy of a green photon is more than that of a red photon. These results are in accordance with the observations made by Berry et al, who reported the three-photon nature of the red emission in β -NaYF₄: 18% Yb³⁺, 2% Er³⁺ [124,178]. We normalized the original spectra by dividing it with the area in the region 510–542 nm which correspond exclusively to two-photon green emission to reconfirm the nature of the peaks and get the resultant spectra as shown in Figure 5.6.

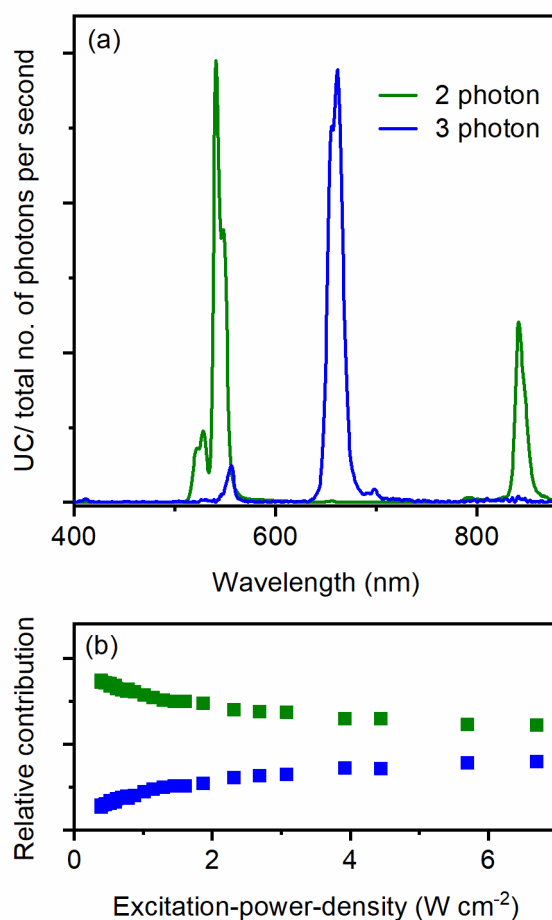


Figure 5.4. (a) Deconvoluted spectra of the total UC spectra of β -NaYF₄:18% Yb³⁺, 2% Er³⁺ obtained using the MCR-ALS algorithm. The blue and green colors are ascribed to three- and two-photon processes, respectively. (b) Relative contributions from the two-component spectra as the excitation power density is increased. Reproduced with permission from Joseph et al. [144] Copyright 2019 American Chemical Society.

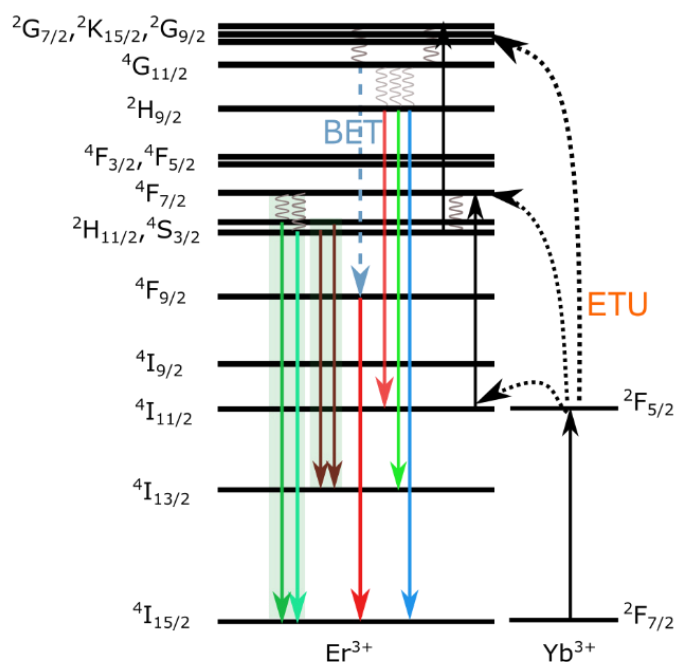


Figure 5.5. Energy level diagram of the β - NaYF_4 :18% Yb^{3+} , 2% Er^{3+} system showing the origin of the UC emissions. Upward solid arrows show photon-absorption. The blue, green and red emissions are marked with solid arrows pointing downwards with the respective colours. The NIR emissions are marked similarly with brown colour. Multiphonon relaxation is indicated by curly lines. ETU and BET stand for energy transfer UC and back-energy Transfer. The light green boxes mark exclusively two-photon UC processes.

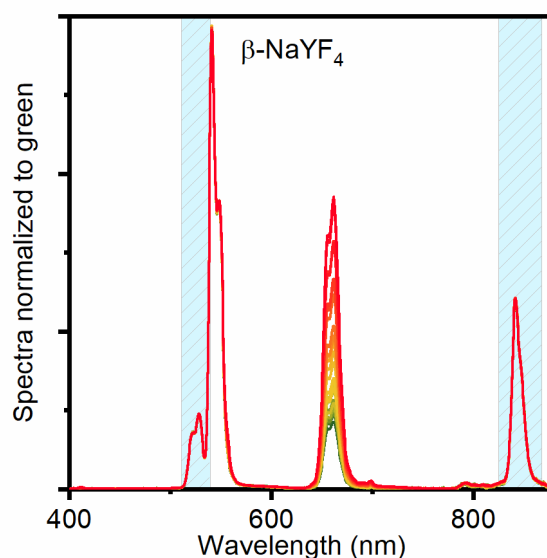


Figure 5.6. UC emission spectra normalized to the region 510–542 nm in β - NaYF_4 : 18% Yb^{3+} , 2% Er^{3+} . The spectra obtained at different excitation power densities are overlaid. The colour of the plotted spectra changes from green to red as the excitation power density of 980 nm radiation increases from 0.4 to 6.7 W cm^{-2} . The shaded areas are selected for integration for evaluating UC dependence from two-photon processes. Adapted with permission from Joseph et al. [144] Copyright 2019 American Chemical Society.

The spectra for increasing EPDs from 0.4 to 6.7 W cm^{-2} are colour coded from green to red. When the spectra normalized in this way are overlaid, the peaks corresponding to the two-

photon ETU processes remain unaltered as opposed to the three-photon peaks which grow in size, with the 660 nm peak being the most notable. In addition, the both the small three-photon peaks at 700 nm and 557 nm grow in intensity due to three-photon ETU. From these series of spectra, the regions 510-542 nm and 820-870 nm are identified as portions of the UC emission spectra exclusively from two-photon ETU. These regions are shaded on the graph with a light blue colour. For fitting with the CPD model, the integrated area under the original UC spectra in these regions are plotted as a function of the EPD.

5.2.2. YF_3 : 18% Yb^{3+} , 2% Er^{3+}

The UC emission from YF_3 : 18% Yb^{3+} , 2% Er^{3+} when excited with 980 nm is quite similar to that from $\beta\text{-NaYF}_4$: 18% Yb^{3+} , 2% Er^{3+} except for the fact that the intensity of the observed UC emission is lower. The resolved spectra from MCR-ALS analysis is shown in Figure 5.7.

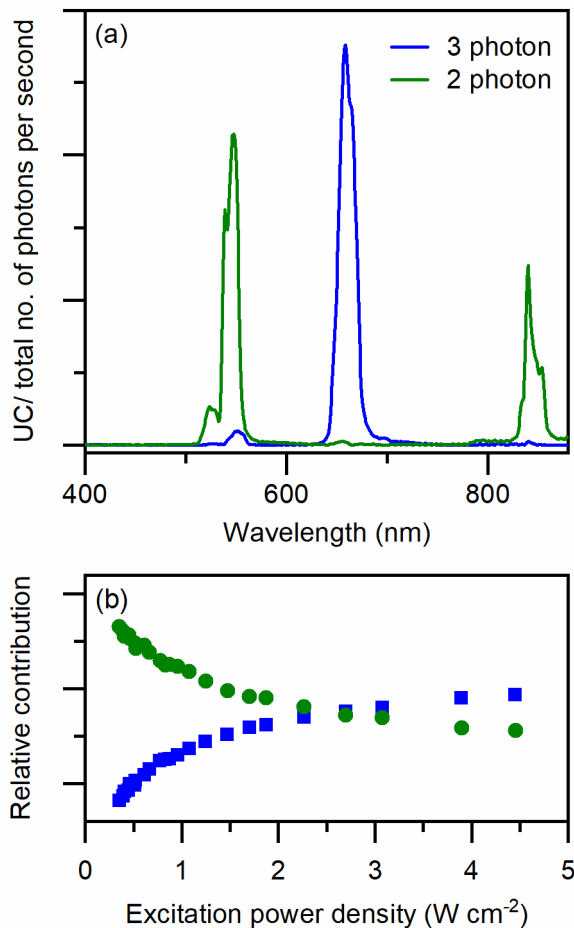


Figure 5.7. (a) Deconvoluted spectra and (b) relative contributions on MCR-ALS analysis of YF_3 : 18% Yb^{3+} , 2% Er^{3+} upon increasing the EPD of 980 nm radiation from 0.3 to 4.5 W cm^{-2} .

Here the EPD of 980 nm radiation is increased from 0.3 to 4.5 W cm^{-2} . The resolved two-photon and three-photon peaks are similar to those observed in $\beta\text{-NaYF}_4$: 18% Yb^{3+} , 2% Er^{3+} . The set of UC spectra normalized to the region under the two-photon portion of the green peak is given in Figure 5.8. The relative growth of the red peaks at 660 nm and 700 nm, and the small

shoulder at 557 nm is observed similar to the case of β -NaYF₄: 18% Yb³⁺, 2% Er³⁺. The regions completely free of three-photon peaks are selected as 510-541 nm and 820-870 nm as observed in Figure 5.7. The area under the original UC spectra for different EPDs in these regions are integrated to obtain the UC-EPD dependence for analysis with CPD model.

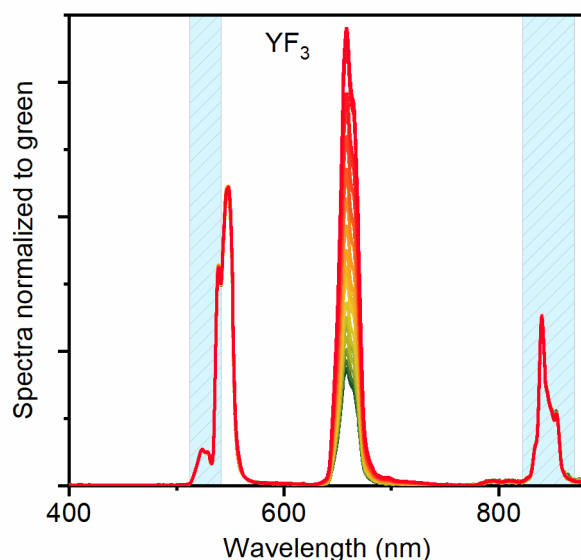


Figure 5.8. Overlaid UC spectra normalized to area under the green peak (510-541 nm) in YF₃: 18% Yb³⁺, 2% Er³⁺. The color changes from green to red as excitation power density increases from 0.3 W cm⁻² to 4.5 W cm⁻². The shaded areas are selected for integration for evaluating UC dependence from two-photon processes. Adapted with permission from Joseph et al. [144] Copyright 2019 American Chemical Society.

5.2.3. La₂O₃: 18% Yb³⁺, 2% Er³⁺

The UC emission from La₂O₃: 18% Yb³⁺, 2% Er³⁺ under 980 nm excitation at low EPDs (< 10 W cm⁻²) is yellow in colour as opposed to the case of the fluorides where a green colour is observed. The reason is that, the red UC emission is much intense in this host, as compared to the green emission. The presence of both the green and red emissions result in a yellow colour. This red emission cannot be of three-photon origin considering the contrast between its intense nature and the low EPD applied in this case. Also La₂O₃ is a host with higher phonon modes compared to the fluorides, with phonon energies measured between 410 to 935 cm⁻¹ in Raman spectroscopy and FTIR measurements [97,179,180]. Higher phonon energies lead to increased MPR rates, leading to a lesser probability of the population of the higher energy states responsible for three-photon ETU as compared to two-photon UC. Considering these two facts, the UC emission spectra is normalized by dividing it with the area under the green peak (515-550 nm) to observe the nature of the different peaks in the spectra for EPDs of 980 nm excitation ranging from 0.5 W cm⁻² to 4.8 W cm⁻². The resulting normalized spectra is provided in Figure 5.9.

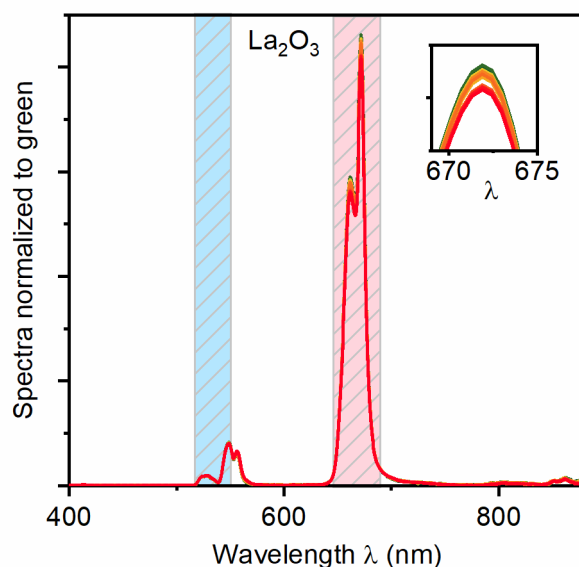


Figure 5.9. Overlay of UC emission spectra normalized by dividing with the area in the green region (510-550 nm) in $\text{La}_2\text{O}_3: 18\% \text{Yb}^{3+}, 2\% \text{Er}^{3+}$ measured at EPDs. The color changes from green to red as EPD increases from 0.5 W cm^{-2} to 4.8 W cm^{-2} . The inset graph shows zoomed-in view of the red peak at 671 nm. The shaded areas in pink and light-blue are selected for analysis with CPD model. Adapted with permission from Joseph et al. [144] Copyright 2019 American Chemical Society.

In contrast to the two previous cases, the red peak is much higher in magnitude compared to the green peak, moreover, a relative growth compared to the green peak is not observed, which would have indicated a three-photon origin. On closer observation, the red peak decreases in magnitude as compared to the green peak (inset figure in Figure 5.9). Therefore, the red peak has a two-photon origin in this case, as the emitted photons have higher energies than the 980 nm excitation-photons but have a different population channel than that of the green emission peaks. The NIR emission in this case, is too small in magnitude to be analyzed with the CPD model considering the poor signal-to-noise ratio. In a nutshell, two different regions can now be identified in the UC spectra of $\text{La}_2\text{O}_3: 18\% \text{Yb}^{3+}, 2\% \text{Er}^{3+}$ which are populated through two different ETU channels. These regions are marked with a light blue (515-550 nm) and light pink shade (640-680 nm) on Fig 5.9. The possible mechanisms at work in this material are illustrated in Figure 5.10. The green-emitting states $^2\text{H}_{11/2}$ and $^4\text{S}_{3/2}$ get populated through the same ETU mechanism observed in the fluorides as described in the previous two sub-sections. The red-emitting state $^4\text{F}_{9/2}$ on the other hand, gets populated through an ETU step from the penultimate state $^4\text{I}_{13/2}$. The Er^{3+} ions move into this state as the ions in the $^4\text{I}_{11/2}$ state undergo radiative and non-radiative decays. It is also to be noted that there exists an alternate pathway for the populating the red emitting state $^4\text{F}_{9/2}$. Considering the higher phonon energies of the oxide lattice, the energy gap between the green-emitting states and the red-emitting state can be bridged using MPR. At lower EPDs, this pathway would not be dominant, but at higher EPDs, a significant contribution from this pathway is also

to be expected. In the EPD regimes that are considered here, this pathway of populating the $^4F_{9/2}$ state is insignificant. The two-photon UC emissions, which are considered for CPD analysis are marked in coloured boxes in this figure.

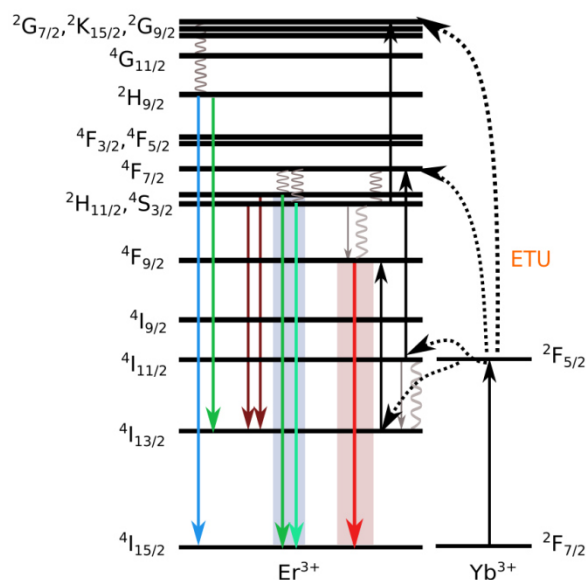


Figure 5.10. Energy transfer UC (ETU) mechanisms leading to UC in La_2O_3 : 18% Yb^{3+} , 2% Er^{3+} upon 980 nm excitation. Upward-arrows indicate ETU and curly arrows indicate multi-phonon relaxations. The colored downward-arrows indicate radiative transitions. The emissions in the colored boxes are purely of two-photon origin and hence used for analysis with the CPD model. Reproduced with permission from Joseph et al. [144] Copyright 2019 American Chemical Society.

5.2.4. YCl_3 : 18% Yb^{3+} , 2% Er^{3+}

Chloride lattices generally have much lower maximum phonon energies ($\sim 260 \text{ cm}^{-1}$) compared to fluorides and oxides [39,96,181,182]. Therefore, MPR is less prominent, and each populated excited state prefers the radiative route for relaxation. The UC spectra observed when excited with 980 nm radiation is again normalized by dividing it with the area under the green region (510 to 550 nm) of the UC emission, which originates exclusively from two-photon processes. The EPD is varied from 0.4 to 3.2 W cm^{-2} and the corresponding normalized spectra are provided in Figure 5.11. The spectra are colour coded in a way that the colour of the lines on the graph changes from green to red as the EPD increases. As expected much more pronounced peaks are seen as compared to the fluorides and oxides. The two-photon peaks in the regions 510–550 nm and 840–880 nm behave in a similar way as in the fluorides. The three-photon peaks are more intense and clearly show relative growth in comparison with the two-photon peaks. The three-photon peaks from $^4G_{11/2}$ and $^4F_{5/2}$ states of Er^{3+} are also visible at 456 and 510 nm, respectively. The emission at 490 nm from the $^4F_{7/2}$ state is also visible in this case unlike in fluorides where it is normally not observed due to efficient non-radiative decay to the lower-lying green-emitting states $^2H_{11/2}$ and $^4S_{3/2}$. The regions

510–550 nm and 840–880 nm are shaded in a light-blue colour, to indicate that this portion of the spectra is suitable for CPD analysis.

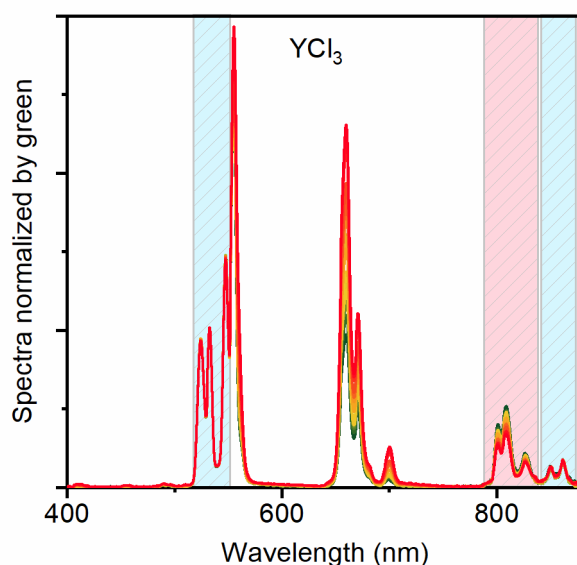


Figure 5.11. Normalized UC spectra obtained by dividing the spectra with the integrated area in the region (510–550 nm) in YCl_3 : 18% Yb^{3+} , 2% Er^{3+} . The color is coded from green to red as the excitation power density increases (0.4 W cm^{-2} to 3.2 W cm^{-2}). The areas shaded in light blue and pink are analyzed with the CPD model. Adapted with permission from Joseph *et al.* [144] Copyright 2019 American Chemical Society.

Surprisingly, an additional peak is observed at 810 nm (shaded in pink) corresponding to the $^4\text{I}_{9/2}$ state, which decreases in intensity as the EPD increases. As the energy of the emitted photon in this case is slightly more than that of the excitation photon, the process can only be of two-photon origin. To understand the mechanisms of the UC peaks, first the lifetimes of the $^4\text{S}_{3/2}$ state are measured. The lifetime data is given in Figure 5.12. The lifetimes of the $^4\text{S}_{3/2}$ state are detected from the NIR emissions at around 840 nm ($^4\text{S}_{3/2} \rightarrow ^4\text{I}_{13/2}$) to avoid interference of the green UC emission (510–560 nm, $^2\text{H}_{11/2}$, $^4\text{S}_{3/2} \rightarrow ^4\text{I}_{15/2}$) with the excitation at 525 nm. The EPD of the 525 nm excitation is set low (2.5 W cm^{-2}), and the laser is driven in quasi-continuous wave (quasi-CW) mode with a pulse period of 40 ms and a pulse width of 20 ms. As observed in Figure 5.12, $^4\text{S}_{3/2}$ state of Er^{3+} in YCl_3 has longer lifetimes than $\beta\text{-NaYF}_4$ (the host with highest PLQY_{sat} [53,86]). These longer lifetimes make the $^4\text{S}_{3/2}$ state act as an intermediate state for an additional ETU step which populates the $^2\text{G}_{7/2}$, $^2\text{K}_{15/2}$, $^2\text{G}_{9/2}$ states as indicated in Figure 5.15. MPR easily bridges the energy gap between these three energy states and the next lower lying state $^4\text{G}_{11/2}$. The $^4\text{G}_{11/2}$ state radiatively relaxes through two major channels. The first channel is back-energy transfer (BET) to a Yb^{3+} ion, leading to red emission about 659 nm from $^4\text{F}_{9/2}$ state of Er^{3+} , similar to the mechanism proposed by Berry *et al.* for $\beta\text{-NaYF}_4$ [178]. The second channel is relaxation to the $^4\text{I}_{13/2}$ state of Er^{3+} with emission around 507 nm. The relaxation probability to $^4\text{I}_{15/2}$, the ground state of Er^{3+} is much less as explained

by Dieke in 1965 [183]. At lower EPDs, population of the immediately lower lying $^2H_{9/2}$ state from the $^4G_{11/2}$ state is difficult to attain by non-radiative decay, due to larger energy gap. The three-photon peaks from the $^2H_{9/2}$ state namely, blue (405 nm), green (560 nm) and red (700 nm) emissions are but observed at higher EPDs indicating that the $^2H_{9/2}$ state is populated. These radiative emissions correspond to the radiative relaxations to the ground state $^4I_{15/2}$, and the two states above it ($^4I_{13/2}$ and $^4I_{11/2}$) as indicated in Figure 5.13. The peak at 800 nm could originate from an ETU between two ions in the $^4I_{13/2}$ state or from a cross-relaxation between an Yb^{3+} ion in the ground state and the Er^{3+} ion in the $^2H_{9/2}$ state. More details about the peak at 800 nm from the $^4I_{9/2}$ state is discussed in Section 5.5 as the relationship between CPD and mechanism of UC is studied. This peak is also considered for CPD analysis owing to its two-photon nature.

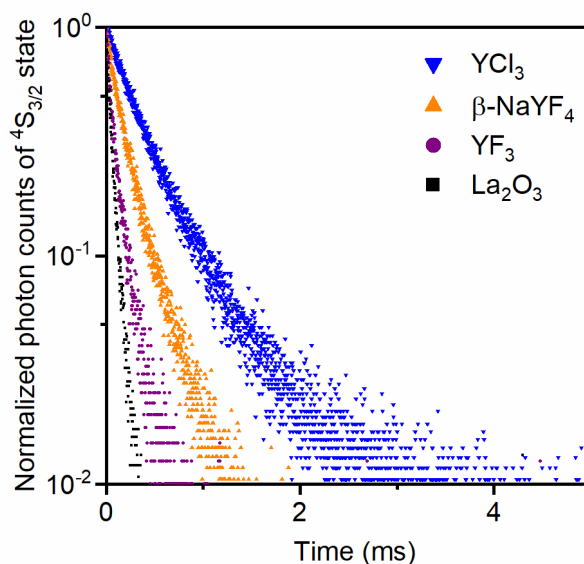


Figure 5.12. $^4S_{3/2}$ state lifetimes in the four hosts when excited at 525 nm with a laser in quasi-CW mode with a pulse period of 40 ms and a pulse width of 20 ms, at an EPD of 5 W cm^{-2} , detected at 840 nm. The chloride host emerges as a clear winner in comparison to the other three hosts with respect to lifetimes, but due to depopulation to the higher excited states, the total PLQY from the chloride host is lesser compared to the fluorides. Reproduced with permission from Joseph et al. [144] Copyright 2019 American Chemical Society.

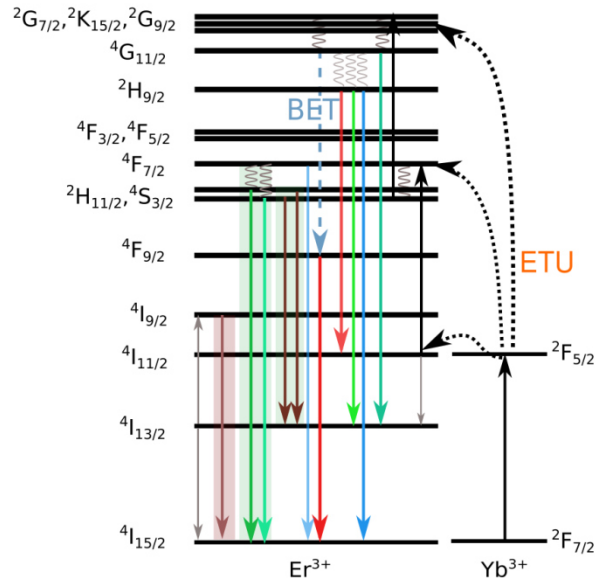


Figure 5.13. Mechanisms of UC in YCl_3 : 18% Yb^{3+} , 2% Er^{3+} excited with 980 nm radiation. Black arrows pointing upwards indicate energy-transfer UC (ETU). The curly arrows show non-radiative relaxations. The arrows pointing downward indicate radiative transitions. BET stands for back-energy transfer (a type of cross relaxation between the $^4\text{G}_{11/2}$ state of Er^{3+} and the $^2\text{F}_{5/2}$ state of Yb^{3+}). The emissions in the colored boxes are purely of two-photon origin and hence used for analysis with our CPD model. Reproduced with permission from Joseph et al. [144] Copyright 2019 American Chemical Society.

5.3. Fitting the UC-EPD dependence with the CPD model

The regions of the spectra identified as two-photon processes are analysed with the CPD model. The integrated area under the spectra corresponding to the two-photon peaks are plotted as a function of the increasing EPD in Figure 5.14. The data is fitted with the equation for the CPD model (Equation 5.12). The fits are indicated with solid lines in the figure. The four panels on the top show the data of UC-EPD dependence of Er^{3+} - Yb^{3+} and the CPD fits in the hosts β - NaYF_4 , YF_3 , La_2O_3 , and YCl_3 , respectively. Green squares show the integrated area of the UC from the $^2\text{H}_{11/2}$ and $^4\text{S}_{3/2}$ states to the ground state at each EPD. Similarly, red circles, and brown diamonds indicate the integrated UC emission from $^4\text{F}_{9/2}$ and $^4\text{I}_{9/2}$ to the ground state. Grey triangles show the integrated UC from $^4\text{S}_{3/2}$ to the $^4\text{I}_{13/2}$ state. The bottom panels give the corresponding percentage residuals from the fit. The residuals for all the four materials lie equally distributed on both sides of the zero axes, indicating that the model describes the UC-EPD dependence quite well.

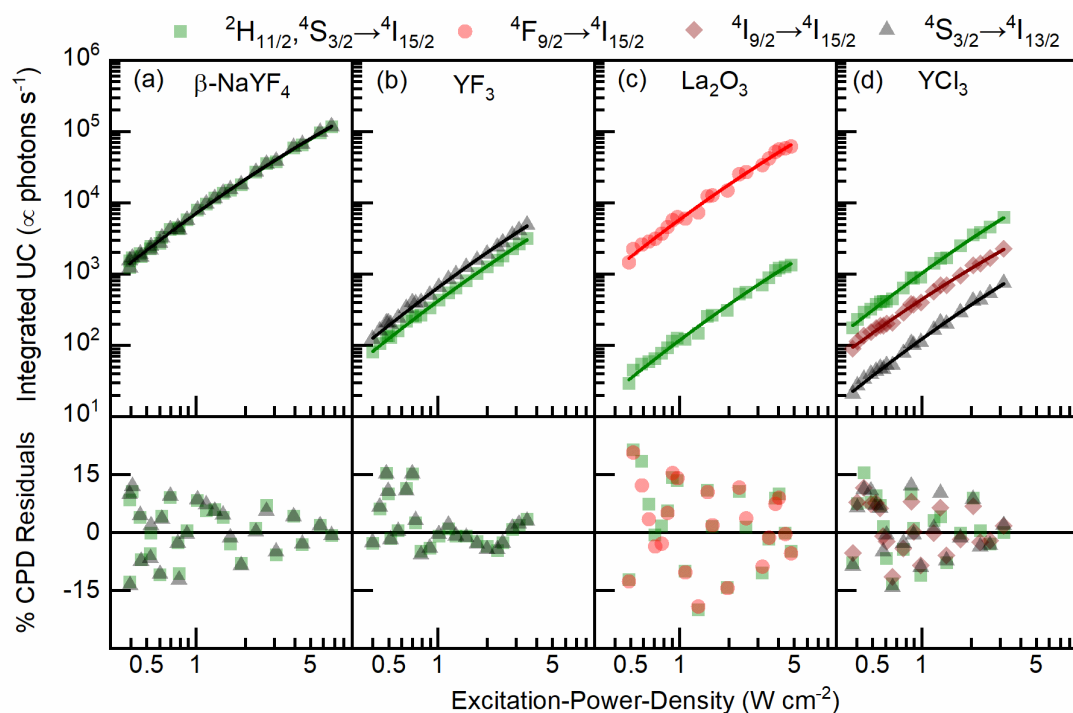


Figure 5.14. Top panels: UC vs excitation power density for the four hosts doped with 18% Yb^{3+} and 2% Er^{3+} with the fits according to the critical power density model: (a) $\beta\text{-NaYF}_4$ (b) YF_3 (c) La_2O_3 and (d) YCl_3 . Bottom panels: percentage residuals from fitting with the model. Adapted with permission from Joseph et al. [144] Copyright 2019 American Chemical Society.

The values of CPD obtained for each of these materials systems by fitting their UC-EPD dependences with the CPD model are tabulated in Table 5.1. $\text{CPD}_{\text{green}}$ refers to the CPD extracted for the ${}^2\text{H}_{11/2}, {}^4\text{S}_{3/2} \rightarrow {}^4\text{I}_{15/2}$ transition. Similarly, CPD_{NIR1} and CPD_{NIR2} refers to the CPD calculated for the NIR and NIR2 transitions. Here, NIR1 refers to the transition ${}^4\text{S}_{3/2} \rightarrow {}^4\text{I}_{13/2}$, and NIR2 indicates the two-photon UC emission ${}^4\text{I}_{9/2} \rightarrow {}^4\text{I}_{15/2}$ at around 810 nm observed only in the YCl_3 host material. Finally, CPD_{red} indicates the CPD for the transition ${}^4\text{F}_{9/2} \rightarrow {}^4\text{I}_{15/2}$ in the La_2O_3 host which is of two-photon nature contrary to the red emissions in the other hosts. This terminology is used in the rest of this chapter for further discussions to refer to the CPD of specific transitions.

Table 5.1. Critical power density values in W cm^{-2} for the four hosts - $\beta\text{-NaYF}_4$, YF_3 , La_2O_3 , and YCl_3 doped with 18% Yb^{3+} and 2% Er^{3+} . Adapted with permission from Joseph et al. [144] Copyright 2019 American Chemical Society.

Host	$\text{CPD}_{\text{green}}$	CPD_{NIR1}	CPD_{NIR2}	CPD_{red}
$\beta\text{-NaYF}_4$	0.7 ± 0.1	0.7 ± 0.1	—	—
YF_3	1.0 ± 0.2	1.0 ± 0.2	—	—
YCl_3	0.8 ± 0.1	0.8 ± 0.1	0.3 ± 0.05	—
La_2O_3	1.1 ± 0.2	—	—	0.9 ± 0.2

5.4. Comparison with Balancing Power Density model

Now, the same data used for fitting with the CPD model is used for fitting with the BPD model for the sake of comparison. The fits and percentage residuals from the BPD model are provided in Figure 5.15 in the same way as in Figure 5.14.

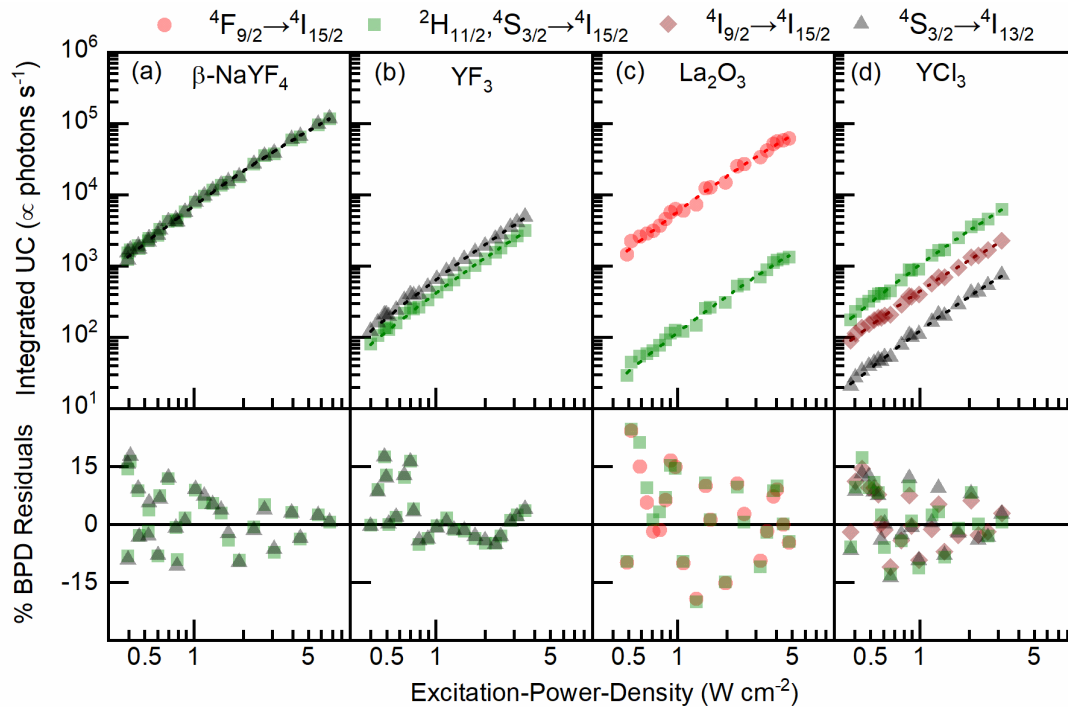


Figure 5.15. UC vs excitation power density for the four hosts doped with 18% Yb^{3+} and 2% Er^{3+} with the fits according to the balancing power density model: (a) $\beta\text{-NaYF}_4$ (b) YF_3 (c) La_2O_3 and (d) YCl_3 . Bottom panels: percentage residuals from fitting with the model. Adapted with permission from Joseph et al. [144] Copyright 2019 American Chemical Society

The BPD model also gives an accurate description of the UC-EPD dependence of all of the four material systems. The equal distribution of the percentage residuals on either side of the zero axis also points out this fact. The CPD model has a slight advantage here as the CPD model results in lower percentage residuals as compared to the BPD model. In the original publication, in which the CPD model was introduced, the model was not in agreement with the data at high EPDs [175]. The reason for this behaviour is laser-excited heating, whose effects were not corrected in the UC measurements. If the UC intensities were corrected according to the method described in Chapter 4, the model would agree with the measured data even at higher EPDs. Therefore, both models reliably describe the UC-EPD dependence of a material.

Another difference between the two models is in the methodology. The CPD model needs just fitting the UC -EPD dependence data with the equation, while the BPD model requires pinpointing the EPD at which the slope of the log-log plot of the UC-EPD dependence becomes 1.5. Finding out the exact region on the curve where the slope is exactly 1.5 is slightly tricky

and prone to experimental error as this region would span a region of measured EPD values. The values of BPD extracted from the fitting with the BPD model is tabulated along with the CPD values in Table 5.2. For all the emissions, the BPD values are roughly about 3 times the value of the CPD, showing the similarity of the methods, though they are not mathematically identical.

Table 5.2. Calculated critical power density and balancing power density values in $W\text{ cm}^{-2}$ extracted for the four hosts $\beta\text{-NaYF}_4$, YF_3 , La_2O_3 , and YCl_3 doped with 18% Yb^{3+} and 2% Er^{3+} . Adapted with permission from Joseph *et al.* [144] Copyright 2019 American Chemical Society

Host	CPD _{green}	BPD _{green}	CPD _{NIR1}	BPD _{NIR1}	CPD _{NIR2}	BPD _{NIR2}	CPD _{red}	BPD _{red}
$\beta\text{-NaYF}_4$	0.7±0.1	2.2±0.1	0.7±0.1	2.3±0.1	—	—	—	—
YF_3	1.0±0.2	2.6±0.2	1.0±0.2	2.7±0.2	—	—	—	—
La_2O_3	1.1±0.2	3.1±0.5	—	—	—	—	0.9±0.2	2.6±0.4
YCl_3	0.8±0.1	2.2±0.2	0.8±0.1	2.1±0.2	0.3±0.05	1.1±0.1	—	—

Both models have also been used for analysis with data obtained from literature and they have successfully described the dependence in each of the cases while maintaining a ratio between CPDs and BPDs at about 3. In the work by Liu *et al.* where they introduced the BPD concept, the BPD of $\text{NaYF}_4:\text{Yb}^{3+},\text{Tm}^{3+}@ \text{NaYF}_4$ nanoparticles is calculated to be 1.3 W cm^{-2} [175]. When the same data is fit with the CPD model, a CPD of 0.4 W cm^{-2} is obtained, which is roughly a third of the BPD value as expected. For $\text{NaYF}_4: 21.4\% \text{ Yb}^{3+}, 2.2\% \text{ Er}^{3+}$ commercial micropowder with a similar PLQY as the $\beta\text{-NaYF}_4: 18\% \text{ Yb}^{3+}, 2\% \text{ Er}^{3+}$, a BPD of 1.2 W cm^{-2} is observed by Kaiser *et al.*, suggesting a CPD about 0.4 W cm^{-2} [59]. The CPD for the $\beta\text{-NaYF}_4: 18\% \text{ Yb}^{3+}, 2\% \text{ Er}^{3+}$ sample is 0.7 W cm^{-2} which is in agreement with the CPD expected for the commercial micropowder. Therefore, both approaches can be used for defining a figure-of-merit for the UC-EPD dependence. But the CPD model has additional advantages as explained in the following sections.

5.5. CPD and UC mechanisms

The CPD is also an indicator of the mechanism of UC. The emissions which have the same population mechanisms have the same value of CPD. The CPD_{green} and CPD_{NIR1} values are equal in the hosts - $\beta\text{-NaYF}_4$, YCl_3 and YF_3 . The reason is that they have the same emissive state $^4\text{S}_{3/2}$ of Er^{3+} as their origin. Therefore, if the CPD of the UC dependence of different two-photon emissions are evaluated, correlations between them could shed light on their mechanisms. In YCl_3 , the CPD_{NIR2} value is strikingly different from the CPD_{green} and CPD_{NIR1} values. The lower value of CPD_{NIR2} suggests that the intermediate state involved in this case

has a longer lifetime. The time-resolved fluorescence measurements of the different emissions observed in YCl_3 is provided in Figure 5.16. The lifetime of the NIR2 emission (800 nm, ${}^4\text{I}_{9/2} \rightarrow {}^4\text{I}_{15/2}$) is much higher than all the other emissions except for the 1530 nm (${}^4\text{I}_{13/2} \rightarrow {}^4\text{I}_{15/2}$) emission. Then only the ${}^4\text{I}_{13/2}$ state has the capability of acting as an intermediate state for the 800 nm emission. Even though MPR rates are comparatively low in this material, the radiative branching ratio from the ${}^4\text{I}_{11/2}$ state to the ${}^4\text{I}_{13/2}$ state obtained from Judd-Ofelt analysis is 20%, which ensures the population of the ${}^4\text{I}_{13/2}$ state. Two ions in the ${}^4\text{I}_{13/2}$ could interact with each other and undergo an ETU to populate the ${}^4\text{I}_{9/2}$ state. Another possibility for the population of the ${}^4\text{I}_{9/2}$ state in YCl_3 is through a cross-relaxation mechanism involving ${}^2\text{H}_{9/2}$ state of Er^{3+} and the ground state ${}^2\text{F}_{7/2}$ of Yb^{3+} . The lifetime data showing longer components attest the involvement of the ${}^4\text{I}_{13/2}$ state, which supports the first mechanism suggested.

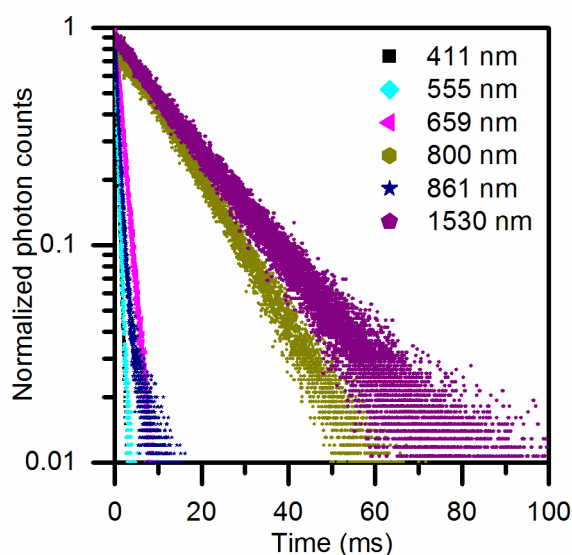


Figure 5.16. Normalized lifetimes of the UC emissions from YCl_3 : 18% Yb^{3+} , 2% Er^{3+} when excited with 980 nm radiation at an EPD of 5 W cm^{-2} with a pulse width of 20 ms. The pulse period was set to 40 ms (or 120 ms for 800 and 1530 nm lifetimes). Reproduced with permission from Joseph et al. [144] Copyright 2019 American Chemical Society

In the host La_2O_3 , the CPD_{red} value is lower than the $\text{CPD}_{\text{green}}$ value. This lower value of CPD_{red} suggests that the intermediate-state involved has a longer lifetime. If the red-emitting state ${}^4\text{I}_{9/2}$ is populated from the green-emitting states through MPR, the CPD_{red} value would have been the same as the $\text{CPD}_{\text{green}}$. Therefore, the population mechanism suggested by the CPD model involves the ${}^4\text{I}_{13/2}$ state getting populated from the ${}^4\text{I}_{11/2}$ state through MPR or radiative relaxations. In addition, direct excitation of the green-emitting states gives a much lower red to green ratio as the one observed with 980 nm excitation, again supporting the mechanism involving the ${}^4\text{I}_{13/2}$ state (Figure 5.25(d)). Both mechanisms are indicated in Figure 5.10. These examples demonstrate how the CPD model helps in understanding the UC mechanisms when the EPD dependence data of UC is carefully analyzed.

5.6. CPD as an indicator of intermediate-state lifetimes

Equation 5.13 gives the expression for the CPD. According to this equation, the CPD is proportional to the square of the decay constant from the intermediate state $-k_1$. In other words, the CPD is quadratically dependent on the inverse lifetime of the intermediate state. Therefore, as the lifetime of the intermediate state increases, the value of CPD decreases, if the other variables (rate-constant - k_{ET} of energy transfer between the intermediate state and the emitting state, and the absorption coefficient - α) in Equation 5.13 remain constant. The intermediate states in consideration for the UC processes discussed here are ${}^2F_{5/2}$ of Yb^{3+} and ${}^4I_{13/2}$ of Er^{3+} , which have emission peaks around 970 nm and 1530 nm, respectively. Each of the four samples is excited at 980 nm and the lifetime of the fluorescence at 990 nm and 1530 nm are observed. The obtained lifetime data is provided in Figure 5.17.

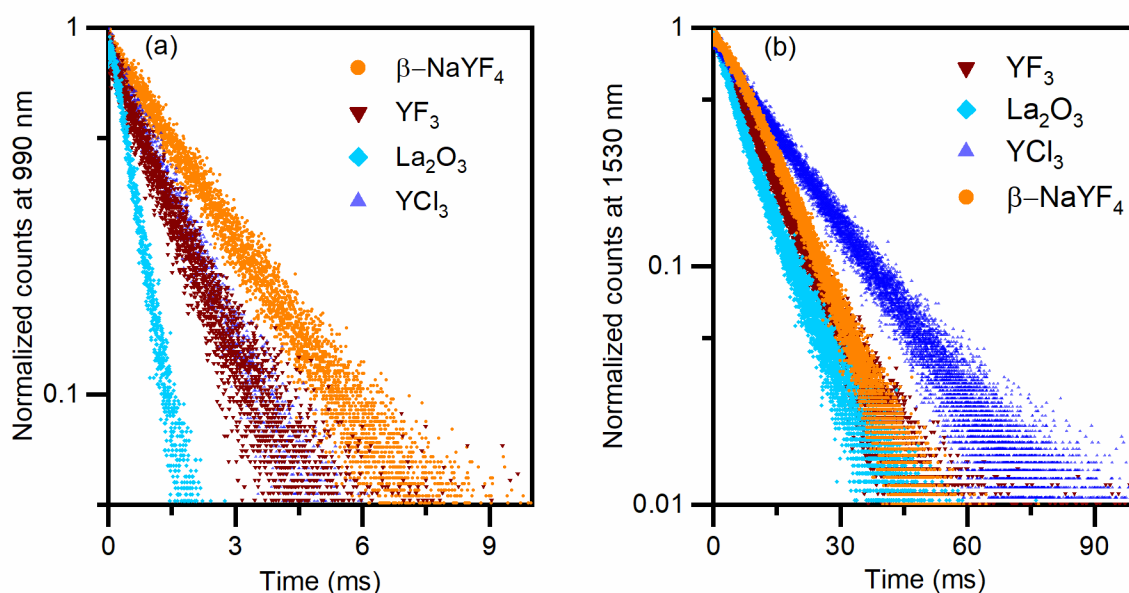


Figure 5.17. Normalized time-resolved fluorescence detected at (a) 990 nm and (b) 1530 nm in 18% Yb^{3+} , 2% Er^{3+} doped β - $NaYF_4$, YF_3 , La_2O_3 , and YCl_3 when excited at 980 nm at an EPD of % $W\ cm^{-2}$, for a pulse-width of 20 ms and pulse-period of 40 ms (for 990 nm lifetimes) or 100 ms (for 1530 nm lifetimes). Adapted with permission from Joseph et al. [144] Copyright 2019 American Chemical Society

The lifetimes are calculated using exponential fits on the time-resolved data. All the lifetimes at 990 nm are obtained using single exponential fits owing to the nature of the time-resolved fluorescence curve. The lifetimes of the ${}^4I_{13/2}$ state in La_2O_3 and YCl_3 are found out using double-exponential fits while in the other two hosts, single-exponential fit is sufficient to describe the decay curve. The lifetimes obtained are tabulated in Table 5.3. The green, red and NIR1 emissions originate in the same excited states, namely ${}^2H_{11/2}$ and ${}^4S_{3/2}$ and have the same intermediate state ${}^2F_{5/2}$ of Yb^{3+} for their ETU mechanisms. The measured intermediate lifetimes increase as the CPD values decrease as expected from Equation 5.13. These results are consistent with other results in the literature. Hossan *et al.* has demonstrated that the PLQY

of $\beta\text{-NaYF}_4\text{:Yb}^{3+},\text{Er}^{3+}$ nanocrystals increases as the intermediate-state lifetime increases [184]. Similarly, Würth *et al.* noted such a relationship between the UC PLQY and lifetime of the intermediate-state in $\text{NaGdF}_4\text{:20% Yb}^{3+}, 2% \text{Er}^{3+}$ [185].

Table 5.3. Measured Intermediate-state lifetimes with corresponding CPDs. Adapted with permission from Joseph *et al.* [144] Copyright 2019 American Chemical Society

Host material	Lifetime of 990 nm emission (ms)	CPD _{green}	CPD _{NIR1}	CPD _{red}	Lifetime of 1530 nm emission (ms)	CPD _{NIR2}
$\beta\text{-NaYF}_4$	2.5	0.7 ± 0.1	0.7 ± 0.1	—	$12\pm 0.5^*$	—
YF_3	1.6	1.0 ± 0.2	1.0 ± 0.2	—	$10\pm 0.5^*$	—
La_2O_3	0.6	1.1 ± 0.2	—	0.9 ± 0.2	$9\pm 0.5^\#$	—
YCl_3	1.6	0.8 ± 0.1	0.8 ± 0.1	—	$15\pm 1^\#$	0.3 ± 0.05

* Single-exponentially fitted and not used here

Double-exponentially fitted and average lifetime calculated

The tabulated results of the lifetimes of the intermediate-state are also graphically presented in Figure 5.18. The general trend is that the CPD values decrease as the lifetime of the intermediate-state increases. As explained in Section 5.8, the CPD is linked with the saturation PLQY, so a material with a longer intermediate-state lifetime has a lower CPD and consequently a higher PLQY at saturation as the EPD is increased. Therefore, maximizing intermediate-state lifetimes are critical for obtaining highly efficient UC materials.

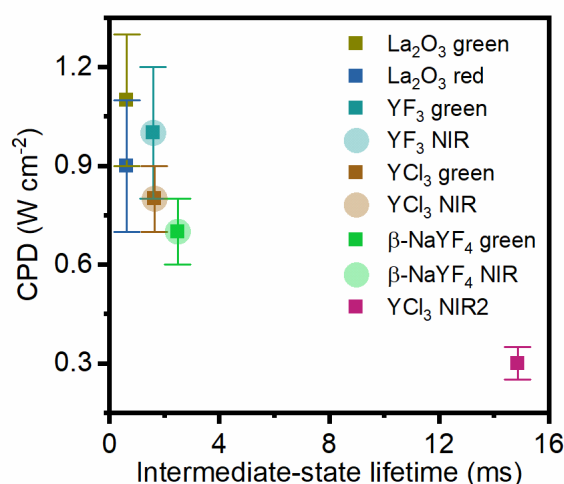


Figure 5.18. CPD vs lifetime of intermediate-state in the four hosts $\beta\text{-NaYF}_4$, YCl_3 , YF_3 , and La_2O_3 doped with 18% Yb^{3+} , 2% Er^{3+} when excited at 980 nm. Reproduced with permission from Joseph *et al.* [144] Copyright 2019 American Chemical Society

5.7. CPD and saturation Quantum Yield

PLQY can be calculated from the equation for the CPD model as:

$$PLQY = \frac{UC}{G} = \frac{k_{2rad}k_1^2}{16k_2k_{ET12}G} \left(-1 + \sqrt{1 + \frac{I}{CPD}} \right)^2 \quad (5.17)$$

$$\Rightarrow PLQY = \frac{CPDk_{2rad}}{2Ik_2} \left(-1 + \sqrt{1 + \frac{I}{CPD}} \right)^2 \quad (5.18)$$

When EPD equals the CPD, $I = CPD$, Equation 5.18 becomes,

$$PLQY_{CPD} = \frac{k_{2rad}}{2k_2} (-1 + \sqrt{2})^2 \quad (5.19)$$

The $PLQY_{sat}$ is the PLQY in the limit of high EPDs. The slope of a log-log plot of the PLQY vs EPD becomes zero at saturation. This saturation of the quantum yield is not effectuated by a depletion of the ground state populations of the sensitizer and emitter ions, but due to a change in the branching kinetics of the intermediate state. The dominant depopulation mechanism of the intermediate state becomes UC and an increase in the EPD, will no longer increase the fraction of photons emitted compared to the number of photons getting absorbed. The expression for $PLQY_{sat}$ can be obtained by evaluation of the limit of Equation 5.18 at an EPD equal to infinity:

$$PLQY_{sat} = \lim_{I \rightarrow \infty} CPD \frac{k_{2rad}}{k_2} \left(\frac{1}{I} + \frac{1}{2CPD} + \sqrt{\frac{1}{I^2} + \frac{1}{CPD \times I}} \right) \quad (5.20)$$

$$\Rightarrow PLQY_{sat} = \frac{1}{2} \frac{k_{2rad}}{k_2} = \frac{PLQY_{CPD}}{(-1 + \sqrt{2})^2} \approx 5.8 \times PLQY_{CPD} \quad (5.21)$$

Equation 5.21 presents two different ways by which the saturation quantum yield can be evaluated. These ways are:

1. The saturation quantum yield of UC from an excited state is equal to half of the quantum yield of direct excitation of that state. The PLQY by its basic definition is the ratio of emitted photons to the absorbed photons, or in other words, it is the ratio of the radiative decay rate to the total decay rate from a level. As evident from the first part of the equation, $PLQY_{sat}$ then corresponds to 50% of the PLQY when all the absorbed photons directly reach the emitting state, i.e., when the emitting state is directly pumped using

a laser. This method presents a very interesting way to determine the PLQY of the state not having to worry about the very high EPDs required for saturation as described in Section 2.4.1.

2. The saturation quantum yield is 5.8 times the PLQY at an EPD equal to the CPD. In materials with poor thermal transport, laser-induced heating will significantly increase the multiphonon relaxation (MPR) rates, which in turn causes a further reduction of the PLQY. Normally when such materials are driven to saturation, the EPDs are sufficiently high enough to cause these unwanted effects. Due to this, special precautions need to be taken, or certain correction methods need to be implemented as described in chapter 5 of this thesis. However, at the CPD, UC is just turned on only, meaning that undesired heating effects are not observed at such low EPDs. Therefore, using this method, $PLQY_{sat}$ can be easily estimated by multiplying the observed PLQY with 5.8.

5.8. Calculating the saturation PLQY with CPD model

As explained in the previous section, the CPD model offers two different ways through which the saturation PLQY ($PLQY_{sat}$) can be determined. This feature of the CPD model is highly advantageous as the CPD and the $PLQY_{sat}$ are the two most important figures-of-merit which can describe the UC behaviour of a system. Often during measurements of $PLQY_{sat}$ the plot of the PLQY is found to decrease instead of saturating after reaching a peak value [165]. The theoretical models predict only a saturation of the UC PLQY. The very high EPDs at which a UC material is driven to saturation is often accompanied by laser-induced heating effects, which increase the temperature of the material, and thereby increase the rate of MPR processes as explained in Section 2.1.6. Figure 5.21 presents such a measurement of the PLQY of the total upconverted emission (500-880 nm) as a function of the EPD in the four different material systems studied in this chapter. For the host La_2O_3 , this effect is much pronounced as evident from the graph, due to its higher phonon energies. However, the PLQY values measured for the other three hosts are also not free of error as illustrated in Figure 5.22. The integrated UC intensity exclusively under the green peak ($^2H_{11/2}, ^4S_{3/2} \rightarrow ^4I_{15/2}$) is calculated from the UC spectra acquired continuously at the smallest time interval possible for the spectrometer (30 μs). The value of the integrated UC intensity at zero time is the original UC intensity which is free of thermal effects. As the material gets heated up, the MPR rate increases, and thereby the intensity of the radiative emissions decreases. Finally, a steady-state is reached where the intensity is much less than the original intensity in the absence of thermal effects. This statement is valid only for the fluorides and the oxide host under consideration, as the steady-state-integrated UC intensity of the green emission in the YCl_3 host seems to increase. One possible reason could be the addition of the MPR assisted radiative channels in this host.

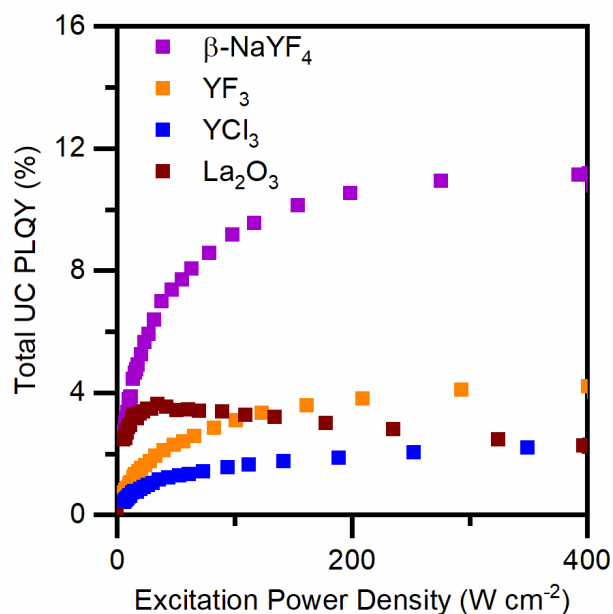


Figure 5.21. UC-PLQY (400-880 nm) as a function of EPD of 980 nm radiation. Adapted with permission from Joseph et al. [144] Copyright 2019 American Chemical Society.

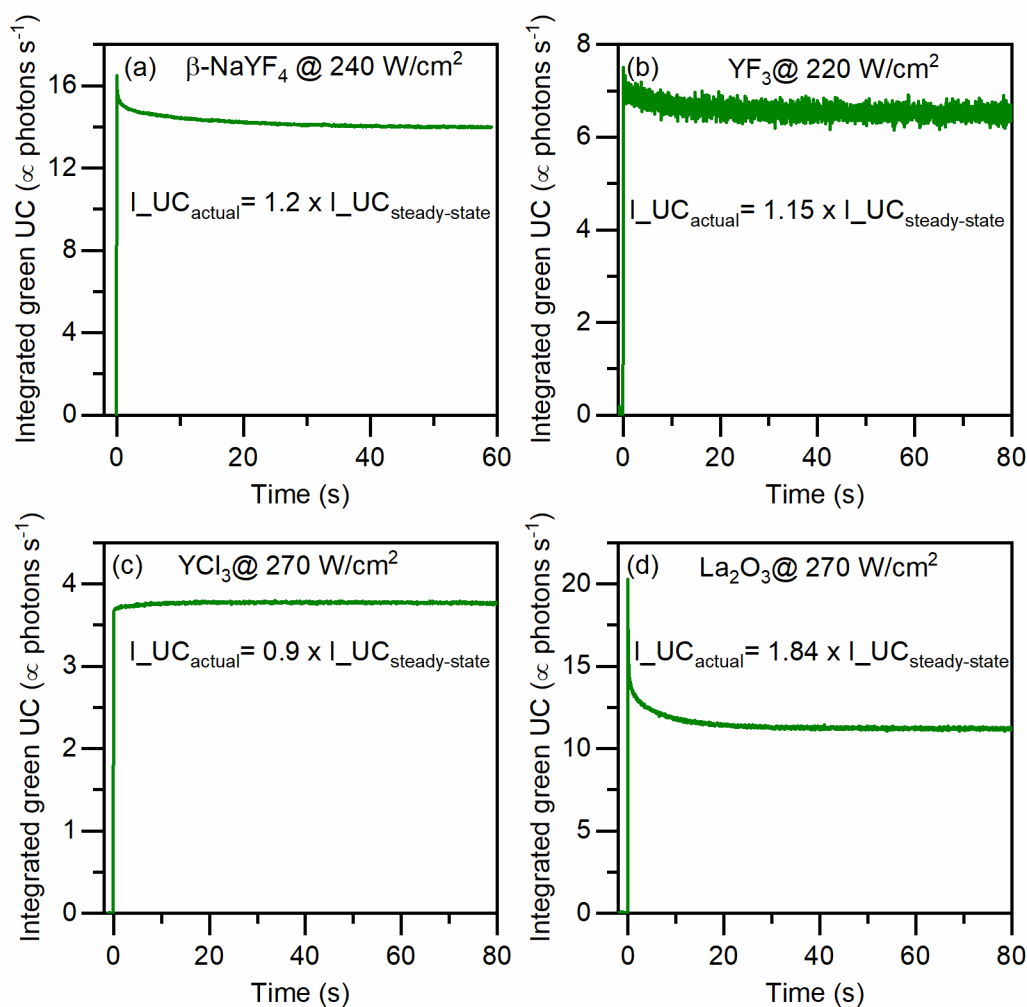


Figure 5.22. Integrated UC intensity of the green peak as a function of time at high excitation-power-densities. Adapted with permission from Joseph et al. [144] Copyright 2019 American Chemical Society

5.8.1. Experimental Determination of PLQY and Correction for Thermal Effects

The PLQY of UC is first measured for each of the four microcrystalline hosts using the 3M method (described in Section 3.2.3) as a function of the EPD (Figure 5.21). The PLQY at an EPD of 250 W cm^{-2} is taken as the PLQY_{sat} , where saturation has set-in in all materials. The measured values of PLQY_{sat} for the total UC emission in the range of 400-880 nm are corrected for each of the four material systems using the method described in chapter 4 [139]. The UC spectra at very high EPDs close to saturation is plotted in Figure 5. 23.

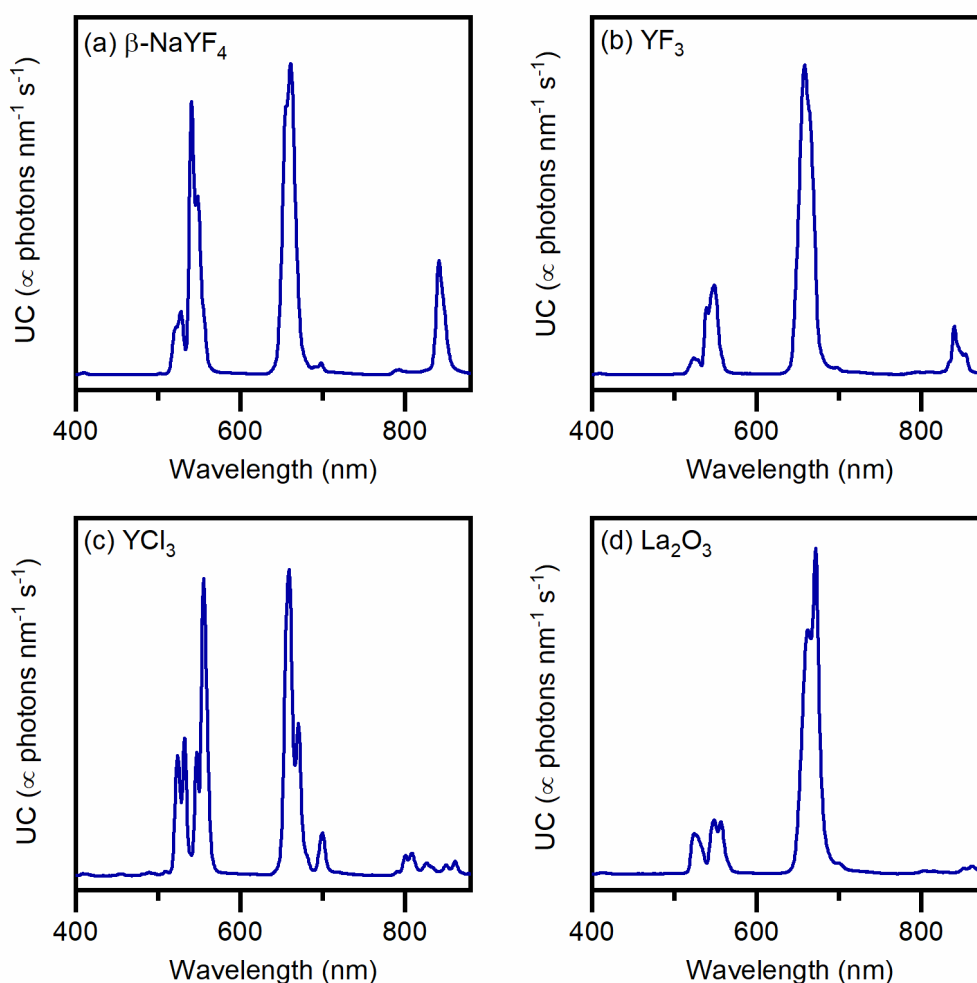


Figure 5.23. UC-emission spectra in the four host materials at high EPDs ($> 200 \text{ W cm}^{-2}$). Excitation wavelength: 980 nm. Adapted with permission from Joseph et al. [144] Copyright 2019 American Chemical Society

The ratio of the area under the total UC spectrum to the area under the green and NIR peaks of the spectra are first calculated to estimate the fraction of the PLQY_{sat} originating from the $^2\text{H}_{11/2}$ and $^4\text{S}_{3/2}$ states. Then the corrected value of the PLQY_{sat} from the total UC emission is divided with this ratio to get the contribution in the PLQY_{sat} from the $^2\text{H}_{11/2}$ and $^4\text{S}_{3/2}$ states. This value then corresponds to the actual PLQY of the UC emissions from these states, i.e., green

and NIR UC emissions. The measured values and corrected values along with the $PLQY_{sat}$ exclusively originating from the states $^2H_{11/2}$ and $^4S_{3/2}$ are tabulated in Table 5.4.

Table 5.4. Calculation of actual PLQY due to green states. Adapted with permission from Joseph et al. [144] Copyright 2019 American Chemical Society

Host	Measured total saturation UC-PLQY (%)	Corrected total saturation UC-PLQY (%)	$Area_{total}/Area_{green+NIR1}$	Saturation PLQY from $^2H_{11/2}$ and $^4S_{3/2}$ state (%)
β -NaYF ₄	11.6	14.4	2	7.2
YF ₃	4.7	5.4	3	1.8
YCl ₃	2.4	2.16	2.1	1.0
La ₂ O ₃	2.8	5.2	4.7	1.1

5.8.2. Calculation from PLQY at CPD

According to Equation 5.21, the PLQY at saturation is 5.8 times the PLQY measured when the EPD equals the CPD. For evaluating the PLQY at the CPD, first, the UC spectra for 980 nm excitation at the CPD is acquired with the help of a spectrometer (Avantes, AvaSpec-ULS2048x64TEC). The acquired spectra are provided in Figure 5.24. The red-to-green ratios of the UC emissions observed at CPD for the hosts β -NaYF₄ (Figure 5.24(a)), YF₃ (Figure 5.24(b)), and YCl₃ (Figure 5.24(c)) are much lower as compared to the red-to-green ratios of the UC emissions observed at EPDs close to saturation as seen in Figure 5.23 (a-c). However, the red-to green ratios for the host La₂O₃ remain more or less the same in Figure 5.23 (d) and Figure 5.24 (d). The reason is that three-photon UC processes are less prominent at lower EPDs around the CPD.

The PLQY of the UC emissions from the $^2H_{11/2}$ and $^4S_{3/2}$ states at the CPD are calculated by adding the PLQY of the green emission and the NIR1 emissions as these two emissions originate from these two states. These PLQYs are calculated at an EPD equal to the CPD, using the 3M method using an integrating sphere as described in chapter 3, in section 3.2.3. Finally, the PLQY at saturation, $PLQY_{sat}$ is calculated by multiplying the total PLQY from the $^2H_{11/2}$ and $^4S_{3/2}$ states with 5.8. The calculated values are tabulated in Table 5.5.

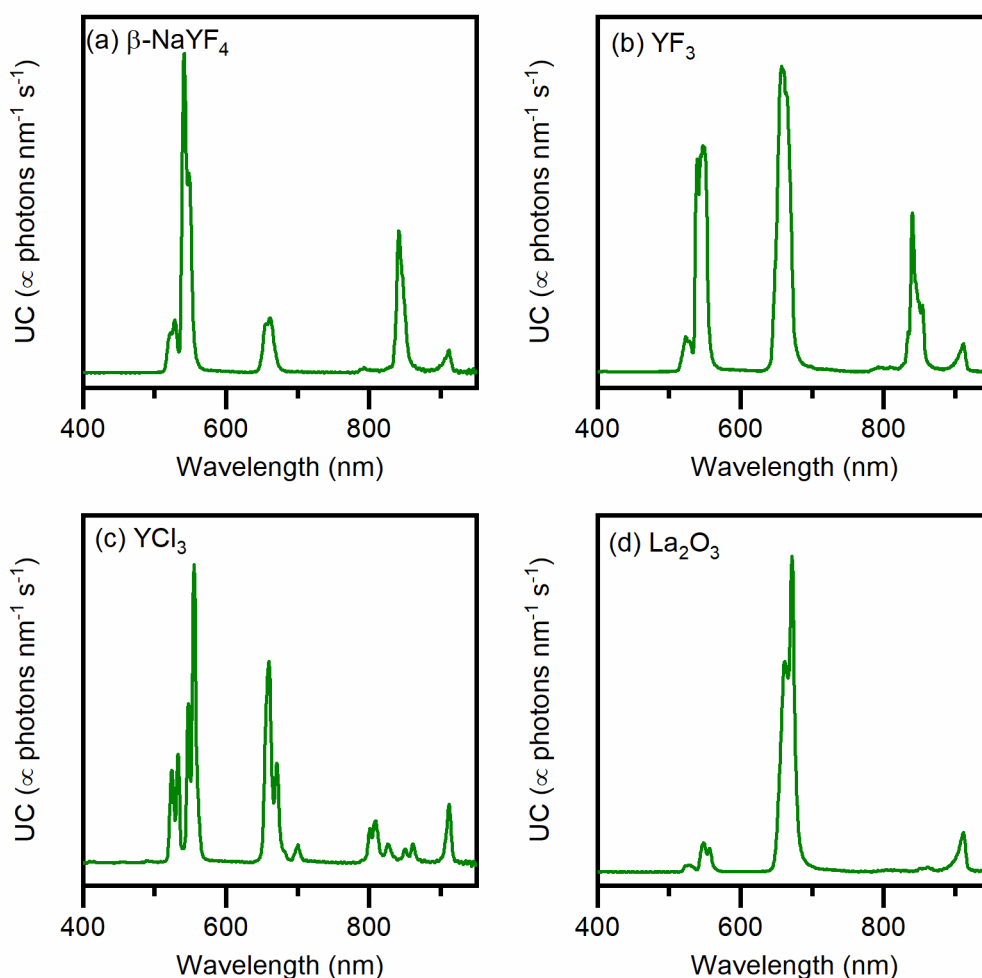


Figure 5.24. UC spectra measured at CPD for the hosts (a) β -NaYF₄, (b) YF₃, (c) YCl₃, and (d) La₂O₃. Adapted with permission from Joseph et al. [144] Copyright 2019 American Chemical Society

Table 5.5. Calculation of saturation UC-PLQY of green state from PLQY at CPD. Reproduced with permission from Joseph et al. [144] Copyright 2019 American Chemical Society

Host	CPD _{green} (W cm ⁻²)	PLQY _{green} (%)	PLQY _{NIR1} (%)	Total PLQY from ² H _{11/2} and ⁴ S _{3/2} states (%)	PLQY _{sat} from ² H _{11/2} and ⁴ S _{3/2} states (%)
β -NaYF ₄	0.7	0.8	0.4	1.2	7.0
YF ₃	1	0.2	0.1	0.3	1.7
YCl ₃	0.8	0.2	0.01	0.2	1.2
La ₂ O ₃	1.1	0.2	0.04	0.2	1.2

5.8.3. Calculation of UC saturation PLQY from Direct Excitation

A 525 nm laser diode (Roithner, LD-515-10MG) at a very low EPD (~ 0.01 W cm⁻²) is used for direct excitation of the ²H_{11/2} and ⁴S_{3/2} states. It is worth noting that it is difficult to separate the laser excitation from the green emission of the ²H_{11/2} and ⁴S_{3/2} states as seen in Figure 5.25

(a-d). To work around this problem, the PLQY of other emissions originating from the $^2H_{11/2}$, $^4S_{3/2}$ states which are not green in colour (shaded in blue colour in Figure 5.25) and hence do not overlap with the laser can be used. When the fraction between these emissions and the green emissions are known, the total PLQY is calculated knowing the fractions. The PLQY of these emissions are tabulated in Table 5.6. These fractions are evaluated from Figure 5.24 (a-d), which give the UC spectra at CPD, when three-photon channels are less prominent similar to the case of direct excitation with 525 nm.

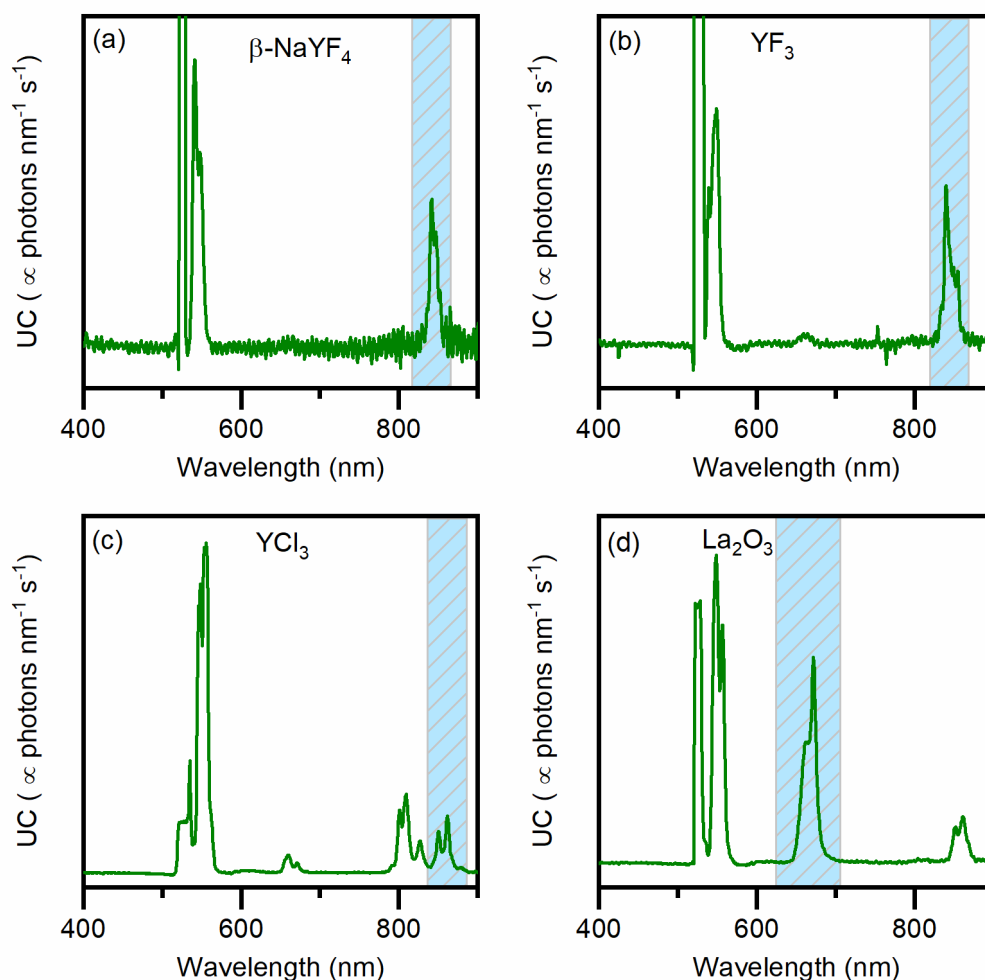


Figure 5.25. Emission spectra of 18% Yb^{3+} , 2% Er^{3+} for 525 nm excitation at an EPD of $0.01 W cm^{-2}$ in (a) $\beta-NaYF_4$, (b) YF_3 , (c) YCl_3 , and (d) La_2O_3 . Light blue shaded areas are integrated for evaluating the PLQY from the $^2H_{11/2}$, $^4S_{3/2}$ states. Reproduced with permission from Joseph et al. [144] Copyright 2019 American Chemical Society

When the $^2H_{11/2}$, $^4S_{3/2}$ states of Er^{3+} in La_2O_3 are directly excited with 525 nm, the red emission exclusively originates from the $^2H_{11/2}$, $^4S_{3/2}$ states after MPR, as the population channel involving the $^4I_{13/2}$ state is not possible due to the absence of 980 nm photons. The PLQY of the red emission is thus used in the case of the host La_2O_3 for evaluating the PLQY of the $^2H_{11/2}$, $^4S_{3/2}$ states:

$$\begin{aligned}
 & \text{Total PLQY from the green states} & (5.22) \\
 & = (1 + \text{Ratio of the area under the peaks}) \\
 & \times \text{PLQY from the NIR peak (or red peak)} \quad .
 \end{aligned}$$

$$\text{Saturation UC PLQY of green states} = \frac{1}{2} \times \text{Total PLQY from green states} \quad (5.23)$$

The PLQY estimated through this method for the host YCl_3 is expected to be higher than the actually observed PLQY. The intrinsic lifetimes of the $^4\text{S}_{3/2}$ state in YCl_3 is the highest among all the four host materials as seen in Figure 5.14. In the presence of 980 nm photons, the $^4\text{S}_{3/2}$ state can act as an intermediate state for the three-photon processes leading to the $^2\text{G}_{7/2}$, $^2\text{K}_{15/2}$, $^2\text{G}_{9/2}$ states. These processes act as a depopulation channel of the $^4\text{S}_{3/2}$ state which results in lesser PLQY of the green UC emission. Therefore, the direct-excitation method for determining the PLQY_{sat} is not suitable for material systems in which the emitting level itself acts as an intermediate-state for UC processes of a higher order.

Table 5.6 Calculation of saturation UC-PLQY from direct excitation. Adapted with permission from Joseph et al. [144] Copyright 2019 American Chemical Society

Host	Green to NIR1 (or red) peak ratio	PLQY from NIR1 (or red) (%)	Total PLQY from $^2\text{H}_{11/2}$, $^4\text{S}_{3/2}$ states (%)	Saturation UC-PLQY of $^2\text{H}_{11/2}$, $^4\text{S}_{3/2}$ states (%)
$\beta\text{-NaYF}_4$	2.5	4.0	14	7.0
YF_3	2.0	1.2	3.6	1.8
YCl_3	6.8	1.9	14.8	7.4
La_2O_3	0.1 (to red)	2.5 (from red)	2.7	1.3

5.8.4. Comparison of PLQY_{sat} estimated with the three methods

Finally, the PLQY of the two-photon UC emission at saturation from the $^2\text{H}_{11/2}$, $^4\text{S}_{3/2}$ states, estimated through the three techniques described in Sections 5.9.1-5.9.3 are plotted together for comparison. The PLQY_{sat} estimated for the hosts $\beta\text{-NaYF}_4$, YF_3 , and La_2O_3 agree well with each other using all three techniques. As expected, the PLQY_{sat} obtained for the host YCl_3 through direct excitation at 525 nm is highly overestimated, as the depopulation mechanism to higher energy states are not considered in the CPD model. Still, the experimentally determined PLQY_{sat} agrees with the PLQY_{sat} estimated by measurement at the CPD.

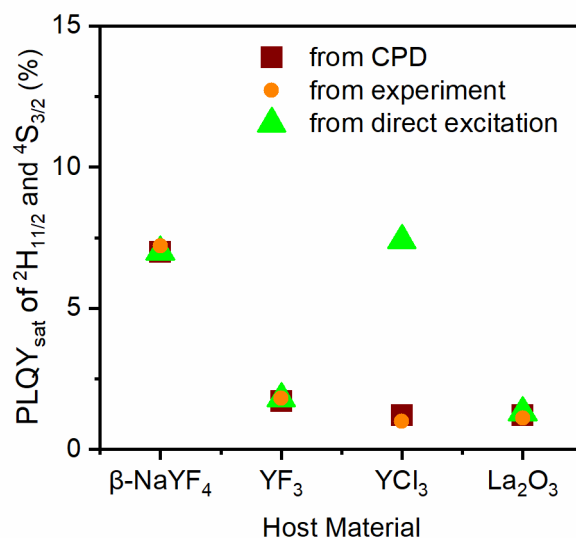


Figure 5.26. Saturation photo luminescent quantum yields ($PLQY_{sat}$) of the $^2H_{11/2}$ and $^4S_{3/2}$ states estimated through three different techniques in four microcrystalline hosts doped with Yb^{3+} , Er^{3+} (18/2%). Adapted with permission from Joseph et al. [144] Copyright 2019 American Chemical Society.

5.9. Summary and Implications for UC displays

To summarize the results presented in this chapter, the CPD model was developed to define a figure-of-merit for comparing different UC materials. This figure-of-merit, the CPD along with the other figure-of-merit, $PLQY_{sat}$ serves the purpose of effective comparison between the efficiency of different UC materials, throwing light into the EPDs at which the UC starts becoming efficient. This helps in identifying UC materials which are particularly suitable for low EPD applications. The CPD model is able to accurately describe the UC-EPD dependence of two-photon UC processes. The CPD model suggests that longer intermediate-state lifetimes lead to lower CPDs, which means that the material would show UC emission at lower EPDs. Selecting host materials with long intermediate-state lifetimes would help in identifying materials with low CPDs. Also, the CPD model suggests two methods for accurately determining the $PLQY_{sat}$ of an excited energy state populated by two-photon processes. Multiplying the PLQY measured at the CPD by a factor of 5.8 correlates well with the experimentally measured $PLQY_{sat}$ corrected for thermal effects. This value also correlates well with half of the PLQY of the level upon direct excitation. The remarkable advantage is that the CPD model presents a way of determining the $PLQY_{sat}$ without having to resort to high EPDs where other detrimental effects set in.

Applying the CPD model to the UC-EPD dependence of a system also gives valuable insights into the UC mechanisms. The UC mechanism observed in the oxide host is entirely different from that of the fluoride hosts, which is again different from that in the chloride host. In La₂O₃, a two-photon process involving ETU from the $^4I_{13/2}$ state leads to a population of the red-

emitting $^4F_{9/2}$ state, along with a minor contribution from the $^4S_{3/2}$ state after MPR. On the contrary, in YCl_3 , owing to its very low phonon energies, even the $^4I_{9/2}$ state is effectively populated through ETU between ions in the $^4I_{13/2}$ state. However, in the fluorides and La_2O_3 , this state is immediately depopulated due to effective MPR to the immediately lower-lying $^4I_{11/2}$ state. Generally speaking, two-photon processes are responsible for populating the $^2H_{11/2}$ state and $^4S_{3/2}$ state in all the four material systems considered causing both green and NIR emissions.

Considering the four microcrystalline hosts analysed in this chapter, β - $NaYF_4$ appears as the best material suitable for a POV UC display. The reason is its low CPD and high $PLQY_{sat}$ compared to the other materials. When translated into a POV display application relying on fast scanning of an excitation laser point, a high $PLQY_{sat}$ is important because it will mean that sufficient emission intensity can be obtained from a single point during the short period of its excitation that each pixel/voxel has the best possible luminance. As seen in the following chapter, achieving sufficient luminance for a UC POV display to be visible under ambient lighting conditions is not trivial. One might be tempted to think YCl_3 is a better choice owing to its long lifetimes. Though it has longer lifetimes, this comes at the cost of overall brightness of the display, which would again limit the use of such a display in ambient light. As explained earlier, these long lifetimes support ETU to higher excited states, which causes a decrease in the total PLQY of the emission, as compared to the situation without such a depopulation mechanism. Therefore, the UC emissions from the Er^{3+}, Yb^{3+} pair in the host β - $NaYF_4$ is brighter and hence more suitable as compared to that in YCl_3 . In addition, YCl_3 is highly hygroscopic which would add more design challenges to a display based on YCl_3 [186]. For monochrome display applications, the host La_2O_3 looks attractive due to its nearly constant emission colour. Though the $PLQY_{sat}$ is not as high as that of β - $NaYF_4$, it suffers from increased MPR as compared to the fluorides due to its higher phonon energies. This situation is also not optimal for a UC display as the MPR causes heating of the material or polymer substrate on which it is embedded. Clearly β - $NaYF_4$ trumps YF_3 due to its relatively high $PLQY_{sat}$. Therefore, β - $NaYF_4: Yb^{3+}, Er^{3+}$ could potentially be used in a UC display. In the next chapter, we examine if such a UC display would meet the requirements to be visible in a well-lit room. Also, we propose a method to keep the emission colour constant, when the EPD is varied, to realise a monochrome UC display.

6. Colour Modification through Dual-Wavelength Pumping

This chapter describes how the colour of UC emission can be controlled by simultaneous excitation with two different wavelengths. It is based on the results included in the third first-author-publication “Bright constant color upconversion based on dual 980 and 1550 nm excitation of SrF₂: 18% Yb³⁺, 2% Er³⁺ and β-NaYF₄: 18% Yb³⁺, 2% Er³⁺ micropowders; considerations for persistence of vision displays”, Optical Materials, 2020 [125]. The idea for a UC display based on dual excitation was developed by the author, Ian A. Howard and Bryce S. Richards. Microcrystals of β-NaYF₄ and SrF₂ were synthesized by Damien Hudry and Daniel Biner using the technique devised by Karl Krämer at the University of Bern. Dmitry Busko helped in building the new optical set-up for two-colour excitation used in this work and guided 3D printing of special sample holders. All the steady-state and time resolved optical measurements, and photographs of the sample showing colour-control were made by the author. The calculations for obtaining the CIE coordinates and the Luminances were performed using a MATLAB code written by the author. The text of the publication was written by the author and Ian A Howard. Andrey Turshatov, Bryce S. Richards, Karl Krämer and Ian A. Howard helped in the finalising the draft through engaging scientific discussions.

Among the many applications of UC, lighting and displays require precise control of the emission colour and intensity. Here, colour tuning and intensity control is demonstrated using two different microcrystalline UC materials, namely β-NaYF₄: 18% Yb³⁺, 2% Er³⁺ and β-SrF₂: 18% Yb³⁺, 2% Er³⁺. In Sections 6.1 and 6.2, the colour obtained by excitation with either 980 nm or 1550 nm radiation or by simultaneous excitation with both 980 nm and 1550 nm radiation in the two materials are demonstrated with the help of the Commission Internationale de l'Eclairage (CIE 1931) chromaticity diagram. The implications on the UC intensity upon incorporation in a transparent host and scanning is discussed in Section 6.3. Then colour tuning from green to yellow to red is demonstrated in dark for SrF₂: 18% Yb³⁺, 2% Er³⁺ micropowder in Section 6.4. Furthermore Section 6.5 shows that, using dual excitation, the colour of the UC emission can be kept constant while the intensity can be varied as per requirement in both SrF₂: 18% Yb³⁺, 2% Er³⁺ and β-NaYF₄: 18% Yb³⁺, 2% Er³⁺ micropowders, thereby demonstrating the proof-of-principle of a monochrome display. A dual-excitation based monochrome display using β-NaYF₄: 18% Yb³⁺, 2% Er³⁺ micropowders would be better than

one using SrF₂: 18% Yb³⁺, 2% Er³⁺ owing to its higher PLQY. Finally, a summary of all the results presented in the chapter and the implications of these results for UC displays are provided in Section 6.6.

6.1. UC Colour for Mono-excitation

The possible UC mechanisms for the observed UC emissions from SrF₂: 18% Yb³⁺, 2% Er³⁺ and β-NaYF₄: 18% Yb³⁺, 2% Er³⁺ upon 980 nm and 1550 nm excitation are given in Figure 6.1.

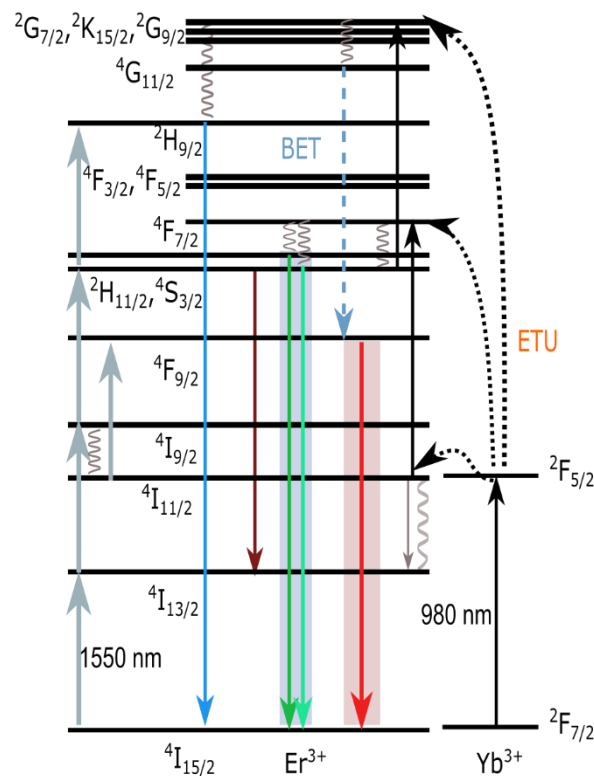


Figure 6.1. UC mechanisms to populate the ⁴S_{3/2} (green) and ⁴F_{9/2} (red) emission states upon 1550 nm and 980 nm excitations in a fluoride host.

The mechanisms of UC emissions resulting from 980 nm excitation in β-NaYF₄: 18% Yb³⁺, 2% Er³⁺ were explained in Chapter 5. Similar mechanisms are observed in SrF₂: 18% Yb³⁺, 2% Er³⁺ upon 980 nm excitation owing to the similarities in the fluoride host lattices. In the case of 1550 nm excitation, a two-photon ETU process populates the ⁴I_{9/2} state of Er³⁺. An ion in the ⁴I_{9/2} state can lose some of its energy through MPR and move into the immediately lower lying ⁴I_{11/2} state. If this bridging to the ⁴I_{11/2} state is faster than the next ETU step to the ⁴S_{3/2} state, then the ETU from the ⁴I_{11/2} state to the ⁴F_{9/2} state occurs, which results in more red UC emission. If this bridging between the ⁴I_{9/2} state and the ⁴I_{11/2} is not as efficient, ⁴S_{3/2} state gets populated leading to more green emission. For this reason, the UC emission from SrF₂: 18% Yb³⁺, 2% Er³⁺ has a higher R/G ratio compared to β-NaYF₄: 18% Yb³⁺, 2% Er³⁺

upon 1550 nm excitation, and upon increasing the EPD, the R/G ratio decreases in both hosts as the $^4I_{9/2} \rightarrow ^4S_{3/2}$ ETU becomes more efficient than the MPR between $^4I_{9/2}$ and $^4I_{11/2}$ (Figures 6.2 and 6.3).

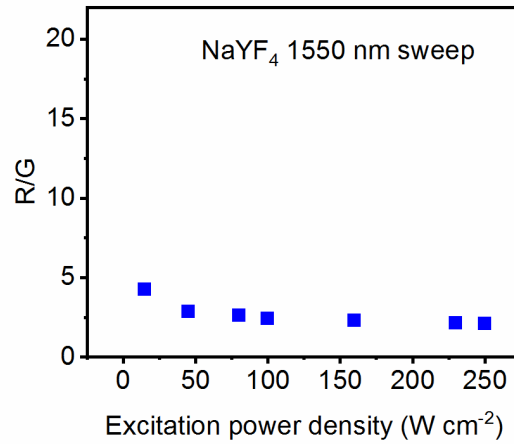


Figure 6.2. Change in the R/G ratio of UC emission as a function of the EPD of 1550 nm radiation in β -NaYF₄: 18% Yb³⁺, 2% Er³⁺. Adapted from Joseph et al. [125]

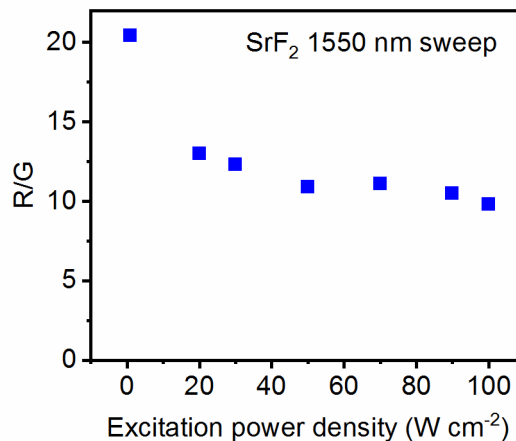


Figure 6.3. R/G ratio of UC emission decreases as a function of the EPD of 1550 nm radiation in SrF₂: 18% Yb³⁺, 2% Er³⁺. Adapted from Joseph et al. [125]

The R/G ratio in the host SrF₂ is 12, whereas it is only 3 in β -NaYF₄ at an EPD of 10 W cm⁻² of 1550 nm excitation. As the EPD increases, the R/G ratio significantly decreases for the host SrF₂ whereas it decreases slightly for the host β -NaYF₄ and remains constant, showing the effect of bridging between the $^4I_{9/2}$ and $^4I_{11/2}$ levels (Figures 6.2 and 6.3).

To examine the range of colour tuning possible with SrF₂: 18% Yb³⁺, 2% Er³⁺ and β -NaYF₄: 18% Yb³⁺, 2% Er³⁺, each of these materials are excited with either 980 nm or 1550 nm. The UC emission spectra normalized to the highest emission peak of SrF₂: 18% Yb³⁺, 2% Er³⁺ and β -NaYF₄: 18% Yb³⁺, 2% Er³⁺ upon mono-excitation with 1550 nm and 980 nm at an EPD

of 10 W cm^{-2} are provided in Figures 6.4 and 6.5, and the calculated CIE 1931 coordinates for the corresponding spectra are provided in Figures 6.6 and 6.7. The CIE coordinates on the chromaticity diagram illustrate that the host SrF_2 offers a wider range for colour tuning from red to green compared to the host $\beta\text{-NaYF}_4$.

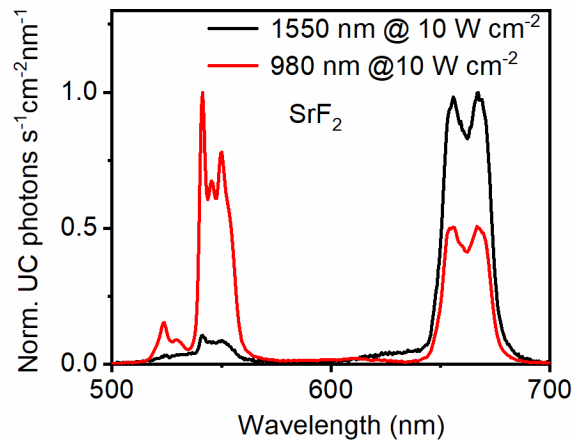


Figure 6.4. Normalized UC emission from $\text{SrF}_2: 18\% \text{Yb}^{3+}, 2\% \text{Er}^{3+}$, upon 1550 nm and 980 nm excitations at 10 W cm^{-2}

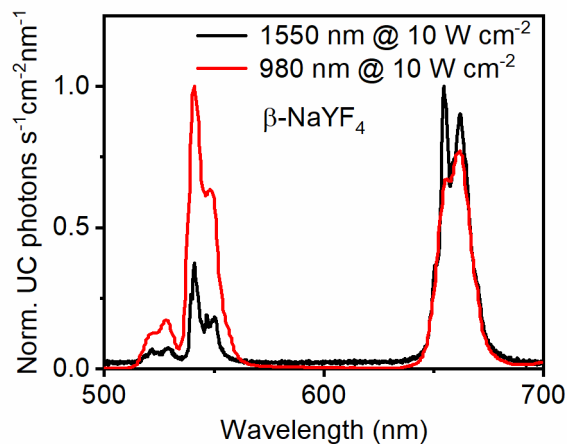


Figure 6.5. Normalized UC emission from $\beta\text{-NaYF}_4: 18\% \text{Yb}^{3+}, 2\% \text{Er}^{3+}$, upon 1550 nm and 980 nm excitations at 10 W cm^{-2}

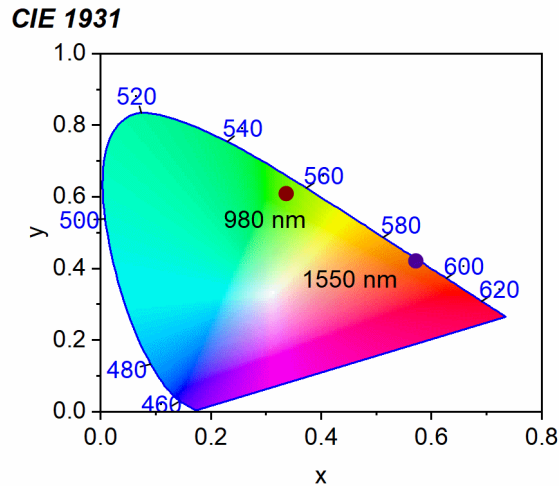


Figure 6.6. CIE colour coordinates of the emission spectra from $\text{SrF}_2: 18\% \text{Yb}^{3+}, 2\% \text{Er}^{3+}$, upon 1550 nm and 980 nm excitations at 10 W cm^{-2}

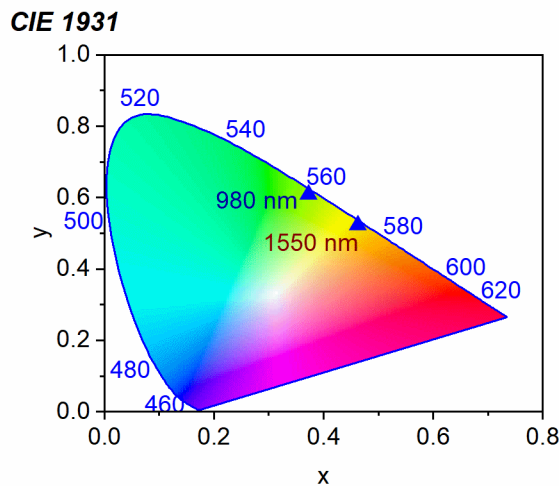


Figure 6.7. CIE colour coordinates of the emission spectra from $\beta\text{-NaYF}_4: 18\% \text{Yb}^{3+}, 2\% \text{Er}^{3+}$, upon 1550 nm and 980 nm excitations at 10 W cm^{-2}

After examining the limits of colour tuning with mono-excitation with either 980 nm or 1550 nm in this Section, the UC colour upon simultaneous excitation of both 980 nm and 1550 nm radiations are examined in the next section.

6.2. UC Colour for Dual-excitation

The UC spectra, CIE 1931 colour coordinates and calculated luminances upon simultaneous excitation of both the hosts with 980 nm and 1550 nm radiations are given in Figures 6.8 and 6.9. The UC spectra are absolutely calibrated in terms of photons $\text{cm}^{-2}\text{s}^{-1}\text{nm}^{-1}$, by multiplying the intensity calibrated spectra with a constant scaling factor which was determined by a measurement at 100 W cm^{-2} of 980 nm excitation inside an integrating sphere. The details of this calibration are given in Section A.3 of the Appendix. The experimental details are provided in Section 3.3. Even though the UC spectra provided in Figure 6.8(a)-(c) and 6.9(a)-(c) are expressed in absolute units of photons $\text{cm}^{-2}\text{s}^{-1}\text{nm}^{-1}$, the luminances and CIE coordinates are

calculated using $W \text{ cm}^{-2}$. Each of the three columns of these two figures, show the effects of a fixed bias of 980 nm excitation at an EPD of 10, 50 or 100 W cm^{-2} , respectively, when the 1550 nm excitation is swept through 10, 20, 30, 50, 70, 90 and 100 W cm^{-2} .

Looking at Figures 6.8 and 6.9, two general trends are observed. 1) The total number of emitted photons increases dramatically as the EPD of 980 nm excitation increases. 2) The change in the R/G ratio of the emission upon increasing the EPD of the 1550 nm excitation, become less pronounced as the 980 nm bias increases. Or in other words, increased 980 nm excitation decreases the tunability of the colour upon sweeping the EPD of 1550 nm radiation.

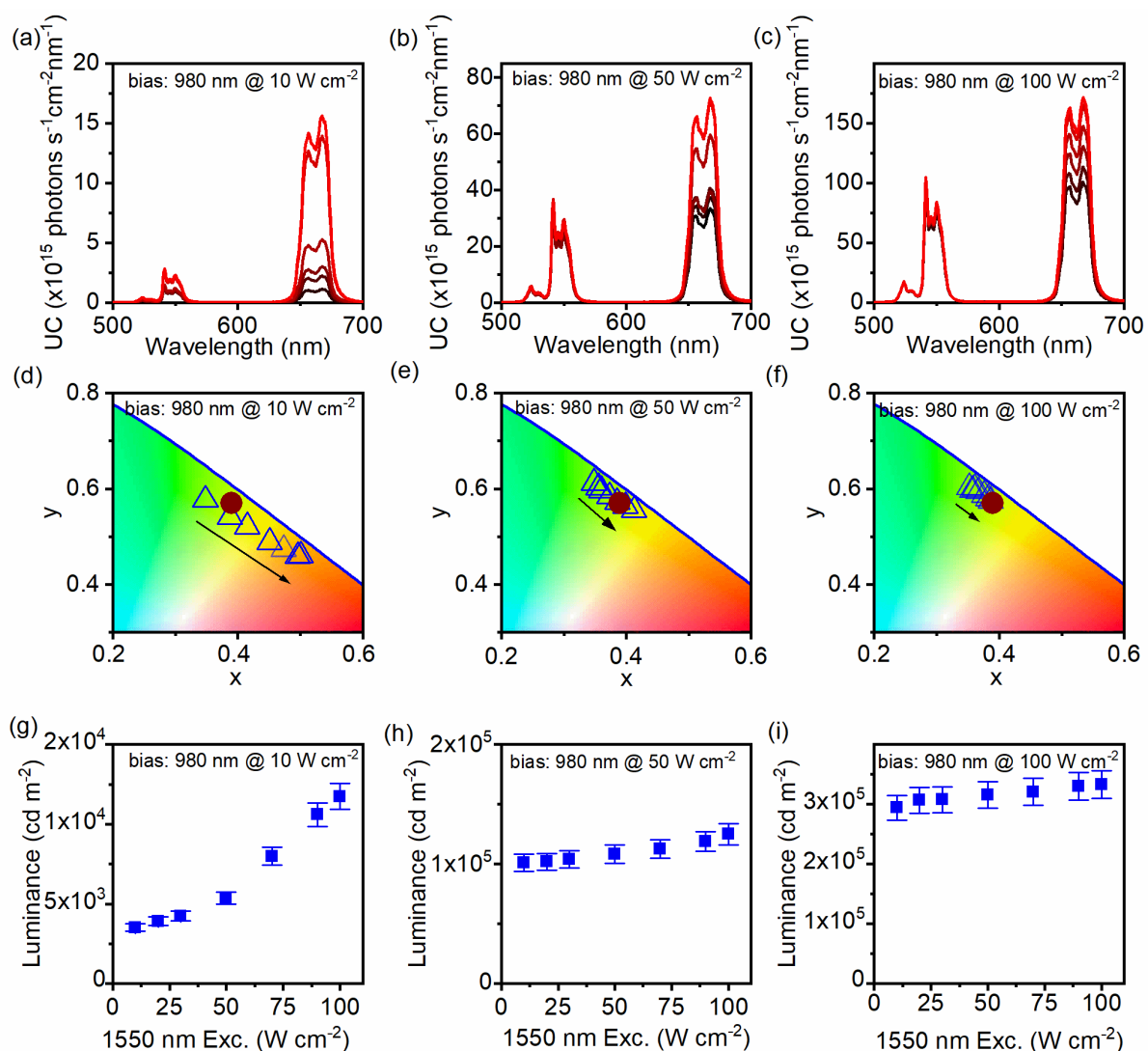


Figure 6.8. UC spectra, CIE 1931 colour coordinates and calculated luminances of $\text{SrF}_2: 18\% \text{ Yb}^{3+}, 2\% \text{ Er}^{3+}$ upon simultaneous excitation with 980 nm and 1550 nm. (a)-(c) UC emission spectra with a fixed bias of 980 nm excitation as the EPD of 1550 nm radiation increases from 10 W cm^{-2} to 100 W cm^{-2} . (d)-(f) Corresponding CIE coordinates on magnified section of the CIE diagram. The arrow gives direction of increasing EPD of 1550 nm radiation. The brown circles show the CIE coordinate (0.39, 0.57) which is accessible in all three cases. (g)-(i) Calculated luminances from the absolute calibration of the UC spectra. Reproduced with permission from Joseph et al. [125].

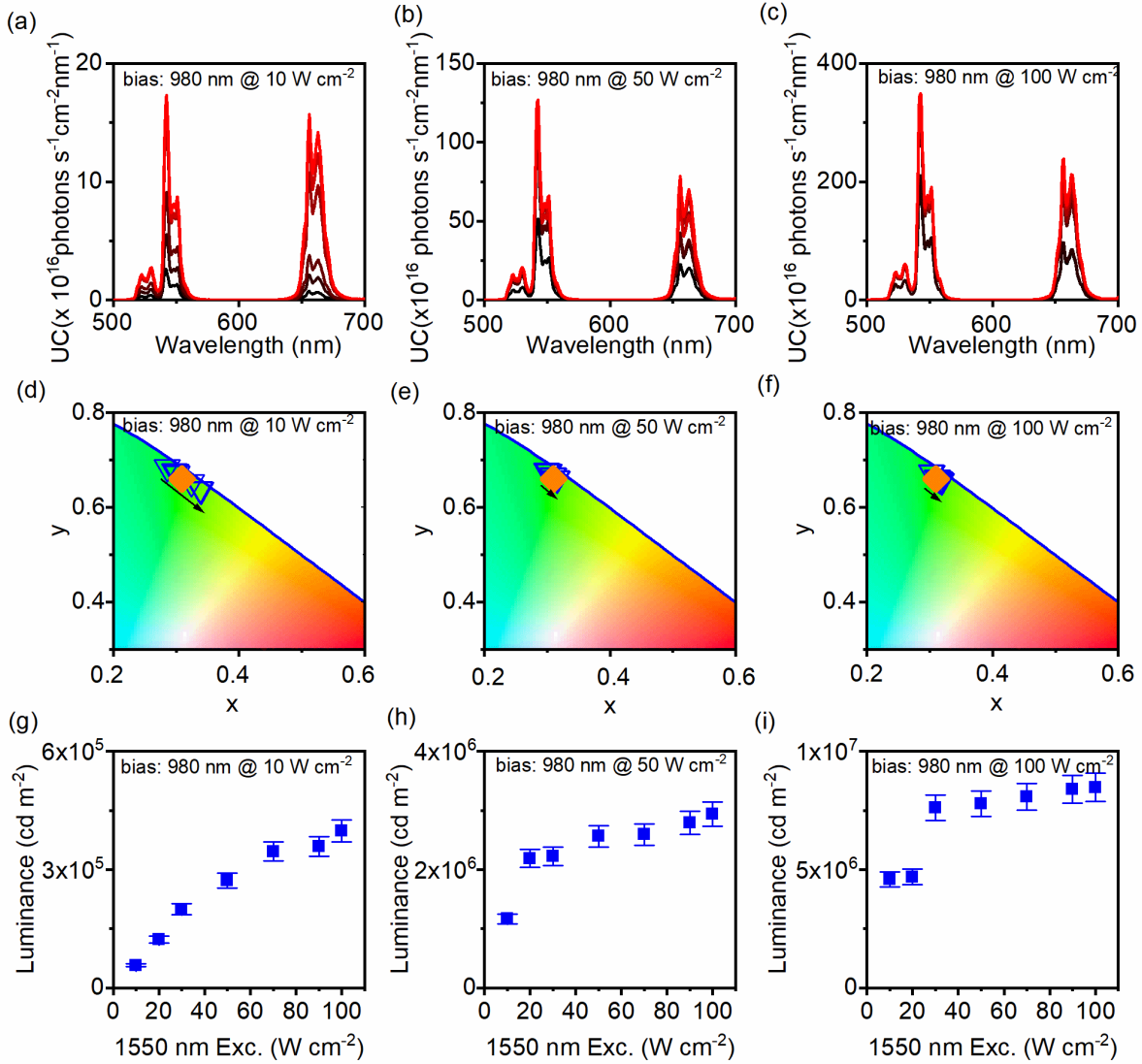


Figure 6.9. UC spectra, CIE 1931 colour coordinates and calculated luminances of β -NaYF₄: 18% Yb³⁺, 2% Er³⁺ upon simultaneous excitation with 980 nm and 1550 nm. (a)-(c) UC emission spectra with a fixed bias of 980 nm excitation as the EPD of 1550 nm radiation increases from 10 $W cm^{-2}$ to 100 $W cm^{-2}$. (d)-(f) Corresponding CIE coordinates on magnified section of the CIE diagram. The arrow gives direction of increasing EPD of 1550 nm radiation. The brown circles show the CIE coordinate (0.31, 0.66) which is accessible in all three cases. (g)-(i) Calculated luminances from the absolute calibration of the UC spectra. Reproduced from Joseph et al. [125].

Figures 6.8(g)-(i) and 6.9(g)-(i) give plots of the calculated luminance as the EPD of the 1550 nm radiation is increased. The luminance at 100 $W cm^{-2}$ of 1550 nm excitation (12×10^3 $cd m^{-2}$) is thrice that of the luminance at 10 $W cm^{-2}$ of 1550 nm excitation (3.5×10^3 $cd m^{-2}$) in the case of a 980 nm bias of 10 $W cm^{-2}$ in SrF₂: 18% Yb³⁺, 2% Er³⁺. At the same time in the more efficient β -NaYF₄: 18% Yb³⁺, 2% Er³⁺, the increase in luminance is 7 times for the same excitation conditions (5.7×10^4 to 40×10^4 $cd m^{-2}$). The luminance is much higher in β -NaYF₄: 18% Yb³⁺, 2% Er³⁺, owing to its higher PLQY and due to the increased contribution of the green emissions in the total UC emission, green being at the peak value of the photopic luminosity function [187].

These measured values of the luminances can be compared with theoretically calculated ones using equation 2.20. Here $\eta_{abs} \sim 0.5$, as the fraction of absorbed photons is high considering the powder nature of our sample, $\eta_{PLQY} \sim 0.001$, considering the lower value of PLQY at such low EPDs, and $\eta_{ff} = 1$, as the excitation laser is not scanned in this case. Considering the R/G ratios from the experimental data, the theoretical luminance is calculated to be $2.8 \times 10^3 \text{ cd m}^{-2}$ under 10 W cm^{-2} of each 980 nm and 1550 nm excitations in SrF₂: 18% Yb³⁺, 2% Er³⁺. The details of the calculations are provided in Section A.4 of the Appendix. This theoretically calculated value agrees well with the experimentally determined value of $3.5 \times 10^3 \text{ cd m}^{-2}$. The experimentally determined value is slightly more than the theoretical value as the synergistic effect due to dual excitation is not accounted in the equation.

Keeping the 1550 nm EPD constant at 10 W cm^{-2} , when the bias of the 980 nm excitation is increased to 50 and 100 W cm^{-2} in SrF₂: 18% Yb³⁺, 2% Er³⁺, the luminances increase dramatically by an order of magnitude to $10 \times 10^4 \text{ cd m}^{-2}$ and $30 \times 10^4 \text{ cd m}^{-2}$, respectively. These values also agree well with theoretically obtained luminances using Equation 2.20, assuming an $\eta_{PLQY} \sim 0.01$ ($93 \times 10^3 \text{ cd m}^{-2}$ for 50 W cm^{-2} and $20 \times 10^4 \text{ cd m}^{-2}$ for 100 W cm^{-2} of 980 nm excitation). β -NaYF₄: 18% Yb³⁺, 2% Er³⁺ in comparison, has much a brighter UC intensity and experimentally determined luminance of $4.5 \times 10^6 \text{ cd m}^{-2}$ for 100 W cm^{-2} of 980 nm and 10 W cm^{-2} of 1550 nm radiation which is in well agreement with the theoretically predicted luminance of $3.4 \times 10^6 \text{ cd m}^{-2}$. As previously described, the theoretical values provide a slight underestimate as the synergetic effects of simultaneous excitation are not taken account of. The details of these calculations are also provided in Section A.4 of the Appendix. In addition, an estimation of the errors is provided in Section A.5 of the Appendix.

6.3. Limitations of Dynamic UC displays in a Transparent Medium

In these laboratory experiments with a stationary laser beam, the luminances are exceptionally bright, but when doped in a transparent thin film with laser scanning, the values of η_{abs} and η_{ff} will be much lower, and the η_{PLQY} will also be reduced due to reduction in pulse-width [49]. In an index-matched transparent polymer host, the value of η_{abs} would become an order of magnitude lower and η_{ff} would become three orders of magnitude lower after scanning and the value of η_{PLQY} would also be an order of magnitude lower. Then the observed luminance would be decreased by five orders of magnitude when implemented in a thin film display with a scanned excitation beam. Looking at the luminance values in Figure 6.8 and 6.9, the suitable candidates are then only 50 W cm^{-2} and 100 W cm^{-2} biases of 980 nm radiation in β -NaYF₄: 18% Yb³⁺, 2% Er³⁺, as the resulting luminances are comparable with 100 cd m^{-2} as required for a display under room-light.

The colour tuning possibility for these configurations are pretty limited as shown in Figure 6.8.(e)-(f). But the exceptional brightness paves the way for tuneable monochrome displays (greyscale display). Then the colour can be maintained constant, but the intensity can be tuned to show greyscale images. But this option cannot be implemented with mono-excitation as the R/G ratio changes a lot when the EPD of 980 nm radiation is decreased (Figure 6.2 and Figure 6.3.). A solution to this problem is to use dual-excitation. By simultaneously manipulating the EPDs of both 980 nm and 1550 nm radiations, the colour can be kept constant and the luminance can be tuned. The point in the CIE diagram (0.39, 0.57) in the host SrF₂ and the point (0.31, 0.66) in the host β -NaYF₄, corresponding to the colour obtained at 100 W cm⁻² each of 1550 nm and 980 nm excitations, are also accessible with other biases of 980 nm excitation. These points are marked with a brown circle and orange diamond in Figure 6.7(d)-(f) and Figure 6.8(e)-(f), respectively. These colour coordinates offer the interesting option of maintaining the colour constant and changing the luminance over two orders of magnitude.

6.4. Colour Tuning in the Dark

For a display to be viewed by the human eye in the dark, even a luminance of 1 cd m⁻² is sufficient. This means that even though the wide colour tuning possibility in the host SrF₂ cannot be used for scanned displays in room-light, the material can be used in a relatively dark environment for a UC display. Alternating the display colours between green, yellow and red is possible by using 980 nm excitation alone, 980 nm excitation in combination with 1550 nm and 1550 nm excitation alone, respectively, as shown in Figure 6.10(a)-(c). The figures are still-frames captured from a video demonstrating the colour change shot with a smartphone (P20 Lite, Huawei) with automatic gain control. The green emission in Figure 6.10(a) has a luminance of 3×10^3 cd m⁻² resulting from 10 W cm⁻² of 980 nm excitation, whereas the red emission in Figure 6.10(c) has a luminance of 1×10^3 cd m⁻² resulting from 70 W cm⁻² of 1550 nm excitation. The yellow colour in Figure 6.10(b) has a luminance of 6×10^3 cd m⁻² resulting from simultaneous excitation with 10 W cm⁻² of 980 nm excitation and 70 W cm⁻² of 1550 nm excitation. In a scanned display, these luminesces would be reduced to 10, 30 and 60 mcd cm⁻², which have the same luminances of commercial glow-in-the-dark phosphors [188]. In such a dark environment the vision of the eye changes to the mesopic range as opposed to photopic range used for calculations in the previous Sections [189]. Nevertheless, the SrF₂ host offers the possibility of a colour tuneable display in the dark.

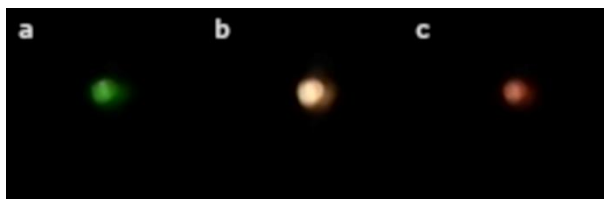


Figure 6.10. Green, yellow and red UC emission in $\text{SrF}_2: 18\% \text{Yb}^{3+}, 2\% \text{Er}^{3+}$ in a dark environment. Photographs of UC emission upon (a) mono-excitation with 980 nm at 10 W cm^{-2} , (b) dual-excitation with 980 nm at 10 W cm^{-2} and 1550 nm at 70 W cm^{-2} , and (c) mono-excitation with 1550 nm at 70 W cm^{-2} . Reproduced from Joseph et al. [125]

6.5. Monochrome UC Display

Photographs of the two samples of in $\beta\text{-NaYF}_4: 18\% \text{Yb}^{3+}, 2\% \text{Er}^{3+}$ and $\text{SrF}_2: 18\% \text{Yb}^{3+}, 2\% \text{Er}^{3+}$ are provided in Fig 6.11 and Figure 6.12, respectively. These samples were excited with 100 W cm^{-2} each of 980 nm and 1550 nm. The photographs were captured with the focus of the smartphone-camera (P20Lite, Huawei) fixed on a white sheet of paper kept behind the sample, to give an idea of the luminance. Note that the emission spots are saturated in these photographs true to the impression one gets, on observation with the naked eye. These UC emissions in these photographs correspond to the CIE colour coordinates (0.31, 0.66) in $\beta\text{-NaYF}_4: 18\% \text{Yb}^{3+}, 2\% \text{Er}^{3+}$, and (0.39, 0.57) in $\text{SrF}_2: 18\% \text{Yb}^{3+}, 2\% \text{Er}^{3+}$ which are accessible across two orders of magnitude of luminance using simultaneous excitation with 980 nm and 1550 nm as noted in Section 6.3.

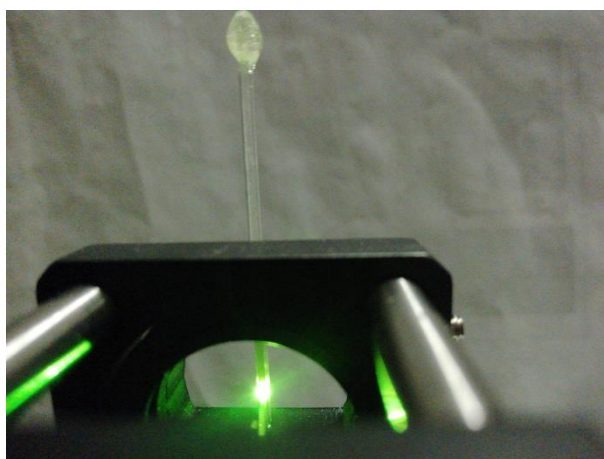


Figure 6.11. Photo of $\text{NaYF}_4: 18\% \text{Yb}^{3+}, 2\% \text{Er}^{3+}$ upon excitation with 100 W cm^{-2} each of 980 nm and 1550 nm radiation having the CIE coordinates (0.31, 0.66) (the image observed with naked eye looks similar). Reproduced from Joseph et al. [125].

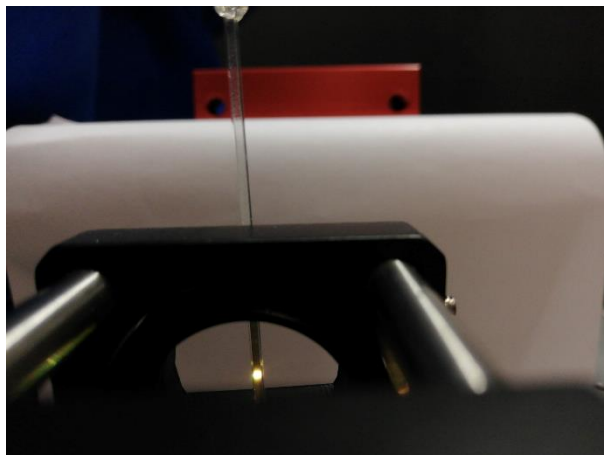


Figure 6.12. Photo of SrF₂: 18% Yb³⁺, 2% Er³⁺ upon excitation with 100 W cm⁻² each of 980 nm and 1550 nm radiation having the CIE coordinates (0.39, 0.57) (the image observed with naked eye looks similar). Reproduced from Joseph et al. [125].

To determine the EPDs of 980 nm excitation and 1550 nm excitation required for constant-colour luminance tuning, sweeps of the 1550 nm excitation were performed for different biases of 980 nm radiation, the CIE colour coordinates for each of these emissions were calculated and the combination that produced the CIE coordinates closest to the coordinates (0.31, 0.66) in β -NaYF₄: 18% Yb³⁺, 2% Er³⁺, and (0.39, 0.57) in SrF₂: 18% Yb³⁺, 2% Er³⁺ were noted along with the corresponding luminances. Using this data, graphs of the luminances based on the EPDs of 980 nm and 1550 nm excitation are plotted for SrF₂: 18% Yb³⁺, 2% Er³⁺ in Figure 6.13(a) and for β -NaYF₄: 18% Yb³⁺, 2% Er³⁺ in Figure 6.13(b). Though the EPDs of 980 nm and 1550 nm were varied to obtain the luminances, the graphs are plotted with luminance on the x-axis, in order to obtain functions of the 980 nm and 1550 nm EPDs with the luminance as the independent variable. These functions can then be used to figure out the EPDs required for a particular luminance, which would enable greyscale imaging. The EPDs of 980 nm excitation and 1550 nm excitation in Figure 6.13 can be fitted with a second order polynomial of the form $P = aL^2 + bL + c$, in the range 10 W cm⁻² to 100 W cm⁻². The best fit parameters ($r^2 > 0.99$) a, b, and c in SrF₂: 18% Yb³⁺, 2% Er³⁺ are: -5×10^{-10} , 4×10^{-4} and 10 for 980 nm excitation, and -1×10^{-9} , 5×10^{-4} and 20 for 1550 nm excitation. In β -NaYF₄: 18% Yb³⁺, 2% Er³⁺, the best fit parameters ($r^2 > 0.99$) a, b, and c: -6×10^{-13} , 1×10^{-5} , and 5 for 980 nm excitation and -1×10^{-12} , 1×10^{-5} , and 65 for 1550 nm excitation. Using these equations, we can calculate the combination of EPDs required for 980 nm and 1550 nm to obtain monochrome UC emission with luminances ranging from 3.9×10^3 cd m⁻² to 3.3×10^5 cd m⁻² for SrF₂: 18% Yb³⁺, 2% Er³⁺ and 3.4×10^5 cd m⁻² to 8.5×10^6 cd m⁻² for β -NaYF₄: 18% Yb³⁺, 2% Er³⁺.

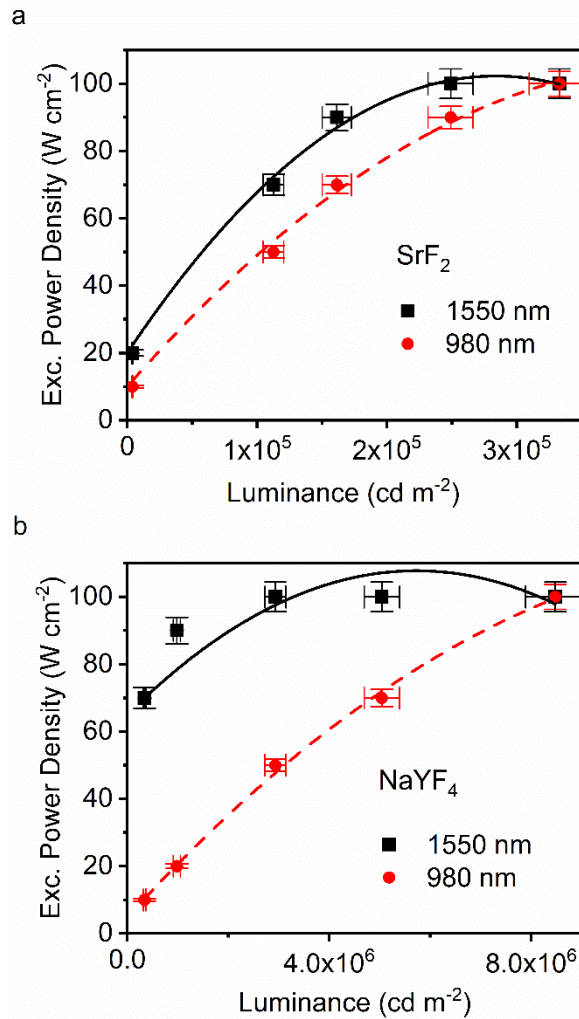


Figure 6.13. Monochrome tuning of UC upon simultaneous excitation with 980 nm and 1550 nm excitation in SrF₂: 18% Yb³⁺, 2% Er³⁺ and β-NaYF₄: 18% Yb³⁺, 2% Er³⁺ (a) EPD of 980 nm radiation and 1550 nm radiation vs luminance of UC emission at CIE coordinates (0.39, 0.57) for SrF₂: 18% Yb³⁺, 2% Er³⁺ (b) EPD of 980 nm radiation and 1550 nm radiation vs luminance of UC emission at CIE coordinates (0.31, 0.66) for β-NaYF₄: 18% Yb³⁺, 2% Er³⁺. Reproduced from Joseph et al. [125].

The photos of the intensity controlled monochrome UC emission are provided in Figure 6.14 (a)-(c) and (g)-(i). The yellowish spots correspond to emission from the host SrF₂ and the greenish spots correspond to the emission from the host β-NaYF₄. The photographs were captured with the room-lights, but through a neutral density filter of optical density 3 to simulate the loss in the intensity due to scanning. The camera was set to an ISO of 1600 for the host SrF₂ and an ISO of 100 for the host β-NaYF₄ and exposure time of 1/30 s, and the white-balance was set to fluorescent. The background appears dark due to the neutral density filter. The luminance varies between each of the images, but the colour remains constant. The greyscale images provided underneath each of the images are provided for easy understanding of the changes in the luminance Figure 6.14 (d)-(f) and (j)-(l). These photographs demonstrate that using dual-excitation, the UC emission colour can be kept constant and luminance can be tuned such that a monochrome display can be realized. The

UC material- β -NaYF₄: 18% Yb³⁺, 2% Er³⁺ is more suitable for this application owing to its high luminance.

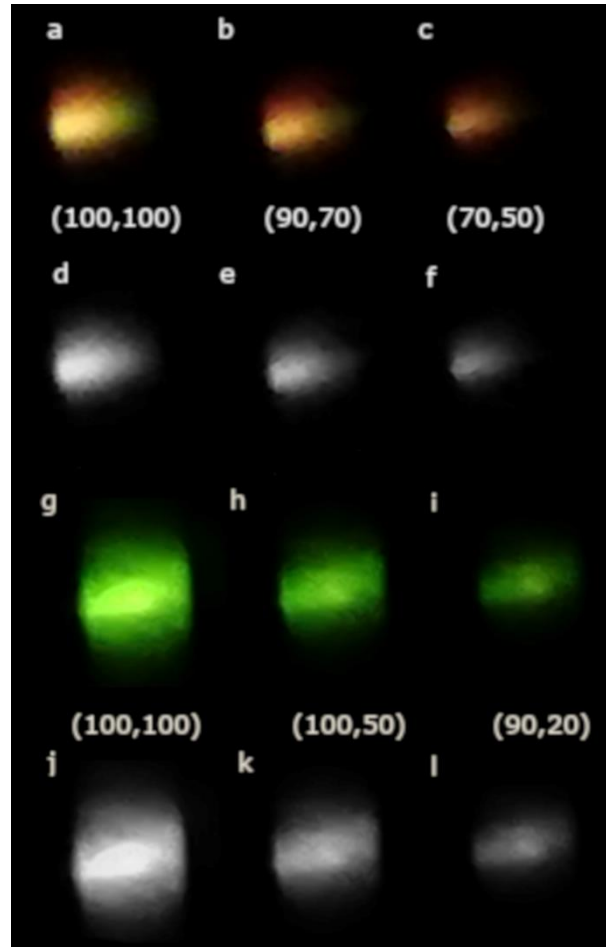


Figure 6.14. Photographs of monochrome UC emission on simultaneous excitation with 980 nm and 1550 nm at different EPDs. CIE coordinates (0.39, 0.57) are maintained in SrF₂: 18% Yb³⁺, 2% Er³⁺ for the luminances - (a) 3.3×10^5 cd m⁻², (b) 1.6×10^5 cd m⁻², and (c) 1.1×10^5 cd m⁻². The EPDs of 1550 nm and 980 nm excitation in W cm⁻² are written below the pictures. (d)-(f) shows the greyscale images of the photographs above them. CIE coordinates (0.31, 0.66) are maintained in β -NaYF₄: 18% Yb³⁺, 2% Er³⁺ for the luminances - (g) 8.5×10^6 cd m⁻², (h) 2.9×10^6 cd m⁻², and (i) 1×10^6 cd m⁻². (j)-(l) shows the greyscale images of the same pictures. Reproduced from Joseph et al. [125].

6.6. Summary

The results presented in this chapter propose two new possibilities for UC displays. The first one is a UC display whose colour could be alternated from red to yellow to green in a dark environment based on the material SrF₂: 18% Yb³⁺, 2% Er³⁺. The second one is a monochrome raster display which could be used for reproducing greyscale images. Monochrome UC display based on β -NaYF₄: 18% Yb³⁺, 2% Er³⁺ is especially interesting as it fulfils the requirements needed for an indoor display as explained in Section 2.2.1. Note that in the dual-excitation experiments, a tuneable CW laser (M squared, SolsTiS) is used as the 980 nm source, instead of a laser diode to be able to span a large range of EPDs. The EPDs

used in the experiments described in this chapter on the other hand, did not require higher EPDs and are well within the power requirements of a general-purpose laser diode. The conclusion is that using low-cost laser diodes and galvanometer scanners, dual-excitation based monochrome UC displays with ETU mechanism can be easily built, and they are up to par with the requirements for such an indoor display. This display could either be a 2D display or a 3D volumetric display depending on the configuration of the projection medium. The strategy of using dual-excitation helps to maintain the colour constant as the intensity of the emission is varied.

7. Conclusion

This thesis provides an insight into the photophysics of inorganic upconversion observed in lanthanides doped in various crystal lattices. The Er^{3+} - Yb^{3+} system is extensively studied, and the underlying mechanisms behind each emission peak are investigated. The following sections provide a brief summary of the results presented in this thesis.

7.1. Effects of Laser-induced Heating in UC Measurements

Laser-induced heating is an often overlooked problem in UC measurements, particularly in the measurement of the EPD dependence of UC and the measurement of the PLQY. In most of the host materials, laser-induced heating causes an underestimation of the UC intensity and thereby the PLQY. The evidence for the presence of such an underestimation is found when the slope of the double-logarithmic plot of the EPD dependence of UC in the limit of high EPDs become sub-unity, in disagreement with theoretical models depicting the same. The temperature rise due to laser-induced heating is estimated by making use of the thermally coupled $^2\text{H}_{11/2}$ and $^4\text{S}_{3/2}$ states of Er^{3+} and was observed to be about 60 K for a microcrystalline sample of β - NaYF_4 : 18% Yb^{3+} , 2% Er^{3+} at an EPD of 240 W cm^{-2} . The temperature rises instantaneously as the excitation laser is incident on the sample and then reaches a steady-state value. The UC intensity on the other hand, decreases due to this effect and reaches a steady-state value. In the case of nanocrystal samples of the same material, β - NaYF_4 : 18% Yb^{3+} , 2% Er^{3+} , no laser-induced heating was observed owing to their better thermal transport. The effect of laser-induced heating becomes prominent in microcrystals of NaYF_4 : 18% Yb^{3+} , 2% Er^{3+} starting from EPDs of 50 W cm^{-2} . By measuring the initial UC intensity and the steady-state UC intensity at a couple of EPDs, the correction factors for calculating the EPD dependence curve of the UC emission can be calculated, which can then be interpolated to correct the entire EPD dependence curve. This method to correct the EPD dependence of UC and the knowledge of the extent of laser-induced heating that can be present in a material is particularly important to identify the suitability of UC materials for different applications, and to compare between different UC materials. In addition, to extract proper figures-of-merit for UC materials, having the corrected EPD dependence curve is of prime importance. The corrected curves then agree with the theoretical models defined for UC and allow extraction of valuable parameters.

7.2. Figures-of-Merit for UC Materials

Comparison between different UC materials are challenging because of a lack of agreement in the scientific community about specific figures-of-merits. A combination of two figures-of-merit is proposed in this work, namely the CPD and the $PLQY_{sat}$, which when defined together give comprehensive information about the UC material and its efficiency. An analytical model called the critical power density model is derived to describe the two-photon ETU. By fitting the equation of the model to the corrected EPD dependence, the defining parameter - CPD, can be extracted. The CPD represents the EPD at which UC starts to become efficient, thus a material with a lower value of CPD will be a better two-photon upconverter. It is also of importance in identifying materials which exhibit UC in the range of low EPDs. The CPD is an interesting parameter which gives information about the intermediate-state lifetimes and the mechanisms behind the emission peaks. A material with longer intermediate-state lifetimes will have a lower value of CPD and so will be a better upconverter at a lower EPD. Also, UC emissions which originate in the same excited states will have the same value of CPD, as in the case of the green (510-560 nm) and NIR (820-860 nm) emissions from Er^{3+} . The CPD model gives two alternate methods for determining the $PLQY_{sat}$, without having to drive the system to saturation using extreme EPDs. These techniques are important because, the undesirable effects at high EPDs like laser-induced heating can be avoided in the process of determining $PLQY_{sat}$. The first method involves, measuring the PLQY at an EPD equal to the CPD, and multiplying it with 5.8 to get the $PLQY_{sat}$. The second method involves, directly exciting the state whose PLQY is to be determined and by dividing the measured PLQY by 2. Using four different microcrystalline material systems, viz. β - $NaYF_4$: 18% Yb^{3+} , 2% Er^{3+} , YF_3 : 18% Yb^{3+} , 2% Er^{3+} , YCl_3 : 18% Yb^{3+} , 2% Er^{3+} , and La_2O_3 : 18% Yb^{3+} , 2% Er^{3+} , the value of the CPD and the $PLQY_{sat}$ were determined, and the $PLQY_{sat}$ values estimated with the CPD model were found to agree with the experimentally determined $PLQY_{sat}$ values. The only exception was when the emissive states had depopulation channels to higher excited states contributing to three-photon UC. The most efficient UC material out of these four different hosts (β - $NaYF_4$: 18% Yb^{3+} , 2% Er^{3+}) was found to be the one with the lowest value of CPD (0.7 W cm^{-2}).

7.3. UC Displays

First the requirements for a UC display, in terms of luminances, scanning rates, efficiencies and dwell-times are explained in Section 2.2.1. Then, two different types of UC displays are proposed in this thesis. The first one involves changing the UC emission colour in the dark by switching the excitation laser between two wavelengths - 980 nm and 1550 nm. Using the microcrystalline powder SrF_2 : 18% Yb^{3+} , 2% Er^{3+} , such a UC display can give red emission

from the ${}^4F_{9/2}$ state, as a result of a three-photon ETU due to the easy bridging between the ${}^4I_{9/2}$ and ${}^4I_{11/2}$ states of Er^{3+} in this material upon 1550 nm excitation. But when excited with 980 nm, the same material gives green UC emission from its ${}^2H_{11/0}$ and ${}^4S_{3/2}$ states. When both 980 nm and 1550 nm excitation are incident on the material the resulting colour is yellow. The obtained luminance values in this case are comparable that of the commercially available glow-in-the-dark phosphors for mesopic vision applications. The second type involves a bright UC display which can be intensity modulated while keeping the emission colour constant by making use of simultaneous excitation with 980 nm and 1550 nm radiation. Combinations of different EPDs of the 980 nm and 1550 nm excitations can yield the same UC emission colour but different UC intensities. By plotting EPDs with respect to the luminance calculated according to the photopic vision of the human eye, a second order polynomial can be found out which gives the combination of EPDs of the two excitation-wavelengths for any required luminance. Using this curve, greyscale imaging can be done, and initial lab scale demonstration of such a greyscale display is made which also incorporates the loss due to raster scanning by making use of a neutral density filter of optical density 3. Microcrystal samples of $\text{SrF}_2: 18\% \text{Yb}^{3+}, 2\% \text{Er}^{3+}$ and $\beta\text{-NaYF}_4: 18\% \text{Yb}^{3+}, 2\% \text{Er}^{3+}$ are used for demonstrating such a monochrome display which could be used indoors as a 2D display panel or a volumetric 3D display. Owing to its excellent PLQY, the $\beta\text{-NaYF}_4$ host emerges as a better candidate for the monochrome display.

7.4. Future work

The formulation critical power density model is very simple, yet it is efficient in obtaining the figures-of-merit for two-photon UC. Further development to the model to include three-photon processes, would enable comparison of the total visible UC emission from a material, instead of only the two-photon emissions. The direct excitation method for determining the PLQY_{sat} did not work for the low phonon energy host YCl_3 , because the green emitting states ${}^2H_{11/2}$ and ${}^4S_{3/2}$ act as intermediate states for three-photon ETU processes, owing to their large lifetimes. Such an effect is not taken account for in the CPD model as it considers only two-photon ETU processes. Though the direct excitation method is not suitable for materials which easily exhibit three-photon UC, the CPD extracted is a true measure of the UC efficiency of the material. The CPD model can be used to classify materials for applications in biomedicine, where a particular two-photon transition is used for phototherapy or bioimaging.

The monochrome UC display could be implemented using a galvanometric scanner and a single crystal of high PLQY_{sat} , for a 3D volumetric display, which would give more points per scanned line of the excitation beam. Such a UC display would benefit from the invisible nature of the NIR beams, as any scattered light due to atmospheric particles like dust would not cause disturbances in the field of vision, and a true 3D image can be formed. In terms of the EPDs

required for normal 3D displays used indoors, the dual-excitation-based UC based displays have an added advantage as lower EPDs are sufficient [138].

Colour tuning in the dark observed in the cytotoxic SrF_2 : 18% Yb^{3+} , 2% Er^{3+} , could be used for bio-imaging for obtaining data at different depths of penetration [190]. The first biological window extends from 700-950 nm, the second from 1000-1350 nm and the third from 1550-1870 nm [41]. Therefore 1550 nm radiation would have a deeper penetration than 980 nm. Imaging the UC emission from SrF_2 : 18% Yb^{3+} , 2% Er^{3+} doped in a biological tissue would therefore give details at two different depths, in red and green colour, which when combined would increase the Z-resolution of the data.

Though work on UC started in the early 1960s, a lot of its mechanisms are not yet understood. The most efficient UC system remains still Yb^{3+} and Er^{3+} doped $\beta\text{-NaYF}_4$, though it was discovered in 1972 by Menyuk [61]. Different studies based on phonon energies, site symmetry of lanthanide ions, sensitizer-emitter distances, unit cell sizes and densities of the crystal lattice, yielded no conclusive evidence till date on what makes a better upconverter. Even the reason for the high PLQY of the $\beta\text{-NaYF}_4$ host is attributed to different properties by different groups [53,108,184]. It is high time that these mysteries are unravelled, so that UC can be used in more challenging applications such as solar energy harvesting. The CPD calculated for microcrystalline powders of $\beta\text{-NaYF}_4$: 18% Yb^{3+} , 2% Er^{3+} in this work was 0.7 W cm^{-2} , which is definitely in the right direction. Perhaps, a sensitizer for transferring the energy to the $^4\text{I}_{13/2}$ state of Er^{3+} is the answer. A little further and UC could be used effectively for solar cells based on silicon, due to the $^4\text{I}_{9/2}$ and $^4\text{I}_{11/2}$ levels which can effectively emit into the band-gap of silicon [191].

References

1. W. Kaiser and C. G. B. Garrett, "Two-Photon Excitation in $\text{CaF}_2:\text{Eu}^{2+}$," *Phys. Rev. Lett.* **7**, 229–231 (1961).
2. C. Ye, L. Zhou, X. Wang, and Z. Liang, "Photon upconversion: from two-photon absorption (TPA) to triplet-triplet annihilation (TTA)," *Phys. Chem. Chem. Phys.* **18**, 10818–10835 (2016).
3. F. Auzel, "Materials and Devices using Double-Pumped-Phosphors with Energy Transfer," *Proc. IEEE* **61**, 758–786 (1973).
4. W. Pauli, *General Principles of Quantum Mechanics* (Springer Berlin Heidelberg, 1980).
5. Michael. Kasha, "Phosphorescence and the Role of the Triplet State in the Electronic Excitation of Complex Molecules," *Chem. Rev.* **41**, 401–419 (1947).
6. D. S. McClure, "Triplet-Singlet Transitions in Organic Molecules. Lifetime Measurements of the Triplet State," *J. Chem. Phys.* **17**, 905–913 (1949).
7. T. N. Singh-Rachford and F. N. Castellano, "Triplet Sensitized Red-to-Blue Photon Upconversion," *J. Phys. Chem. Lett.* **1**, 195–200 (2010).
8. T. N. Singh-Rachford and F. N. Castellano, "Photon upconversion based on sensitized triplet–triplet annihilation," *Coord. Chem. Rev.* **254**, 2560–2573 (2010).
9. M. Wu, D. N. Congreve, M. W. B. Wilson, J. Jean, N. Geva, M. Welborn, T. Van Voorhis, V. Bulović, M. G. Bawendi, and M. A. Baldo, "Solid-state infrared-to-visible upconversion sensitized by colloidal nanocrystals," *Nat. Photon.* **10**, 31–34 (2016).
10. K. Mase, K. Okumura, N. Yanai, and N. Kimizuka, "Triplet sensitization by perovskite nanocrystals for photon upconversion," *Chem. Commun.* **53**, 8261–8264 (2017).
11. N. Yanai and N. Kimizuka, "Recent emergence of photon upconversion based on triplet energy migration in molecular assemblies," *Chem. Commun.* **52**, 5354–5370 (2016).
12. Y. Sasaki, S. Amemori, H. Kouno, N. Yanai, and N. Kimizuka, "Near infrared-to-blue photon upconversion by exploiting direct S-T absorption of a molecular sensitizer," *J. Mater. Chem. C* **5**, 5063–5067 (2017).
13. N. Bloembergen, "Solid State Infrared Quantum Counters," *Phys. Rev. Lett.* **2**, 84–85 (January 2).
14. F. Auzel, "Quantum Counter Obtained by using Energy Transfer between Two Rare Earth Ions in a Mixed Tungstate and in a Glass," *C.R. Acad. Sci.* **263**, 819 (1966).
15. V. V. Ovsyankin and P. P. Feofilov, "Mechanism of summation of electronic excitations in activated crystals," *JETPL* **3**, 322 (1966).
16. K. Zheng, W. Qin, C. Cao, D. Zhao, and L. Wang, "NIR to VUV: Seven-Photon Upconversion Emissions from Gd^{3+} Ions in Fluoride Nanocrystals," *J. Phys. Chem. Lett.* **6**, 556–560 (2015).
17. G. H. Dieke and H. M. Crosswhite, "The Spectra of the Doubly and Triply Ionized Rare Earths," *Appl. Opt.* **2**, 675–686 (1963).
18. G. H. Dieke, "Spectra and Energy Levels of Rare Earth Ions in Crystals," *Am. J. Phys.* **38**, 399–400 (1970).
19. S. Wen, J. Zhou, P. J. Schuck, Y. D. Suh, T. W. Schmidt, and D. Jin, "Future and challenges for hybrid upconversion nanosystems," *Nat. Photon.* **13**, 828–838 (2019).
20. X. Wu, H. Lee, O. Bilsel, Y. Zhang, Z. Li, T. Chen, Y. Liu, C. Duan, J. Shen, A. Punjabi, and G. Han, "Tailoring dye-sensitized upconversion nanoparticle excitation bands towards excitation wavelength selective imaging," *Nanoscale* **7**, 18424–18428 (2015).

21. M. Safdar, A. Ghazy, M. Lastusaari, and M. Karppinen, "Lanthanide-based inorganic–organic hybrid materials for photon-upconversion," *J. Mater. Chem. C* **8**, 6946–6965 (2020).
22. B. Joarder, A. Mallick, Y. Sasaki, M. Kinoshita, R. Haruki, Y. Kawashima, N. Yanai, and N. Kimizuka, "Near-Infrared-to-Visible Photon Upconversion by Introducing an S–T Absorption Sensitizer into a Metal–Organic Framework," *ChemNanoMat* **6**, 916–919 (2020).
23. S. M. Kirkpatrick, L. B. Shaw, S. R. Bowman, S. Searles, B. J. Feldman, and J. Ganem, "Mid-Infrared Spectroscopy of Erbium Doped Chloride Laser Crystals," *Opt. Express* **1**, 78–86 (1997).
24. S. Fischer, A. Ivaturi, P. Jakob, K. W. Krämer, R. Martin-Rodriguez, A. Meijerink, B. S. Richards, and J. C. Goldschmidt, "Upconversion solar cell measurements under real sunlight," *Opt. Mater.* **84**, 389–395 (2018).
25. Y. Zhang and X. Liu, "Shining a light on upconversion," *Nat. Nanotechnol.* **8**, 702–703 (2013).
26. J. M. Meruga, W. M. Cross, P. Stanley May, Q. Luu, G. A. Crawford, and J. J. Kellar, "Security printing of covert quick response codes using upconverting nanoparticle inks," *Nanotechnology* **23**, 395201 (2012).
27. G. Gao, A. Turshatov, I. A. Howard, D. Busko, R. Joseph, D. Hudry, and B. S. Richards, "Up-Conversion Fluorescent Labels for Plastic Recycling: A Review," *Adv. Sustain. Syst.* **1**, 1600033 (2017).
28. L. Kador, "A three-color, three-dimensional, solid-state display," *Adv. Mater.* **9**, 83–85 (1997).
29. Z. Hou, K. Deng, M. Wang, Y. Liu, M. Chang, S. Huang, C. Li, Y. Wei, Z. Cheng, G. Han, A. A. Al Kheraif, and J. Lin, "Hydrogenated Titanium Oxide Decorated Upconversion Nanoparticles: Facile Laser Modified Synthesis and 808 nm Near-Infrared Light Triggered Phototherapy," *Chem. Mater.* **31**, 774–784 (2019).
30. E. Hemmer, P. Acosta-Mora, J. Mendez-Ramos, and S. Fischer, "Optical nanoprobe for biomedical applications: shining a light on upconverting and near-infrared emitting nanoparticles for imaging, thermal sensing, and photodynamic therapy," *J. Mater. Chem. B* **5**, 4365–4392 (2017).
31. D. Jaque and C. Jacinto, "Luminescent nanoprobe for thermal bio-sensing: Towards controlled photo-thermal therapies," *J. Lumin.* **169**, 394–399 (2016).
32. D. Jaque and F. Vetrone, "Luminescence nanothermometry," *Nanoscale* **4**, 4301–4326 (2012).
33. W. Lenth and R. M. Macfarlane, "Upconversion Lasers," *Opt. Photonics News* **3**, 8–15 (1992).
34. T. J. Whitley, C. A. Millar, R. Wyatt, M. C. Brierley, and D. Szebesta, "Upconversion pumped green lasing in erbium doped fluorozirconate fibre," *Electron. Lett.* **27**, 1785–1786 (1991).
35. S. G. Grubb, K. W. Bennett, R. S. Cannon, and W. F. Humer, "CW room-temperature blue upconversion fibre laser," *Electron. Lett.* **28**, 1243–1244 (1992).
36. P. Xie and T. R. Gosnell, "Room-temperature upconversion fiber laser tunable in the red, orange, green, and blue spectral regions," *Opt. Letters* **20**, 1014–1016 (1995).
37. M. Cai, B. Zhou, F. Wang, T. Wei, Y. Tian, J. Zhou, S. Xu, and J. Zhang, "R₂O₃ (R = La, Y) modified erbium activated germanate glasses for mid-infrared 2.7 μm laser materials," *Sci. Rep.* **5**, 13056 (2015).
38. M. Pollnau, R. Spring, C. Ghisler, S. Wittwer, W. Luthy, and H. P. Weber, "Efficiency of erbium 3-mm crystal and fiber lasers," *IEEE J. Quantum Electron.* **32**, 657–663 (1996).
39. A. Shalav, B. S. Richards, and M. A. Green, "Luminescent layers for enhanced silicon solar cell performance: Up-conversion," *Sol. Energy Mater. Sol. Cells* **91**, 829–842 (5).
40. J. C. Goldschmidt and S. Fischer, "Upconversion for Photovoltaics - a Review of Materials, Devices and Concepts for Performance Enhancement," *Adv. Opt. Mater.* **3**, 510–535 (2015).

41. E. Hemmer, A. Benayas, F. Légaré, and F. Vetrone, "Exploiting the biological windows: current perspectives on fluorescent bioprobes emitting above 1000 nm," *Nanoscale Horiz.* **1**, 168–184 (2016).
42. M. Nyk, R. Kumar, T. Y. Ohulchanskyy, E. J. Bergey, and P. N. Prasad, "High Contrast in Vitro and in Vivo Photoluminescence Bioimaging Using Near Infrared to Near Infrared Up-Conversion in Tm³⁺ and Yb³⁺ Doped Fluoride Nanophosphors," *Nano Letters* **8**, 3834–3838 (2008).
43. X. Li, D. Liu, Y. Wang, S. Xu, and H. Liu, "Water dispersive upconversion nanoparticles for intelligent drug delivery system," *Colloids Surf. A Physicochem. Eng. Asp.* **555**, 55–62 (2018).
44. D. Yang, P. Ma, Z. Hou, Z. Cheng, C. Li, and J. Lin, "Current advances in lanthanide ion (Ln³⁺)-based upconversion nanomaterials for drug delivery," *Chem. Soc. Rev.* **44**, 1416–1448 (2015).
45. N. M. Idris, M. K. Gnanasammandhan, J. Zhang, P. C. Ho, R. Mahendran, and Y. Zhang, "In vivo photodynamic therapy using upconversion nanoparticles as remote-controlled nanotransducers," *Nat. Med.* **18**, 1580–1585 (2012).
46. B. del Rosal, A. Pérez-Delgado, E. Carrasco, D. J. Jovanović, M. D. Dramićanin, G. Dražić, Á. J. de la Fuente, F. Sanz-Rodríguez, and D. Jaque, "Neodymium-Based Stoichiometric Ultrasmall Nanoparticles for Multifunctional Deep-Tissue Photothermal Therapy," *Adv. Opt. Mater.* **4**, 782–789 (2016).
47. J. D. Lewis, C. M. Verber, and R. B. McGhee, "A true three-dimensional display," *IEEE Trans Electron Devices* **18**, 724–732 (1971).
48. E. Downing, L. Hesselink, J. Ralston, and R. Macfarlane, "A Three-Color, Solid-State, Three-Dimensional Display," *Science* **273**, 1185–1189 (1996).
49. J.-H. Cho, M. Bass, and H. P. Jenssen, "Volumetric three-dimensional up-conversion display medium," *J Soc. Inf. Disp.* **15**, 1029–1036 (2007).
50. T. Honda, T. Doumuki, A. Akella, L. Galambos, and L. Hesselink, "One-color one-beam pumping of Er³⁺-doped ZBLAN glasses for a three-dimensional two-step excitation display," *Opt. Lett., OL* **23**, 1108–1110 (1998).
51. X. Liu, G. Dong, Y. Qiao, and J. Qiu, "Transparent colloid containing upconverting nanocrystals: an alternative medium for three-dimensional volumetric display," *Appl. Opt.* **47**, 6416–6421 (2008).
52. H. Zhong, Z. Wang, W. Lu, J. Liu, and Y. Wang, "Luminescent Materials for 3D Display Technology," in *Phosphors, Up Conversion Nano Particles, Quantum Dots and Their Applications: Volume 2*, R.-S. Liu, ed. (Springer, 2016), pp. 503–523.
53. J. F. Suyver, J. Grimm, K. W. Krämer, and H. U. Güdel, "Highly efficient near-infrared to visible up-conversion process in NaYF₄:Er³⁺, Yb³⁺," *J. Lumin.* **114**, 53–59 (2005).
54. K. W. Krämer, D. Biner, G. Frei, H. U. Güdel, M. P. Hehlen, and S. R. Lüthi, "Hexagonal Sodium Yttrium Fluoride based Green and Blue Emitting Upconversion Phosphor," *Chem. Mater.* **16**, 1244–1251 (2004).
55. J. A. Capobianco and R. Naccache, "Foreword," in *Upconverting Nanomaterials: Perspectives, Synthesis, and Applications*, C. Altavilla, ed. (CRC Press, 2016).
56. D. Hudry, I. A. Howard, R. Popescu, D. Gerthsen, and B. S. Richards, "Structure–Property Relationships in Lanthanide-Doped Upconverting Nanocrystals: Recent Advances in Understanding Core–Shell Structures," *Adv. Mater.* **31**, 1900623 (2019).
57. F. Auzel, "Multiphonon-assisted anti-Stokes and Stokes fluorescence of triply ionized rare-earth ions," *Phys. Rev. B* **13**, 2809–2817 (1976).
58. H. Wu, Z. Hao, L. Zhang, X. Zhang, Y. Xiao, G.-H. Pan, H. Wu, Y. Luo, H. Zhao, and J. Zhang, "Phonon Energy Dependent Energy Transfer Upconversion for the Red Emission in the Er³⁺/Yb³⁺ System," *J. Phys. Chem. C* **122**, 9611–9618 (2018).
59. M. Kaiser, C. Wurth, M. Kraft, I. Hyppanen, T. Soukka, and U. Resch-Genger, "Power-Dependent Upconversion Quantum Yield of NaYF₄:Yb³⁺, Er³⁺ Nano- and Micrometer-Sized Particles - Measurements and Simulations," *Nanoscale* **9**, 10051–10058 (2017).
60. P. Aleksandra, W. Christian, K. Martin, W. Dominika, K. Michalina, A. Sebastian, P. Katarzyna, S. Marek, S. Wiesław, R. Ute, and B. Artur, "Shaping Luminescent

- Properties of Yb³⁺ and Ho³⁺ Co-Doped Upconverting Core–Shell β-NaYF₄ Nanoparticles by Dopant Distribution and Spacing," *Small* **13**, 1701635 (2017).
61. N. Menyuk, K. Dwight, and J. W. Pierce, "NaYF₄: Yb,Er—an efficient upconversion phosphor," *Appl. Phys. Lett.* **21**, 159–161 (1972).
 62. E. C. Ximendes, U. Rocha, C. Jacinto, K. U. Kumar, D. Bravo, F. J. Lopez, E. M. Rodriguez, J. Garcia-Sole, and D. Jaque, "Self-monitored photothermal nanoparticles based on core-shell engineering," *Nanoscale* **8**, 3057–3066 (2016).
 63. B. del Rosal, E. Ximendes, U. Rocha, and D. Jaque, "In Vivo Luminescence Nanothermometry: from Materials to Applications," *Adv. Opt. Mater.* **5**, 1600508 (2017).
 64. E. C. Ximendes, U. Rocha, K. U. Kumar, C. Jacinto, and D. Jaque, "LaF₃ core/shell nanoparticles for subcutaneous heating and thermal sensing in the second biological-window," *Appl. Phys. Lett.* **108**, 253103 (2016).
 65. J.-C. G. Bünzli and S. V. Eliseeva, "Basics of Lanthanide Photophysics," in *Lanthanide Luminescence: Photophysical, Analytical and Biological Aspects*, P. Hänninen and H. Härmä, eds., Springer Series on Fluorescence (Springer, 2011), pp. 1–45.
 66. H. N. Russell and F. A. Saunders, "New Regularities in the Spectra of the Alkaline Earths," *Astrophys. J.* **61**, 38 (1925).
 67. W. Finkelburg, "Atomic Spectra and Atomic Structure," in *Structure of Matter*, W. Finkelburg, ed. (Springer, 1964), pp. 47–147.
 68. T. J. Zielinski, E. Harvey, R. Sweeney, and D. M. Hanson, "Quantum States of Atoms and Molecules," *J. Chem. Educ.* **82**, 1880 (2005).
 69. R. Xu and Z. Dai, "Alternative mathematical technique to determine LS spectral terms," *J. Phys. B: At. Mol. Opt. Phys.* **39**, 3221–3239 (2006).
 70. D. J. Newman, "Theory of lanthanide crystal fields," *Advances in Physics* **20**, 197–256 (1971).
 71. Maschen, "LS coupling (Wikimedia Commons)," https://commons.wikimedia.org/wiki/File:LS_coupling.svg.
 72. W. T. Carnall, G. L. Goodman, K. Rajnak, and R. S. Rana, "A systematic analysis of the spectra of the lanthanides doped into single crystal LaF₃," *J. Chem. Phys.* **90**, 3443–3457 (1989).
 73. W. T. Carnall, H. Crosswhite, and H. M. Crosswhite, "Energy level structure and transition probabilities in the spectra of the trivalent lanthanides in LaF₃," (1978).
 74. P. S. Peijzel, A. Meijerink, R. T. Wegh, M. F. Reid, and G. W. Burdick, "A complete 4fn energy level diagram for all trivalent lanthanide ions," *J. Solid State Chem.* **178**, 448–453 (2005).
 75. I. N. Levine, *Quantum Chemistry* (Pearson, 2014).
 76. B. Walsh, "Judd-Ofelt Theory: Principles and Practices," in *Advances in Spectroscopy for Lasers and Sensing*, D. B. B. and F. O., eds. (Springer, 2006), pp. 403–433.
 77. M. P. Hehlen, M. G. Brik, and K. W. Krämer, "50th Anniversary of the Judd–Ofelt Theory: An Experimentalist's View of the Formalism and its Application," *J. Lumin.* **136**, 221–239 (2013).
 78. F. Auzel, "Upconversion and Anti-Stokes Processes with f and d Ions in Solids," *Chem. Rev.* **104**, 139–174 (2004).
 79. O. Laporte and W. F. Meggers, "Some Rules of Spectral Structure*," *J. Opt. Soc. Am.* **11**, 459–463 (1925).
 80. D. L. Dexter, "A Theory of Sensitized Luminescence in Solids," *J. Chem. Phys.* **21**, 836–850 (1953).
 81. J. R. Lakowicz, ed., "Introduction to Fluorescence," in *Principles of Fluorescence Spectroscopy* (Springer US, 2006), pp. 1–26.
 82. D. Song, S. Zhao, and Z. Xu, "Upconversion Luminescent Materials: Properties and Luminescence Mechanisms," in *Principles and Applications of Up-Converting Phosphor Technology*, R. Yang, ed. (Springer, 2019), pp. 1–32.
 83. S. Heer, K. Petermann, and H. U. Güdel, "Upconversion excitation of Cr³⁺ emission in YAlO₃ codoped with Cr³⁺ and Yb³⁺," *J. Lumin.* **102–103**, 144–150 (2003).

84. E. Song, X. Han, Y. Zhou, Y. Wei, X.-F. Jiang, S. Ye, B. Zhou, Z. Xia, and Q. Zhang, "Long-lived Photon Upconversion Phosphorescence in $\text{RbCaF}_3:\text{Mn}^{2+}, \text{Yb}^{3+}$ and the Dynamic Color Separation Effect," *iScience* **19**, 597–606 (2019).
85. M. Pollnau, D. R. Gamelin, S. R. Lüthi, H. U. Güdel, and M. P. Hehlen, "Power dependence of upconversion luminescence in lanthanide and transition-metal-ion systems," *Phys. Rev. B* **61**, 3337–3346 (2000).
86. C. Homann, L. Krukewitt, F. Frenzel, B. Grauel, C. Würth, U. Resch-Genger, and M. Haase, " $\text{NaYF}_4:\text{Yb}, \text{Er}/\text{NaYF}_4$ Core/Shell Nanocrystals with High Upconversion Luminescence Quantum Yield," *Angew. Chem. Int. Ed.* **57**, 8765–8769 (2018).
87. F. Auzel, "History of upconversion discovery and its evolution," *J. Lumin.* **223**, 116900 (2020).
88. F. Huang, X. Liu, Y. Ma, S. Kang, L. Hu, and D. Chen, "Origin of near to middle infrared luminescence and energy transfer process of $\text{Er}^{3+}/\text{Yb}^{3+}$ co-doped fluorotellurite glasses under different excitations," *Sci. Rep.* **5**, 8233 (2015).
89. E. Nakazawa and S. Shionoya, "Cooperative Luminescence in YbPO_4 ," *Phys. Rev. Lett.* **25**, 1710–1712 (1970).
90. G. M. Salley, R. Valiente, and H. U. Guedel, "Luminescence upconversion mechanisms in $\text{Yb}^{3+}-\text{Tb}^{3+}$ systems," *J. Lumin.* **94–95**, 305–309 (2001).
91. F. Auzel, D. Meichenin, F. Pellé, and P. Goldner, "Cooperative luminescence as a defining process for RE-ions clustering in glasses and crystals," *Opt. Mater.* **4**, 35–41 (1994).
92. P. S. May, A. Baride, M. Y. Hossan, and M. T. Berry, "Measuring the Internal Quantum Yield of Upconversion Luminescence for Ytterbium-Sensitized Upconversion Phosphors using the Ytterbium(iii) Emission as an Internal Standard," *Nanoscale* **10**, 17212–17226 (2018).
93. J. F. Suyver, J. Grimm, M. K. van Veen, D. Biner, K. W. Krämer, and H. U. Güdel, "Upconversion spectroscopy and properties of NaYF_4 doped with Er^{3+} , Tm^{3+} and/or Yb^{3+} ," *J. Lumin.* **117**, 1–12 (2006).
94. S. A. Miller, H. E. Rast, and H. H. Caspers, "Lattice Vibrations of LiYF_4 ," *J. Chem. Phys.* **52**, 4172–4175 (1970).
95. W. R. Wilmarth, G. M. Begun, S. E. Nave, and J. R. Peterson, "The Raman spectra of polycrystalline orthorhombic YF_3 , SmF_3 , HoF_3 , YbF_3 , and single crystal TbF_3 ," *J. Chem. Phys.* **89**, 711–715 (1988).
96. G. N. Papatheodorou, "Raman Spectroscopic Studies of Yttrium (III) chloride–Alkali Metal Chloride Melts and of $\text{Cs}_2\text{NaYCl}_6$ and YCl_3 Solid Compounds," *J. Chem. Phys.* **66**, 2893–2900 (1977).
97. G. Gao, D. Busko, S. Kauffmann-Weiss, A. Turshatov, I. A. Howard, and B. S. Richards, "Finely-Tuned NIR-to-Visible Up-conversion in $\text{La}_2\text{O}_3:\text{Yb}^{3+}, \text{Er}^{3+}$ Microcrystals with High Quantum Yield," *J. Mater. Chem. C* **5**, 11010–11017 (2017).
98. H. U. Güdel and M. Pollnau, "Near-infrared to visible photon upconversion processes in lanthanide doped chloride, bromide and iodide lattices," *J. Alloys Compd.* **303–304**, 307–315 (2000).
99. L. A. Riseberg and H. W. Moos, "Multiphonon Orbit-Lattice Relaxation in LaBr_3 , LaCl_3 , and LaF_3 ," *Phys. Rev. Lett.* **19**, 1423–1426 (12).
100. L. A. Riseberg and H. W. Moos, "Multiphonon Orbit-Lattice Relaxation of Excited States of Rare-Earth Ions in Crystals," *Phys. Rev.* **174**, 429–438 (October 10).
101. R. Hull, *Spectroscopic Properties of Rare Earths in Optical Materials*, Springer Series in Materials Science ; 83 (Springer Berlin Heidelberg, 2005).
102. M. J. Weber, "Chapter 35 Rare earth lasers," in *Handbook on the Physics and Chemistry of Rare Earths*, Non-Metallic Compounds - II (Elsevier, 1979), Vol. 4, pp. 275–315.
103. M. Pollnau, "The route toward a diode-pumped 1-W erbium 3- μm fiber laser," *IEEE J. Quantum Electron.* **33**, 1982–1990 (1997).
104. F. Auzel, G. Baldacchini, L. Laversenne, and G. Boulon, "Radiation trapping and self-quenching analysis in Yb^{3+} , Er^{3+} , and Ho^{3+} doped Y_2O_3 ," *Optical Materials* **24**, 103–109 (2003).

105. R. Martín-Rodríguez, F. T. Rabouw, M. Trevisani, M. Bettinelli, and A. Meijerink, "Upconversion Dynamics in Er³⁺-Doped Gd₂O₂S: Influence of Excitation Power, Er³⁺ Concentration, and Defects," *Adv. Opt. Mater.* **3**, 558–567 (2015).
106. S. Fischer, N. J. J. Johnson, J. Pichaandi, J. C. Goldschmidt, and F. C. J. M. van Veggel, "Upconverting core-shell nanocrystals with high quantum yield under low irradiance: On the role of isotropic and thick shells," *J. Appl. Phys.* **118**, 193105 (2015).
107. M. K. Mahata, T. Koppe, T. Mondal, C. Brüsewitz, K. Kumar, V. K. Rai, H. Hofsäss, and U. Vetter, "Incorporation of Zn²⁺ ions into BaTiO₃:Er³⁺/Yb³⁺ nanophosphor: an effective way to enhance upconversion, defect luminescence and temperature sensing," *Phys. Chem. Chem. Phys.* **17**, 20741–20753 (2015).
108. C. Renero-Lecuna, R. Martín-Rodríguez, R. Valiente, J. González, F. Rodríguez, K. W. Krämer, and H. U. Güdel, "Origin of the High Upconversion Green Luminescence Efficiency in β-NaYF₄:2%Er³⁺,20%Yb³⁺," *Chem. Mater.* **23**, 3442–3448 (2011).
109. D. T. Klier, "Upconversion luminescence in Er-codoped NaYF₄ nanoparticles," (2016).
110. M. W. Pin, E. J. Park, S. Choi, Y. I. Kim, C. H. Jeon, T. H. Ha, and Y. H. Kim, "Atomistic evolution during the phase transition on a metastable single NaYF₄:Yb,Er upconversion nanoparticle," *Scientific Reports* **8**, 2199 (2018).
111. D. Przybylska, A. Ekner-Grzyb, B. F. Grześkowiak, and T. Grzyb, "Upconverting SrF₂ nanoparticles doped with Yb³⁺/Ho³⁺, Yb³⁺/Er³⁺ and Yb³⁺/Tm³⁺ ions – optimisation of synthesis method, structural, spectroscopic and cytotoxicity studies," *Sci. Rep.* **9**, 1–12 (2019).
112. A. V. R. Warriar and R. S. Krishnan, "Raman spectrum of strontium fluoride (SrF₂)," *Sci. Nat.* **51**, 8–9 (1964).
113. A. M. Pak, J. A. Ermakova, S. V. Kuznetsov, A. V. Ryabova, D. V. Pominova, and V. V. Voronov, "Efficient visible range SrF₂:Yb:Er- and SrF₂:Yb:Tm-based up-conversion luminophores," *J. Fluor. Chem.* **194**, 16–22 (2017).
114. S. Kuznetsov, Y. Ermakova, V. Voronov, P. Fedorov, D. Busko, I. A. Howard, B. S. Richards, and A. Turshatov, "Up-conversion quantum yields of SrF₂:Yb³⁺,Er³⁺ sub-micron particles prepared by precipitation from aqueous solution," *J. Mater. Chem. C* **6**, 598–604 (2018).
115. International Electrotechnical Commission, *Multimedia Systems and Equipment – Colour Measurement and Management – Part 2-1: Colour Management – Default RGB Colour Space – SRGB* (1999), p. 51.
116. A. de Vries, J. L. Souman, B. de Ruyter, I. Heynderickx, and Y. A. W. de Kort, "Lighting up the office: The effect of wall luminance on room appraisal, office workers' performance, and subjective alertness," *Building and Environment* **142**, 534–543 (2018).
117. "Continental Automotive-Windshield HUD," <https://www.continental-automotive.com/en-gl/Passenger-Cars/Information-Management/Head-Up-Displays/Windshield-HUD>.
118. R. V. Karandikar, "Luminance of the Sun," *J. Opt. Soc. Am.*, *JOSA* **45**, 483–488 (1955).
119. W. E. K. Middleton and A. G. Mungall, "On the psychophysical basis of meteorological estimates of "visibility,"" *Eos, Transactions American Geophysical Union* **33**, 507–512 (1952).
120. "Units in Photometry-Natural Scene Examples," http://retina.anatomy.upenn.edu/~rob/lance/units_photometric.html.
121. L. T. Sharpe, A. Stockman, W. Jagla, and H. Jägle, "A luminous efficiency function, V*(λ), for daylight adaptation," *J. Vis.* **5**, 3–3 (2005).
122. A. Stockman, L. T. Sharpe, S. Merbs, and J. Nathans, "Spectral sensitivities of human cone visual pigments determined in vivo and in vitro," *Meth. Enzymol.* **316**, 626–650 (2000).
123. J. Bergstrand, Q. Liu, B. Huang, X. Peng, C. Würth, U. Resch-Genger, Q. Zhan, J. Widengren, H. Ågren, and H. Liu, "On the decay time of upconversion luminescence," *Nanoscale* **11**, 4959–4969 (2019).

124. R. B. Anderson, S. J. Smith, P. S. May, and M. T. Berry, "Revisiting the NIR-to-Visible Upconversion Mechanism in β -NaYF₄:Yb³⁺, Er³⁺," *J. Phys. Chem. Lett.* **5**, 36–42 (2014).
125. R. E. Joseph, D. Hudry, D. Busko, D. Biner, A. Turshatov, K. W. Krämer, B. S. Richards, and I. A. Howard, "Bright constant color upconversion based on dual 980 and 1550 nm excitation of SrF₂:Yb³⁺, Er³⁺ and β -NaYF₄:Yb³⁺, Er³⁺ micropowders; considerations for persistence of vision displays (Accepted)," *Opt. Mater.* (2020).
126. A. Nadort, J. Zhao, and E. M. Goldys, "Lanthanide upconversion luminescence at the nanoscale: fundamentals and optical properties," *Nanoscale* **8**, 13099–13130 (2016).
127. B. Chen, T. Sun, X. Qiao, X. Fan, and F. Wang, "Directional Light Emission in a Single NaYF₄ Microcrystal via Photon Upconversion," *Adv. Opt. Mater.* **3**, 1577–1581 (2015).
128. M. Yuan, R. Wang, C. Zhang, Z. Yang, X. Yang, K. Han, J. Ye, H. Wang, and X. Xu, "Revisiting the Enhanced Red Upconversion Emission from a Single β -NaYF₄:Yb/Er Microcrystal By Doping with Mn²⁺ Ions," *Nanoscale Res. Lett.* **14**, 103 (2019).
129. L. Tu, X. Liu, F. Wu, and H. Zhang, "Excitation energy migration dynamics in upconversion nanomaterials," *Chem. Soc. Rev.* **44**, 1331–1345 (2015).
130. D. Hudry, D. Busko, R. Popescu, D. Gerthsen, I. A. Howard, and B. S. Richards, "An enhanced energy migration strategy in upconverting nanocrystals: color-tuning with high quantum yield," *J. Mater. Chem. C* **7**, 7371–7377 (2019).
131. R. Deng, F. Qin, R. Chen, W. Huang, M. Hong, and X. Liu, "Temporal full-colour tuning through non-steady-state upconversion," *Nat. Nanotechnol.* **10**, 237–242 (2015).
132. M. Wu, L. Yan, T. Wang, B. Zhou, and Q. Zhang, "Controlling Red Color-Based Multicolor Upconversion through Selective Photon Blocking," *Adv. Funct. Mater.* **29**, 1804160 (2019).
133. X. Yin, H. Wang, Y. Tian, M. Xing, Y. Fu, and X. Luo, "Three primary color emissions from single multilayered nanocrystals," *Nanoscale* **10**, 9673–9678 (2018).
134. A. Baride, P. S. May, and M. T. Berry, "Cross-Relaxation from Er³⁺(²H_{11/2}, ⁴S_{3/2}) and Er³⁺(²H_{9/2}) in β -NaYF₄:Yb,Er and Implications for Modeling Upconversion Dynamics," *J. Phys. Chem. C* **124**, 2193–2201 (2020).
135. Z. Wang and A. Meijerink, "Concentration Quenching in Upconversion Nanocrystals," *J. Phys. Chem. C* **122**, 26298–26306 (2018).
136. D. Hudry, D. Busko, R. Popescu, D. Gerthsen, A. M. M. Abeykoon, C. Kübel, T. Bergfeldt, and B. S. Richards, "Direct Evidence of Significant Cation Intermixing in Upconverting Core@Shell Nanocrystals: Toward a New Crystallochemical Model," *Chem. Mater.* **29**, 9238–9246 (2017).
137. H. Wang, X. Yin, M. Xing, Y. Fu, Y. Tian, T. Pang, X. Feng, T. Jiang, and X. Luo, "Luminescence property tuning of Yb³⁺-Er³⁺ doped oxysulfide using multiple-band co-excitation," *RSC Advances* **8**, 16557–16565 (2018).
138. L. Gao, X. Shan, X. Xu, Y. Liu, B. Liu, S. Li, S. Wen, C. Ma, D. Jin, and F. Wang, "Video-rate upconversion display from optimized lanthanide ion doped upconversion nanoparticles," *Nanoscale* (2020).
139. R. E. Joseph, D. Busko, D. Hudry, G. Gao, D. Biner, K. Krämer, A. Turshatov, B. S. Richards, and I. A. Howard, "A Method for Correcting the Excitation Power Density Dependence of Upconversion Emission due to Laser-Induced Heating," *Opt. Mater.* **82**, 65–70 (2018).
140. G. Meyer, "The Ammonium Ion for Inorganic Synthesis," in *Advances in the Synthesis and Reactivity of Solids*, T. E. Mallouk, ed. (JAI Press, 1994), Vol. 2, pp. 1–26.
141. S. K. W. MacDougall, A. Ivaturi, J. Marques-Hueso, and B. S. Richards, "Measurement procedure for absolute broadband infrared up-conversion photoluminescent quantum yields: Correcting for absorption/re-emission," *Rev. Sci. Instrum.* **85**, 063109 (2014).
142. R. Bitter, T. Mohiuddin, and M. Nawrocki, *LabVIEW: Advanced Programming Techniques* (CRC Press, 2006).

143. P. S. May and M. Berry, "Tutorial on the acquisition, analysis, and interpretation of upconversion luminescence data," *Methods Appl. Fluoresc.* **7**, 023001 (2019).
144. R. E. Joseph, C. Jimenez, D. Hudry, G. Gao, D. Busko, D. Biner, A. Turshatov, K. Krämer, B. S. Richards, and I. A. Howard, "Critical Power Density: A Metric To Compare the Excitation Power Density Dependence of Photon Upconversion in Different Inorganic Host Materials," *J. Phys. Chem. A* **123**, 6799–6811 (2019).
145. J. C. de Mello, H. F. Wittmann, and R. H. Friend, "An Improved Experimental Determination of External Photoluminescence Quantum Efficiency," *Adv. Mater.* **9**, 230–232 (1997).
146. D. O. Faulkner, J. J. McDowell, A. J. Price, D. D. Perovic, N. P. Kherani, and G. A. Ozin, "Measurement of Absolute Photoluminescence Quantum Yields using Integrating Spheres – Which Way to Go?," *Laser Photonics Rev.* **6**, 802–806 (2012).
147. C. Würth, M. Grabolle, J. Pauli, M. Spieles, and U. Resch-Genger, "Relative and absolute determination of fluorescence quantum yields of transparent samples," *Nat. Protoc.* **8**, 1535–1550 (2013).
148. "Tech Guide: Integrating Sphere Theory and Applications - Labsphere | Internationally Recognized Photonics Company," <https://www.labsphere.com/support/system-product-brochures/tech-guide-a-guide-to-integrating-sphere-theory-and-applications/>.
149. J. R. Lakowicz, ed., "Time-Domain Lifetime Measurements," in *Principles of Fluorescence Spectroscopy* (Springer US, 2006), pp. 97–155.
150. "TimeHarp 260 | PicoQuant," <https://www.picoquant.com/products/category/tcspc-and-time-tagging-modules/timeharp-260-tcspc-and-mcs-board-with-pcie-interface#custom1>.
151. G. R. Harrison, R. C. Lord, J. R. Loofbourow, and J. B. Loofbourow, "Spectroscopy as a Scientific Tool," in *Practical Spectroscopy* (Prentice-Hall, 1948), pp. 1–26.
152. N. Katumo, G. Gao, F. Laufer, B. S. Richards, and I. A. Howard, "Smartphone-Based Luminescent Thermometry via Temperature-Sensitive Delayed Fluorescence from $\text{Gd}_2\text{O}_2\text{S}:\text{Eu}^{3+}$," *Adv. Opt. Mater.* 2000507 (2020).
153. C. D. S. Brites, A. Millán, and L. D. Carlos, "Chapter 281 - Lanthanides in Luminescent Thermometry," in *Handbook on the Physics and Chemistry of Rare Earths*, B. Jean-Claude and P. Vitalij K., eds., Including Actinides (Elsevier, 2016), Vol. 49, pp. 339–427.
154. R. G. Geitenbeek, P. T. Prins, W. Albrecht, A. van Blaaderen, B. M. Weckhuysen, and A. Meijerink, " $\text{NaYF}_4:\text{Er}^{3+}, \text{Yb}^{3+}/\text{SiO}_2$ Core/Shell Upconverting Nanocrystals for Luminescence Thermometry up to 900 K," *J. Phys. Chem. C* **121**, 3503–3510 (2017).
155. C. Zaldo, "Lanthanide-Based Luminescent Thermosensors: From Bulk to Nanoscale," in *Lanthanide-Based Multifunctional Materials*, P. Martín-Ramos and M. Ramos Silva, eds. (Elsevier, 2018), pp. 335–379.
156. S. Balabhadra, M. L. Debasu, C. D. S. Brites, R. A. S. Ferreira, and L. D. Carlos, "Upconverting Nanoparticles Working As Primary Thermometers In Different Media," *J. Phys. Chem. C* **121**, 13962–13968 (2017).
157. A. de Juan and R. Tauler, "Chemometrics applied to unravel multicomponent processes and mixtures: Revisiting latest trends in multivariate resolution," *Analytica Chimica Acta* **500**, 195–210 (2003).
158. "MCR-ALS," <https://mcrals.wordpress.com/theory/mcr-als/>.
159. J. Jaumot, A. de Juan, and R. Tauler, "MCR-ALS GUI 2.0: New features and applications," *Chemom. Intell. Lab. Syst.* **140**, 1–12 (2015).
160. P. D. Wentzell, D. T. Andrews, D. C. Hamilton, K. Faber, and B. R. Kowalski, "Maximum likelihood principal component analysis," *J. Chemom.* **11**, 339–366 (1997).
161. C. Wyman, P. Sloan, and P. Shirley, "Simple Analytic Approximations to the CIE XYZ Color Matching Functions," *J. Comp. Graph. Tech.* **2**, (2013).
162. S. J. Williamson and H. Z. Cummins, *Light and Color in Nature and Art* (John Wiley and Sons, 1983).
163. "Prismalence Scotopic and Photopic Luminous Efficacy Curves," http://www.prismalenceuk.com/image_display?ccid=1174&blid=6&ppid=936&maxwidth=2.

164. X. Bai, H. Song, G. Pan, Y. Lei, T. Wang, X. Ren, S. Lu, B. Dong, Q. Dai, and L. Fan, "Size-Dependent Upconversion Luminescence in Er³⁺/Yb³⁺-Codoped Nanocrystalline Yttria: Saturation and Thermal Effects," *J. Phys. Chem. C* **111**, 13611–13617 (2007).
165. T. C. Rich and D. A. Pinnow, "Exploring the Ultimate Efficiency in Infrared-to-Visible Converting Phosphors Activated with Er and Sensitized with Yb," *J. Appl. Phys.* **43**, 2357–2365 (1972).
166. J. F. Suyver, A. Aebischer, S. García-Revilla, P. Gerner, and H. U. Güdel, "Anomalous power dependence of sensitized upconversion luminescence," *Phys. Rev. B* **71**, 125123 (3).
167. M. D. Shinn, W. A. Sibley, M. G. Drexhage, and R. N. Brown, "Optical transitions of Er³⁺ ions in fluorozirconate glass," *Phys. Rev. B* **27**, 6635–6648 (January 6).
168. M. L. Debasu, D. Ananias, I. Pastoriza-Santos, L. M. Liz-Marzán, J. Rocha, and L. D. Carlos, "All-In-One Optical Heater-Thermometer Nanoplatfrom Operative From 300 to 2000 K Based on Er³⁺ Emission and Blackbody Radiation," *Adv. Mater.* **25**, 4868–4874 (2013).
169. G. Liu, "Advances in the theoretical understanding of photon upconversion in rare-earth activated nanophosphors," *Chem. Soc. Rev.* **44**, 1635–1652 (2015).
170. I. N. Stanton, J. A. Ayres, J. T. Stecher, M. C. Fischer, D. Scharpf, J. D. Scheuch, and M. J. Therien, "Power-Dependent Radiant Flux and Absolute Quantum Yields of Upconversion Nanocrystals under Continuous and Pulsed Excitation," *J. Phys. Chem. C* **122**, 252–259 (2018).
171. C. Mi, J. Wu, Y. Yang, B. Han, and J. Wei, "Efficient upconversion luminescence from Ba₅Gd₈Zn₄O₂₁:Yb³⁺, Er³⁺ based on a demonstrated cross-relaxation process," *Sci. Rep.* **6**, 22545 (2016).
172. Y. Zhou, F. N. Castellano, T. W. Schmidt, and K. Hanson, "On the Quantum Yield of Photon Upconversion via Triplet–Triplet Annihilation," *ACS Energy Lett.* **5**, 2322–2326 (2020).
173. R. H. Page, K. I. Schaffers, P. A. Waide, J. B. Tassano, S. A. Payne, W. F. Krupke, and W. K. Bischel, "Upconversion-pumped luminescence efficiency of rare-earth-doped hosts sensitized with trivalent ytterbium," *J. Opt. Soc. Am. B* **15**, 996–1008 (1998).
174. A. H. Li and Q. Lü, "Power-dependent upconversion luminescence intensity in NaYF₄:Yb³⁺,Er³⁺ nanoparticles," *EPL* **96**, 18001 (2011).
175. H. Liu, C. T. Xu, D. Lindgren, H. Xie, D. Thomas, C. Gundlach, and S. Andersson-Engels, "Balancing Power Density based Quantum Yield Characterization of Upconverting Nanoparticles for Arbitrary Excitation Intensities," *Nanoscale* **5**, 4770–4775 (2013).
176. J. Christiansen, H. Lakhotiya, E. Eriksen, S. P. Madsen, P. Balling, and B. Julsgaard, "Analytical Model for the Intensity Dependence of 1500 nm to 980 nm Upconversion in Er³⁺: A New Tool for Material Characterization," *J. Appl. Phys.* **125**, 043106 (2019).
177. A. Monguzzi, J. Mezyk, F. Scotognella, R. Tubino, and F. Meinardi, "Upconversion-Induced Fluorescence in Multicomponent Systems: Steady-State Excitation Power Threshold," *Phys. Rev. B* **78**, 195112 (2008).
178. M. T. Berry and P. S. May, "Disputed Mechanism for NIR-to-Red Upconversion Luminescence in NaYF₄:Yb³⁺,Er³⁺," *J. Phys. Chem. A* **119**, 9805–9811 (2015).
179. J. H. Denning and S. D. Ross, "The Vibrational Spectra and Structures of Rare Earth Oxides in the A Modification," *J. Phys. C: Solid State Phys.* **5**, 1123 (1972).
180. M. Scheithauer, H. Knözinger, and M. A. Vannice, "Raman Spectra of La₂O₃ Dispersed on γ -Al₂O₃," *J. Catal.* **178**, 701–705 (1998).
181. Y. Iwodate, "Structures and Properties of Rare-Earth Molten Salts," in *Handbook on the Physics and Chemistry of Rare Earths*, J. G. Bünzli and V. K. Pecharsky, eds. (Elsevier, 2014), Vol. 44, pp. 87–168.
182. E. Cohen and H. W. Moos, "Vibronic Transitions of Hexagonal Rare-Earth Trichlorides. I. Pr³⁺ and Nd³⁺ in NdCl₃," *Phys. Rev.* **161**, 258–268 (1967).
183. J. W. Rakestraw and G. H. Dieke, "Spectra and Energy Levels of Er³⁺ in YCl₃," *J. Chem. Phys.* **42**, 873–878 (1965).

184. M. Y. Hossan, A. Hor, Q. Luu, S. J. Smith, P. S. May, and M. T. Berry, "Explaining the Nanoscale Effect in the Upconversion Dynamics of β -NaYF₄:Yb³⁺, Er³⁺ Core and Core–Shell Nanocrystals," *J. Phys. Chem. C* **121**, 16592–16606 (2017).
185. C. Würth, S. Fischer, B. Grauel, A. P. Alivisatos, and U. Resch-Genger, "Quantum Yields, Surface Quenching, and Passivation Efficiency for Ultrasmall Core/Shell Upconverting Nanoparticles," *J. Am. Chem. Soc.* **140**, 4922–4928 (2018).
186. Monayenkova A. S., Lezhava S. A., Popova A. A., and L. A. Tiphlova, "Enthalpy of formation of the yttrium ion in aqueous solution at infinite dilution," *The Journal of Chemical Thermodynamics* **33**, 1679–1686 (2001).
187. "Colour & Vision Research laboratory and database," <http://www.cvrl.org/>.
188. D. Poelman, N. Avci, and P. F. Smet, "Measured luminance and visual appearance of multi-color persistent phosphors," *Opt. Express* **17**, 358–364 (2009).
189. A. Stockman and L. T. Sharpe, "Into the twilight zone: the complexities of mesopic vision and luminous efficiency," *Ophthalmic Physiol. Opt.* **26**, 225–239 (2006).
190. Q.-C. Sun, Y. C. Ding, D. M. Sagar, and P. Nagpal, "Photon upconversion towards applications in energy conversion and bioimaging," *Progress in Surface Science* **92**, 281–316 (2017).
191. K. Krämer, "Resonance in Er³⁺ upconversion excitation," *J. Lumin.* **189**, 78–83 (2016).

Appendix

A.1. Method to find the ground term

- Fully filled orbitals do not contribute to angular momentum coupling.
- Use Hund's rules:
 - a. The lowest energy term will be the one with the largest value of spin multiplicity ($2S+1$)
 - b. If there are more than one term with same spin multiplicity, the lowest energy term will be the one with the largest value of L
 - c. The lowest energy level will be the one with $J = |L-S|$, if the orbital is less than half filled or $J = (L+S)$, if the orbital is more than half filled

Two examples are provided below for finding the ground terms:

1. $\text{Sm}^{3+} - [\text{Xe}] 4f^5$

Fully filled orbitals do not take part in coupling as their momenta cancel out.

Maximum possible total intrinsic spin, $S = 5 \times \frac{1}{2}$

Spin multiplicity = $2S+1 = 6$

Maximum possible total orbital momentum, $L = 3 + 2 + 1 + 0 - 1 = 5$ ($\rightarrow H$)

Therefore, ground term will be 6H with $(2L+1)(2S+1) = 66$ microstates

The orbital is less than half filled ($5 < 7$) \rightarrow for the ground level, total angular momentum $J = |L-S| = |5 - 5/2| = 5/2$

Therefore, ground level will be ${}^6H_{5/2}$ with $(2J+1) = 6$ degenerate microstates

2. $\text{Yb}^{3+} - [\text{Xe}] 4f^{13}$

Fully filled orbitals do not take part in the angular momentum coupling.

Maximum possible intrinsic spin, $S = 7 \times \frac{1}{2} + 6 \times -\frac{1}{2} = \frac{1}{2}$

Spin multiplicity = $2S + 1 = 2$

Maximum possible angular momentum, $L = 3 + 2 + 1 + 0 + -1 + -2 + -3 + 3 + 2 + 1 + 0 + -1 + -2 = 3$ ($\rightarrow F$)

Therefore, ground term will be 2F with $(2S+1)(2L+1) = 14$ microstates

The orbital is more than half filled ($13 > 7$) \rightarrow for the ground level, the total angular momentum $J = (L+S) = 7/2$

Therefore, ground level will be ${}^2F_{7/2}$ with $(2J+1) = 8$ degenerate microstates.

A.2. Microstate approach for finding all the energy levels of a configuration

1. Consider only the partially filled orbitals
2. Find the total number of microstates possible for the orbital
3. List all these microstates and find out the total intrinsic spin and total orbital spin for each state
4. Form a table showing the frequencies of all obtained values of total intrinsic spin and total orbital spin
5. To obtain different spectroscopic terms and corresponding levels, deduce smaller arrays from this table till an array consisting of only '1's is obtained.

Examples for finding all energy states of a configuration of 4f orbitals

1) $\text{Yb}^{3+} - [\text{Xe}] 4f^{13}$

Total number of possible microstates = $14! / (13! \times (14-13)!) = 14$

Table describing all possible 14 microstates:

No.	m_l							$M_L = \sum m_l$	$M_S = \sum m_s$
	3	2	1	0	-1	-2	-3		
1	$\uparrow\downarrow$	$\uparrow\downarrow$	$\uparrow\downarrow$	$\uparrow\downarrow$	$\uparrow\downarrow$	$\uparrow\downarrow$	\uparrow	3	$\frac{1}{2}$
2	$\uparrow\downarrow$	$\uparrow\downarrow$	$\uparrow\downarrow$	$\uparrow\downarrow$	$\uparrow\downarrow$	\uparrow	$\uparrow\downarrow$	2	$\frac{1}{2}$
3	$\uparrow\downarrow$	$\uparrow\downarrow$	$\uparrow\downarrow$	$\uparrow\downarrow$	\uparrow	$\uparrow\downarrow$	$\uparrow\downarrow$	1	$\frac{1}{2}$
4	$\uparrow\downarrow$	$\uparrow\downarrow$	$\uparrow\downarrow$	\uparrow	$\uparrow\downarrow$	$\uparrow\downarrow$	$\uparrow\downarrow$	0	$\frac{1}{2}$
5	$\uparrow\downarrow$	$\uparrow\downarrow$	\uparrow	$\uparrow\downarrow$	$\uparrow\downarrow$	$\uparrow\downarrow$	$\uparrow\downarrow$	-1	$\frac{1}{2}$
6	$\uparrow\downarrow$	\uparrow	$\uparrow\downarrow$	$\uparrow\downarrow$	$\uparrow\downarrow$	$\uparrow\downarrow$	$\uparrow\downarrow$	-2	$\frac{1}{2}$

7	↑	↑↓	↑↓	↑↓	↑↓	↑↓	↑↓	-3	1/2
8	↑↓	↑↓	↑↓	↑↓	↑↓	↑↓	↓	3	-1/2
9	↑↓	↑↓	↑↓	↑↓	↑↓	↓	↑↓	2	-1/2
10	↑↓	↑↓	↑↓	↑↓	↓	↑↓	↑↓	1	-1/2
11	↑↓	↑↓	↑↓	↓	↑↓	↑↓	↑↓	0	-1/2
12	↑↓	↑↓	↓	↑↓	↑↓	↑↓	↑↓	-1	-1/2
13	↑↓	↓	↑↓	↑↓	↑↓	↑↓	↑↓	-2	-1/2
14	↓	↑↓	↑↓	↑↓	↑↓	↑↓	↑↓	-3	-1/2

Frequency table of M_S and M_L :

		M_S	
		$-1/2$	$1/2$
M_L	3	1	1
	2	1	1
	1	1	1
	0	1	1
	-1	1	1
	-2	1	1
	-3	1	1

Here, the array consists of only '1's.

Hence only one spectroscopic term exists.

M_L varies from -3 to 3, indicating $L = 3 \rightarrow F$

M_S varies from $-1/2$ to $1/2$, $\rightarrow S = 1/2$

$$2S+1 = 2$$

Therefore, the spectroscopic term is 2F .

J varies from $|L-S|$ to $L+S$ in steps of 1 $\rightarrow 5/2$ to $7/2 \rightarrow 5/2 + 1 = 7/2 \rightarrow$ only two levels

So, the spectroscopic levels are ${}^2F_{5/2}$ and ${}^2F_{7/2}$.

The microstates of ${}^2F_{5/2}$ are ones with m_j values $-5/2, -3/2, -1/2, 1/2, 3/2, 5/2$ and the microstates of ${}^2F_{7/2}$ are ones with m_j values $-7/2, -5/2, -3/2, -1/2, 1/2, 3/2, 5/2, 7/2$ giving a total of 14 microstates

The ground level will be then ${}^2F_{7/2}$ according to Hund's rules.

2) $\text{Pr}^{3+} - [\text{Xe}] 4f^2$

Total number of possible microstates = $14! / (2! \times (14-2)!) = 91$

Table describing all possible 91 microstates:

No.	m_l							$M_L = \sum m_l$	$M_S = \sum m_s$
	3	2	1	0	-1	-2	-3		
1	$\uparrow\downarrow$							6	0
2	\uparrow	\uparrow						5	1
3	\uparrow		\uparrow					4	1
4	\uparrow			\uparrow				3	1
5	\uparrow				\uparrow			2	1
6	\uparrow					\uparrow		1	1
7	\uparrow						\uparrow	0	1
8	\downarrow	\uparrow						5	0
9		$\uparrow\downarrow$						4	0
10		\uparrow	\uparrow					3	1
11		\uparrow		\uparrow				2	1
12		\uparrow			\uparrow			1	1
13		\uparrow				\uparrow		0	1
14		\uparrow					\uparrow	-1	1

15	↓		↑					4	0
16		↓	↑					3	0
17			↑↓					2	0
18			↑	↑				1	1
19			↑		↑			0	1
20			↑			↑		-1	1
21			↑				↑	-2	1
22	↓			↑				3	0
23		↓		↑				2	0
24			↓	↑				1	0
25				↑↓				0	0
26				↑	↑			-1	1
27				↑		↑		-2	1
28				↑			↑	-3	1
29	↓				↑			2	0
30		↓			↑			1	0
31			↓		↑			0	0
32				↓	↑			-1	0
33					↑↓			-2	0
34					↑	↑		-3	1
35					↑		↑	-4	1
36	↓					↑		1	0
37		↓				↑		0	0
38			↓			↑		-1	0

39				↓		↑		-2	0
40					↓	↑		-3	0
41						↑↓		-4	0
42						↑	↑	-5	1
43	↓						↑	0	0
44		↓					↑	-1	0
45			↓				↑	-2	0
46				↓			↑	-3	0
47					↓		↑	-4	0
48						↓	↑	-5	0
49							↑↓	-6	0
50	↓	↓						5	-1
51	↓		↓					4	-1
52	↓			↓				3	-1
53	↓				↓			2	-1
54	↓					↓		1	-1
55	↓						↓	0	-1
56	↑	↓						5	0
57		↓	↓					3	-1
58		↓		↓				2	-1
59		↓			↓			1	-1
60		↓				↓		0	-1
61		↓					↓	-1	-1

62	↑		↓					4	0
63		↑	↓					3	0
64			↓	↓				1	-1
65			↓		↓			0	-1
66			↓			↓		-1	-1
67			↓				↓	-2	-1
68	↑			↓				3	0
69		↑		↓				2	0
70			↑	↓				1	0
71				↓	↓			-1	-1
72				↓		↓		-2	-1
73				↓			↓	-3	-1
74	↑				↓			2	0
75		↑			↓			1	0
76			↑		↓			0	0
77				↑	↓			-1	0
78					↓	↓		-3	-1
79					↓		↓	-4	-1
80	↑					↓		1	0
81		↑				↓		0	0
82			↑			↓		-1	0
83				↑		↓		-2	0

84					↑	↓		-3	0
85						↓	↓	-5	-1
86	↑						↓	0	0
87		↑					↓	-1	0
88			↑				↓	-2	0
89				↑			↓	-3	0
90					↑		↓	-4	0
91						↑	↓	-5	0

Frequency table of M_S and M_L :

		M_L												
		6	5	4	3	2	1	0	-1	-2	-3	-4	-5	-6
M_S	1		1	1	2	2	3	3	3	2	2	1	1	
	0	1	2	3	4	5	6	7	6	5	4	3	2	1
	-1		1	1	2	2	3	3	3	2	2	1	1	

The largest variation in M_L is from -6 to 6 indicating the presence of an $L = 6$ term.

In this case, $M_S = 0 \rightarrow S = 0$, a singlet state ($2S+1 = 1$)

Hence, we obtain the term 1I with $(2S+1)(2L+1) = 13$ microstates

J ranges from $L+S$ to $|L-S| \rightarrow 6$

The term thus has a single level 1I_6

The remaining frequency table is:

	M_L												
	6	5	4	3	2	1	0	-1	-2	-3	-4	-5	-6

M_S	1		1	1	2	2	3	3	3	2	2	1	1	
	0		1	2	3	4	5	6	5	4	3	2	1	
	-1		1	1	2	2	3	3	3	2	2	1	1	

Now, M_L varies from -5 to 5 when M_S varies from -1 to 1

Hence, $L = 5$ and $S = 1 \rightarrow 2S+1 = 3$, a triplet state

Spectroscopic term = 3H with $(2S+1)(2L+1) = 33$ microstates

J ranges from $L+S$ to $|L-S| \rightarrow J = 6, 5, 4$

Spectroscopic levels $\rightarrow {}^3H_6, {}^3H_5, {}^3H_4$

The remaining frequency table:

		M_L												
		6	5	4	3	2	1	0	-1	-2	-3	-4	-5	-6
M_S	1				1	1	2	2	2	1	1			
	0			1	2	3	4	5	4	3	2	1		
	-1				1	1	2	2	2	1	1			

Now, M_L varies from -4 to 4 when $M_S = 0$

Hence, $L = 4$ and $S = 0 \rightarrow 2S+1 = 1$, a singlet state

Spectroscopic term = 1G with $(2S+1)(2L+1) = 9$ microstates

J ranges from $L+S$ to $|L-S| \rightarrow J = 4$

Spectroscopic levels $\rightarrow {}^1G_4$

The remaining frequency table:

		M_L											
		6	5	4	3	2	1	0	-1	-2	-3	-4	-5

M_S	1				1	1	2	2	2	1	1			
	0				1	2	3	4	3	2	1			
	-1				1	1	2	2	2	1	1			

Now, M_L varies from -3 to 3 when M_S varies from -1 to 1

Hence, $L = 3$ and $S = 1 \rightarrow 2S+1 = 3$, a triplet state

Spectroscopic term = 3F with $(2S+1)(2L+1) = 21$ microstates

J ranges from $L+S$ to $|L-S| \rightarrow J = 4, 3, 2$

Spectroscopic levels $\rightarrow {}^3F_4, {}^3F_3, {}^3F_2$

The remaining frequency table:

		M_L												
		6	5	4	3	2	1	0	-1	-2	-3	-4	-5	-6
M_S	1						1	1	1					
	0					1	2	3	2	1				
	-1						1	1	1					

Now, M_L varies from -2 to 2 when $M_S = 0$

Hence, $L = 2$ and $S = 0 \rightarrow 2S+1 = 1$, a singlet state

Spectroscopic term = 1D with $(2S+1)(2L+1) = 5$ microstates

J ranges from $L+S$ to $|L-S| \rightarrow J = 2$

Spectroscopic level $\rightarrow {}^1D_2$

The remaining frequency table:

		M _L												
		6	5	4	3	2	1	0	-1	-2	-3	-4	-5	-6
M _S	1						1	1	1					
	0						1	2	1					
	-1						1	1	1					

Now, M_L varies from -1 to 1 when M_S varies from -1 to 1

Hence, L = 1 and S = 1 → 2S+1 = 3, a triplet state

Spectroscopic term = ³P with (2S+1)(2L+1) = 9 microstates

J ranges from L+S to |L-S| → J = 2, 1, 0

Spectroscopic levels → ³P₂, ³P₁, ³P₀

The remaining frequency table:

		M _L												
		6	5	4	3	2	1	0	-1	-2	-3	-4	-5	-6
M _S	1													
	0							1						
	-1													

Now, an array with only '1' as an element is remaining.

This gives the last term with L = 0 and S = 0.

2S+1 = 1, a singlet state → ¹S.

J ranges from L+ S to |L-S| → J = 0.

Spectroscopic level – 1S_0

Hence, the spectroscopic levels for Pr^{3+} : 1S_0 , 3P_2 , 3P_1 , 3P_0 , 1D_2 , 3F_4 , 3F_3 , 3F_2 , 1G_4 , 3H_6 , 3H_5 , 3H_4 and 1I_6 .

Using Hund's rule, the ground level can be predicted, but the order of excited states is determined experimentally.

The ground level is the one with maximum multiplicity, L value and $J = |L-S|$ (orbital less than half filled) $\rightarrow ^3H_4$.

A.3. Calculation of Scaling Factor

The spectrometer gives a value of photon counts proportional to the actual number of photons emitted. To convert this value of photon counts to the actual number of photons emitted, the scaling factor needs to be determined. This scaling factor is dependent on the measurement set-up and can be estimated from the number of emitted photons calculated from the input power translated into the photon-flux and the PLQY.

A.3.1. Using SrF_2 spectra

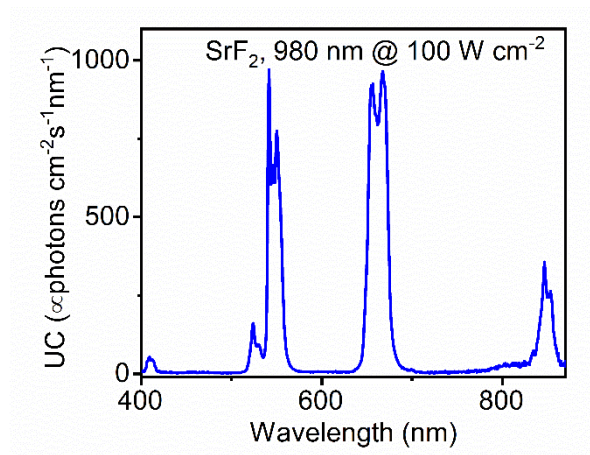


Figure A.1. UC spectra of $\text{SrF}_2:\text{Yb}^{3+}$, Er^{3+} (18%, 2%) at 100 W cm^{-2} of 980 nm excitation. Reproduced from Joseph et al [125]

$$P = 100 \text{ W cm}^{-2} = 493 \times 10^{18} \text{ photons s}^{-1} \text{ cm}^{-2} = 4.93 \times 10^{20} \text{ photons s}^{-1} \text{ cm}^{-2}$$

$$\text{PLQY of } \text{SrF}_2 \text{ at } 100 \text{ W cm}^{-2} = 0.9\% = 0.009$$

$$\Rightarrow \text{Expected UC in photons s}^{-1} \text{ cm}^{-2} = 4.93 \times 10^{20} * 0.009 = 4.4370 \times 10^{18}.$$

$$\Rightarrow \text{Scaling factor} = \frac{\text{Expected UC}}{\text{Area measured under UC spectra}} = \frac{4.4370e \times 10^{18}}{45165} = 9.8 \times 10^{13}.$$

This scaling factor is used for all spectra for SrF_2

A.3.2. Using NaYF₄ spectra

- Beam-line from M squared laser slightly changed as new shutter was included
- ND filter of OD 1 was placed before spectrometer
- UC Data corrected for the OD1 filter based on data from Thorlabs website¹

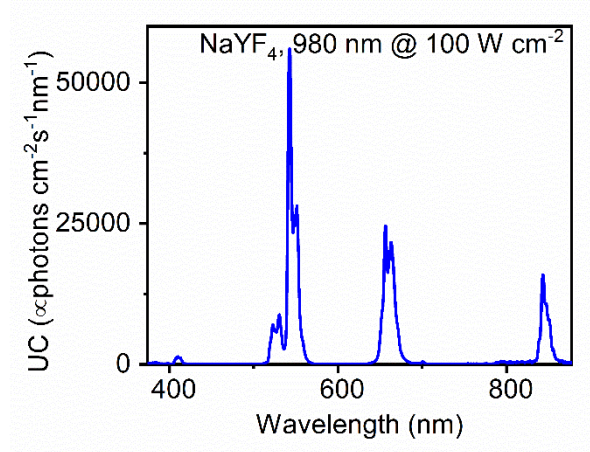


Figure A.2. UC spectra of NaYF₄:Yb³⁺, Er³⁺ (18%, 2%) at 100 W cm⁻² of 980 nm excitation. Reproduced from Joseph et al [125]

$$P = 100 \text{ W cm}^{-2} = 493 \times 10^{18} \text{ photons s}^{-1} \text{ cm}^{-2} = 4.93 \times 10^{20} \text{ photons s}^{-1} \text{ cm}^{-2}$$

$$\text{PLQY of SrF}_2 \text{ at } 100 \text{ W cm}^{-2} = 9\% = 0.09$$

$$\Rightarrow \text{Expected UC in photons s}^{-1} \text{ cm}^{-2} = 4.93 \times 10^{20} \times 0.09 = 4.437 \times 10^{19}$$

$$\Rightarrow \text{Scaling factor} = \frac{\text{Expected UC}}{\text{Area measured under UC spectra}} = \frac{4.437 \times 10^{19}}{1206168} = 3.67 \times 10^{13}$$

This scaling factor is used for all spectra for NaYF₄

A.4. Comparison of Calculated and Measured Luminance

To check if the calculations of luminance from experimentally measured UC intensity agrees with the calculations of theoretically calculated luminance using the following equation, certain assumptions are made.

$$L = P \frac{\lambda_{ex}}{hc} \eta_{abs} \eta_{plqy} \eta_{ff} \frac{hc}{\lambda_{em}} V(\lambda) 683 \frac{1}{4\pi} \quad (1)$$

¹Thorlabs, Thorlabs - ND10A Reflective Ø25 mm ND Filter, SM1-Threaded Mount, Optical Density: 1.0. <https://www.thorlabs.de/thorproduct.cfm?partnumber=ND10A> (accessed July 13, 2020).

Assumptions:

All green photons are emitted at the green peak of the emission spectrum, namely at 545 nm.

All red photons are assumed to be emitted at the peak of the red emission at 660 nm.

$\eta_{ff} = 1$ (the laser is not scanned)

$\eta_{abs980} = 0.5$, (powder sample has higher absorption)

\therefore , Absorption coefficient of Yb^{3+} at 980 nm is $1 \times 10^{-20} \text{ cm}^2$

\therefore , Absorption coefficient Er^{3+} at 1550 nm is $4 \times 10^{-21} \text{ cm}^2$

$\eta_{abs1550} = 0.2$ (as absorption is lesser at 1550 nm)

The values of the photopic luminosity function at 545 nm and 660 nm are:

$$V(\lambda)_{545} = 1$$

$$V(\lambda)_{660} = 0.1$$

A.4.1. 980 nm @ 10 W cm⁻² and 1550 nm @ 10 W cm⁻² in SrF₂

$\eta_{plqy980} = 0.001$, both green and red peaks are having approximately the same area, refer Figure 6.9(a).

Only red and green PLQYs contribute to luminance as NIR light is not visible.

So green PLQY = red PLQY = 0.0005

$$L_{980} = \frac{10 \times 10^4 \times 683 \times 980 \times 0.5}{4\pi} \left[\frac{1 \times 0.0005}{545} + \frac{0.1 \times 0.0005}{660} \right] = 2645 \text{ cd m}^{-2}$$

$\eta_{plqy1550} = 0.001$, (say)

R/G = 12, for SrF₂ excited with 1550 nm @ 10 W cm⁻², refer to Figure 6.3,

green PLQY = 0.08 × 0.001,

red PLQY = 0.92 × 0.001

$$L_{1550} = \frac{10 \times 10^4 \times 683 \times 0.001 \times 1550 \times 0.2}{4\pi} \left[\frac{1 \times 0.08}{545} + \frac{0.1 \times 0.92}{660} \right] = 482 \text{ cd m}^{-2}$$

Calculated $L_{\text{total}} = 3127 \text{ cd m}^{-2} \approx 3000 \text{ cd m}^{-2}$

Measured total L = 3500 cd m⁻²

A.4.2. 980 nm @ 100 W cm⁻² and 1550 nm @ 10 W cm⁻² in NaYF₄

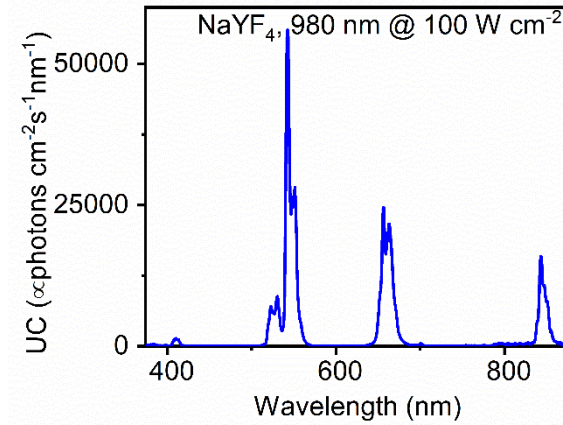


Figure A.3. UC spectra of NaYF₄:Yb³⁺, Er³⁺ (18%, 2%) at 100 W cm⁻² of 980 nm excitation with integrated areas of red and green emission. Reproduced from Joseph et al [125]

$$\eta_{plqy980} = 0.09$$

For pure 980 nm exc. at 100 W cm⁻²,

Total area = 1206168

Green area = 621490 (fraction = 0.5) => green PLQY = 0.52 × 0.09 = 0.047

Red area = 369584 (fraction = 0.3) => red PLQY = 0.3 × 0.09 = 0.027

$$L_{980} = \frac{100 \times 10^4 \times 683 \times 980 \times 0.5}{4\pi} \left[\frac{1 \times 0.047}{545} + \frac{0.1 \times 0.027}{660} \right] = 2.4 \times 10^6 \text{ cd m}^{-2}$$

For pure 1550 nm exc. at 10 W cm⁻²,

R/G = 3, refer Figure 6.2.

$\eta_{plqy1550} = 0.01$ (assuming to be an order low due to lower absorption),

red PLQY = 0.75 × 0.01 = 0.075,

green PLQY = 0.25 × 0.01 = 0.025

$$L_{1550} = \frac{100 \times 10^4 \times 683 \times 1550 \times 0.2}{4\pi} \left[\frac{1 \times 0.025}{545} + \frac{0.1 \times 0.075}{660} \right] = 9.6 \times 10^5 \text{ cd m}^{-2}$$

Calculated $L_{\text{total}} \approx 3.4 \times 10^6 \text{ cd m}^{-2}$

Measured total L = 4.5 × 10⁶ cd m⁻²

A.4.3. 980 nm @ 50 W cm⁻² and 1550 nm @ 10 W cm⁻² in SrF₂

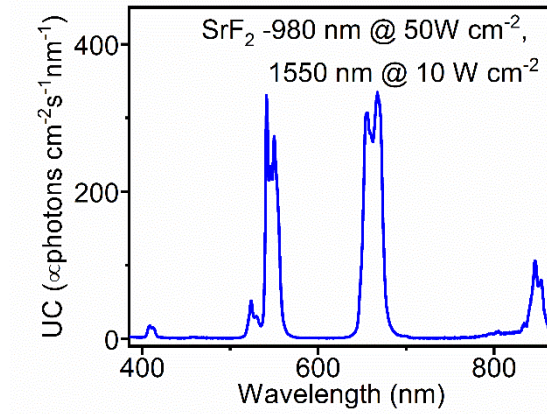


Figure A.4. UC spectra of SrF₂:Yb³⁺, Er³⁺ (18%, 2%) at 50 W cm⁻² of 980 nm excitation and 10 W cm⁻² of 1550 nm excitation. Reproduced from Joseph et al [125]

Assuming $\eta_{plqy980} = 0.01$, at such a low EPD

$$\text{Green fraction} = 4916/15021 = 0.3273$$

$$\text{Red fraction} = 7640/15021 = 0.508$$

$$L_{980} = \frac{50 \times 10^4 \times 683 \times 980 \times 0.5 \times 0.01}{4\pi} \left[\frac{1 \times 0.3273}{545} + \frac{0.1 \times 0.508}{660} \right] = 9.02 \times 10^4 \text{ cd m}^{-2}$$

$$\eta_{plqy1550} = 0.001 \text{ (assuming to be an order low due to lower absorption)}$$

R/G = 12 for SrF₂ excited with 1550 nm @ 10 W cm⁻², (refer to Figure 6.3),

$$\text{green PLQY} = 0.08 \times 0.001, \text{ red PLQY} = 0.92 \times 0.001$$

$$L_{1550} = \frac{50 \times 10^4 \times 683 \times 0.001 \times 1550 \times 0.2}{4\pi} \left[\frac{1 \times 0.08}{545} + \frac{0.1 \times 0.92}{660} \right] = 2.4 \times 10^3 \text{ cd m}^{-2}$$

$$\text{Calculated } L_{\text{total}} = 9.3 \times 10^4 \text{ cd m}^{-2}$$

$$\text{Measured total } L = 1 \times 10^5 \text{ cd m}^{-2}$$

A.4.4. 980 nm @ 100 W cm⁻² and 1550 nm @ 10 W cm⁻² in SrF₂

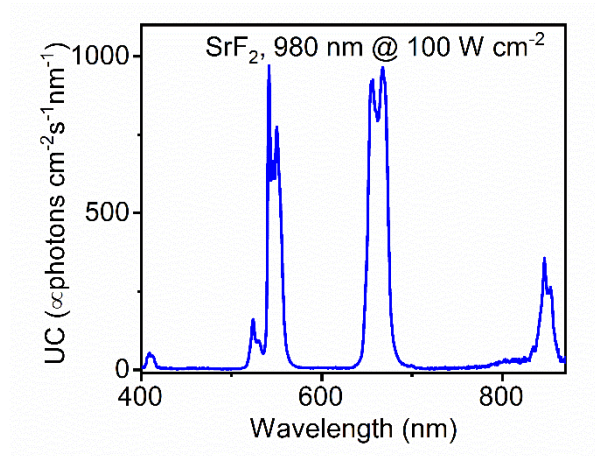


Figure A.5. UC spectra of SrF₂:Yb³⁺, Er³⁺ (18%, 2%) at 100 W cm⁻² of 980 nm. Reproduced from Joseph et al [125]

$$\eta_{plqy980} = 0.01 \text{ (measured value)}$$

$$\text{Green fraction} = 14247/45165 = 0.3154$$

$$\text{Red fraction} = 22608/45165 = 0.5006$$

$$L_{980} = \frac{100 \times 10^4 \times 683 \times 980 \times 0.5 \times 0.01}{4\pi} \left[\frac{1 \times 0.3154}{545} + \frac{0.1 \times 0.5006}{660} \right] = 1.7 \times 10^5 \text{ cd m}^{-2}$$

$$\eta_{plqy1550} = 0.001 \text{ (assuming to be an order lower than PLQY at 980 nm due to lower absorption)}$$

$$R/G = 12 \text{ for SrF}_2 \text{ excited with 1550 nm @ 10 W cm}^{-2}, \text{ (refer to Figure 6.3)}$$

$$\text{green PLQY} = 0.08 \times 0.001$$

$$\text{red PLQY} = 0.92 \times 0.001$$

$$L_{1550} = \frac{100 \times 10^4 \times 683 \times 0.001 \times 1550 \times 0.2}{4\pi} \left[\frac{1 \times 0.08}{545} + \frac{0.1 \times 0.92}{660} \right] = 4.8 \times 10^3 \text{ cd m}^{-2}$$

$$\text{Calculated } L_{\text{total}} = 1.75 \times 10^5 \text{ cd m}^{-2} \approx 2 \times 10^5 \text{ cd m}^{-2}$$

$$\text{Measured total } L = 2.9 \times 10^5 \text{ cd m}^{-2}$$

A.5. Estimation of errors

$$\text{Excitation power density} = \frac{\text{Measured power}}{\text{Area}}$$

- ⇒ Relative error in excitation power density = relative error in measured power + relative error in measured area

$$\text{Relative error in measured power of 980 nm beam} = \pm 1/30 = \pm 3.33 \%$$

$$\text{Relative error in area of 980 nm beam} = \pm 1/300 = \pm 0.33 \%$$

- ⇒ Relative error in 980 nm excitation power density = ± 3.66 %

$$\text{Relative error in measured power of 1550 nm beam} = \pm 1/25 = \pm 4 \%$$

$$\text{Relative error in area of 1550 nm beam} = \pm 1/250 = \pm 0.4 \%$$

- ⇒ Relative error in 1550 nm excitation power density = ± 4.4 %

Luminance is calculated with the equation,

$$L = P \frac{\lambda_{ex}}{hc} \eta_{abs} \eta_{plqy} \eta_{ff} \frac{hc}{\lambda_{em}} V(\lambda) 683 \frac{1}{4\pi}$$

Assuming 1% relative error in each of η_{abs} and η_{plqy}

Relative error in $V(\lambda)$ is assumed to be 1% when we consider all green photons to be emitted at 545 nm and red photons to be emitted at 650 nm.

Relative error in excitation power density = ± 4 % (taking highest error)

- ⇒ Relative error in Luminance = sum of relative errors of each term in the equation
- $$= \pm (4 \% + 1 \% + 1 \% + 1 \%)$$
- $$= \pm 7 \%$$